24153

National Library of Canada | Bibliothèque nationale du Canada | CANADIAN THESES ON MICROFICHE | THÈSES CANADIENNES SUR MICROFICHE

NAME OF AUTHOR/*NOM DE L'AUTEUR* GRAHAM WALKER

TITLE OF THESIS/*TITRE DE LA THÈSE* MICROWAVE BREAKDOWN OF ALUMINA COATED CERAMIC

UNIVERSITY/*UNIVERSITÉ* ALBERTA

DEGREE FOR WHICH THESIS WAS PRESENTED/ *GRADE POUR LEQUEL CETTE THÈSE FUT PRÉSENTÉE* PhD.

YEAR THIS DEGREE CONFERRED/*ANNÉE D'OBTENTION DE CE GRADE* 1975

NAME OF SUPERVISOR/*NOM DU DIRECTEUR DE THÈSE* DR. G.B. WALKER

Permission is hereby granted to the NATIONAL LIBRARY OF CANADA to microfilm this thesis and to lend or sell copies of the film.

The author reserves other publication rights, and neither the thesis nor extensive extracts from it may be printed or otherwise reproduced without the author's written permission.

L'autorisation est, par la présente, accordée à la BIBLIOTHÈQUE NATIONALE DU CANADA de microfilmer cette thèse et de prêter ou de vendre des exemplaires du film.

L'auteur se réserve les autres droits de publication; ni la thèse ni de longs extraits de celle-ci ne doivent être imprimés ou autrement reproduits sans l'autorisation écrite de l'auteur.

DATED/*DATÉ* 28/4/1975 SIGNED/*SIGNÉ* Graham Walker

PERMANENT ADDRESS/*RÉSIDENCE FIXÉ* 4134 - 44 Street
Red Deer, Alberta
Canada

NL-91 (3-74)

THE UNIVERSITY OF ALBERTA

MICROWAVE BREAKDOWN OF ALUMINA COATED CERAMIC

by

Graham Walker

A Thesis

Submitted to the Faculty of Graduate Studies and Research

In Partial Fulfilment of the Requirements for the Degree

of Doctor of Philosophy

Department of Electrical Engineering

Edmonton, Alberta

Spring, 1975

© Graham Walker 1975

THE UNIVERSITY OF ALBERTA

FACULTY OF GRADUATE STUDIES AND RESEARCH

The undersigned certify that they have read, and recommend to the Faculty of Graduate Studies and Research, for acceptance, a thesis entitled MICROWAVE BREAKDOWN OF ALUMINA COATED CERAMIC submitted by GRAHAM WALKER in partial fulfilment of the requirements for the degree of Doctor of Philosophy in Electrical Engineering.

.....G.B. Walker.....
Supervisor

..F.E. Vermeulen

.....J. Charles

...J. John McDonald

..F. Kreyszig.....
External Examiner

Date.....8 Jan. 76

ABSTRACT

The feasibility of using optical coatings to prevent discharge induced surface breakdown of titania ceramic in a high power microwave field was investigated. Titania discs polished to optical flatness were coated with up to 4μm of alumina utilizing RF reactive sputtering in a triode system constructed for this project. The films were uniform and controllable and resulted in no net reduction of the titania provided a set procedure was followed. The discs were tested in one of two cavity geometries: either a short cylindrical cavity containing one disc; or a longer structure with up to five discs to simulate conditions in an electron accelerator. The systems necessary for conducting the high power breakdown studies have been described in some detail in addition to the relevant low power measurements. The single disc cavity was adapted to permit the excitation of higher order TE_{01n} modes in quadrature to the high power TM_{011} mode. By observing the response of the probing TE modes the nature of microwave vacuum discharges at low and high power was studied. Multipactor discharges prevalent at low power with alumina coated discs were eliminated by means of a thin titanium film to suppress secondary electron emission. Titania discs coated with over 1μm of alumina were not subject to surface breakdown at fields up to 350 kV/cm and were capable of supporting fields up to 250 kV/cm continuously without damage.

ACKNOWLEDGEMENTS

The author wishes to acknowledge the contribution of Dr.E.Sang who proposed the research topic and provided initial guidance. For his continual encouragement and patience, the author is deeply indebted to Dr.G.B.Walker, who supervised the project to completion.

Appreciation is expressed for the excellent standard of technical support provided by the non-academic staff of the department, especially to Mr.W.B.Arnold who devoted much time in polishing the titania discs, to Mr.E.Buck who undertook the construction of the sputtering apparatus and to Mr.J.J.George who aided in his capacity as technician of the accelerator group.

In addition to funding a portion of the research expenses, the National Research Council also made available a bursary and postgraduate scholarships which the author very gratefully acknowledges. Gratitude must also be conveyed to the University of Alberta for further financial assistance.

TABLE OF CONTENTS

		Page
CHAPTER 1	INTRODUCTION	1
1.1	Motivation for the Investigation	1
1.2	Breakdown of Titania in Vacuum	4
	1.2.1 The Nature of TiO_2	4
	1.2.2 Breakdown in DC Fields	5
	1.2.3 Breakdown in Microwave Fields	7
1.3	Breakdown Mechanisms in Solid Dielectrics	9
1.4	Breakdown Initiated by Surface Discharges	13
	1.4.1 Multipactor Induced Breakdown	13
	1.4.2 Surface Charging	14
	1.4.3 Spark Discharge Initiated Breakdown	15
	1.4.4 Field Emission breakdown	16
1.5	Scope of the Present Work	16
CHAPTER 2	METHODS OF INHIBITING BREAKDOWN	18
2.1	Introduction	18
2.2	Micron Thick Optical Coatings	19
2.3	Thin Titanium Coatings	20
	2.3.1 Metallic Films for Multipactor Suppression	20
	2.3.2 S.E.E. Dependence Upon Film Thickness	23
	2.3.3 Electrical Properties	24
	2.3.4 EM Wave Propagation Through Metallic Films	26
2.4	Prevention of Edge Breakdown	27

		Page
CHAPTER 3	THIN FILM DEPOSITION	29
3.1	Introduction	29
3.2	Physical Sputtering	29
	3.2.1 Background	29
	3.2.2 RF Reactive Sputtering	30
3.3	The Sputtering System	33
	3.3.1 General Description	33
	3.3.2 Operation	36
3.4	Characteristics of Sputtered Films	37
	3.4.1 Measurement of Film Thickness	37
	3.4.2 The Sputtered Alumina Films	40
	3.4.3 The Sputtered Titanium Film	43
3.5	Effects of Sputtering onto Titania Substrates	47
	3.5.1 Heating in Vacuum	47
	3.5.2 Reduction during Sputtering	47
	3.5.3 Resistivity Measurements	49
3.6	Edge Coating of the Discs	51
3.7	Preparation of the Titania Discs	52
	3.7.1 Machining of the Discs	52
	3.7.2 Sputtering of the Alumina Layer	52
	3.7.3 Rim Coating and Fitting of the Copper Ring	53
	3.7.4 Titanium Surface Coating	53
	3.7.5 Some Comments on Ceramic Preparation	54

		Page
CHAPTER 4	THE SINGLE CELL MICROWAVE CAVITY	55
4.1	The π Mode Structure	55
	4.1.1 Introduction	55
	4.1.2 Field Relationships	56
	4.1.3 Cavity Dimensions	58
	4.1.4 Cavity-Coupling Calculations	61
4.2	Construction of the Cavity	64
	4.2.1 Geometry	64
	4.2.2 Clamping of the Cavity	66
	4.2.3 Cavity-Mount Contact	66
4.3	Thermal Effects	67
	4.3.1 Introduction	67
	4.3.2 Heat Flow in the Disc	67
	4.3.3 Thermal Stress	76
CHAPTER 5	LOW POWER MICROWAVE TESTS	81
5.1	The Low Power Test Bench	81
	5.1.1 Basic S-Band Equipment	81
	5.1.2 Polarad Frequency Lock Circuit	83
	5.1.3 Analog Division Circuit	87
5.2	Perturbation Measurements	80
	5.2.1 Introduction	89
	5.2.2 The Axial Electric Field Profile	90
	5.2.2.1 Effect of Bead Size on Field Profile	93
	5.2.2.2 Effect of the Waveguide-Cavity Coupling Iris	95

		Page
	5.2.2.3 Effect of an Electron Beam Iris through the Disc	95
	5.2.3 Calculation of R_o/Q	99
	5.2.4 R_o/Q Measurement-Micrometer Method	100
5.3	Determination of Peak Axial Field	103
	5.3.1 Calculation of Q	103
	5.3.2 Measurement of Q	107
	5.3.3 Calculation of Axial Field	107
5.4	Cavity Thermal Characteristics	110
	5.4.1 Introduction	110
	5.4.2 Frequency Dependence upon Temperature	110
	5.4.3 Dependence of Q on Temperature	116
CHAPTER 6	EXPERIMENTAL SYSTEMS	119
6.1	Introduction	119
6.2	High Power Microwave Systems	121
	6.2.1 The Pulse Modulator	121
	6.2.2 The Magnetron	123
	6.2.3 Waveguide Circuit for High Power	123
	6.2.4 Calibration of the High Power System	127
6.3	Vacuum System	130
	6.3.1 Description	130
	6.3.2 Capabilities and Limitations of the Vacuum System	132

		Page
6.4	Other Instrumentation	133
	6.4.1 Radiation Detectors	133
	6.4.2 Temperature Measurements	134
	6.4.3 Photography	134
CHAPTER 7	EXPERIMENTS AT HIGH POWER	135
7.1	Experimental Procedure	135
	7.1.1 Preliminary Considerations	135
	7.1.2 TM_{011} Mode Experiments	136
	7.1.3 Experimental Quantities Monitored	137
7.2	Experimental Measurements	137
	7.2.1 Peak Power	138
	7.2.2 Pressure Fluctuations	143
	7.2.3 Radiation Measurements	143
	7.2.4 Thermal Measurements at High Power	144
7.3	Cavity Discharges	147
	7.3.1 Introduction	147
	7.3.2 Conditioning Discharges	147
	7.3.3 Multipactor	148
	7.3.4 High Power Phenomena	148
7.4	Microscopic Investigation of the Discs	151
7.5	Quantitative Results	152

		Page
CHAPTER 8	DISCHARGE DIAGNOSTICS USING A MICROWAVE PROBE	159
8.1	Introduction	159
8.2	Microwave Discharges in Vacuum	160
	8.2.1 Electron Motion in the Cavity	160
	8.2.2 Ionization Efficiency of Energetic Electrons	165
	8.2.3 Ionization Initiated Discharges	166
8.3	The Microwave Probe	173
	8.3.1 Perturbation of EM Waves in a Plasma	173
	8.3.2 Selection of Probing Modes	177
	8.3.3 Cavity Modifications for Probe	178
	8.3.4 The Microwave Probe Circuit	179
8.4	Microwave Probe Measurements	182
8.5	Interpretation of the Probe Results	185
	8.5.1 Frequency Dependence of TE_{01n} Modes	185
	8.5.2 Comparison of the TE_{014} and TE_{015} Modes	187
	8.5.3 Comparison of the TE_{014} and TM_{011} Modes	191
	8.5.4 Electron Density	196
CHAPTER 9	EXPERIMENTS WITH MULTI-DISC CAVITY	198
9.1	Development of a Longer Structure	198
	9.1.1 Introduction	198
	9.1.2 The Confluent Structure	198
	9.1.3 Practical Considerations of the Confluent Structure	200

		Page
9.2	Low Power Measurements	201
	9.2.1 Introduction	201
	9.2.2 Field Profile	201
	9.2.3 Effect of Cavity Length on Parameters	201
9.3	The Electron Gun and Detector Circuits	206
	9.3.1 The Electron Gun	206
	9.3.2 The Gun Trigger Circuit	207
	9.3.3 The Electron Beam Detector	209
9.4	High Power Experiments	209
	9.4.1 Introduction	209
	9.4.2 Experimental Results	210
	9.4.3 Results Using 4 Disc Structure	212
	9.4.4 Summary of Results	213
CHAPTER 10	CONCLUDING REMARKS	216
REFERENCES		221
APPENDIX A	PROPERTIES OF TITANIA	231
APPENDIX B	ERROR ANALYSIS	233

LIST OF TABLES

		Page
3.1	Characteristic Colours of Thin Transparent Films	41
3.2	Sputtering of Titanium Films	46
3.3	Surface Resistance and Resistivity of Titania	50
4.1	Summary of Cavity Dimensions for Disc #8	59
5.1	Bead Perturbation	101
5.2	Summary of Low Power Tests	109
7.1	Discharge Pulses	149
7.2	Summary of High Power Breakdown Tests	154
7.3	Comparison of Different Surfaces	157
8.1	Cavity Electron Energies	163
8.2	Parameters for TM_{011}, TE_{013}, TE_{014} and TE_{015} Modes	188
9.1	Maximum Frequency Perturbation for Various Cavity Lengths	203
9.2	Disc Characteristics	211
9.3	Summary of Breakdown Tests	214
9.4	Characteristics of Discs after Breakdown	214

LIST OF FIGURES

Figure		Page
1.1	Dielectric Loaded Accelerator	3
1.2	Damage Observed in Titania Discs Subjected to a Microwave Field	8
2.1	Talysurf Profiles of Titania Surfaces	21
2.2	Representative S.E.E. Curves	22
2.3	Energy Spectrum of Secondary Electrons Emitted from Ti	22
2.4	Propagation Through Thin Metallic Films	26
3.1	Geometry of Triode Sputtering System	31
3.2	Thin Film Deposition Facilities	34
3.3	View Inside Chamber during the Sputtering of Alumina onto a Titania Disc	34
3.4	Determination of Sputtering Rate for Al_2O_3	39
3.5	AC Ohmmeter Circuit	44
3.6	Change of Titanium Film Resistance on Exposure to Air	46
4.1	The Single Cell Cavity	55
4.2	Cavity Geometry	59
4.3	Dependence of Cavity Resonance on Disc Thickness	60
4.4	Cavity Assembly and Clamping	65
4.5	Relative Energy Density through the Ceramic Disc	68
4.6	Temperature Distribution in Ceramic Disc at $\eta=0$	72
4.7	Radiative Contribution to Heat Loss from the Disc	75
4.8	Thermal Stresses Induced in the Ceramic Disc	77
4.9	Operating Limits for Titania Discs	80

Figure		Page
5.1	The Low Power Microwave Bench	82
5.2	Frequency Locking Circuit (a) Reference Circuit and Phase Detector	84
5.3	Frequency Locking Circuit (b) Error Signal Processing	85
5.4	Output Characteristics of Cavity	86
5.5	Tracking Error of Lock Circuit	86
5.6	Analogue Multiplication/Division Circuit	88
5.7	Physical Layout for Bead Perturbation Measurements	92
5.8	Effect of Bead Dimensions on Field Profile	94
5.9	Effect of Coupling Iris on Field Profile	96
5.10	Effect of Disc Iris on the Field Profile	97
5.11	Effect of Disc Iris Diameter on Cavity Resonance	98
5.12	Perturbation Measurements Using Micrometer	102
5.13	Cavity Temperature Dependence	115
5.14	Thermal Time Constant of Cavity	117
5.15	Effect of Wall Losses on Temperature	118
6.1	View of High Power Facility	120
6.2	Block Diagram of Pulse Modulator	122
6.3	Block Schematic of Pulse Modulator	122
6.4	High Power System	124
6.5	Frequency Pulling Characteristics of Magnetron	126
6.6	High Power Calibration Circuit	128
6.7	Vacuum System	131

Figure		Page
7.1	Pulse Waveforms for Disc #8	139
7.2	Effect of Cavity Filling Time	142
7.3	Variation of Cavity Parameters with Power	146
7.4	Discharge Regions	149
7.5	Luminescence on Ceramic Surface and Cavity Discharges Observed at High Power	150
7.6	Summary of Breakdown Results for Titania Discs	156
8.1	Electron Trajectories	164
8.2	Ionization Efficiency of Electrons	167
8.3	Electron Trajectories and Velocities at 300 kV/cm	170
8.4	Electron Trajectories and Velocities at 100 kV/cm	171-2
8.5	Exploded View of Cavity Fitted with Probe Adapter	180
8.6	Assembled Cavity with Probe Modification	180
8.7	Microwave Probe Circuit	181
8.8	Perturbation of Microwave Probe at High Power	184
8.9	Comparison of TE_{014} and TE_{015} Modes	190
8.10	Comparison of TE_{014} and TM_{011} Modes	194
9.1	Field Profile in a Four Disc Structure	202
9.2	Resonant Frequency vs Cavity Length	204
9.3	Variation of Cavity Parameters with Cavity Length	205
9.4	Electron Gun and Detector Circuits	208

LIST OF SYMBOLS

Where notation has not been extensively used, the chapter to which it is restricted has been indicated in brackets.

A	defined absorption factor [2]; temperature normalization factor [4]
a	waveguide dimension [4]; bead radius [5]
B, B_2	defined constants
B_z, B_r, B_ϕ	components of magnetic flux density
b	waveguide dimension [4]
C_v	heat capacity
c	velocity of light
D	electric displacement
d	film thickness [3]; electron cloud thickness [8]
$E; E_0, E_2$	electric field intensity; in vacuum, in dielectric
E_z, E_r, E_ϕ	electric field components in cylindrical co-ordinates
E_c	critical (breakdown) electric field
E_∞	steady state electric field [7]
E_y	Young's Modulus of elasticity
e	electronic charge
F_H, F_E	magnetic, electric force
$f, (f_0)$	(resonant) frequency
f_c	cut-off frequency in waveguide
g	electron cloud dimension =R-r [8]
H	magnetic field intensity
H_z, H_r, H_ϕ	magnetic field components in cylindrical co-ordinates
Δh	penetration of micrometer in cavity [5]

J	conduction current
$J_n(k_c r)$	Bessel's function of order n
K	thermal conductivity [4]; defined mode factor [8]
k	shape factor in perturbation measurements [5]
k_c	wave constant
L	cavity length $=2n(q+p)$
m	interferometer fringe shift [3]
m_e	electron mass
N_e	electron density (with mode subscript)
n	refractive index [3]; number of discs in cavity [4]; electron density [8]; mode subscript (as in TM_{01n})
$P; P_i, P_r, P_t$	power; incident, reflected, transmitted power
P_d	power absorbed in dielectric
P_∞	state state power absorption in cavity [7]
p	pressure [4]; vacuum half-length of single cell cavity
$Q; Q_o, Q_L, Q_{ext}$	quality factor; unloaded, loaded, external Q
$Q_{in}, Q_{cond}, Q_{rad}$	input, conduction and radiation heat transfer terms
q	half-thickness of disc in single cell cavity
R	cavity radius; defined reflection factor [2]
R_s	surface resistance in ohms/square
R_o	shunt impedance
r	radius of coupling iris [4]; radial variable or subscript
r_{imax}	radius of maximum ionization probability
T	defined transmission factor [2]; temperature
T_c	critical (breakdown) temperature
T_ε	temperature in dielectric
T_o	cavity wall temperature (taken as 300°K)
TE_{01n}	transverse electric field mode in waveguide

TM_{01n}	transverse magnetic field mode in waveguide
t	time variable; defined variable [2]; ring thickness [4]
U	stored energy; electron energy [8]
U_{vac}, U_{diel}	cavity energy in vacuum, in dielectric
U_{sum}	$U_{vac}+U_{diel}$
U_m	mean electron energy
V	voltage; volume [5]
v	electron velocity
W	cavity losses
W_{side}, W_{end}	losses in side and end walls of cavity
W_{diel}	losses in dielectric
W_{wall}	$W_{side}+W_{end}$
W_{sum}	$W_{wall}+W_{diel}$
x,y	dimensional variables in waveguide
Z_0, Z_2	cavity wave impedances
z	axial variable or subscript
α	attenuation factor in dB; defined variable [2]
α_i	ionization coefficient
α_ε	thermal coefficient of dielectric constant
$\alpha_{TiO_2}, \alpha_{Cu}$	coefficients of thermal linear expansion
β_0, β_2	propagation constant in vacuum, in dielectric
β_c	cavity coupling coefficient
γ	complex propagation constant
δ	skin depth; secondary electron emission (SEE) coefficient
δ'	'true' SEE coefficient
$\varepsilon; \varepsilon_0, \varepsilon_2$	permittivity; of vacuum, of dielectric

ε_r	relative dielectric constant = $\frac{\varepsilon_2}{\varepsilon_0}$
ε'	real part of permittivity
ε''	imaginary part of permittivity
ε_p	plasma permittivity [8]
ε_T	thermal emissivity
η	axial variable (referred to disc); coefficient for inelastically reflected electrons in SEE [2]
Θ	defined temperature constant [1] or variable [5]
θ	phase angle
κ	defined parameter [2]
λ	wavelength (optical [2,3] otherwise microwave)
λ_ε	wavelength in dielectric
λ_g	guide wavelength
λ_c	waveguide cut-off wavelength
λ_{Ti}	electron mean free path length in Ti [2]
μ, μ_0	permeability
ν_m	electron-molecular collision frequency
ρ	resistivity; defined parameter
ρ_m	mass density
ρ_0	bulk resistivity
σ	electrical conductivity; mechanical stress [4]; surface charge density [8]
σ_0	bulk conductivity
σ_{Ti}	surface conductivity of Ti
σ_T	Stefan-Boltzmann constant
σ_h	hoop stress [4]
σ_r	radial stress [4]
σ_θ	tangential stress [4]

τ	defined time constant
$\delta\tau$	perturbing volume [5]
ϕ	variable or subscript in cylindrical co-ordinates
$\omega, (\omega_0)$	(resonant) angular frequency
ω_p	plasma frequency
tan δ	loss tangent = $\frac{\varepsilon''}{\varepsilon'}$
VSWR,SWR	voltage standing wave ratio

CHAPTER 1

INTRODUCTION

1.1 Motivation for the Investigation

An electric field within a dielectric material will, under certain conditions, alter the physical or chemical properties of the dielectric. The dynamic rise of conductivity in a gas or liquid, or the failure of a solid as the electric field is increased is termed dielectric breakdown, the study of which is of considerable theoretical and practical interest as advanced materials and technologies are introduced.

In fluid media, a definition which may be extended to vacuum, the most common manifestation is the electrical discharge, a complex phenomenon involving the ionization, recombination, attachment and diffusion of charged particles. After removal of the field, the liquid or gas usually returns to its original state but during the discharge, the particles may interact with the walls of the containing chamber, generate RF, visible or ionizing radiation, or initiate chemical reactions.

Dielectric breakdown in solids is an irreversible effect characterized by increased electrical conductivity, a change in chemical composition and in severe cases, mechanical failure due to thermally induced stress and melting of the bulk material. Strictly the term should be applied to breakdown resulting from the direct influence of the electric field by some mechanism such as ohmic loss or the excitation of lattice electrons. It will be appreciated however, that when electrical discharges occur at

the surface of the dielectric, breakdown may be accelerated by the combined effect of the internal field and the external discharge.

In recent years dielectrics have been incorporated in microwave components designed to operate at high average and peak power. Examples include phase shifters, klystron windows, filters and slow wave structures such as travelling wave tubes, particle accelerators and high energy particle separators. In each of the above cases, the dielectric, usually a ceramic, is a primary element in the system and consequently is located in a region of high electric field. The presence of a microwave discharge has often led to failure of such dielectric elements.

In one such instance, titania ceramic, which possesses a very low loss at microwave frequencies and a permittivity an order of magnitude higher than most other ceramics, has not been an unqualified success when incorporated in slow wave structures which could exploit these desirable properties.

By employing titania discs spaced along the inside of a cylindrical waveguide as illustrated in Figure 1.1, Harvie and his co-workers constructed an anisotropic dielectric-loaded accelerator [1]. A central iris through each disc allows the transit of electrons which are then accelerated by a TM mode wave. The laminated dielectric retards the propagation of the travelling wave in order that energy may be coupled from the axial electric field to the electron beam. Although the accelerator demonstrated the higher efficiency of the dielectric loaded structure in comparison to its metal iris counterpart, discharges at the titania surface resulted in degraded performance at high power. Oil contamination of the titania was subsequently discovered to be the source of the trouble, but more complex problems were to be encountered with titania in such an

application.[1]

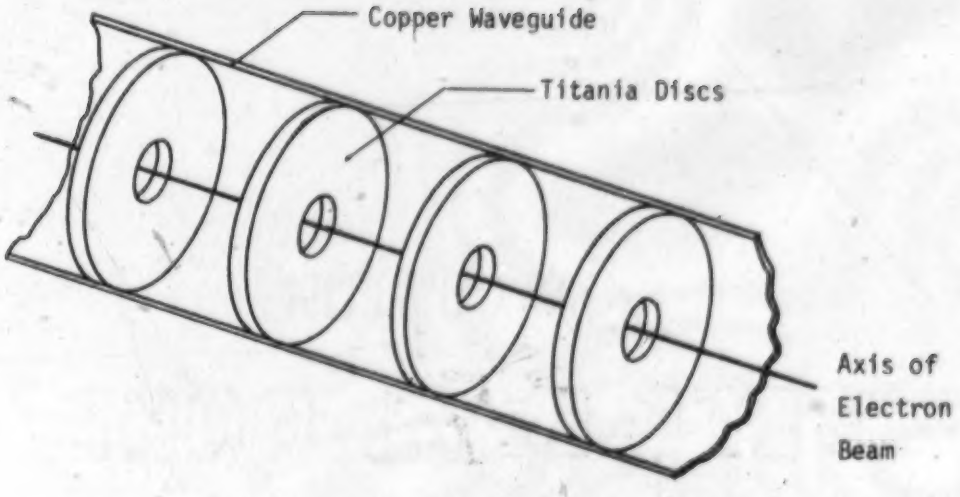

Figure 1.1 Dielectric Loaded Accelerator

An alternative to the travelling wave structure described utilizes a similar disc loaded tube; however, by operating it in a resonant mode higher fields can be achieved. As in other linear accelerators, the electric field is pulsed to a few hundred kV/cm. Unfortunately at such field strengths, discharges are not uncommon despite care in designing and preparing the system and it was discovered that titania was highly susceptible to damage in a vacuum environment.

In an endeavour to acquire data on the behaviour of titania in microwave and also DC fields a program of research was initiated at Queen Mary College, London and later transferred to the University of British Columbia. The present work is an extension of that research.

1.2 Breakdown of Titania in Vacuum

1.2.1 The Nature of TiO_2

Titania (titanium dioxide, also called rutile) is abundant in nature but may be distinguished from other common refractory ceramics by individual properties which are in high demand for selected applications and other negative characteristics which limit more widespread use. A high refractive index makes it attractive to both paint manufacturers and the optics industry. Of greater significance to the electronic engineer is the associated high relative dielectric constant (~100) and a very low loss ($\tan\delta \sim .0003$ at microwave frequencies). It has thus found wide use in the manufacture of capacitors over the past few decades. In normal capacitor applications the high thermal dependence of the permittivity is the most undesirable characteristic; however, when incorporated in slow wave structures handling high average and high peak powers, two other restricting properties of titania become troublesome: inadequate thermal conductivity and chemical instability when heated in vacuum.

Although single crystal rutile is available, most applications use polycrystalline material. Pure rutile powder is white prior to sintering and firing but due to binding agents the final product assumes a straw-yellow colour. Upon heating in vacuum an irreversible colour change takes place for temperatures in excess of 350°C, the surface becoming a light grey. At higher temperatures (over 600°C) it becomes much darker, indicating a change in the stoichiometry of the rutile ceramic. In the oxygen deficient environment, the chemical formula for titania may be given as TiO_n, where $1.95<n<2$, the structure remaining tetragonal [2,3]. As

further reduction occurs, other oxides with a triclinic structure appear until there is a shift to the monoclinic lattice of Ti_2O_5. Other lower order oxides are Ti_2O_3 and TiO [4], possessing semiconductor and metallic characteristics respectively, although in fact the titania will include a continuous sequence of lower oxides specified by $1<n<2$, in a manner similar to other transition metal oxides. These lower oxides have a brown-velvet-black colour which accounts for the colour change on heating. This is accompanied by a substantial increase of electrical conductivity which aids thermal runaway and may lead to catastrophic failure by an accelerated mechanism, that of electrochemical breakdown [5].

If the ceramic is in a high power microwave field it will be readily appreciated that the heat generated by dielectric losses could develop such temperatures. Bombardment by energetic particles present in a microwave vacuum discharge could also contribute to breakdown.

1.2.2 Breakdown in DC Fields

In view of the unstable nature of titania, it is not surprising that it fails at lower fields than ordinary ceramics. Hayes [6], working with DC fields, clamped titania discs between two shaped electrodes to determine the breakdown strength in vacuum. Normally in such tests a certain degree of sparking is observed within the test chamber and since it tends to clean the electrode and specimen surfaces of occluded gasses and impurities at relatively low fields, such sparking may be beneficial and is usually termed conditioning. However, with titania little conditioning was noticed since breakdown occurred at the onset of sparking near 20 kV/cm. Damage was characterized by tracking between the electrodes along the exposed

surface of the titania. Application of a vitreous glaze to this surface prior to testing resulted in an improved breakdown strength of 67 kV/cm. The best results were obtained by silvering the faces in contact with the electrodes in addition to the glazing: breakdown after normal conditioning was at 78 kV/cm, comparable to that of alumina and magnesium titanate. It was noted that the breakdown was at the edge of the sample and not through the bulk of the material, or what is usually called punch-through breakdown; hence it is feasible to assume that the intrinsic strength of titania is still higher than 78 kV/cm.

To minimize the effect of the tangential field at the edge of the disc, the electrode geometry was altered to give a primarily normal field. The disc was separated from a spherical electrode by a small gap. Depending whether the sphere was negative or positive, the breakdown field in the titania was 35 kV/cm and 28.5 kV/cm respectively. By simultaneously taking mechanical force measurements, Englefield et al. [7] were able to correct for any charging of the titania surface and arrived at fields of 52 kV/cm and 35 kV/cm respectively. Field emission from either the electrode or the ceramic (depending on the polarity) resulted in a net reduction of the field across the gap as the charge on the ceramic increased. Since the lower breakdown strength in the ceramic cathode case was accompanied by much lower prebreakdown currents it was concluded that electrons were emitted from localized sites on the surface. The current density would be higher, resulting in higher local temperatures which contributed to earlier reduction of the titania at the point of electron emission. This was confirmed by Ryall [8], in a refinement to the above

experiments. By incorporating an optical flat (which had been previously coated with a conducting chromium film) into one of the electrodes and optically polishing the titania surface, interference fringes were obtained in the vacuum gap. Localized heating by emission currents resulted in thermal expansion of the ceramic which appeared as a distortion in the fringe pattern. The growth of this distortion was recorded by high speed photography until breakdown 150 msec later.

In the normal field titania invariably suffered more severe damage. Punch-through was indicated by a conducting path through the material and the intense heating often resulted in localized reduction, formation of pits at the point of punch through by the ejection of particles of titania from the surface, and possible cracking of the disc.

1.2.3 Breakdown in Microwave Fields

Titania discs have also been tested in microwave structures which simulate the field patterns found in the disc loaded accelerator. The types of damage observed after breakdown are illustrated in Figure 1.2.

Referring to the figure, these may be classified in the following manner:

- Face punch-through- - Similar to that observed in DC with a small pit (typically 1 mm diameter and .5 mm deep) except that there is no breakdown path through the dielectric. The probable cause is intense local heating with thermal stresses sufficient to force out a small chip of titania (Indicated as "1" in Figure 1.2, in the following discussions this will be referred to as Type 1)

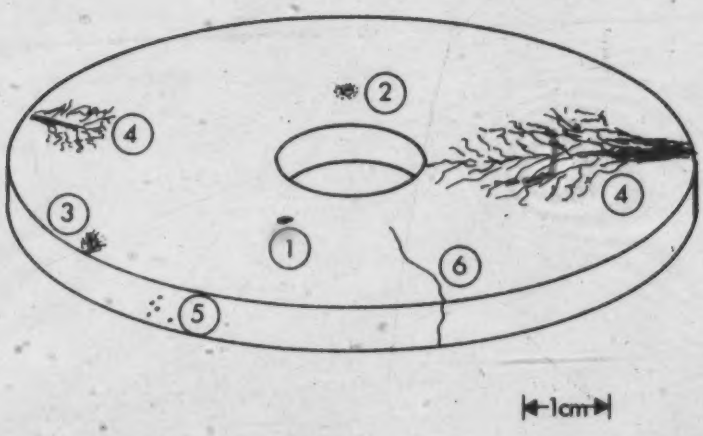

Figure 1.2 Damage Observed in Titania Discs Subjected to a Microwave Field.

- Darkened spots on titania surface - - Indicating reduction of the titania and possibly an early form of Type 1 (Type 2)
- Small tree-like patterns or so-called Lichtenberg figures extending from the edge about 2-3 mm toward the center of the disc (Type 3)
- Longer treeing patterns extending to the center of the disc in certain cases (Type 4)
- Black dots on the edge of the disc indicating points of discharge between the ceramic and the metal wall of the cavity (Type 5)
- Cracks in the ceramic due to thermal shock as a result of microwave heating (Type 6)

- The presence of a brown stain on the surface of the disc after breakdown was noted by Hayes [6], but this was attributed to poor vacuum conditions and multipactor initiated by an oil film (Type 7)

These do not necessarily all occur in any one instance; in fact usually only one form is observed if the breakdown is detected before the ceramic deteriorates excessively. It is obvious that local breakdown spots or treeing increases the conductivity of the ceramic and the resulting energy dissipation could lead to fracture (Type 6).

The fields within the disc and at the disc surface will be given in Chapter 4. Let it suffice to say that the maximum field within the disc is normal to the curved surface and that the peak external field (assuming no gap between the ceramic and the cavity wall: the ideal interface) is normal to the face and on the disc axis. Disc breakdown has been observed at peak powers that would correspond to 5 - 15 kV/cm and 100 - 300 kV/cm for the internal and external fields respectively. The wide variation is indicative of the unpredictable nature of titania when subjected to microwave fields. Even more obvious is the failure of the titania to support fields comparable to those observed in DC tests.

1.3 Breakdown Mechanisms in Solid Dielectrics

Under ideal laboratory conditions where practical considerations may be ignored, a number of fundamental mechanisms for breakdown of solid dielectrics have been identified. These classical breakdown mechanisms are generally classified as thermal, intrinsic, avalanche and field emission [9-12].

Most straightforward is thermal breakdown, which is dependent upon the lattice conductivity as a function of temperature. At low temperatures ($\sim$300°K) ceramics generally have a very low conductivity ($\sim 10^{-13}$ cm^{-1} for TiO_2). However there exists an exponential dependence upon temperature given by

$$\sigma = A\, e^{-\Theta/T}$$

where A is a constant and $\Theta \sim 10^4$ °K [13].

It can be seen that with an increasing electric field, the ohmic loss in the dielectric, $\sigma(E)E^2$, increases the temperature and consequently the conductivity. Provided the Joule heat generated increases at a slower rate than the loss of heat by conduction or radiation, for any field, an equilibrium is achieved:

$$C_v \frac{dT}{dt} + \mathrm{div}(K\nabla T) = \sigma(E)E^2$$

where C_v is the heat capacity

K the thermal conductivity

T the temperature (°K)

At some field E_c, the lattice temperature reaches a critical value T_c such that the system becomes unstable. The conductivity increases catastrophically and the dielectric becomes a conductor; i.e., breakdown occurs.

If the applied field is alternating, dielectric losses must also be considered. In complex notation, the permittivity of a dielectric is given as $\varepsilon = \varepsilon' - j\varepsilon''$, and the effective conductivity is taken as

$\sigma = \omega\varepsilon''$, or more usually as $\sigma = \omega\varepsilon'$ tan δ, where tan $\delta = \frac{\varepsilon''}{\varepsilon'}$ and is generally termed the loss tangent. The Joule heat generated within the dielectric (per unit volume) due to an alternating field is substantially larger than that observed with DC fields and is

$$P = \omega\varepsilon' \tan \delta \, E^2$$

Since the temperature is dependent on average power dissipated within the dielectric, thermal breakdown can be minimized by applying a pulsed field. It will be seen that thermal breakdown may be one of the major contributors to the breakdown of titania.

In thermal breakdown the conductivity is dependent on the lattice temperature and only indirectly upon the applied field. Intrinsic breakdown relates the electron density and hence the electron conductivity directly to the applied field. An ideal crystalline dielectric at absolute zero would have no electrons in the conduction band; however, at normal temperatures and due to lattice defects, a finite number of free electrons are present and contribute in part to the conductivity of the dielectric. These electrons are capable of acquiring energy from the applied field and transferring it to the lattice. The exact nature of the breakdown is not yet fully established and a number of mechanisms have been proposed, the two major ones differing primarily in the assumed distribution of the electron energies.

In his collective theory, von Hippel [14] considered that a sufficient electron density must exist such that electron-electron interactions result in a mean electron energy U_m. Thus higher energy electrons will exchange energy with the lower energy electrons and hence to the lattice. In an analogous manner to the thermal breakdown case, for any field less than a critical field E_{c_2} the electron temperature approaches a steady state value. Above E_{c_2}, the electron temperature rises rapidly since the average energy gain from the field exceeds that lost to the lattice. The electron energy is then sufficient to ionize the lattice electrons and the electron density increases, resulting in breakdown.

Fröhlich [15], however, advanced a low density, high energy theory in which electron-electron interactions are negligible and the electron energy is transferred directly to the lattice. Since there is more probability of higher energy electrons existing, these collisions result in ionization and breakdown at a critical field E_{c_3}, which is lower than that required by von Hippel.

There are variations on the above theories, but intrinsic breakdown is a low temperature phenomenon independent of the dielectric size and geometry and requires fields of the order 10^6V/cm.

Seitz [16], on the basis of a thick specimen and an electron with a velocity of 10^6cm/sec, estimated that the electron could create 10^{12} ionized electrons (40 ionization generations) raising the local temperature above a critical value and initiate breakdown at a field strength of 10^6 V/cm. This avalanche theory does not take into account inter-electron collisions; however, it does give a physically realisable value. In

this case the breakdown is local and dependent upon a specimen thickness sufficient to allow the necessary avalanche to continue.

An alternative method of increasing the electron density directly is by field emission from the valence band to the conduction band. Stratton [9] gives a required field strength in excess of 10^6 V/cm for field emission to occur. This is higher than the breakdown fields usually observed in dielectric materials, although such fields may occur at interfaces or voids due to enhancement.

In view of the foregoing discussion and the damage thresholds observed in actual tests it is safe to postulate that failure occurs well before the intrinsic strength is reached. After taking into account the possibility of thermal breakdown either due to bulk heating or the presence of lossy impurities within the dielectric, it is evident that other mechanisms are responsible.

1.4 Breakdown Initiated by Surface Discharges

1.4.1 Multipactor Induced Breakdown

In the development of high power klystrons for accelerator applications a large number of vacuum window failures were recorded at power levels far lower than expected; this was later attributed to thermal stresses arising from multipactor heating [17,18].

Multipactor is an electron resonance phenomenon which may occur in microwave cavities of suitable geometry and material [19]. Electrons emitted from a surface are accelerated by the field and strike a parallel surface during a half period of the RF field, ejecting secondary electrons which may then travel to the original surface. If the secondary electron

emission coefficient, δ, is greater than one, as it is for most metals and dielectric solids, electron multiplication takes place, with rapid increase of energy transfer from the field to the electron cloud and subsequently to the cavity surfaces. The maximum voltage at which multipactor can occur is [20]

$$V_{max} = \frac{m_e \omega^2 x}{2e}$$

In the present work the distance, x, between cavity surfaces was 3 cm and the frequency 2868 MHz, giving a V_{max} = 831 kV: the corresponding field strength, 277 kV/cm is of the same order as the actual applied fields.

Priest and Talcott [21] indicate that if tangential RF fields exist at a dielectric surface, a similar single surface multipactor effect may result in electron bombardment heating.

The high energy electrons transfer energy to the crystal lattice at a very rapid rate. In relatively stable ceramics this could cause thermal shock; for titania however, the consequences could be more severe from the discussion of section 1.2.1.

1.4.2 Surface Charging

Consider another result of multipactor. The ceramic is bombarded by electrons which generate secondary electrons such that the surface becomes positively charged [23]. This would give rise to a normal E field at the ceramic surface, and if the charging is not uniform, a corresponding tangential field. If the charge leakage is low, continued

bombardment could theoretically create fields sufficiently high for breakdown to occur, especially at points of field intensification.

1.4.3 Spark Discharge Initiated Breakdown

The vacuum spark is a highly dynamic microdischarge of relatively short duration (<1μsec, depending upon conditions). Attempts have been made to identify the mechanisms initiating the discharge; however the consensus is that the electrode surface and cleanliness are overriding factors. On the assumption that ionization remains a fundamental requirement, classical thermionic electron emission or field emission from oxide or impurity films on the electrode are proposed to account for the necessarily high electron density required to vaporize the anode material. A second group of theories depend upon a regenerative effect: electrons or negative ions accelerated into the anode create secondary positive ions which in turn strike the cathode resulting in a particle multiplication sufficient to support a discharge. Hawley and Zaky, [23], in reviewing the various hypotheses, emphasize the "clump" theory. Instead of elementary charged particles, much larger micro-particles or clumps are pulled out of the electrode by the high local field and accelerated to the other surface. Since the micro-particle is relatively massive, on collision with the other electrode material is vaporized to create the discharge. Of course at microwave frequencies transit time becomes prohibitive for the heavier particles and only electron effects need be considered. Because it generally dissipates the stored energy within a system, a vacuum discharge at a titania surface could transfer that energy via the bombarding

particles to a localized area with subsequent reduction. With some theoretical justification, Kilpatrick [24] presented a semi-empirical criterion to specify a threshold field for sparking. While it holds up to the microwave region for most cases, it may fail when applied to applications where there is sufficient temperature increase to open trapped gas voids. By low energy electron ionization, discharges could be created at fields below the specified threshold.

A possible secondary effect of the spark discharge is to increase the loss by photoelectric induced conductivity in either TiO_2 or other oxides [25].

1.4.4 Field Emission Breakdown

Walker and Hayes [26] observed that breakdown occurred in microwave fields at the edge of titania discs clamped in copper rings. Field intensification at the microscopically rough edge and resultant field emission were proposed as the reason. Fields over 1 MV/cm could develop in gaps between the ceramic and the copper.

1.5 The Scope of the Present Work

Recognizing that discharges could result in breakdown of certain ceramics, the initial aim of the research was to employ thin film coating techniques to provide a protective layer on the titania ceramic.

To test the effectiveness of the coatings, a high power microwave facility was constructed. The titania, in disc form, was placed in a high field cavity to simulate conditions in a dielectric slow wave accelerator.

After the first few trials it became apparent that for all but the shortest duty cycles (pulse length x pulse frequency) the average power limitation was more significant than discharge induced breakdown. In the actual coating of the ceramic, similar thermal limitations were observed, indicating that additional investigation into the sputtering procedure was warranted. Thus, although not originally intended, study of the thermal characteristics of titania both in coating and at high power had to be included.

Following the experiments with single discs, the cavity was expanded up to a five disc structure. It was proposed to correlate results from this structure with those of the single disc experiments, and by adding an electron beam, to better simulate the conditions in an accelerator.

From the breakdown data, the behaviour of the cavity under power and the dependence of dielectric breakdown and discharges upon various coatings, it was expected to evaluate the effectiveness of the thin film protection method and also to gain further insight into the nature of dielectric breakdown and vacuum discharges.

CHAPTER 2

METHODS OF INHIBITING BREAKDOWN

2.1 Introduction

The types of breakdown classified in section 1.2.3 are apparently either thermal or a result of surface discharges or high surface fields. The thermal effects can be reduced by modifying the operating conditions of the system, either by reducing the duty cycle of the applied field, or by cooling the titania to obtain improved heat transfer by way of increased thermal conductivity. Since the intrinsic breakdown strength of the titania is not achieved before surface breakdown occurs, by eliminating the effects of the surface discharges and high fields at the ceramic-metal interface, the titania should be capable of withstanding higher peak powers.

To protect the titania from surface discharges, the group at QMC resorted to a lead borate glaze. The glaze enabled fields of 300 kV/cm to be maintained at the titania surface without breakdown [26]. The three-fold improvement in breakdown strength for glazed titania in DC fields has already been mentioned. Although it demonstrated the applicability of coating techniques to this particular problem, it was discovered that the glazed titania was more lossy at microwave frequencies. Not only was the intrinsic loss tangent of the glaze quite high ($\tan\delta \sim .03$) [27], but in the glazing process, which involved spraying the discs with a fluid suspension of glaze particles in water and firing of the ceramic at 500°C, a reaction between the glaze and the titania

resulted in additional loss. Thus the method would be unsuitable in higher frequency structures where the glaze thickness (about .005 cm) would no longer be negligible compared to the disc dimensions. It was therefore proposed that much thinner, more inert coatings should be applied to ascertain if they would be as effective as the glaze.

Application of the glaze did suppress breakdown at the vacuum surface; however breakdown could still occur at the ceramic metal interface because of the edge finish of the titania. Silvering of the edge to provide a more ideal interface was successful at DC, but high wall currents present in the microwave cavity stripped the silver layer off the edge and no improvement was noted. Chute [28] in a cavity of similar geometry but excited in a different field pattern observed that an evaporated aluminum film did reduce edge breakdown. In the absence of any permanent ceramic-metal bonding technique for titania, a similar evaporation method was adopted to eliminate possible edge breakdown in the present work.

2.2 Micron Thick Optical Coatings

Using the film coating methods developed for optics manufacture, a considerably thinner and more homogeneous layer could be applied to the ceramic in place of the glaze. The criteria to be satisfied in selecting the coating material include the following: first, it must be stable and capable of sustaining higher fields than titania; second, since reduction of the titania is the fundamental cause of breakdown, the coating must be non-porous to prevent oxygen migration from the titania to the vacuum; third, the coating should demonstrate good adhesion to the titania substrate and therefore possess a similar coefficient of

thermal expansion; fourth, it should not affect the titania substrate; and fifth, it should have a low loss tangent to minimize dissipation in thicker coatings.

Alumina is one material possessing these properties. It is particularly suited because of a very low oxygen diffusion coefficient even at elevated temperatures [29].

One complication in optical coating is the necessity of optically polishing the substrate prior to deposition. A Talysurf was used to obtain the surface profiles in Figure 2.1. Simple grinding of the sintered titania leaves numerous irregularities which not only inhibit uniform coating, but also present potential points of field enhancement. A surface polished to a flatness of $\lambda/2$ over a 8 cm diameter exhibits only occasional pits about 1μm in depth and 100μm across. Consequently a surface coating of 1μm was thought sufficient to provide uniform protection.

A second consideration is the high melting point of alumina. Since vaporization in vacuum only begins above 1700°C, normal evaporation techniques are not suggested, particularly when the substrate is a thermally unstable material such as titania. The alternative is RF reactive sputtering which is described in Chapter 3.

2.3 Thin Titanium Coatings

2.3.1 Metallic Films for Multipactor Suppression

One intrinsic property characteristic of most oxides is the high secondary electron emission coefficient δ. Although the alumina was intended to protect the titania, its higher coefficient could increase

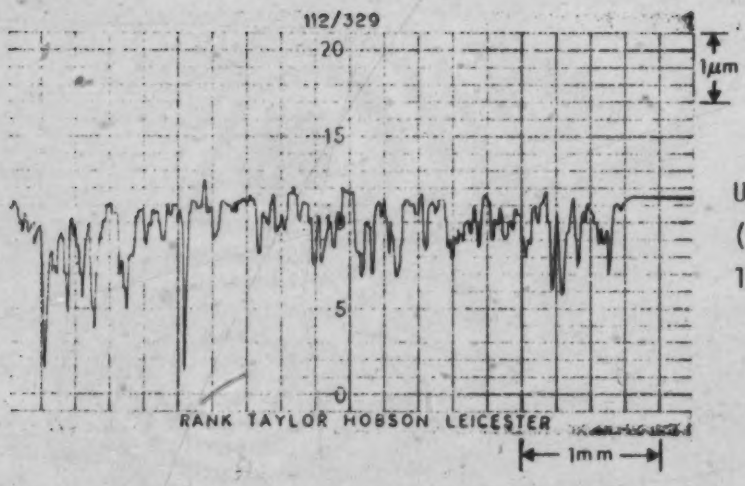

(a)
Unpolished face
(ground and
lapped only)

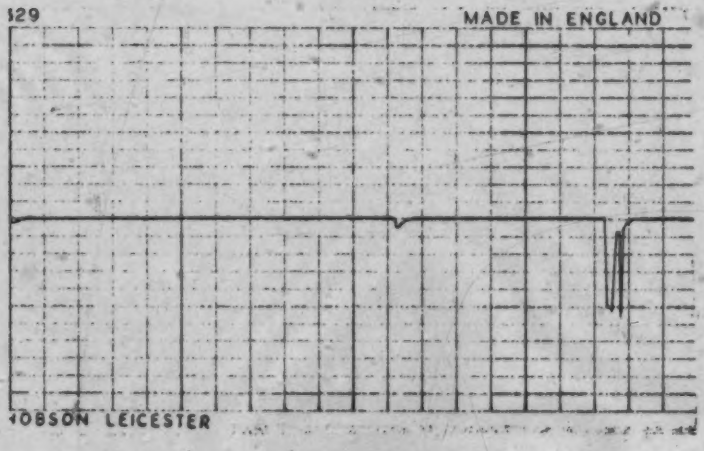

(b)
Face polished
but uncoated

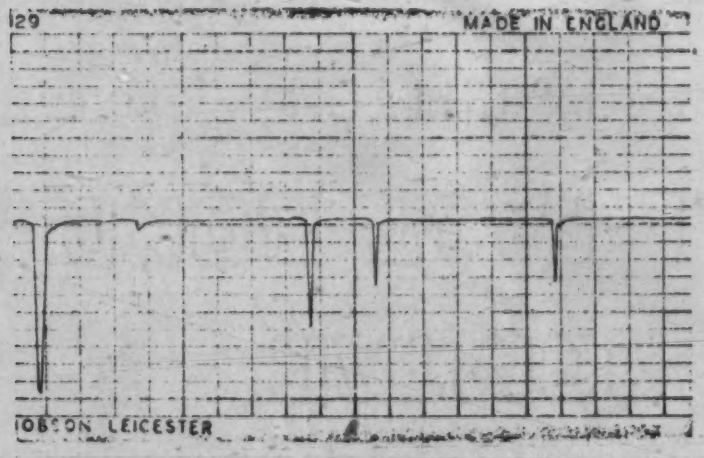

(c)
Face polished
and coated with
1.2 μm Al_2O_3

Figure 2.1 Talysurf Profiles of Titania Surfaces

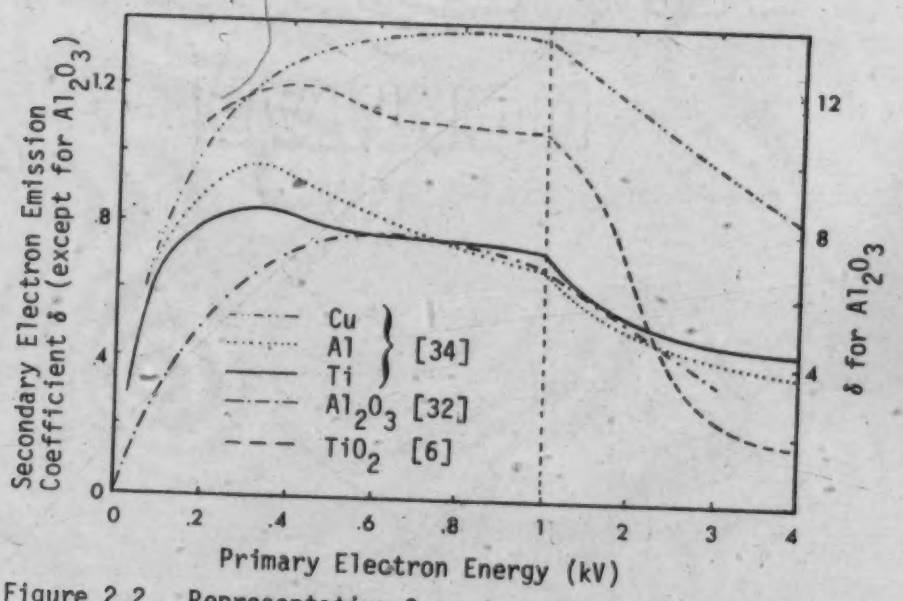

Figure 2.2 Representative Secondary Electron Emission Curves (from the sources indicated in brackets)

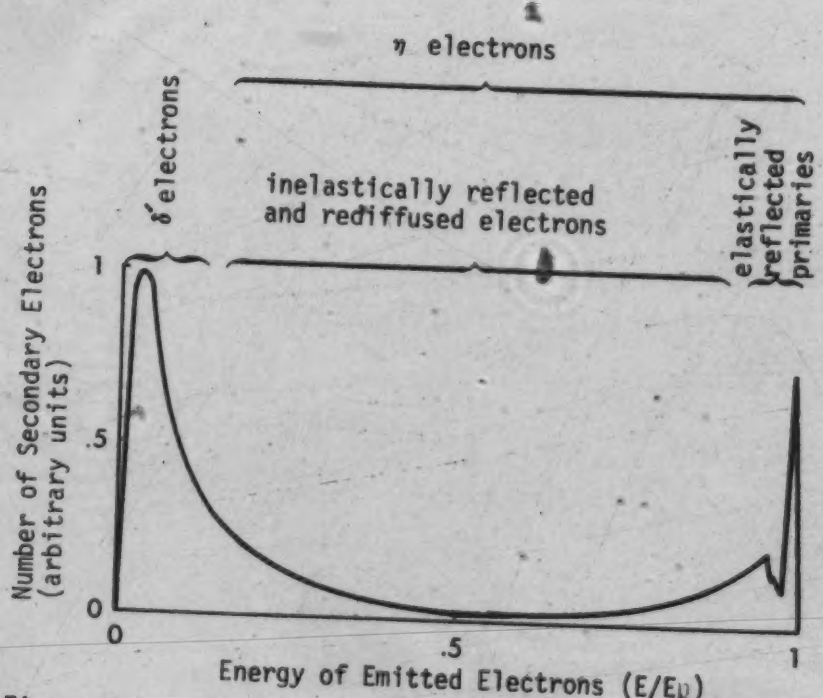

Figure 2.3 Energy Spectrum of Secondary Electrons Emitted from Ti (after Arifov [39]: E_p=534 eV)

the probability of multipactor. Such was the case, as will be seen in Chapter 7.

By using materials with a coefficient less than unity, it is possible to eliminate multipactor entirely. Titanium has been used on metal accelerating cavities [30] and on dielectric interfaces in electron tubes [31] with success, since for pure Ti metal, δ=.9. Other possible metals are aluminum, δ<1; beryllium, δ=.6; barium, δ=.83; and magnesium, δ=.95; however the high specific resistivity of Ti makes it desirable for coating dielectric surfaces situated in high tangential electric fields.

The high melting point of titanium also eliminates evaporation and conventional DC sputtering is the usual deposition method used.

2.3.2 S.E.E. Dependence Upon Film Thickness

Secondary electron emission is a surface phenomenon [33-37]. Some of the incident (primary) electrons are reflected with almost no loss of energy, but most experience collisions within the bulk material and are either inelastically rediffused, or dissipate their energy below the surface partly by creating secondary and higher order electrons by ionization. These low energy electrons have a low probability of emerging out of the material, travelling only about 100 Å before re-capture. Consequently, 'true' secondary electrons originate within a thin layer near the surface [38]. Figure 2.3 is the energy spectrum of electrons emitted from titanium: for convenience true secondary electrons are usually defined as electrons with energies of 50 eV or less.

By observing the true secondary electron emission coefficient δ' and the coefficient for the faster reflected electrons, η, for different incident energies as thickness of a titanium film deposited upon a silver substrate, was increased, Bronshtein [40] obtained a maximum depth of origin of 12 atomic layers (35 Å) [41] for titanium. The corresponding values for platinum and nickel were 28 Å and 18 Å [38]; those for insulators being approximately 10 times higher [42]. Similar results have been reported by Bruining [33], and Dekker [35]. A thin film of 50 Å of titanium deposited on a polished substrate should be more than sufficient to give a total coefficient $\delta(=\delta'+\eta)<1$, even at high angles of incidence [43].

2.3.3 Electrical Properties

The bulk resistivity of titanium is 42×10^{-6} Ωcm [44]. The corresponding surface resistance for a layer of thickness d=50 Å would be 84Ω/square; however, it is known that thin films exhibit a higher resistivity than that of the bulk material [45]. The electron mean free path length λ_{Ti} in Ti is 220Å [46], and a correction can be applied to the resistivity using the Sonderheimer-Fuchs relation for conductivity [47]:

$$\sigma=\sigma_0\left[1-\frac{3}{4}\left(\kappa-\frac{\kappa^2}{12}\right)E_1(-\kappa)-\frac{3}{8\kappa}(1-e^{-\kappa})-\left(\frac{5}{8}+\frac{\kappa}{16}-\frac{\kappa^3}{16}\right)e^{-\kappa}\right] \qquad 2.1$$

where $\kappa=\frac{d}{\lambda}$ and $-E_1(-\kappa)=\int_{\kappa}^{\infty} t^{-1}\,e^{-t}dt$.

Using the above values, $\kappa=.227$, $E_1=-1.12$ and $\sigma=.348\sigma_0$ or in terms of

resistivity $\rho = 2.87\rho_0$.

Even allowing for this, the resulting resistivity of $120 \times 10^{-6}\Omega$ cm is much lower than that observed for 50 Å films; values of 300 to 600 x 10^{-6} being more typical [48-49] (240×10^{-6} in cases where a 10^{-9} torr vacuum was maintained [46,50]). Explanations suggested are: nonuniformity or porosity in the coating; reaction between Ti and residual O and N during the coating process; and ion bombardment by A^+ ions [51]. Since the titanium was sputtered, the figure reported by Gertsenberg [48] would be most applicable ($\rho = 600 \times 10^{-6}\Omega$cm), resulting in a surface resistivity of 1200Ω/square.

It must be emphasized that these are the resistances measured prior to exposure of the film to atmosphere. Immediately air enters the vacuum chamber the surface resistance increases. Chander [49] found an increase of 80% for a 80 Å film of Ti after 3 hours of exposure to air. For a Ti film at room temperature, Hass [52] reported an oxide growth of 15 Å after 2 hours, 20 Å after 20 hours and 35 Å over 30 days, although at elevated temperatures the oxidation rate is appreciably higher and the final oxide thickness much thicker.

Hence, when dealing with Ti films it is essential to keep the temperature as low as possible prior to any exposure to air, otherwise it is entirely feasible that a 50 Å metallic film could be entirely converted to oxide.

Secondary electron emission studies for thin films of titanium 200 Å thick were done by Laurensen and Holland [53]. At a pressure of

10^{-9} torr, δ_{Ti}=.9 with E_p=350 V. This compares well with results for clean bulk Ti. Upon increasing the pressure to .1 torr the coefficient became δ=1.5 at E_p=200 to 300 V, similar to results for oxidized Ti sheet. It is anticipated that inside the microwave cavity the oxidized film will be subjected to electron bombardment and heating, the reduction of the Ti oxides restoring a clean Ti film with low δ.

2.3.4 EM Wave Propagation Through Metallic Films

Kaplan [54] has theoretically investigated the effect of a thin metallic film on a plane electromagnetic wave. The coefficients of transmission, reflection and absorption are [55]:

$$T = \frac{1}{(1+\alpha)^2} \qquad 2.2$$

$$A = \frac{2\alpha}{(1+\alpha)^2} \qquad 2.3$$

$$R = \frac{1}{(1+1/\alpha)^2} \qquad 2.4$$

$$\alpha = 2\pi\sigma \frac{d}{c} \text{ [esu]} \qquad 2.5$$

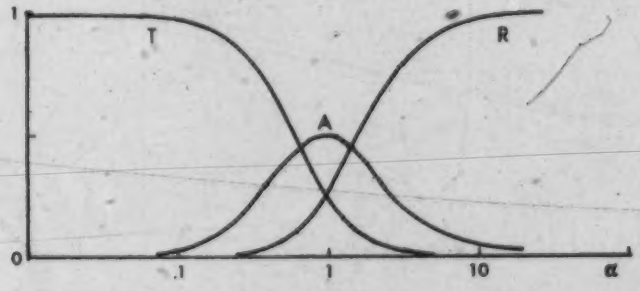

Figure 2.4 Propagation Through Thin Metallic Films

For Ti ρ=4 2 x $10^{-6}\Omega$ cm, thus in esu σ=.073 x 10^{-17} sec^{-1} and for a film of 50 A, α=.77 and T=.32. Using the more realistic resistivity ρ=600 x 10^{-6} Ω cm, the corresponding transmission coefficient is .90. The difference between theoretical and experimental results is illustrated by Ramsey and Lewis [56] who used iron, silver and nickel films across X-band waveguide. Although in this case the wave was no longer propagating normal to the film plane, similar results were obtained. Allowing for the much higher resistivity of Ti, the 50 Å film considered is comparable to thicknesses of 5 to 10 Å of the other metals.

In the actual application, the Ti film was on a titania disc within a microwave cavity and the loss due to the film depends upon the magnitude of the tangential E field at the film surface. This will be determined in section 5.3.

Understandably then, the thickness of the Ti layer must be carefully controlled; if too thin it will not be effective and may oxidize too readily; if too thick it will absorb energy and only contribute to the surface heating of the titania.

2.4 Prevention of Edge Breakdown

Aluminum had proved more successful than silver in eliminating edge breakdown, however, copper was proposed for the present series of experiments. The main advantages of copper were its high conductivity and malleability. Losses would be reduced and since in the application a copper ring was to be shrink-fitted onto the titania, a homogeneous bond would result.

The problem in metal-ceramic bonding is the generally poor adherence. In the experiments however, no peeling of the coating was encountered due to high fields, possibly due to the high mechanical forces created by the thermal shrinking of the ring. The main source of difficulty was in obtaining a satisfactory edge finish, although this was not noticed until a careful analysis of the various edge coatings was conducted after conclusion of the high power tests.

The coating thickness is quite critical. The skin depth of copper can be calculated from the relation [57]

$$\delta = \frac{1}{\sqrt{\pi f \mu \sigma}} \qquad 2.6$$

and at 2870 MHz is 1.2×10^{-6} m. The minimum thickness should be an order of magnitude greater so that negligible field exists at the interface of the ring and coating. Discharges in any voids that may be present are avoided and high currents can flow without heating the coating. The maximum thickness is theoretically unlimited, but in the case of vacuum deposited films is dependent on the ability of the film to withstand the severe thermal stresses involved.

CHAPTER 3

THIN FILM DEPOSITION

3.1 Introduction

Due to the refractory nature of both alumina and titanium, sputtering was selected as the deposition technique for coating the titania discs. For this purpose there was constructed a system which was eventually to be incorporated into the optics processing facility of the Department of Electrical Engineering. The majority of this chapter is devoted to a description of that sputtering system and observations made on some of the films obtained. This is supplemented by a description of the copper edge coating using more conventional vacuum evaporation. The last section summarizes the procedure for preparing the discs for eventual testing.

3.2 Physical Sputtering

3.2.1 Background

Over a century ago it was observed that in glow discharge tubes an opaque deposit developed on the glass adjacent to the cathode [58]. This film resulted from cathode disintegration under the influence of the ionized gas molecules accelerated towards the cathode. This process became known as cathodic sputtering. One of the earliest vacuum deposition techniques, it was later superseded by vacuum evaporation since the pressure required to support the glow discharge ($\sim$.1 torr) was not conducive to critical optical coatings.

More recently, due to the demands of the semiconductor industry, sputtering has been revived and films comparable to those evaporated have been achieved by an extensive re-thinking of sputtering system philosophy [59]. Instead of utilizing a low vacuum glow discharge, a plasma is created by using a hot cathode to generate electrons of sufficient energy (~50eV) to ionize the enert gas, usually argon [60]. By confining the ionized gas with a magnetic field, a plasma beam is established between the anode and cathode.

In a second adaptation, an additional third electrode is introduced and biased negatively with respect to the cathode. Instead of sputtering the cathode, the positive ions are accelerated to this target electrode. The molecules ejected from this target are then deposited on an adjacent unbiased substrate. A simplified representation of the sputtering process is given in Figure 3.1.

3.2.2 RF Reactive Sputtering

In the above it is apparent that only conducting materials can be sputtered, since the impinging ions would charge the surface of an insulated target and in time halt the process. However, if the target bias is a high radio frequency voltage, sputtering of the insulator occurs in the same manner as for a conductor.

The exact nature of the sputtering process is not fully understood despite considerable research conducted over a great many years. The simplest explanation is that A^+ ions accelerated through several hundred volts have sufficient energy to travel a few atomic layers below the surface of the target material [61]. Most of the ion energy is dissipated

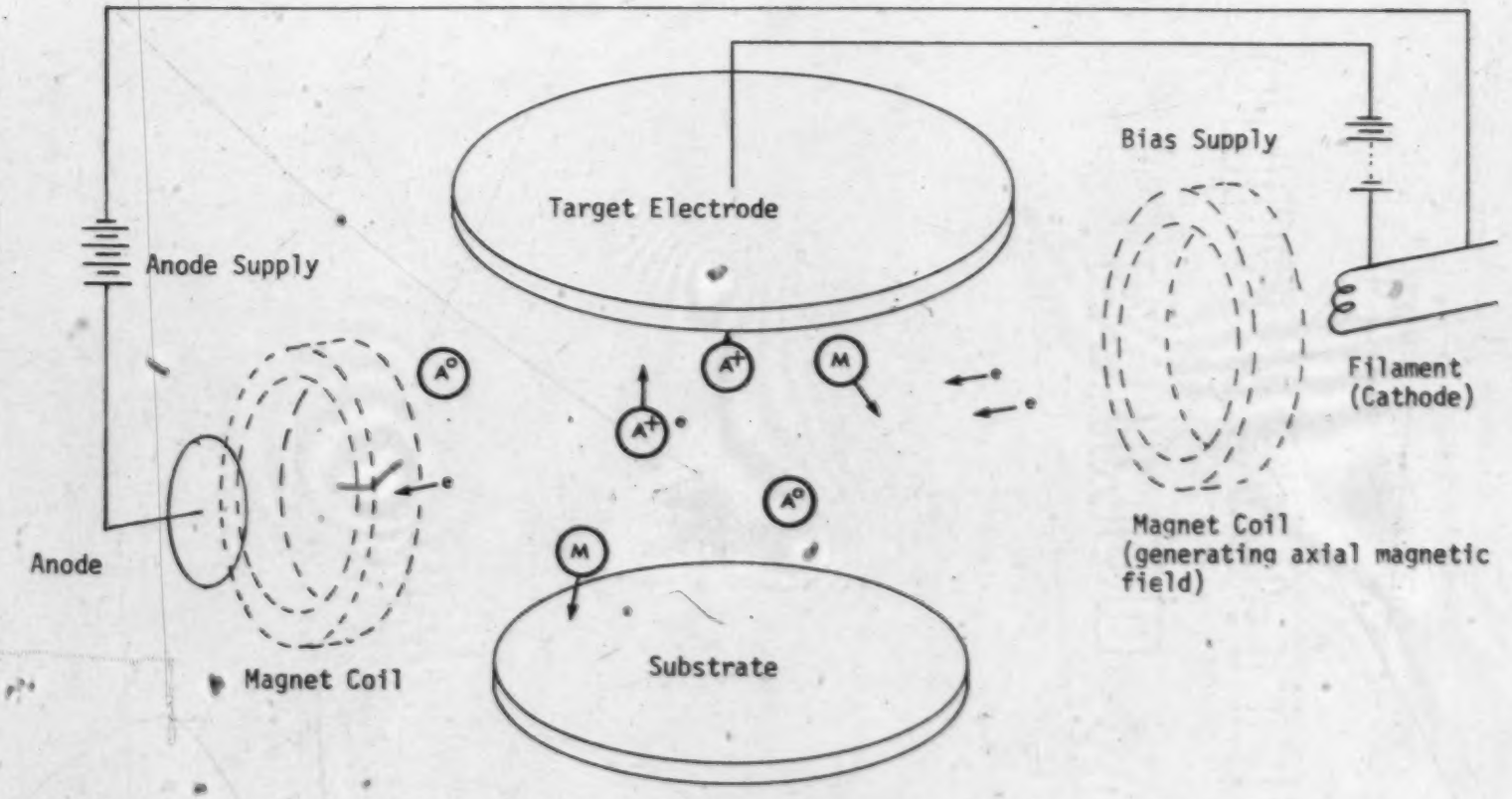

Figure 3.1 Geometry of Triode Sputtering System

in collisions with the target molecules and is manifested by heating of the target; however there is some momentum transfer to molecules which are emitted from the target with energies substantially lower than those of the incident ions (i.e. 16eV for Pt [62]). The ratio of sputtered molecules to incident ions is termed sputtering yield.

The temperature rise at the surface of an insulator target could be sufficient to cause some decomposition and reduction of a dielectric such as alumina. The stoichiometry of the mass transfer mechanism must also be considered: in Al_2O_3 the different atoms have different sputtering yields and also might be pumped from the vacuum at differing rates; therefore on recombination at the substrate there is an oxygen deficiency. The effect of the molecular energy dumped at the substrate is a third possible cause of a reduced alumina film [63]. To overcome this disability, a partial pressure of some active gas, in this case oxygen, is added to the normal argon pressure. This reactive sputtering technique ensures that the film has properties similar to the original target material, but the presence of the active gas tends to reduce the sputtering rate to a half or quarter of that in pure argon [64].

The main advantage of sputtering over conventional vacuum evaporation are:

1. The capability to deposit high melting point materials,
2. The higher energies of sputtered molecules (10-30eV) in comparison to the thermal energies of evaporated material, resulting in denser, more adherent coatings.
3. A deposition rate which is constant for any specified set of parameters (voltage, pressure, temperature) and therefore readily controlled.

4. The use of a target which may be considered infinite in contrast to evaporation sources which must be replenished regularly.
5. The use of a cathode which may be effectively hidden from the the substrate and target, in contrast to evaporation where both the source and the substrate see the hot filament.

The main disadvantage of sputtering, in addition to the increased complexity of the system, is the lower deposition rate necessary to prevent excessive heating of the substrate.

3.3 The Sputtering System

3.3.1 General Description

Operationally the sputtering system may be divided into three main elements: the vacuum station and the sputtering chamber, both in the center of the photographic view, Figure 3.2; and the RF supply situated in the left foreground.

The vacuum pumping station incorporates an Edwards 6" oil diffusion pump with a liquid nitrogen trap. The mechanical forepump is also used to rough out the sputtering chamber. Located on the front panel are the vacuum system controls, the vacuum gauge control unit and the electrical supplies for the plasma beam. Thermocouple gauges and two Penning cold cathode gauges monitor the pressure inside the vacuum pump and the sputtering chamber. A butterfly valve isolates the vacuum system from the sputtering chamber which sits on top of the vacuum station.

The stainless steel chamber is .3m in diameter and .27m high. The cathode and anode are mounted on detachable components bolted to

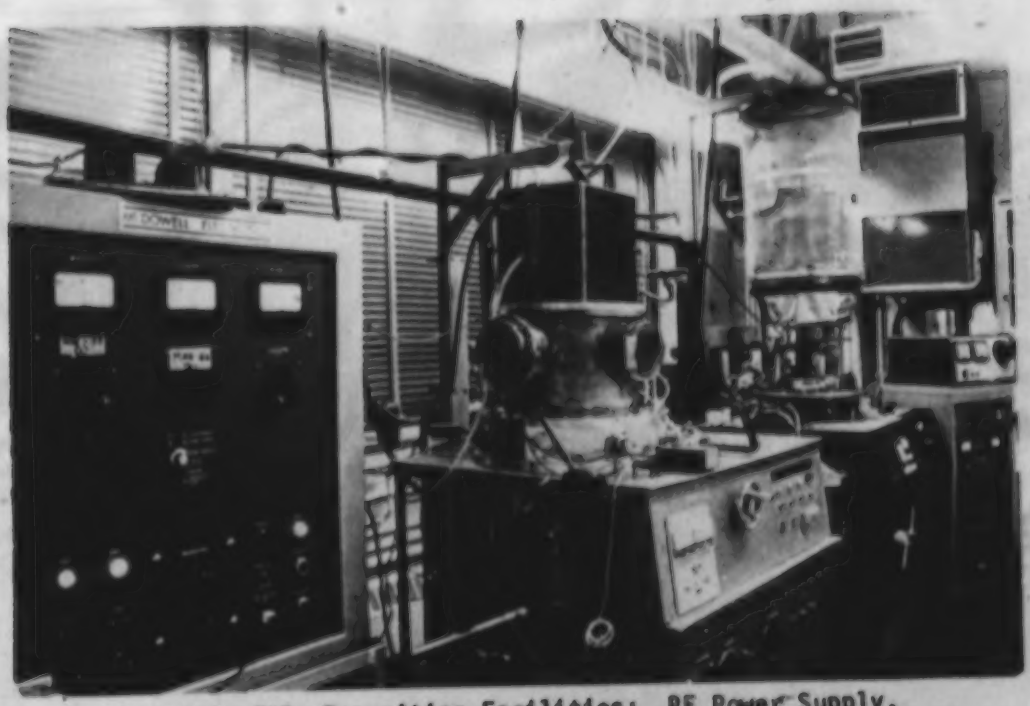

Figure 3.2 Thin Film Deposition Facilities: RF Power Supply, Sputtering Chamber and Vacuum Evaporation System

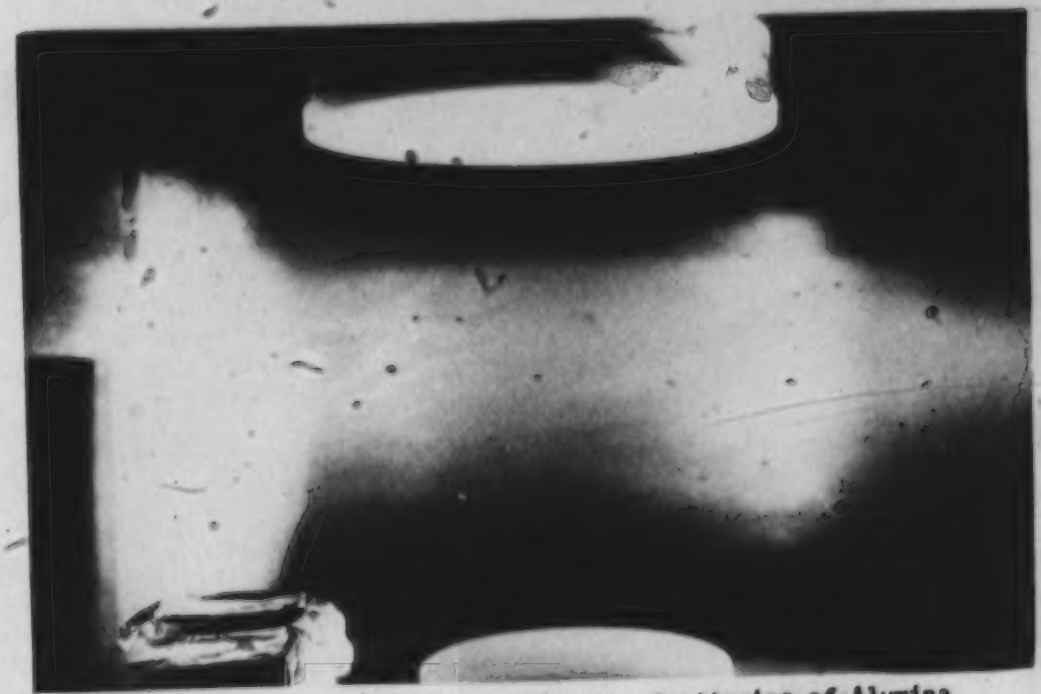

Figure 3.3 View Inside Chamber during the Sputtering of Alumina onto a Titania Disc

two ports on opposite sides of the circular wall. Access to the sputtering chamber is through a 4" viewing port at the front, or for larger items, through the top after first hoisting the plate which carries the target. Inside the chamber is a watercooled substrate table and a fan-shaped shutter, both which may be rotated from outside the vacuum by means of sealed mechanical couplings. The shutter can be placed between the target and the substrate to interupt the coating process. The individual 4" diameter sputtering targets are cemented onto copper backing plates with high temperature conducting epoxy and are screwed into the RF sputtering probe mounted in, but electrically isolated from, the top end plate of the chamber. The top plate also carries the watercooling lines for the target, the probe matching circuits (inside an interlock protected cabinet) and the control valves for the sputtering gases. The anode is a 5cm disc of molybdenum and the cathode simply a 10 cm length of .5 mm thoriated tungsten wire formed into a three turn helix about 1 cm in diameter. Provision was made for two separate filaments in order that sputtering could be continued for long periods without the necessity of breaking the vacuum to replace filaments. The anode, cathode and also the two adjacent magnet coils are watercooled.

The other part of the system is a McDowell Electronics RF supply operating at 13.65 MHz. It is capable of supplying up to 1 kW of RF power to the target probe. Interlocks were added to interrupt the power source in the event of an open filament or a decrease in pressure which would result in the beam being extinguished and a mismatch in the probe circuit.

3.3.2 Operation

Figure 3.3 shows a titania disc being coated. The anode and cathode are out of the line of vision to the left and right respectively, but the plasma beam, about 7 cm in diameter, can be distinguished between the 4" alumina target at the top and the titania disc on the substrate table 10 cm below.

In an argon pressure of 4×10^{-4} torr, the filament, passing 20 amps at 12 volts, will support an argon plasma having the following parameters:

Anode current	1.5 amp
Anode voltage	49 volts

The plasma is confined by a magnetic field of 100 G (maximum on axis) generated by a current of 20 amps at 12 volts through the coils near the anode and the cathode.

In sputtering alumina, the argon pressure was set to 4×10^{-4} torr using a controlled leak valve and then oxygen was introduced through a second valve to bring the indicated pressure to 6×10^{-4} torr. It was necessary to increase the pressure momentarily to 10^{-4} torr to first initiate the discharge. Previously, in the RF supply, the grid and plate coils had been tuned for maximum power into a dummy load, so that when coupled to the target probe it was only necessary to match the probe using a coil in the cabinet above the target to obtain minimum

reflected power. The impedance of the probe was 17 kΩ; an input of 110W (of which 10 watts was reflected) giving a target voltage 3.7 kV peak to peak.

To sputter the titanium target only the argon atmosphere was used and the required DC voltage of 5 kV at 70 ma obtained from a conventional glow discharge supply.

3.4 Characteristics of Sputtered Films

3.4.1 Measurement of Film Thickness

Methods of determining film thickness are adequately reviewed in the literature [65-67]. Where the deposition rate must be continually monitored the instrumentation may become excessively complex. This is particularly true for the microgram balance and quartz crystal oscillator techniques [68], and to a lesser degree, for reflectivity measurements. The need for prior calibration of the crystal or the dependence upon some other film parameter (density in the balance method, or index of refraction) implies some uncertainty in the film thickness. One of the advantages of sputtering is a controllable rate of deposition, thus these difficulties are avoided and it is possible to measure film thickness more directly and conveniently after coating is completed. Because of its simplicity and, if due care is taken, accuracy, the optical interference method was selected; however results were occasionally verified by some independent measurement.

Assuming uniform film deposition, one can determine the height of a step where a substrate has been partially masked prior to coating. If

the substrate has been optically polished and an optical flat is placed over the step, under monochromatic light, there will be a shift in the interference fringes at the step. The degree of shift indicates the thickness of the film according to the well known relation:

$$d = \frac{m\lambda}{2n} \qquad 3.1$$

where λ = the wavelength of the light source

n = refractive index of the film (1.76 for Al_2O_3)

m = the degree of fringe shift

A further stage is to overcoat the step with a reflective layer of silver or aluminum a few hundred Å thick and form a multiple-beam interferometer. Fringes become more distinct and any uncertainty in the refractive index no longer contributes to error in d (in equation 3.1, n can be taken as 1).

The first application was to determine the deposition rate of alumina for different input powers in the system built. Ten polished titania samples were coated for various lengths of time and the step heights were evaluated (two or more steps per sample). In this instance each measurement was checked by running Talysurf profiles of the step and the resulting thicknesses plotted in Figure 3.4. The sputtering rates from this diagram are valid for the parameters of section 3.2.2, but changes in the sputtering atmosphere (either the gas or pressure) [69-70], the target to substrate distance, or the beam shape will affect the rate so that two or more calibration tests are best conducted before sputtering

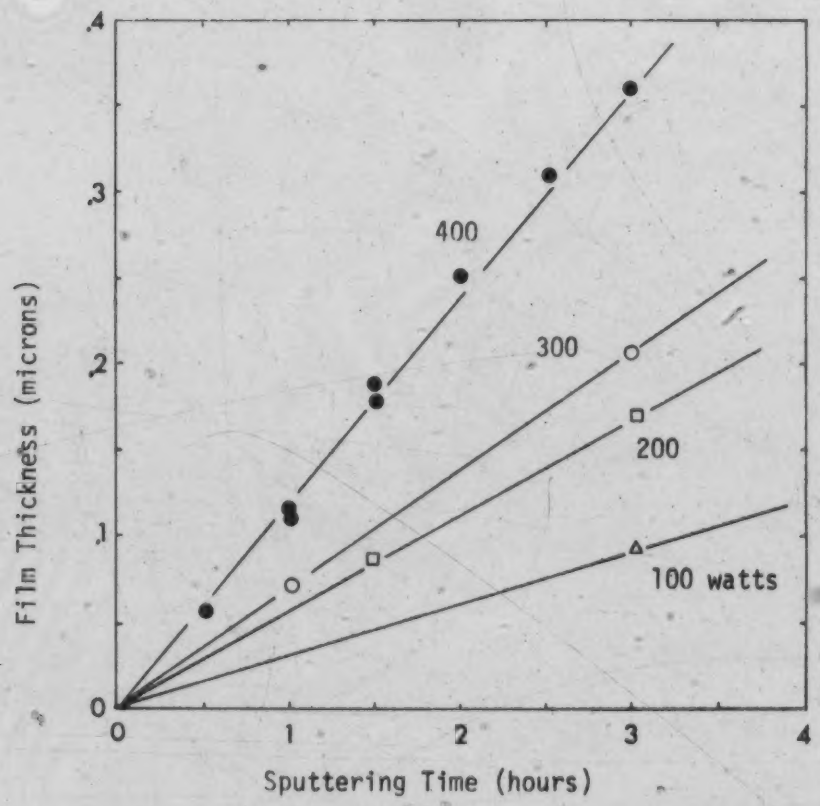

Figure 3.4 Determination of the Sputtering Rate for Al_2O_3

onto the final substrates.

During the actual disc coating, the increase of the alumina layer could also be monitored by observing the changes in the colour of the film (see Table 3.1). This is not exact, however, and the final thickness was ascertained using monitor substrates of TiO_2 or quartz placed next to the discs. A masked quartz flat may be seen to the left of the titania disc in Figure 3.3.

For the sputtering of titanium, the critical parameter was film resistivity measured during sputtering and immediately after exposure to air. The actual deposition rate was measured by depositing a thick film and using the interference method.

3.4.2 Sputtered Alumina Films

Certain properties of the alumina films sputtered are of interest. Films were deposited on substrates of titania, quartz and glass, and compared for thickness, mechanical strength, chemical resistance and thermal behavior. The following general observations were made.

All films underwent some reduction, the degree depending upon the applied power level. They had a slight grey discoloration, which disappeared on heating. The electrical measurements described in section 3.5 would confirm this conclusion.

Films deposited on glass were consistently thinner than those simultaneously deposited on quartz or titania. The sticking coefficient, the parameter indicating the number of incident sputtered molecules that stick to the substrate, decreases with temperature [72-74]. Evidently the lower thermal conductivity of the glass contributed to a lower

Table 3.1 - Characteristic Colours of Thin Transparent Films

(after Banning [71])

optical thickness $= \frac{d}{n_1}$	film colour	
	$\frac{n_1}{n_2} > 1$	$\frac{n_1}{n_2} < 1$
	bluish-white	yellow
$\lambda/4$ 1st order maximum	white	magenta
	yellow	blue
$\lambda/2$ 1st order minimum	magenta	white
	blue	yellow
$3\lambda/4$ 2nd order maximum	greenish-white	magenta
	yellow	blue
λ 2nd order minimum	magenta	greenish-white
	blue	yellow
$5\lambda/4$ 3rd order maximum	green	magenta

notes 1. Optical thickness is in terms of wavelengths of green light (λ=5550 Å) corresponding to the peak response of the human eye

2. $\frac{n_1}{n_2} > 1$ is for ZnS (n_1=2.35) on glass (n_2=1.4) or for our case Al_2O_3 (n_1=1.76) on glass or quartz

3. $\frac{n_1}{n_2} < 1$ is for Na_3AlF_6 (n_1=1.35) on glass or for Al_2O_3 on TiO_2 (n_2=2.61)

4. The intentsity of the colour increases with the ratio of refractive indices

effective sputtering rate. This is relevant in that even in identical materials, a difference in the bulk thickness could result in different surface temperatures and hence affect the sputtering rate.

Using Table 3.1, films were compared prior to, and after heating to 800°C. The optical thickness was greater immediately after sputtering than after subsequent reoxidation; that is, the colour shifted towards a lower order. Two possible explanations exist: either the density of the film increased, making the true thickness less or; the refractive index increased. Multiple-beam interferometry indicated that the physical thickness changes very little; hence the refractive index of sputtered alumina is less than 1.76 and due care must be taken in applying equation 3.1.

The films obtained were resistant to moderately concentrated acids and bases; however the films could be removed by applying a concentrated solution of sodium hydroxide heated to about 50°C. After two hours, the film was apparently lifted from the substrate, possibly by the solvent action of the base attacking the thinnest portions of the film and then acting at the alumina-titania interface. Titania so treated appeared slightly etched and the procedure is not recommended since repolishing of the surface would be required.

The adherence of the films was excellent. Only the application of a sharp point would result in scratching of the surface. One problem, encountered with films thicker than 4 μm, was the thermally induced mechanical stress which arises when the surface of the substrate, heated by the source or the impinging molecules, cools after deposition is

completed. These films tended to flake, and heating of the substrate did not anneal the film but only accelerated the flaking. The only apparent solution was to lower the sputtering rate.

The best films were obtained after careful cleaning of the sputtering chamber and of the substrate. The presence of oil or water vapour from the pumps or coolant systems is detrimental to the film, and any particles settling upon the substrate mask the surface and create thin points in the film.

3.4.3 The Sputtered Titanium Film

Because of its inherent reactivity with atmosphere, the thin titanium film was much more difficult to produce.

The titanium target, upon being exposed to air, develops an oxide layer which takes some time to sputter away each time. The procedure followed after unsuccessful attempts to obtain a good film was to place the shutter between the target and the substrate and to presputter the target for 15 minutes. To lay down the 30 to 50 Å necessary to prevent secondary electron emission, the shutter was removed for about 25 seconds and then the discharge extinguished. Even by this method precautions had to be employed. The shutter, originally a thin sheet of molybdenum, was modified to allow watercooling since the shutter would heat and contaminate the substrate from its underside. The substrate had to be surrounded by a glass cylinder to shield it from the cathode and from particles apparently emitted from the substrate table during the presputtering period. The shutter was also sandblasted and cleaned between coatings.

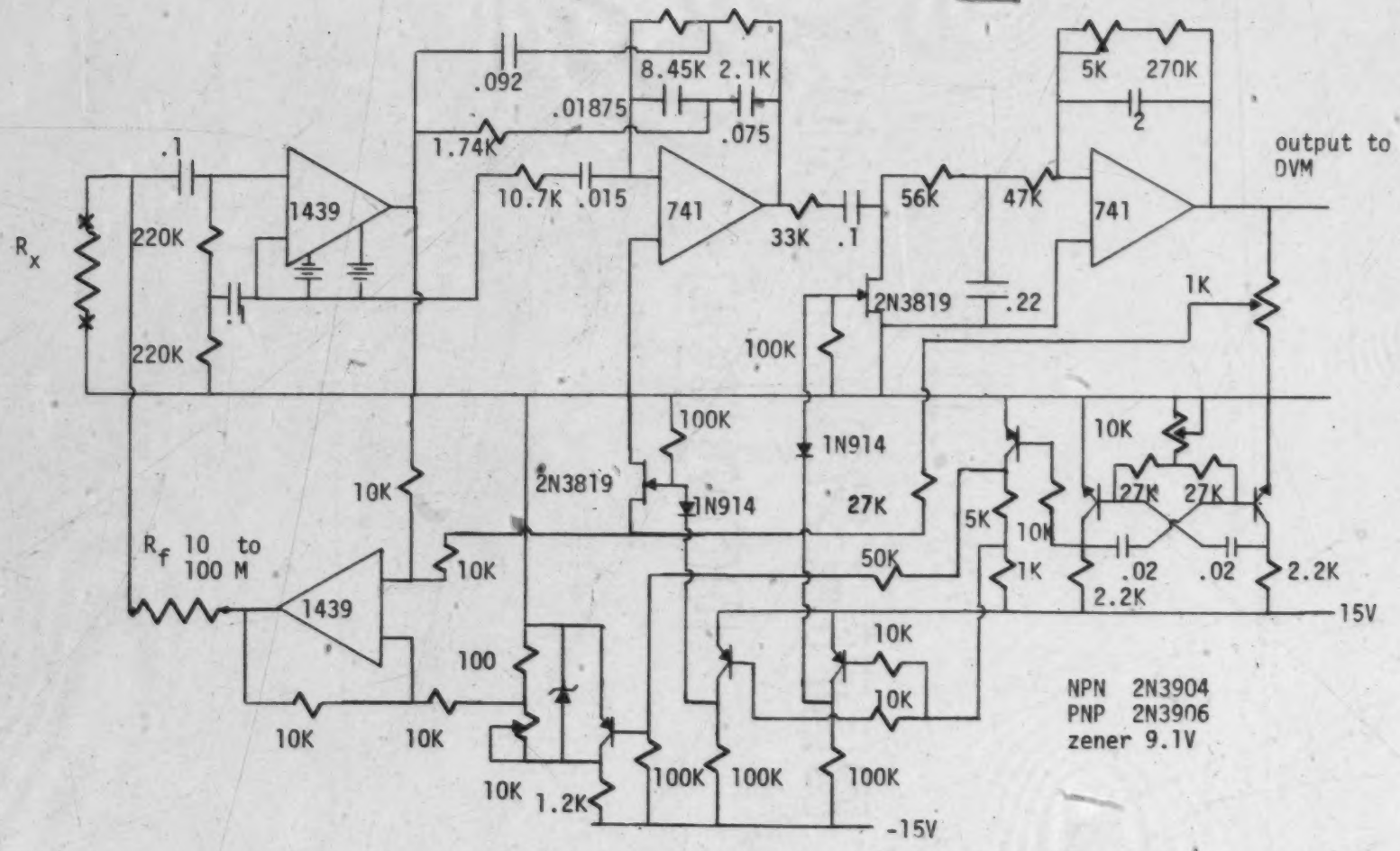

Figure 3.5 AC Ohmmeter Circuit

Monitoring of the film resistance posed difficulty due to heating of the monitor substrates (usually of glass) and because of the ion and electron currents in the chamber. A circuit, which may be termed an AC ohmmeter, was built to filter out the noise generated by the beam. Figure 3.5 is the schematic of the circuit which comprises a high input impedance amplifier, a high Q active filter and a 1 KHz multivibrator driving both the reference supply and the synchronous demodulation chopper. With the appropriate choice of feedback resistors, the output voltage is proportional to the resistance between two gold-plated contact points on the glass substrate. The useful resistance range was from 10Ω to 100 kΩ with the beam on. Ordinary ohmmeters may be used but require the beam to be turned off. Trouble is encountered during this off period since very thin films oxidize rapidly even within the chamber, and the resistance reading will no longer be indicative of the true thickness.

The degree of resistance change on exposure of the films to atmosphere, as a function of the initial film resistance, is illustrated in Figure 3.6. Table 3.2 relates film resistance to sputtering time for two cases: in coating of the discs the 7kΩ film was used, corresponding to a thickness of about 30 Å.

The titania discs, after coating, were allowed to sit in the vacuum to cool before exposure to air. In this way, good quality, repeatable films were obtained. Of course these were dependent on the condition of the disc surface. For this purpose a conventional toluene-acetone-alcohol-distilled water sequence was followed for cleaning

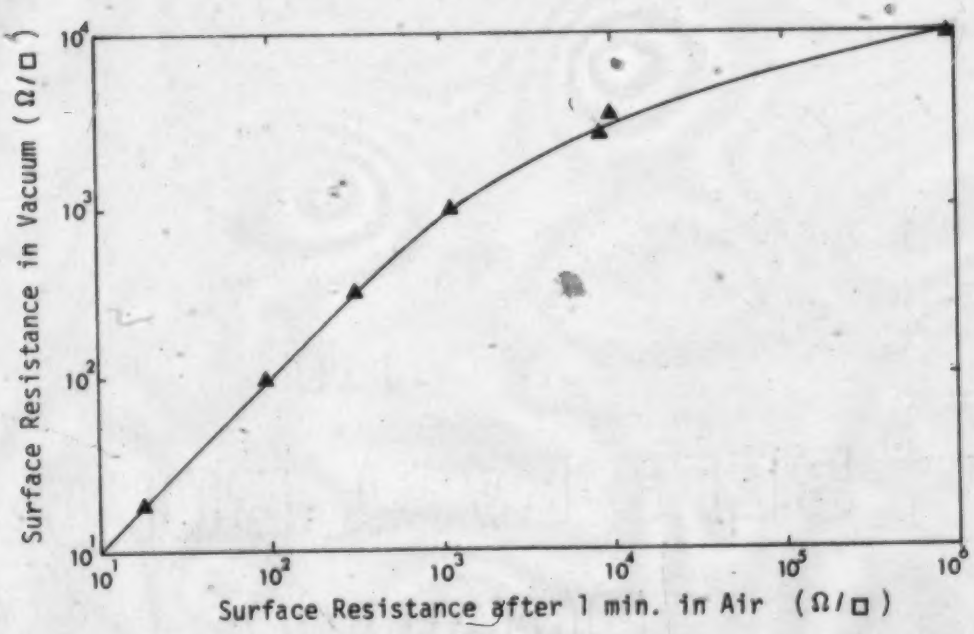

Figure 3.6 Change of Titanium Film Resistance on Exposure to Air

Table 3.2 Sputtering of Titanium Films

Sputtering Duration	Surface Resistance	
15 sec	150 KΩ/□	4×10^{-4} torr argon 5 KV DC (80 mA) 60 Å/min
20	20 - 30 K	
22.5	10 K	
25	7 K	
30	5 K	
30 sec	20 KΩ/□	5×10^{-4} torr argon 3 KV DC (55 mA) 42 Å/min
60	1.2 K	

resistance measured within one minute of exposure to air:
in the last two cases resistance increased to 40 K and 1.7 K respectively after 4 hours in air.

of the disc.

3.5 Effects of Sputtering onto Titania Substrates

3.5.1 Heating in Vacuum

Hayes [75] compared a number on titania ceramics at various temperatures but did not indicate the actual composition of the particular samples. He reported that all specimens were stable up to 350°C but that most demonstrated surface reduction above this temperature. To obtain more relevant data for the ceramics to be used, a number of samples with ε_r ranging from 63 to 96 were heated in a vacuum furnace, the surface temperature being monitored by an optical pyrometer.

Samples of TM63, TM76 and TM84 all underwent a distinct transition from the normal straw yellow colour to a dark grey between 300 and 400°C. TK86, TK92 and TK96 all showed slight surface discolouration at 400° and gradually darkened at temperatures above 500°C. The change was irreversible in vacuum, the original colour returning only after the samples were heated to 800° for at least one hour in atmosphere. Re-oxidation took much longer at temperatures below 750°C. It was also noted that whereas the discolouration of the surface was uniform for the other samples, in the case of TK96 ceramic, the greying was in patches, creating a speckled effect.

3.5.2 Reduction During Sputtering

The samples were sputtered with a layer of Al_2O_3. RF power application levels of 400 watts resulted in reduction of the surface within a few minutes before the alumina could effectively seal the

surface, but at 200 watts the rate of reduction was far slower and at 100 watts there was only very slight reduction over 10 hours. After removal from the sputtering unit, the coated samples were heated in air to 825°C. The grey discolouration of the reduced discs gradually disappeared, being replaced by numerous black spots approximately .1mm in diameter beneath the surface of the alumina. Since the density of the spots varied with the sputtering power and additional heating did not have any effect, it was presumed that the alumina layer obtained after 10 hours of sputtering was sufficient to seal the surface, the spots being caused by oxygen migration beneath the alumina developing localized points of reduction within otherwise oxidized regions.

Since it was evident that some reduction was occurring even at 100 watts, coatings of different thicknesses were deposited on other samples. After reoxidation at 825° the samples were compared. For layers less than 300 Å, the surface was sealed for temperatures under 800°C; however at 825° the titania could still be reoxidized. From this a definite procedure could be established for mass coating of the discs to be tested. A preliminary coating at 100 watts (about 300 Å/hour) was applied for one hour, after which the discs were oxidized in air at 825°. To prevent thermal shock, a lengthy cooling period was allowed before returning the discs to the sputtering unit to complete the alumina coating at 100 watts or higher power. On removal, the discs showed a slight surface discolouration evidently due to the reduction of the top layers of the alumina, since after reheating to 825° again, the discs would take on the normal straw yellow colour superimposed with the colour fringe characteristic of the layer thickness.

One unfortunate factor in this procedure was the degree of high temperature cycling that TiO_2 can undergo: any more than 4 times to 825° apparently increased the probability of the ceramic cracking. Of the 12 discs so treated, only 2 developed cracks after two cycles but in these cases the discs had been previously chipped in transit, possibly increasing the chance of failure. One possible reason for the fractures may have been the temperature differential across the disc during sputtering. The table supporting the discs was water-cooled whereas the upper surfaces of the discs were relatively hot. Surface temperature, measured using an optical pyrometer was 260°C at an applied power of 220 watts.

On one occasion it was found necessary to evaporate a silver film onto some TiO_2 samples. Although they were placed about 25 cm from the evaporating source, all three discs were reduced to various shades of grey within the 2 or 3 minutes required to evaporate the silver. Al_2O_3 coating was not attempted by this means, but the higher temperature essential for the evaporation of the alumina would obviously reduce the surface before any alumina reached the titania.

3.5.3 Resistivity Measurements

Using a Keithley electrometer, resistance measurements were carried out on the samples used in the sputtering tests. Surface resistance in ohms/square was measured by painting two parallel 2 cm lines 2 cm apart on the surface of the discs using conductive paint: bulk resistivity by painting 2 cm diameter circles on opposite faces of the discs. The results for variously treated discs are listed in Table

Table 3.3 -(a) - Surface Resistance of Titania

Sample	Condition	Size	Resistance
Al_2O_3	sputtering target	10 cm dia x .65cm	$10^{14}\Omega/\square$
TiO_2	unpolished surface	8 x .56	2.8×10^{11}
TiO_2(4)	polished, uncoated	8 x .42-.56	$3.3\text{-}14\times10^{11}$
TiO_2	coated, reduced coating removed oxidized	8 x .56	$1.5\text{-}2.9\times10^{6}$ 1.4×10^{7} 2.9×10^{12}
TiO_2	coating reduced oxidized	8 x .53	$3.3\text{-}5\times10^{10}$ $1.4\text{-}2.5\times10^{11}$
TiO_2(3)	polished, uncoated	4-5 x .30	$10^{11}\text{-}10^{12}$
TiO_2(3)	polished, coated speckled oxidized(one only)	4-5 x .30 5 x .30	$1\text{-}2\times10^{11}$ 10^{14}
TiO_2(3)	coated, oxidized	4-5 x .30	$.5\text{-}1\times10^{13}$

(b) - Resistivity

Sample	Condition	Size	Resistivity
Al_2O_3	sputtering target	10cmdia x .65cm	$1.6\times10^{15}\Omega$ cm
TiO_2	unpolished	8 x .56	1.2×10^{12}
TiO_2	polished, coated	8 x .53	5.9×10^{10}
TiO_2	reoxidized	8 x .56	2.9×10^{12}

3.3, the figure in parentheses indicating the number of discs in certain cases.

Most noticeable is the relatively low resistance of the reduced discs compared with untreated samples and the improved characteristics of the alumina coated discs, especially after reoxidation. The highly reduced disc also demonstrated a Q10% lower than an untreated disc in microwave measurements.

3.6 Edge Coating of the Discs

Since copper was chosen for edge coating, ordinary vacuum evaporation was used to obtain the thickest film possible. One or more titania discs were mounted in a motor driven jig which rotated at a few rpm while the copper was being evaporated, to ensure uniform coating of the entire circumference. Two or three successive evaporations, each of a few grams of copper, were sufficient to give film thicknesses of 10 to 15μm when the source to disc separation was about 12 cm.

The film thickness was measured by micrometer and compared to resistance readings between points diametrically opposed on the circumference of the discs. For the given resistivity of copper, the 0.12 ohms typically observed was five times too high for the physically measured film. This would be expected considering that the edge was neither lapped nor polished, but only given a ground finish.

By sandwiching the titania discs between two aluminum discs of the same diameter, the end faces were masked from the evaporation source. These also acted as heat sinks to prevent reduction of the titania during

coating.

3.7 Preparation of the Titania Discs

3.7.1 Machining of the Discs

The titania discs as received from Schaefer Dielectrics were 3 $\frac{1}{4}$" in diameter and $\frac{1}{4}$" thick. After determining the optimum dimensions to obtain the required resonant frequency with unity coupling, the final size was specified as 8.022 cm in diameter and .54 cm thick. The titania was first ground to correct diameter, then thickness reduced to within .15 mm of the final thickness on the same rotary grinder. The disc faces were lapped down to the required thickness prior to polishing both surfaces to an optical flatness of $\lambda/2$ in preparation for coating.

3.7.2 Sputtering of the Alumina Layer

The discs were carefully cleaned using a toluene-acetone-alcohol-distilled water sequence and placed on the watercooled substrate table in the sputtering unit (see Figure 3.3), ensuring that no dust particles settled on the surface of the titania during this operation. The discs were then additionally cleaned in vacuum by electron bombardment for 10 minutes.

With the parameters specified in section 3.3.2, 100 watts of RF power was applied for 60 minutes to each side of the discs. The titania sustained some reduction during this operation so the discs were removed from the sputtering chamber and heated to 825° at atmosphere to permit oxygen diffusion through the alumina layer for reoxidation of the titania. After allowing sufficient time to cool naturally the discs were replaced

in the chamber and 100 watts reapplied for a total of 30 hours to each side. In practice three discs could be coated at once in the chamber by rotating the discs regularly to ensure a uniform layer thickness. The final thickness was about 1 μm, (the actual thicknesses for the different discs are given in Table 5.2). Even with oxygen reactive sputtering, reduction of the alumina did occur. Hence following the procedure described in the preceding section, the discs were again heat treated to 825°.

3.7.3 Rim Coating and Fitting of the Copper Ring

Copper coating of the rim has been described in section 3.6. The copper ring, machined 0.1 mm undersize in diameter, was fitted by heating the ring and disc to 150° on a hotplate and using the differential expansion of the two materials. An alignment template was used to ensure ring and disc surfaces were parallel while cooling. The completed disc was then ready for testing except for cleaning and coating with Ti.

3.7.4 Titanium Surface Coating

After all the low power tests were completed, the discs selected for Ti coating were carefully cleaned and placed in the sputtering unit, being left to degas for a few hours. A shutter was placed between the disc and the Ti sputtering target and 5 KVDC applied in a 4×10^{-4} torr Argon atmosphere to presputter the target for 15 minutes. In this manner the surface oxides on the titanium target were removed and a relatively clean Ti source was present for the short period that the shutter was removed to obtain the required coating (this was 25 seconds for a coating with a surface resistance of 7kΩ/square). The discharge was turned off

and the disc allowed to sit in the vacuum for several hours to cool. The disc was then turned over and the procedure repeated. The coated disc was assembled into the test cavity immediately to prevent unnecessary oxidation of the Ti layer. For the single disc cavity the Ti coating was applied to discs individually because of the time between tests, however, it was possible to coat three discs at a time.

3.7.5 Some Comments on Ceramic Preparation

In processing ceramics fatalities are bound to occur. Of the total of 21 discs available at one time or another; two were accidentally but irreparably damaged by thermal shock in preparation; two were chipped in machining but salvaged for useful testing; two developed minor cracks while being sputtered; and two were slightly chipped in fitting the copper ring. Fortunately 17 of the discs were suitable for testing, but the failures indicate that ceramic is very temperamental especially when heated and due caution must be observed in preparation and handling.

CHAPTER 4

THE SINGLE CELL MICROWAVE CAVITY

4.1 The π- Mode Structure

4.1.1 Introduction

The accelerating field in a dielectric loaded linear accelerator is obtained by exciting a cylindrical cavity in the TM_{01n} mode. The cavity length is $n\ \lambda_g/2$, such that the travelling waves forming the cavity standing wave field have a phase velocity $v_p = c$, and electrons of sufficient initial velocity gain energy from the axial electric

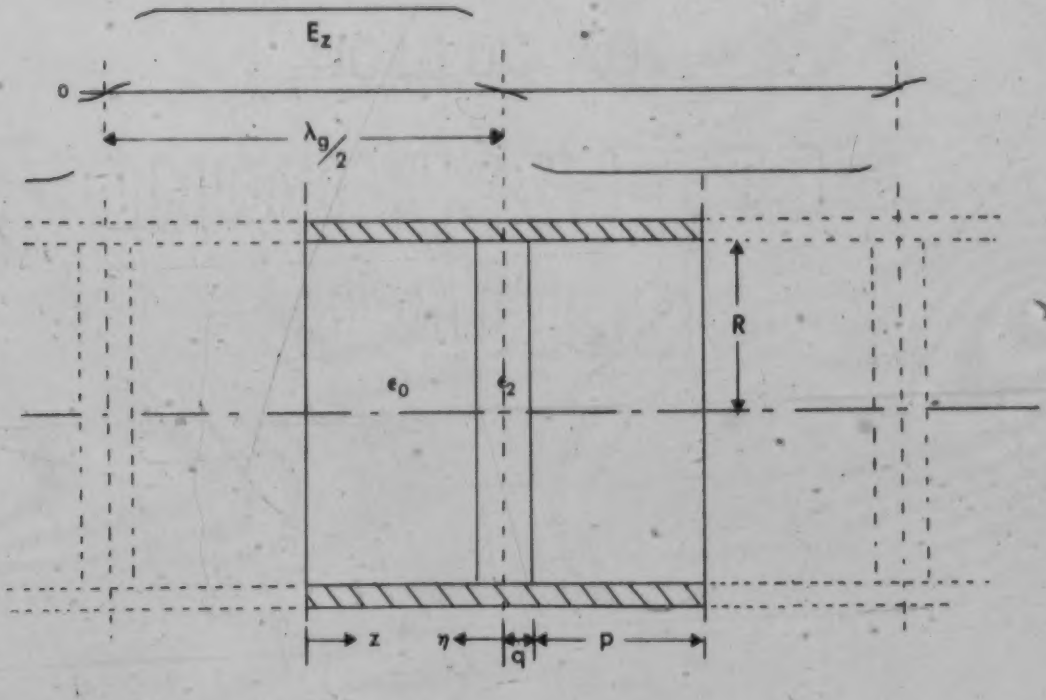

Figure 4.1 The Single Cell Cavity

field of the component travelling waves. If the structure is loaded with n equally spaced discs, the phase change of the electric field between discs is π, and the structure is said to be operating in the π mode. Such a structure is spatially periodic and fields λ_g apart are identical with an axial field node at the center of each disc and an anti-node halfway between adjacent discs. Thus by placing a shorting plane at any anti-node position there will be no perturbation of the field pattern. In this way the same field pattern that exists in a long structure can be generated using a cylindrical cavity of length $\lambda_g/2$ with a single disc, as shown in Figure 4.1.

4.1.2 Field Relationships

The standing wave fields in a TM_{011} mode cavity are [76]:

$$E_z = E_o J_o(k_c r)\cos\beta z\, e^{j\omega t} \qquad 4.1(a)$$

$$E_r = \frac{\beta}{k_c} E_o J_1(k_c r)\sin\beta z\, e^{j\omega t} \qquad 4.1(b)$$

$$H_\phi = \frac{j\omega\epsilon}{k_c} E_o J_1(k_c r)\cos\beta z\, e^{j\omega t} \qquad 4.1(c)$$

$$k_c^2 = \gamma^2 + k^2 = \gamma^2 + \omega^2\mu\epsilon \qquad 4.1(d)$$

where $\gamma = j\beta$ for a wave above the cut-off angular frequency ω_c. Using the conventions in Figure 4.1, in the vacuum region (subscript o) we get:

$$E_z = E_o J_o(k_c r)\cos\beta_o z\, e^{j\omega t} \qquad 4.2(a)$$

$$E_r = \frac{\beta_o}{k_c} E_o J_1(k_c r)\sin\beta_o z\, e^{j\omega t} \qquad 4.2(b)$$

$$H_\phi = \frac{j\omega\epsilon_o}{k_c} E_o J_1(k_c r)\cos\beta_o z\, e^{j\omega t} \qquad 4.2(c)$$

and in the dielectric (region 2),

$$E_z = E_2 J_o(k_c r)\sin\beta_2 n\, e^{j\omega t} \qquad 4.3(a)$$

$$E_r = \frac{\beta_2}{k_c} E_2 J_1(k_c r)\cos\beta_2 n\, e^{j\omega t} \qquad 4.3(b)$$

$$H_\phi = \frac{j\omega\epsilon_2}{k_c} E_2 J_1(k_c r)\sin\beta_2 n\, e^{j\omega t} \qquad 4.3(c)$$

At the interface, $z=p$, $n=q$, the components must be matched.

$$D_{zo} = D_{z2}$$

$$E_o J_o(k_c r)\cos\beta_o p = E_2 J_o(k_c r)\sin\beta_2 q$$

or

$$\epsilon_2 E_2 = \frac{\cos\beta_o p}{\sin\beta_2 q}\ \epsilon_o E_o \qquad 4.4$$

Similarly the condition $E_{ro}=E_{r2}$ yields the equation

$$E_o \sin\beta_o p = E_2 \cos\beta_2 q \qquad 4.5$$

Combining 4.4 and 4.5 gives the conditional equation:

$$\tan\beta_o p\ \tan\beta_2 q = \frac{\beta_2 \epsilon_o}{\beta_o \epsilon_2} = \frac{\beta_2}{\epsilon_r \beta_o} \qquad 4.6$$

The propagation constants for the vacuum and djelectric regions are derived from equation 4.1(d) and are respectively:

$$\beta_o = \frac{2\pi}{\lambda}\left(1 - \left(\frac{\lambda}{\lambda_c}\right)^2\right)^{\frac{1}{2}} \qquad 4.7$$

$$\beta_2 = \frac{2\pi}{\lambda}\left(\epsilon_r - \left(\frac{\lambda}{\lambda_c}\right)^2\right)^{\frac{1}{2}} \qquad 4.8$$

λ_c is the wavelength corresponding to the cut-off frequency f_c and for TM_{01} modes is 2.613R (R is the inside radius of the cavity).

4.1.3 Cavity Dimensions

Equation 4.6 relates the cavity variables: the dimensions, p, q and R; the dielectric constant ε_r; and the resonant frequency f_o. For titania, ε_r=95, but the other quantities are arbitrary provided they satisfy the conditional equation.

It will be seen later in Chapter 9 that in a practical structure the ratio $\frac{\lambda}{\lambda_c}$ will be fixed by a constraint placed on equation 4.6, but for the purposes of the initial breakdown research λ_c was specified such that the cylindrical cavity could also operate in the TM_{010} mode when the disc was omitted, to enable comparison between the two modes.

The high power magnetron to be used was only tuneable through a narrow bandwidth of 2864 to 2874 MHz, with the most desirable frequency at 2868 MHz. Therefore for the TM_{010} mode λ_c = 10.453 cm and the corresponding cavity radius (= $\frac{\lambda_c}{2.613}$) was 4.005 cm. In practice the radius required to obtain this frequency was 4.011 cm which corresponds to a theoretical cut-off frequency of 2860.5 MHz. The difference was due to the perturbing effect of the iris used to couple power into the cavity.

An arbitrary restriction was placed on the minimum cavity length to permit shortening later to form part of a longer accelerating structure. Setting p = .030 m and substituting the above quantities into equations 4.1(d), 4.7 and 4.8 the following relations were obtained:

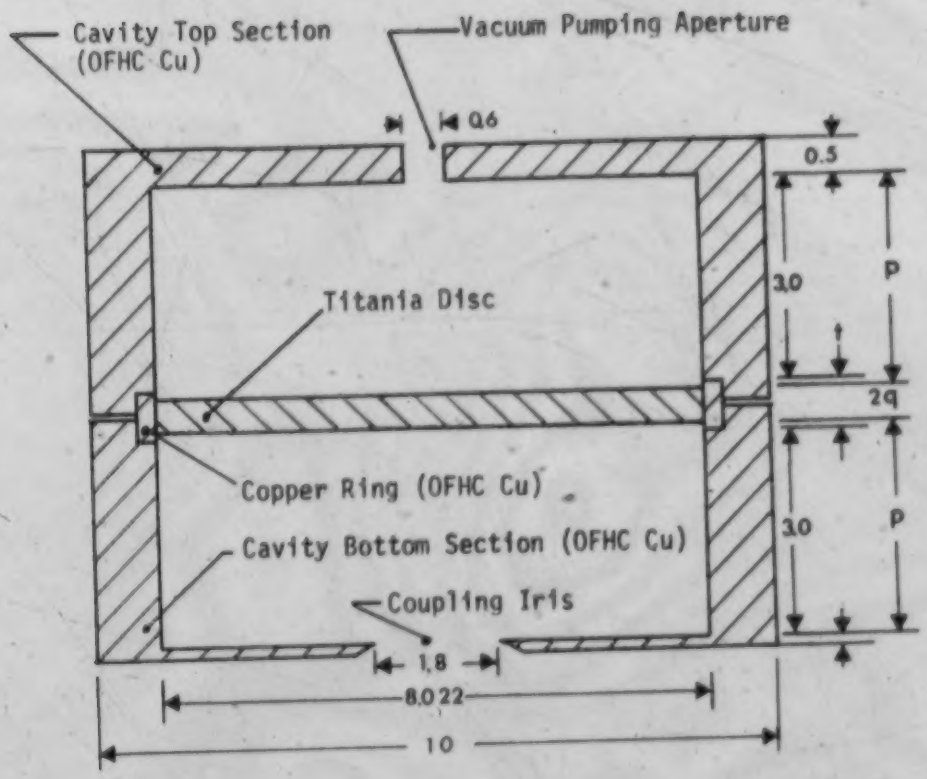

Figure 4.2 Cavity Geometry (dimensions in cm)

Table 4.1 Summary of Cavity Dimensions for Disc #8

	calculated	actual
radius R (cm)	4.0005	4.011
disc thickness 2q (cm)	.5067	.539
ring thickness t (cm)	2q	.575
vacuum length (cm)	2p=6	6.036

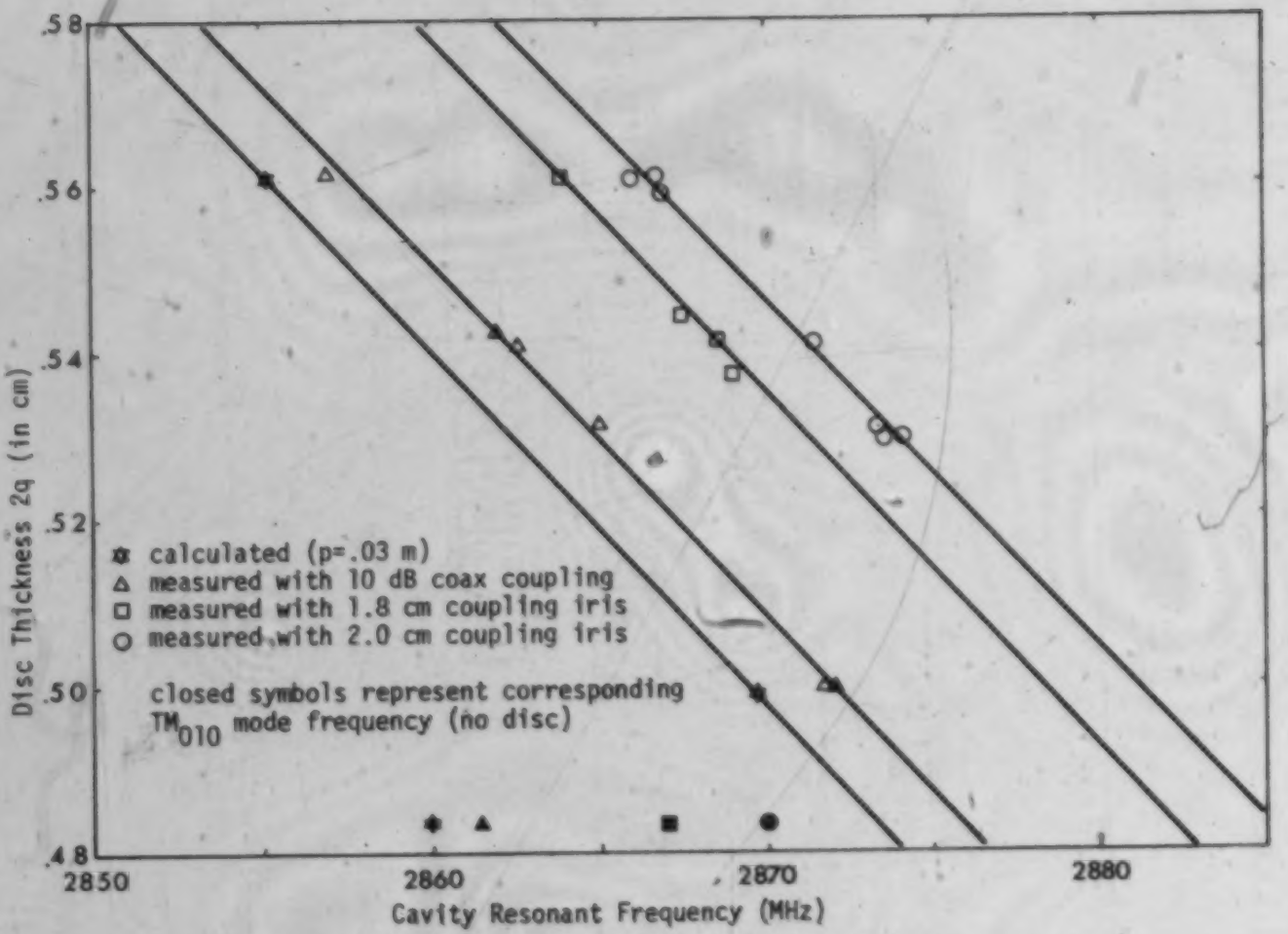

Figure 4.3 Dependence of Cavity Resonance on Disc Thickness

$\beta_o = 4.393\ m^{-1}$

$\beta_2 = 582.8\ m^{-1}$

$k_c = 59.95\ m^{-1}$

The calculated disc thickness for a 2868 MHz resonance was 2q = .5067 cm. Again in practice the coupling iris made it mandatory to increase the disc thickness by 5% for the designed frequency.

Figure 4.2 illustrates the cavity used for the initial high power tests. Calculated dimensions and those actually used for one particular disc (#8) are listed in Table 4.1.

As expected the resonant frequency was more dependent upon q than p. The vacuum distance p was increased up to 5% with little or no change in f_o. The disc thickness was the parameter utilized to vary the cavity resonant frequency. The actual thickness-frequency relationship is plotted in Figure 4.3 for different coupling parameters.

4.1.4 Cavity Coupling Calculations

Power is coupled from a rectangular waveguide into the cavity through an iris in the center of one end wall of the cylindrical cavity, the rectangular TE_{01} mode exciting the TM_{01n} mode within the cavity. To indicate the amount of incident energy coupled into the cavity there is defined a coupling parameter, β_c, which can be related to the measured voltage standing wave ratio in the main guide. For an undercoupled cavity, β_c = 1/VSWR; whereas for overcoupling, β_c = VSWR. Only for an VSWR of unity (β_c=1) is the cavity matched to the main guide, all incident energy being dissipated in the cavity.

The coupling parameter is defined in terms of the various Q's of the guide and cavity circuit. The Q of a circuit is given as

$$Q = \frac{\omega_o U}{W} \qquad 4.9$$

where ω_o is the cavity resonant angular frequency; U, the energy stored in the cavity; and W, the average power dissipated. The unloaded Q_o is simply the Q of a cavity which is not coupled to any external circuit and consequently is not directly measurable. Q_L is the actual measurable loaded Q of the cavity when coupled to one or more external circuits and includes power loss from the cavity through the coupling iris. The external Q, Q_{ext} is introduced to relate Q_o and Q_L and includes only the internal energy and the external (iris) losses. If W_{int} and W_{ext} are the internal and external losses respectively, the relationship between Q_o, Q_L and Q_{ext} is

$$\frac{1}{Q_L} = \frac{W_{int} + W_{ext}}{\omega_o U_{int}} \qquad 4.10$$

$$= \frac{1}{Q_o} + \frac{1}{Q_{ext}}$$

and by applying the definition $\frac{Q_o}{Q_{ext}} = \beta_c$,

$$\frac{1}{Q_L} = \frac{1 + \beta_c}{Q_o} = \frac{1 + \beta_c}{\beta_c Q_{ext}} \qquad 4.11$$

Thus for optimal coupling (β_c=1), $2Q_L = Q_{ext}$. For a similar coupling problem, Slater [77] derived the relation

$$\frac{1}{Q_{ext}} = \left(\frac{2r^3}{3}\right)^2 \frac{|E_y|^2 \quad |E_z|^2}{\int_{\square} |E_y|^2 \, da \int_{O} |E_z|^2 \, dv} \qquad 4.12$$

where r is the iris radius and E_y and E_z are respectively the fields in the rectangular and circular guides. If the TM_{010} mode is considered (β=o in equation 4.1), this reduces to

$$\frac{1}{Q_{ext}} = \left(\frac{2r^2}{3}\right)^3 \frac{E_y^2 \quad E_z^2}{b \int_o^a E_y^2 \sin^2 \pi/a \, dx \int_o^R E_z^2 J_o^2(k_c\rho) 2\pi\rho L d\rho} \qquad 4.13$$

Evaluating and substituting a=3.4 cm, b=7.21 cm and values from section 4.1.3:

$$\frac{1}{Q_{ext}} = \frac{2.32 \times 10^{-3} \, r^6}{L}$$

For a 6.775 cm long cavity with a measured Q_L = 8000 (section 5.3) the required iris radius should be 0.757 cm. In fact, the actual iris used had a diameter of 0.9 cm (with slight overcoupling). This discrepancy can be accounted for by considering the attenuating effect of the iris which has a finite thickness, and behaves like a short section of circular guide below cut-off. Attenuation in the cut-off guide is

$$\alpha = 54.6 \sqrt{\left(\frac{1}{2.61}\right)^2 - 1/\lambda^2} \text{ dB} \qquad 4.14$$

and for the particular iris used, α = 22.65 dB/cm. The iris thickness was .17 cm giving an attenuation of 3.85 dB or a transmission of .412. Correction of iris radius by the term $\left(\frac{1}{.412}\right)^{1/6}$ yields r = .878 cm which

is in better agreement with 0.9 cm.

Since the iris radius was fixed slightly oversize, the final matching was accomplished by adjusting the position of the vacuum sealed short terminating the rectangular guide.

In evaluating equation 4.12 a TM_{010} mode was assumed. In the case of the TM_{011} mode the volume integral in the denominator is effectively reduced by the factor $\frac{L - 2q}{L}$ since the field in the dielectric is much lower than the field in vacuum. However this is counteracted by the increase in loss due to the dielectric and a corresponding decrease in Q_o and Q_{ext}. In section 5.2 it will be seen that there is little difference in the field patterns of the two modes near the iris.

4.2 Construction of the Cavity

4.2.1 Geometry

The required dimensions for the cavity have been given in section 4.1.3. Two cavity halves were machined from 4" diameter OFHC copper, allowing a suitably thick wall for mechanical strength. The bottom half had an end wall of .15 cm thickness with the 1.8 cm diameter coupling iris; whereas the end wall of the top section had a thickness of .5 cm to allow mounting of a coaxial probe through the .6 cm diameter coupling hole in the center. To seat the dielectric disc a step was machined in each cavity half to fit the copper ring that was shrunk onto the disc. For maximum contact on the inner surface of the cavity, the step was tapered to ensure maximum pressure at the inner edge of the ring when the

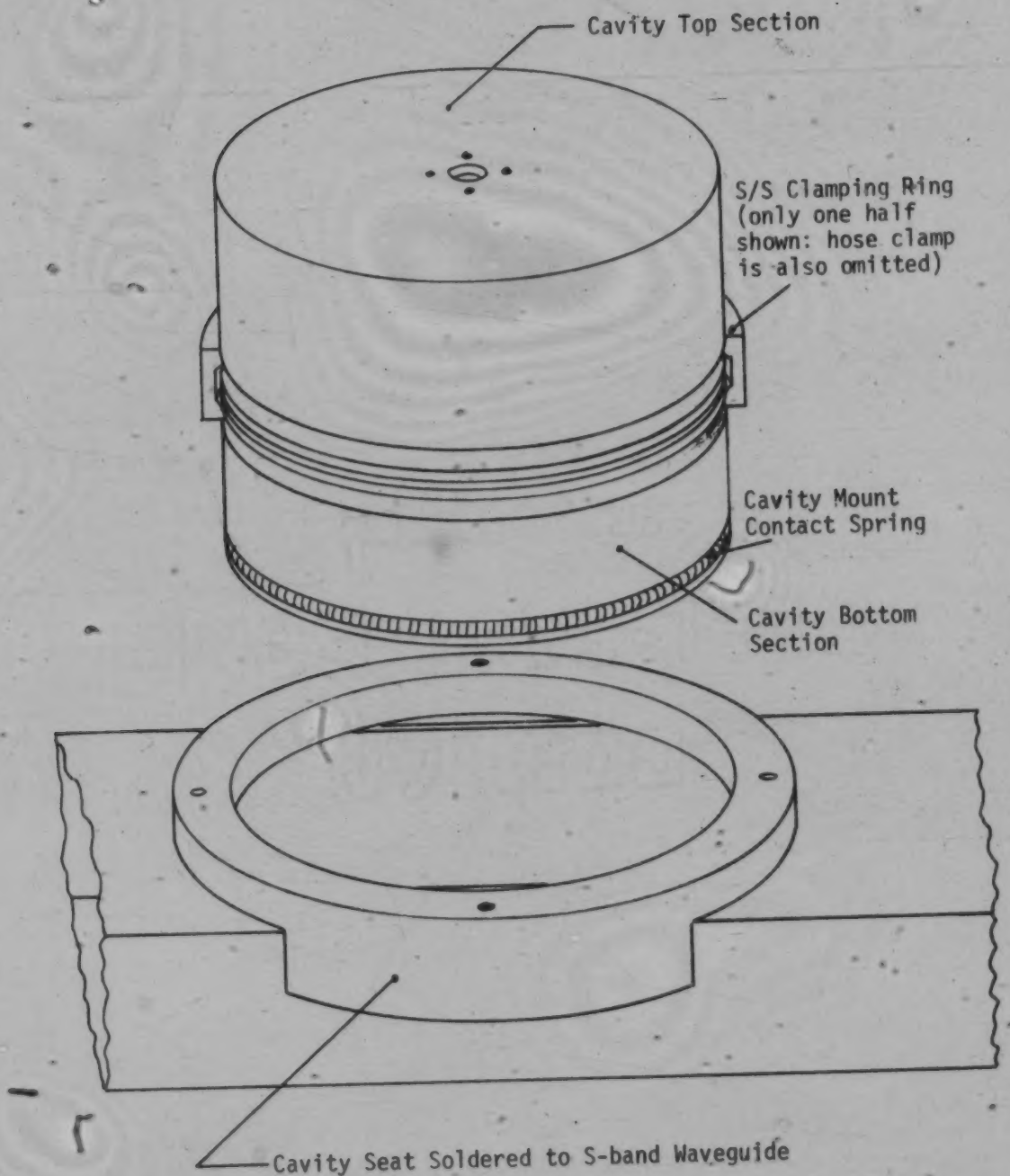

Figure 4.4 Cavity Assembly and Clamping

two cavity halves were clamped together.

4.2.2 Clamping of the Cavity

Initially the cavity sections were placed in the cavity mount and clamped together using a backing plate over the top cavity with four rods extending to the mount. After a number of tests this method was abandoned since uniform contact pressure could not be ensured and the cavity edges and ring may be distorted, especially when heated. To prevent this and to increase portability (to allow the removal of the clamped cavity from one cavity mount to another) the cavity halves were modified to the design shown in Figure 4.4. A groove was machined at 45° into each half; a sectioned stainless steel ring with the inner surface machined to mate with the grooves was then placed around the cavity. An ordinary 4" diameter pipe clamp was tightened about the S/S ring, forcing the sections of the ring together and consequently drawing the cavity halves together on the copper ring. The pressure was thus uniform on the entire circumference of the cavity and the cavity edges not deformed. Logically this was extended to longer cavity sections and enabled the insertion of single discs in a structure without destroying the seating of other discs, enabling repeatable measurement of cavity parameters.

4.2.3 Cavity-mount Contact

Simultaneous with the new clamping arrangement, a groove of semi-circular cross section was machined into the bottom cavity half, 3mm from the end. A 28cm length of 3mm diameter helix spring was made

from .5mm diameter spring steel and formed into a loop to fit in the machined groove. The outside diameter of the loop being greater than the outer diameter of the cavity, it was compressed when the cavity was rotated to seat it in the cavity mount, giving good electrical and mechanical contact in the same manner as in microwave tube installation.

4.3 Thermal Effects

4.3.1 Introduction

The energy dissipation per unit volume in a dielectric subjected to a microwave field E, is $\frac{1}{2}\sigma|E|^2$. If the field is non-uniform through the material, then the resulting heat generation and temperature rise will not be the same at all points in the dielectric. For any material with a non-zero coefficient of thermal expansion there will be a thermally induced stress within the material.

Taking the electric fields given in equation 4.3, the dissipation at any point in the dielectric is:

$$\frac{1}{2}\sigma|E|^2 = \frac{1}{2}\sigma E_2^2 (J_0^2(k_c r)\sin^2\beta_2\eta + \frac{\beta_2^2}{k_c^2} J_1^2(k_c r)\cos^2\beta_2\eta) \qquad 4.15$$

For the .54 cm thick disc of section 4.1, the factor $\frac{E^2}{E_2^2}$ is plotted versus r/R and η/q in Figure 4.5(a). From this can be derived a contour diagram in $\frac{E^2}{E_2^2}$(proportional to energy density and also the dielectric loss) in the r-η plane. Figure 4.5(b) is necessarily not to scale since q = .27 cm and r = 4.011 cm, but does indicate that maximum dissipation occurs at η = 0 and r = .765 R, the field being entirely radial.

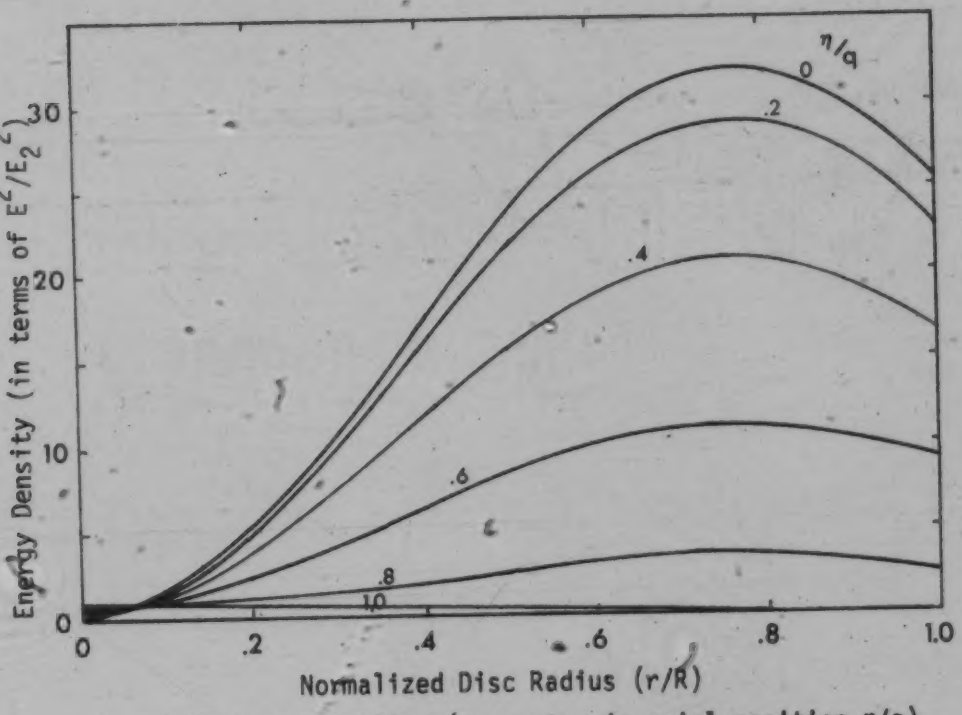

(a) Energy in Disc (parameter is axial position η/q)

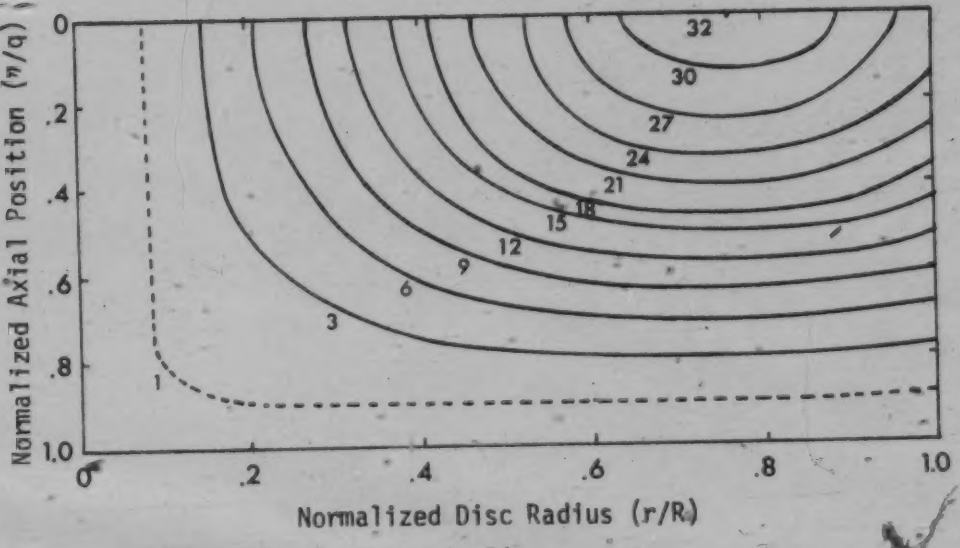

(b) Energy Contours in Disc

Figure 4.5 Relative Energy Density E^2/E_2^2 through the Ceramic Disc For the TM_{01n} modes, the field is a function of the radial and axial position only.

4.3.2 Heat Flow in the Disc

Since temperature is dependent upon the heat input, Figure 4.5(a) would represent the temperature distribution in the dielectric if it did not suffer any radiative or conductive heat loss. However, in practice the surface at r=R is in contact with an effective heat sink, namely the copper wall of the cavity, and the surface η=q radiates into vacuum; therefore the temperature distribution will be modified from that suggested by Figure 4.5(a).

An elemental volume dV with internal heat sources Q_{in} will undergo an increase of temperature and there will be a corresponding heat flow out of the volume due to the temperature gradient. Integrating over the volume and taking into account radiation, one obtains the balanced equation

$$\int \rho C_v \frac{dT}{dt} dV = \int Q_{in} \cdot dV - \int Q_{cond} \cdot ds - \int Q_{rad} \cdot ds \qquad 4.16$$

where $Q_{in} = = \frac{1}{2}\sigma E^2$ $(\sigma=\omega\varepsilon \tan\delta)$

$Q_{cond} = -K\nabla T$

$Q_{rad} = \varepsilon_T \sigma_T (T^4 - T_o^4)$

Equation 4.16 is non-linear; therefore before attempting a more complete solution, it is desirable to make a few simplifications to determine the relative contribution of each term. If it is assumed that heat generation is uniform throughout the disc ($P_d = Q_{in}V$); that the radiative loss is zero; and that the copper cavity wall is maintained at a constant temperature T_o= 300°K; then for the case of a short cylinder in the steady state, equation 4.16 reduces to the following:

$$\int_V Q_{in} dV = -\int K \nabla T \cdot ds = -K \int \nabla \cdot \nabla T \, dV = -K \int \nabla^2 T \, dV$$

from which

$$Q_{in} = -K\nabla^2 T = -K \frac{1}{r} \frac{d}{dr} \left(r \frac{dT}{dr} \right) \qquad 4.17$$

which has the solution [78]

$$T = \frac{P_d}{K} \frac{R^2 - r^2}{4\pi R^2 2q} + T_o \qquad 4.18$$

For titania, $K = 16 \times 10^{-3}$ cal/cm-sec-°C ($T<100°C$), such that for the disc described in section 4.1.3, absorbing 29 watts of RF (typical average power at breakdown), the temperature distribution would be

$$T = 64 \left(1 - \frac{r^2}{16}\right) + T_o . \qquad 4.19$$

The maximum temperature at the center of the disc would be 364°K.

Now reintroduce the radiative term and consider the heat loss by radiation on the basis of this temperature distribution. Radiation from an elemental area of the surface is

$$Q_{rad} \, ds = \sigma_T \varepsilon_T (T(r)^4 - T_o^4) \, ds . \qquad 4.20$$

Substituting $T(r)$ and integrating over both sides of the disc, the energy radiated is

$$2\sigma_T \varepsilon_T \int (T(r)^4 - T_o^4) 2\pi r dr = 1.22 \text{ watts},$$

indicating that conduction is the more important heat transfer mechanism and that the initial assumption $Q_{rad} \simeq 0$ was valid.

Returning again to equation 4.16 and re-writing it for the steady state and $Q_{rad}=0$, but with the specified energy dissipation we obtain:

$$\frac{d^2T}{dr^2} + \frac{1}{r}\frac{dT}{dr} + \frac{d^2T}{dn^2} = -\frac{1}{K}\frac{\sigma E^2}{2} \qquad 4.21$$

Being a non-homogeneous second order partial differential equation in two variables, the easiest method of obtaining a solution is by a numerical or analog technique. Choosing the latter method, a resistor mesh, dimensions of which (4x60), were proportional to the disc half thickness, q, and radius, R, respectively, was constructed; the energy input being simulated by currents into each of the 5x61 nodes according to the distribution of Figure 4.5. Applying the boundary conditions $V(r=R)=0$ and $\frac{dV}{dr}(r=0) = 0$, the measured node voltages represented the temperatures at the corresponding points in the disc. The resulting normalized values are plotted in Figures 4.6. It is significant that, the thinness of the disc results in very little axial temperature variation, the maximum difference between temperature at the center and on the surface being .007, thus allowing simplification in the following calculations.

One analytical function that approximates T in Figure 4.5 within 3% is:

$$T = A \qquad 0 < r = .3R$$
$$T = A\left(1-\left(\frac{r-.3R}{.7R}\right)^2\right) \qquad .3R < r = R \qquad 4.22$$

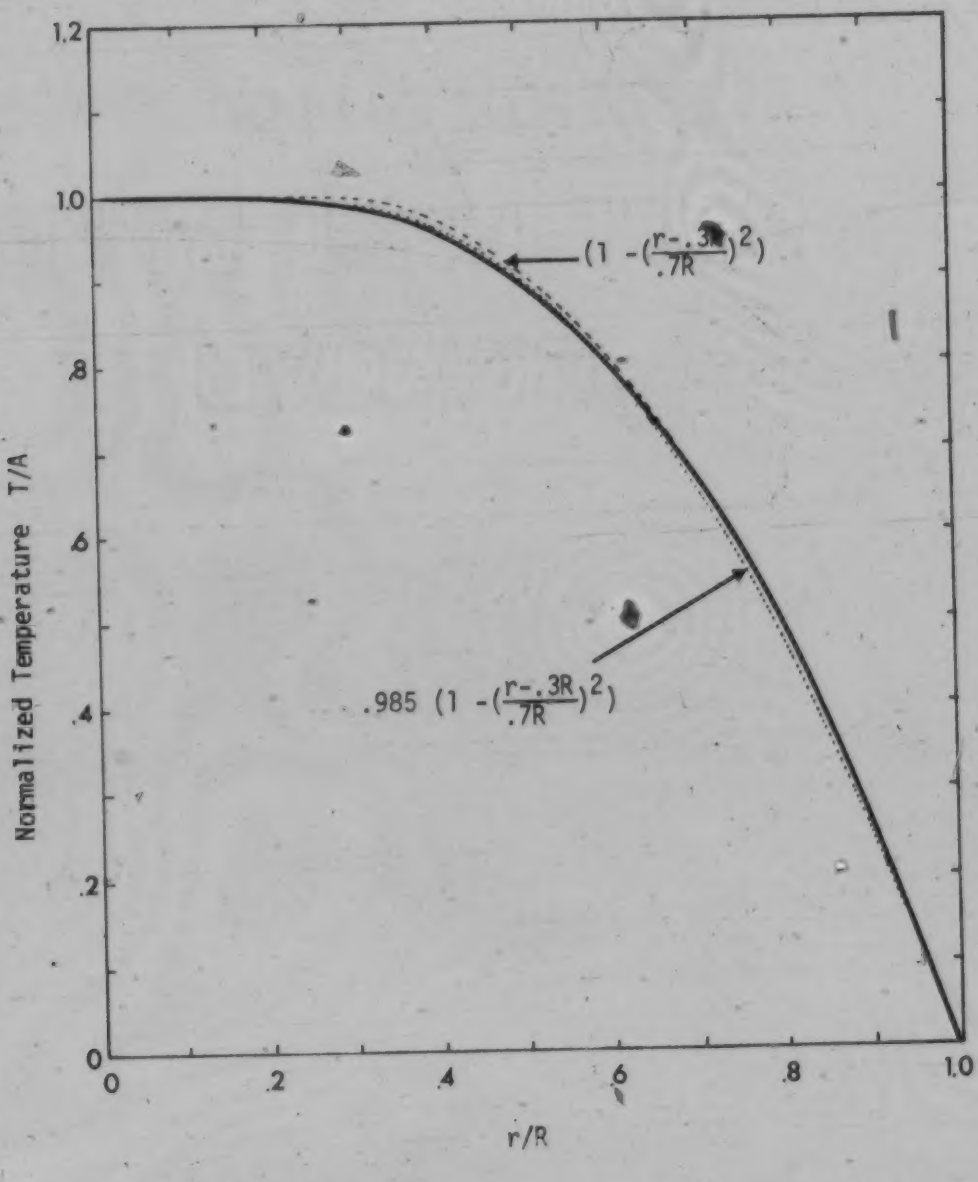

Figure 4.6 Temperature Distribution in Ceramic Disc at $\eta=0$
The distribution at the disc surface ($\eta=q$) was at most .007 lower than at the center ($\eta=0$). The two approximations to the experimental curve are also shown.

A better fit (to within 1.5%) is given by:

$$\left.\begin{aligned} T &= A(1-3.28r) && 0 < r = .3R \\ T &= A(.984)(1-(\tfrac{r-.3R}{.7R})^2) && .3R < r = R \end{aligned}\right\} \qquad 4.23$$

however considering the assumptions applied to aid in the linearization of equation 4.16 (including the assumption that the thermal conductivity for titania is constant over a narrow temperature range), the simpler equation 4.22 will be used.

The normalizing factor 'A' in equation 4.22 is proportional to the average power absorbed by the disc and can be calculated in the following manner. From equation 4.15 the average energy dissipated in the disc is:

$$P_d = \frac{\sigma}{2} \int E_2^2 [\, J_o^2(k_c r)\sin^2\beta_2 n + \frac{\beta_2^2}{k_c^2} J_1^2(k_c r)\cos^2\beta_2 n]dv \qquad 4.24$$

E_2 in this case being the effective average field strength corresponding approximately to E_2 peak multiplied by the duty factor of the pulse. Evaluating over the volume of the disc:

$$P_d = \frac{2\pi\sigma}{2}\frac{R^2}{4} E_2^2 \frac{J_1^2(k_c R)}{\beta_2}\left[2\beta_2 q(1 + \frac{\beta_2^2}{k_c^2}) + \sin 2\beta_2 q(\frac{\beta_2^2}{k_c^2} - 1)\right] \qquad 4.25$$

and for the standard disc of section 4.1.3,

$$P_d = 3.493 \times 10^2 \frac{\sigma}{2} E_2^2 \qquad 4.26$$

Substituting equation 4.26 into 4.21 noting that 1 cal = 4.182 watt sec,

$$\frac{d^2T}{dr^2} + \frac{1}{r}\frac{dT}{dr} + \frac{dT^2}{dz^2} = -\ .684 \times 10^{-3}\ \frac{P_d}{K}\left[J_o^{\,2}(k_c r)\sin^2\beta_2 n + \frac{\beta_2^{\,2}}{k_c^{\,2}}\,J_1^{\,2}(k_c r)\cos^2\beta_2 n\right] \qquad 4.27$$

Considering only the radial dependence

$$\frac{d^2T}{dr^2} + \frac{1}{r}\frac{dT}{dr} = -\ .684 \times 10^{-3}\ \frac{P_d}{2K}\left[J_o^{\,2}(k_c r) + \frac{\beta_2^{\,2}}{k_c^{\,2}}\,J_1^{\,2}(k_c r)\right] \qquad 4.28$$

Equation 4.22 provides a good fit for T in the region r=R;therefore evaluating derivatives at r=R:

$$\frac{dT}{dr} = -\ \frac{2A(r-.3R)}{(.7R)^2} \qquad 4.29$$

$$\frac{d^2T}{dr^2} = -\ \frac{2A}{.49R^2} \qquad 4.30$$

From Figure 4.5 at r=R, equation 4.28 becomes

$$-\ \frac{A(1+.7)}{.49R^2} = -\ \frac{P_d}{2K} \times .684\times10^{-3} \times 25.33 \qquad 4.31$$

and $A = 1.248\ P_d$. Thus for an input (to the disc) of 30 watts average, the temperature at the center of the disc would be 37.4°C above the copper wall temperature, T_o.

Recalculating equation 4.20 using the temperature function of equation 4.22, for an input of 30 watts, the radiative term accounts for only .84 watts of the total. Figure 4.7 illustrates that for power

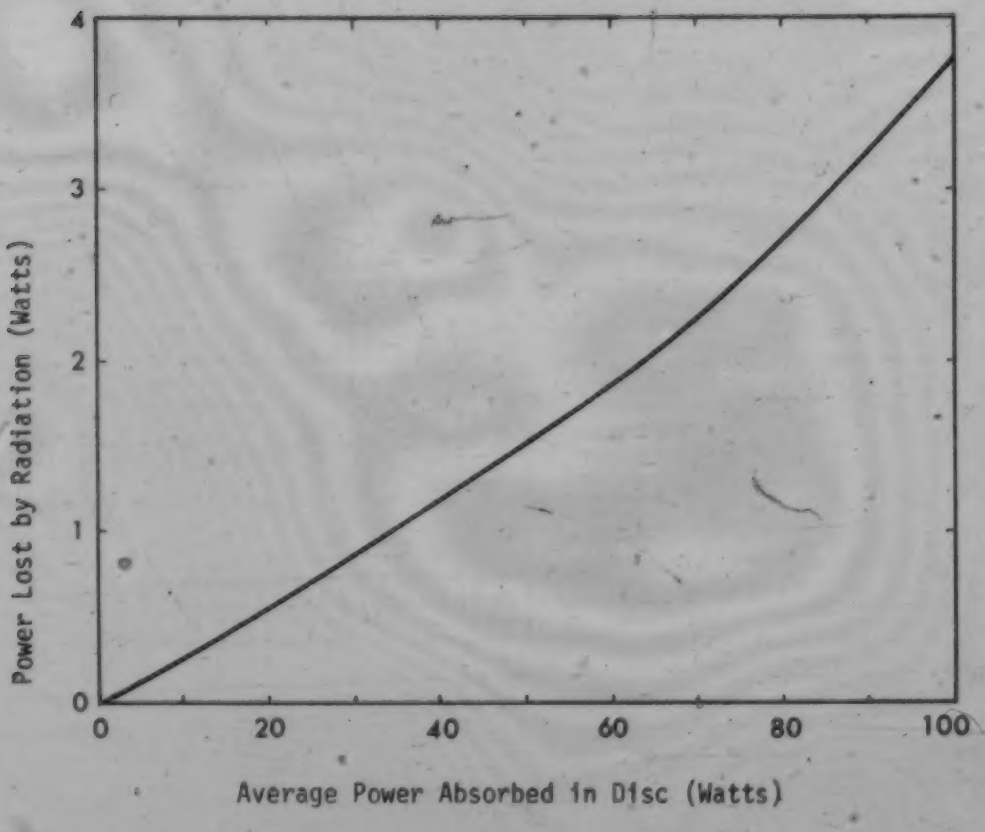

Figure 4.7 Radiative Contribution to Heat Loss from the Disc (assuming conductivity is primary loss mechanism)

dissipation up to 100 watts, the radiative contribution to heat loss is less than 4%.

4.3.3 Thermal Stress

For radial and tangential stress in a cylinder with no axial variation of temperature, Timoshenko [79] gives the relations

$$\sigma_r = \alpha E_y \left(\frac{1}{R^2}\int_0^R T(r)rdr - \frac{1}{r^2}\int_0^r T(r)rdr\right) \qquad 4.32$$

$$\sigma_\theta = \alpha E_y \left(-T + \frac{1}{R^2}\int_0^R T(r)rdr + \frac{1}{r^2}\int_0^r T(r)rdr\right) \qquad 4.33$$

where E_y is Youngs modulus and α is thermal coefficient of linear expansion. Substituting equation 4.22, the equations for thermal stress become:

$$\sigma_r = \begin{cases} .1925\ \alpha E_y A & 0 < r < .3R \\ \alpha E_y A(.10066 + .51024\left(\frac{r}{R}\right)^2 - .40816\frac{r}{R} - .0013775\left(\frac{R}{r}\right)^2) & .3R < r < R \end{cases} \qquad 4.34$$

$$\sigma_\theta = \begin{cases} .1925\ \alpha E_y A & 0 < r < .3R \\ \alpha E_y A(-.10066 + 1.53058\left(\frac{r}{R}\right)^2 - .81633\frac{r}{R} + .0013775\left(\frac{R}{r}\right)^2) & .3R < r < R \end{cases} \qquad 4.35$$

σ_r and σ_θ are shown in Figure 4.7.

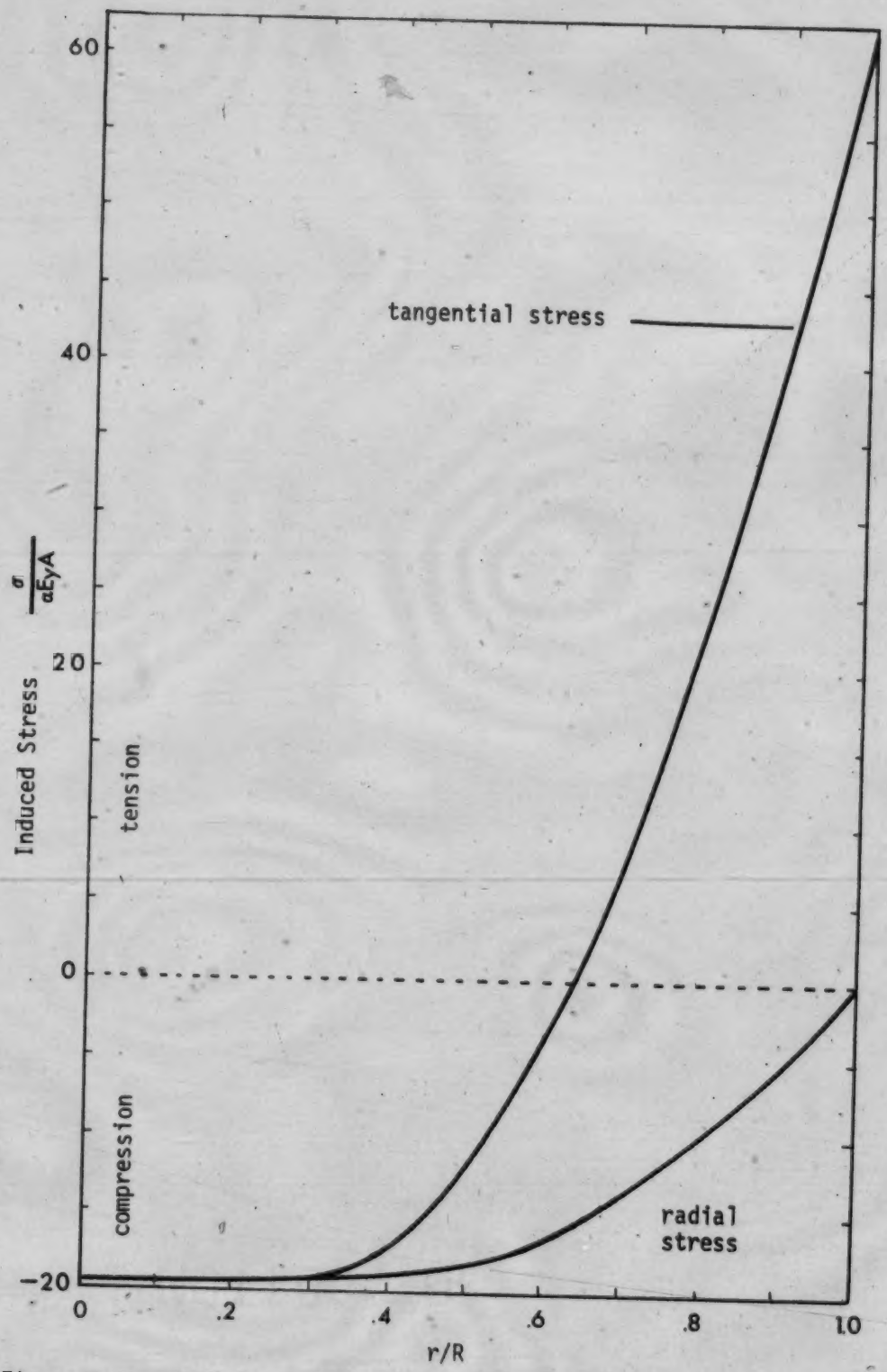

Figure 4.8 Thermal Stresses Induced in the Ceramic Disc

It should be noted that in evaluating the stresses the compressive effect of the copper ring fitted onto the ceramic was not considered. The rings were .18 cm thick and machined .1 mm undersize in diameter. After being heated to fit around the disc and left to cool, there is developed a hoop stress σ_h (equal to E_y x strain of the copper [80]= 1.1×10^6 kg/cm^2 x $\frac{.01 \text{ cm}}{8.022\text{cm}}$) = 1.37×10^3 kg/cm^2. This results in a compressive pressure on the circumference of the disc given by $p = \sigma_h \frac{\text{thickness}}{R} = 1.37 \times 10^3 \times \frac{.18}{4.011} = 61.5$ kg/cm^2 For a solid disc the resulting radial and tangential stresses are constant; both are compressive and equal to p. Taking these into account in studying Figure 4.8, the thermal operating bounds for this disc geometry can be determined.

The relevant data for titania are listed in Appendix A. The tensile strength of titania is given as 300-800 kg/cm^2, the crushing strength being ten times greater (Table A.1). In the disc, maximum compressive stress is at the center (tangential and radial stress being equal at this point) and is

$$\sigma = .1925 \, \alpha_{TiO_2} E_y A + 61.5 \qquad 4.36$$

Accepting the worst case compressive strength of 3000 kg/cm^2 the limit on A would be 1908 (since this is equal to the maximum temperature at the center, obviously decomposition would have occurred first). However, if the tangential stress at the edge is considered

$$\sigma = .615 \, \alpha_{TiO_2} E_y A - 61.5 \qquad 4.37$$

and at the lower limit of tensile strength of 300 kg/cm^2, A = 73.48. This is a more realistic limitation and corresponds to an average power of 58.9 watts.

Combining equations 4.31 and 4.37

$$12.28 \times 10^{-3} \quad \frac{P_d}{K} \alpha_{TiO_2} E_y - 61.5 = 300 \text{ to } 800 \qquad 4.38$$

The uncertainty of α_{TiO_2} and E_y is probably less than 30%; the hoop stress may actually be 50% higher due to machining variations and thermal expansion of the ceramic; however as seen from Table A.1 the greatest error will be due to the thermal conductivity and tensile strength. Figure 4.9 is therefore equation 4.38, plotted within the limits given by K and the tensile strength, showing the probability of failure of a titania disc due to thermal stresses.

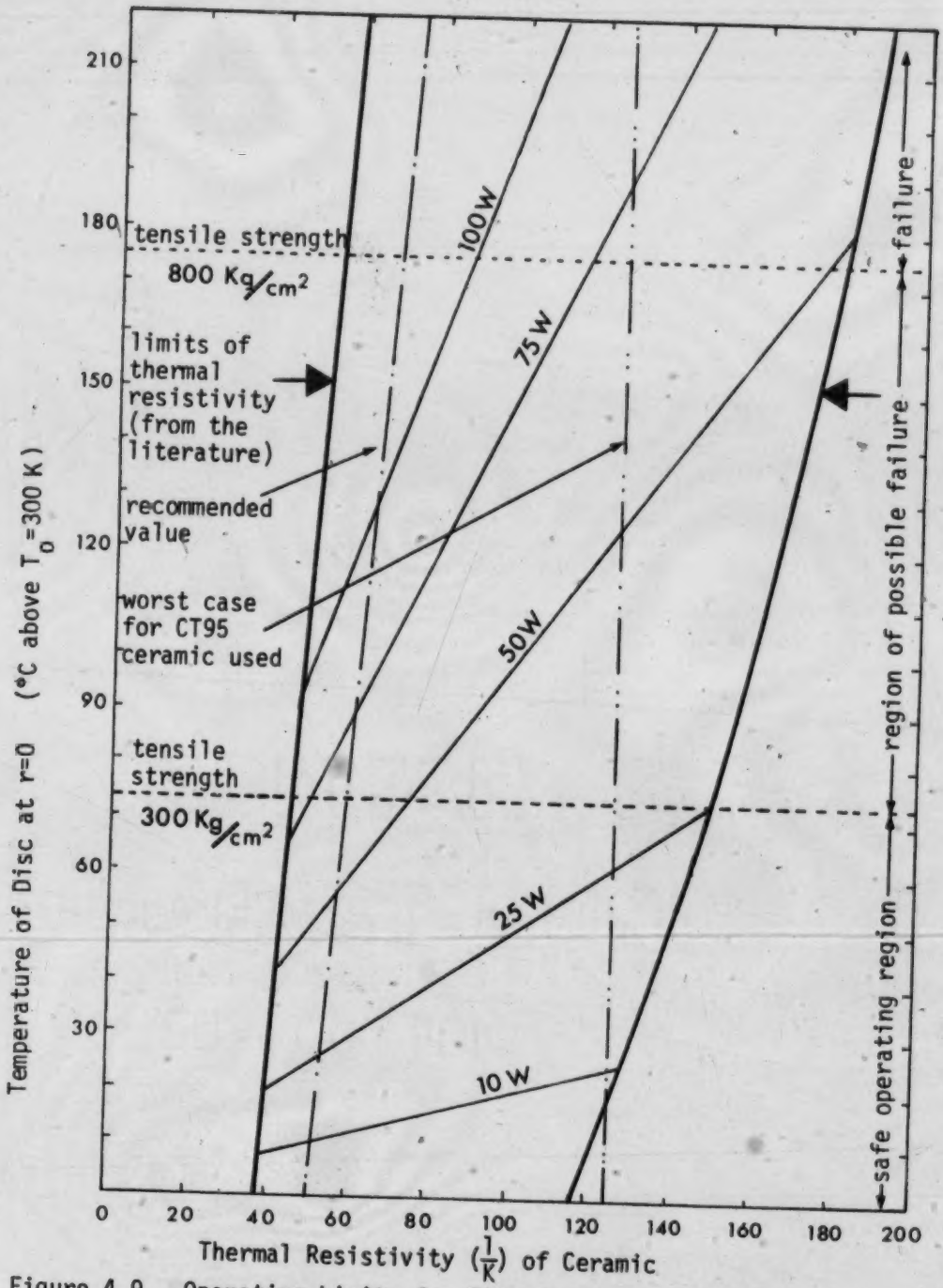

Figure 4.9 Operating Limits for Titania Discs Depending on the Properties of the Ceramic and the Average Power Dissipated in the Discs (the parameter is average power)

CHAPTER 5

LOW POWER MICROWAVE TESTS

5.1 The Low Power Test Bench

5.1.1 Basic S-band Equipment

Figure 5.1 outlines the components of the low power bench. Numerous measurements were to be made over an extended time so that from the start the system was envisaged as a fixed unit. The design philosophy was to minimize the number of reconnections between measurements of different parameters. In this way, calibration was simplified, resetability guaranteed and consistent results obtained.

The signal source was a solid state sweeper (Kruse Storke 5000 or HP8690) or more usually, a Polarad 1206 reflex klystron with an output power of 80 mW. At the other end was a cavity mount fabricated from copper S-band guide and a waveguide adjustable short. Interconnection of these two elements was by coaxial components which included an isolator, wavemeter and three directional couplers.

As shown, one power meter-crystal unit sampled the output of the signal generator, while the other unit measured the power either reflected from, or transmitted through the cavity, as determined by a coaxial switch. By adding a frequency counter with a transfer oscillator plug-in and a D/A converter, the quantities required for the following sections could be ascertained. A slotted line could also be introduced into the main line to assess the SWR.

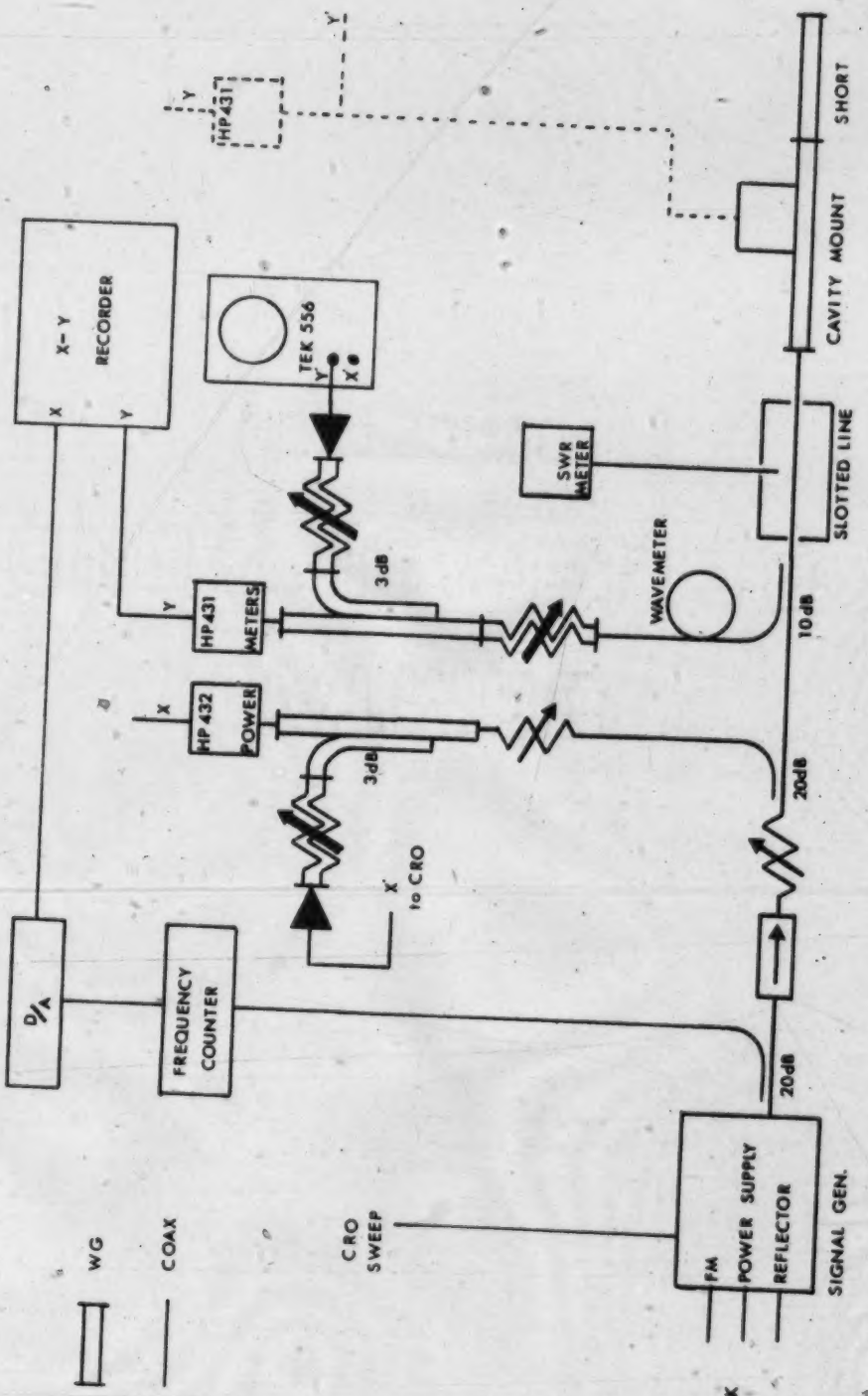

Figure 5.1 The Low Power Microwave Bench

By disconnecting the test cavity mount and attaching the line to the high power cavity, the parameters (Q, SWR) for the cavity under vacuum, immediately prior to the application of high power, could be obtained. It was only necessary to make two reconnections in preparation for the breakdown experiments. The same low power components were also used to measure the high power.

Two electronic circuits developed to simplify the measurements are described in the following sections.

5.1.2 Polarad Frequency Lock Circuit

When perturbing the resonant frequency of a cavity, an oscillator locked onto the frequency of the cavity facilitates monitoring and recording the change of frequency. A number of simple phase detector circuits are described in the literature [81-86], and after evaluating several, the one in Figure 5.2 was chosen, being inserted in the high voltage (600 V) reflector circuit of the reflex klystron. The 5KHz oscillator [87] in Figure 5.2 provides two signals: a reference signal of 3.5 V pk/pk; and a modulation signal of 0-5 V applied to the FM input of the Polarad source, which had a sensitivity of 70 KHz/V. When the generator is tuned near the cavity resonance, a 1 volt modulating signal will sweep the generator through 70 KHz of the cavity output vs frequency characteristic of Figure 5.4, resulting in a detected 5 KHz signal, which is amplified with automatic level control [88] and filtered [89] in the circuit of Figure 5.3. The phase of this 1.2 V pk/pk signal is then compared to that of the reference signal in the phase detector which applies the necessary DC correction to the reflector to pull the generator

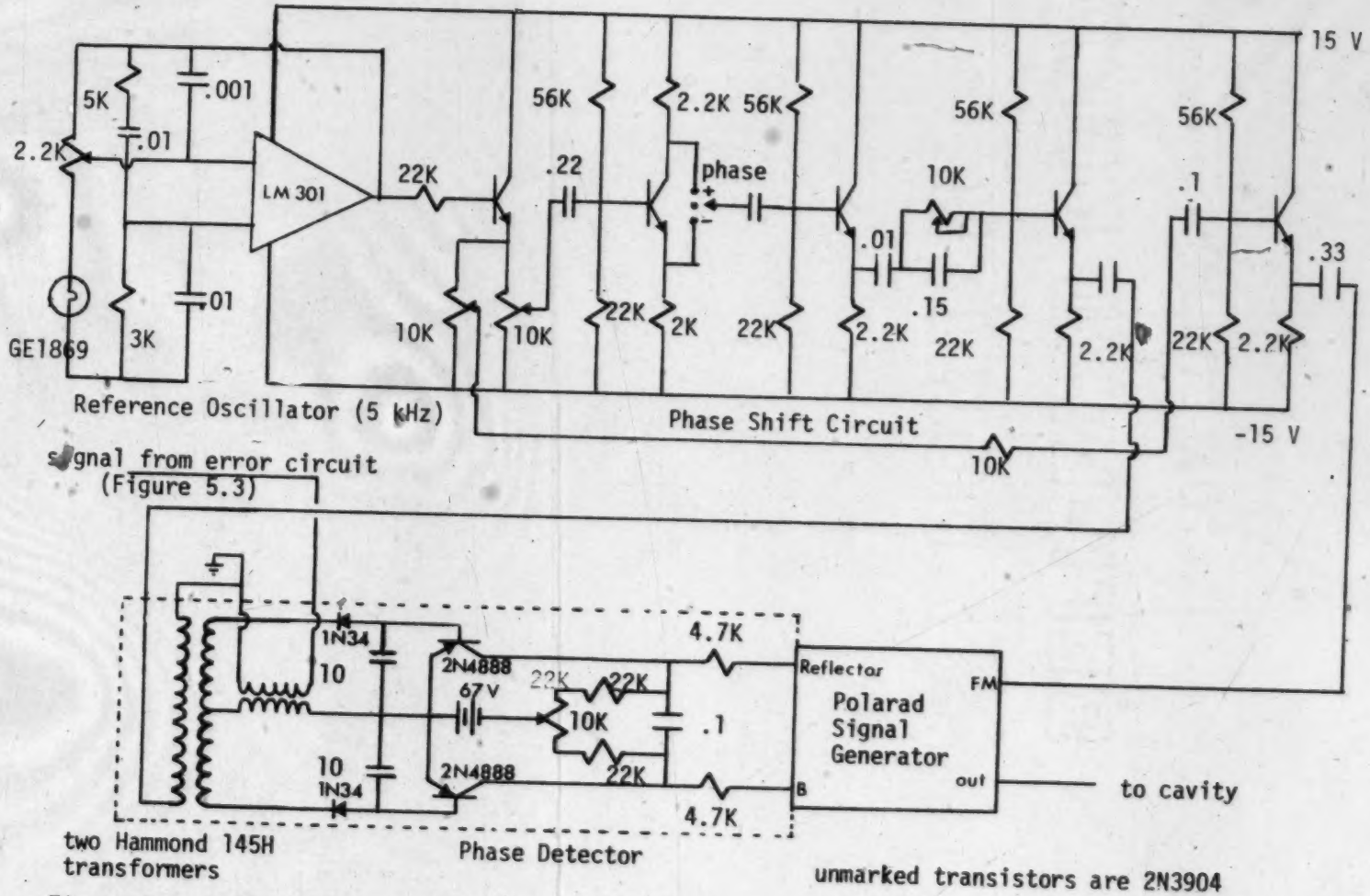

Figure 5.2 Frequency Locking Circuit (a): Reference Circuit and Phase Detector

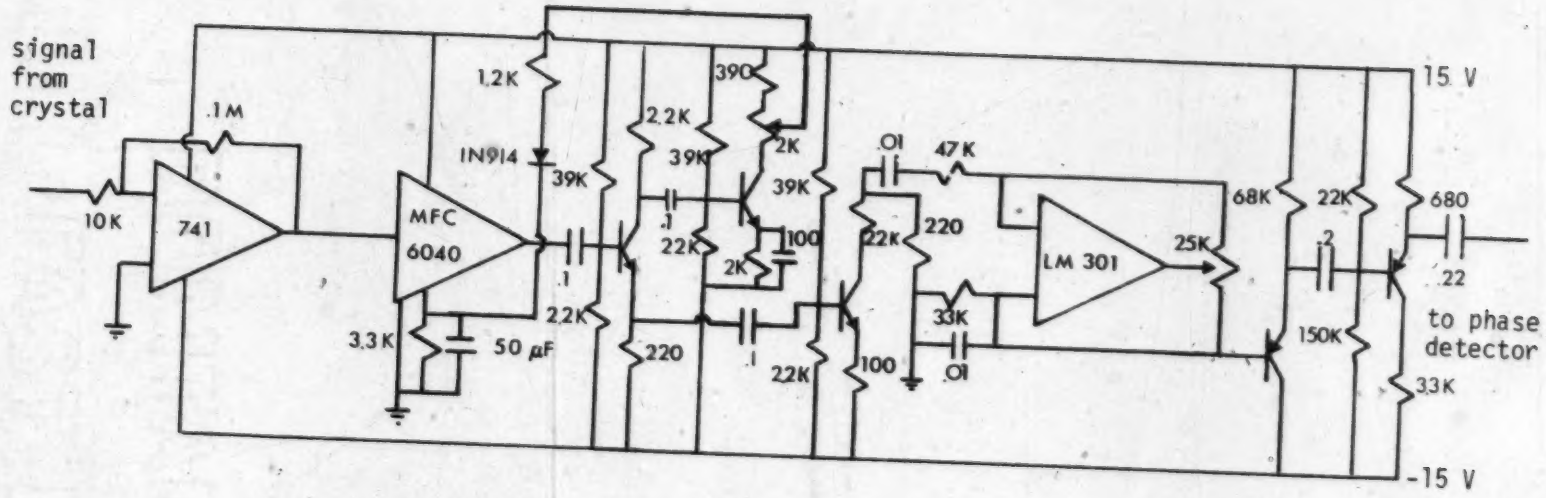

Input Amplifier AGC and Buffer Amplifier 5 kHz Active Filter Output Amplifier

Figure 5.3 Frequency Locking Circuit (b): Error Signal Processing

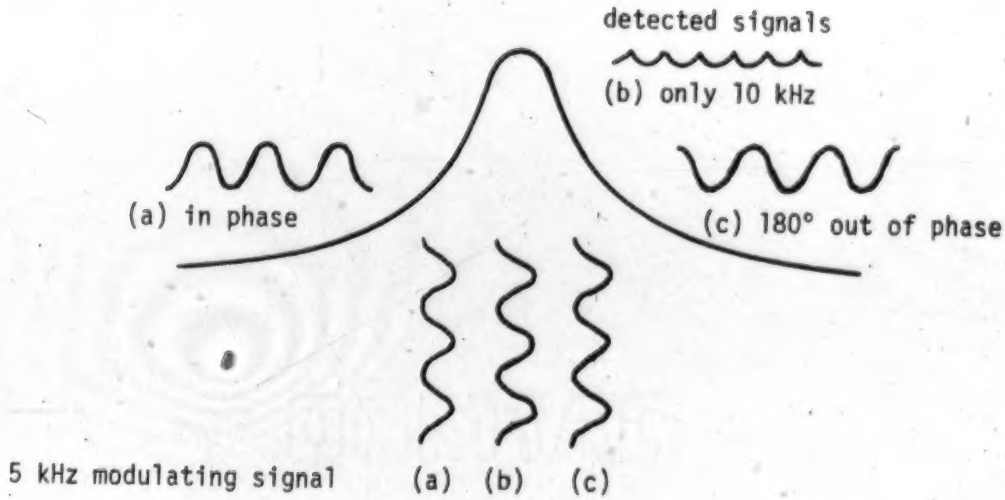

Figure 5.4 Output Characteristics of Cavity

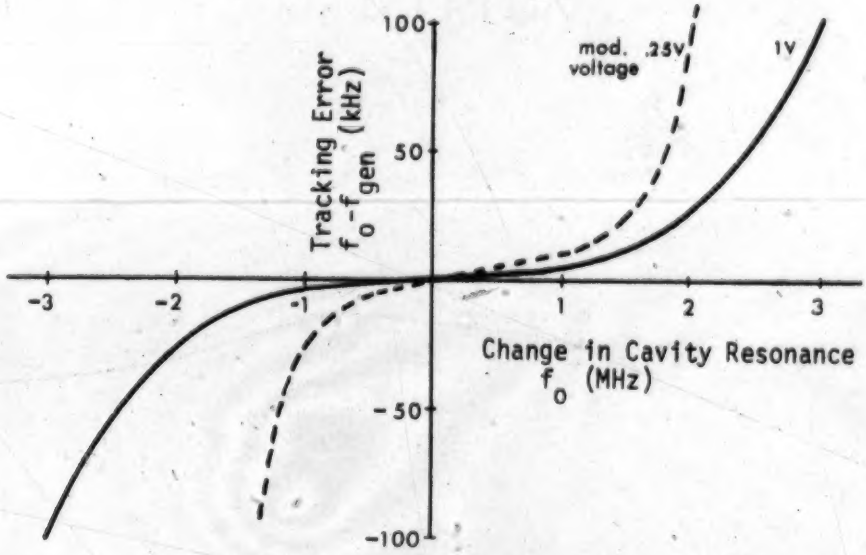

Figure 5.5 Tracking Error of Lock Circuit

frequency onto the resonance of the cavity. The generator thus tracks the cavity resonance and is also stabilized to better than 1 KHz.

Since this is a frequency lock circuit there does exist a small error between the actual resonance and the tracking frequency, but as Figure 5.5 indicates, a perturbation of 1 MHz would generate an error of <10 KHz, or less than 1%. The capture range of the circuit depends upon the cavity bandwidth but is typically $2\Delta f$: the tracking range is limited to 3 or 4 MHz by the phase detector battery voltage.

5.1.3 Analog Division Circuit

In measuring the power reflected from the cavity as the signal generator is tuned through resonance a levelled or constant input signal is desirable. This could be accomplished to some degree by use of a solid state sweeper such as the HP8690 or Kruse Storke 5000; however the Polarad was mainly used due to the higher output power. Since the reflected power is a function of frequency, a circuit was built to normalize the reflected or transmitted power in cavity measurements. A Motorola MC1494 integrated circuit multiplier [90] with an accuracy of 1% was incorporated into the circuit shown in Figure 5.6. By adding operational amplifiers and switching, the functions of multiplication, division, squaring, and root extraction were obtained. After careful calibration the circuit gave excellent results, the reflected power from the HP431C Power meter into input Y being normalized to the forward or input power level sampled by the HP432A and fed into X. The output was then plotted versus frequency on an X-Y recorder. In addition, the circuit was used to determine the square root of the

Switching Logic: S1-1 output $10XY$
-2 $10X^2$
-3 $Y/10X$
-4 $(10X)^{1/2}$
-5 $(-10X)^{1/2}$

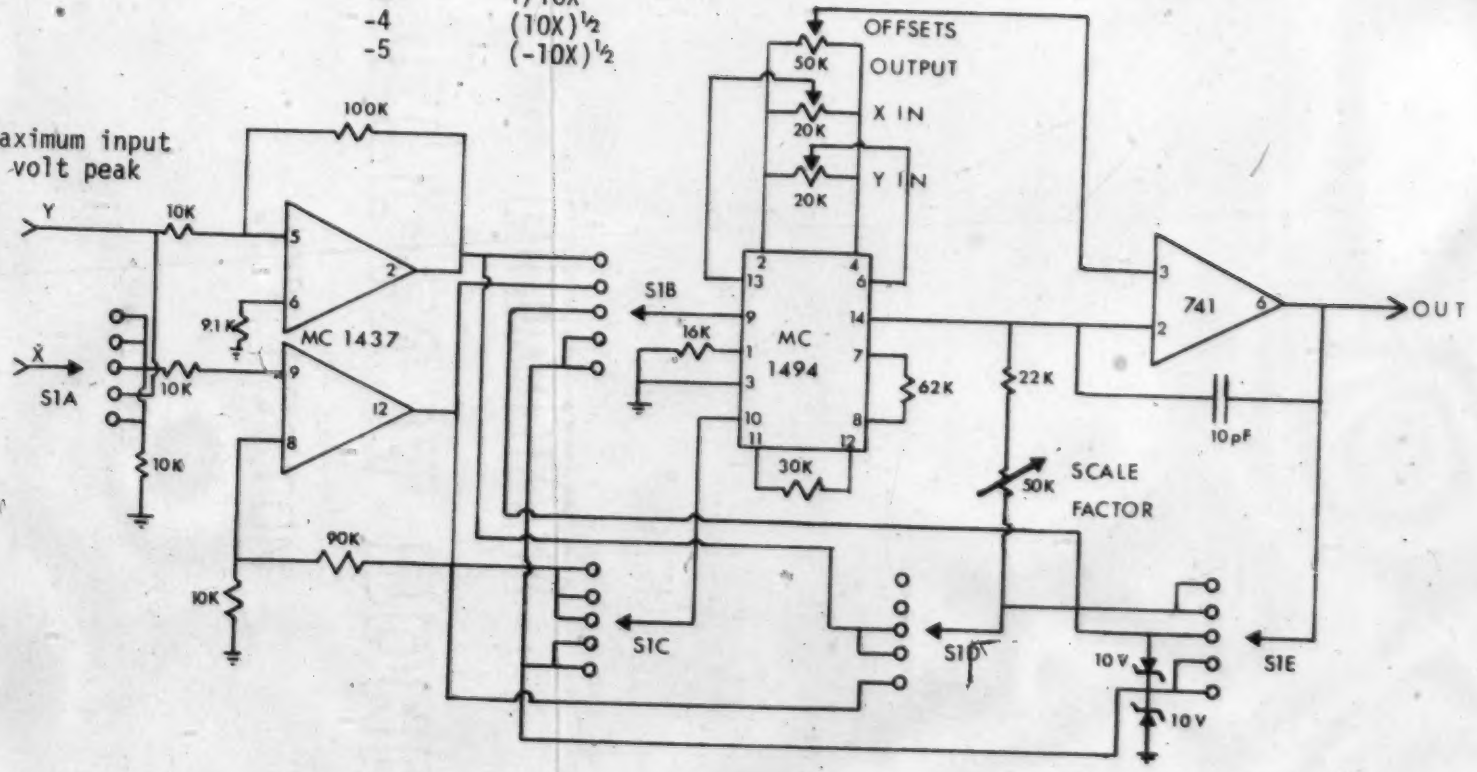

Figure 5.6 Analogue Multiplication/Division Circuit

frequency perturbation to plot the field pattern directly during bead perturbation measurements.

5.2 Perturbation Measurements

5.2.1 Introduction

Precise low power measurements are essential for interpretation of the high power experiments and to verify the theoretical calculations. The aims of the low power tests were:

1. To determine the electric field distribution
2. To determine the peak axial field in relation to the peak power input to the cavity
3. To determine the percentage average power dissipated in the disc

The two basic quantities from which this information can be extracted are the quality factor Q mentioned in section 4.1.4 and the shunt impedance R_o. Shunt impedance may be defined in a number of ways depending on the coupling factor of the cavity and whether the peak or effective electric field is considered, but for this thesis is taken as

$$R_o = \frac{V^2}{2W} = \frac{(\int E dz)^2}{2W} \qquad 5.1$$

E being the peak axial electric field E_z and W, the total power dissipated in the cavity. R_o is usually obtained indirectly from the ratio R_o/Q, a readily measured quantity.

Mention has been made in section 4.1.3, of the desirabiliy of operating the same cavity in the TM_{010} and TM_{011} modes for comparison

purposes. The TM_{010} mode not only aids directly in simplifying calculations and measurements, but more important, serves as a reliable reference, since its characteristics over time are readily repeatable. Therefore analysis is generally applied to this mode and then extended to cover the actual TM_{011} test mode.

5.2.2 The Axial Electric Field Profile

By pulling a small metallic bead of volume $d\tau$ along the axis of a cavity, the resonant angular frequency ω_o will be perturbed to some value ω if the bead is in the region of some field E. Ginzton [91] gives the relation

$$\omega^2 = \omega_o^2 \left[1 + k \left(\frac{\int_\tau (\mu H^2 - \varepsilon E^2) d\tau}{\int_v (\mu H^2 + \varepsilon E^2)\, dv} \right) \right] \qquad 5.2$$

Since the perturbation can be made sufficiently small, $\omega - \omega_o = \Delta\omega << \omega_o$, and equation 5.2 reduces to

$$-2\Delta\omega\omega_o = \omega_o^2 \; k \left(\frac{\int (\mu H^2 - \varepsilon E^2) d\tau}{\int (\mu H^2 + \varepsilon E^2) dv} \right) \qquad 5.3$$

or since $U = \frac{1}{2} \int (\mu H^2 + \varepsilon E^2) dv$

$$\frac{\Delta\omega}{\omega_o} = \frac{k}{2} \frac{\int (\varepsilon E^2 - \mu H^2) d\tau}{2U} \qquad 5.4$$

For the TM_{010} and TM_{011} modes, H=0 along the axis of the cavity and:

$$\frac{\Delta\omega}{\omega_o} = \frac{k\varepsilon}{4U} \int E^2 d\tau \qquad 5.5$$

If the bead is sufficiently small, the field E can be taken as constant in the region of the bead and equation 5.2.5 further reduces to:

$$\frac{\Delta\omega}{\omega_o} = \frac{k\epsilon E^2 \delta\tau}{4U} \qquad 5.6$$

The frequency perturbation $\Delta\omega$ is thus proportional to the square of the electric field at the position of the bead, and by plotting the perturbation with respect to position, a relatively accurate field profile can be obtained for the cavity.

The frequency perturbation was small (typically <1 MHz), and since the temperature dependence of the cavity was at best 17.5 KHz/°C, runs had to be as rapid as possible. The beads were attached to a monofilament line which passed through alignment holes in the cavity and cavity mount, along a centimeter scale and around the shaft of a ten-turn potentiometer as shown in Figure 5.7. The voltage on the potentiometer wiper was proportional to the axial displacement of the bead within the cavity and was connected to the X input of the X-Y recorder of Figure 5.1. The Polarad signal generator incorporated the frequency locking circuit. In this manner numerous plots of E_z^2 vs z were made for various sizes of cavity, discs and coupling holes. It was necessary to machine a .5 cm diameter hole through the center of the discs used for the TM_{011} mode profiles in order to pass the line and bead.

Some of the more important results will be summarized by referring to particular field plots.

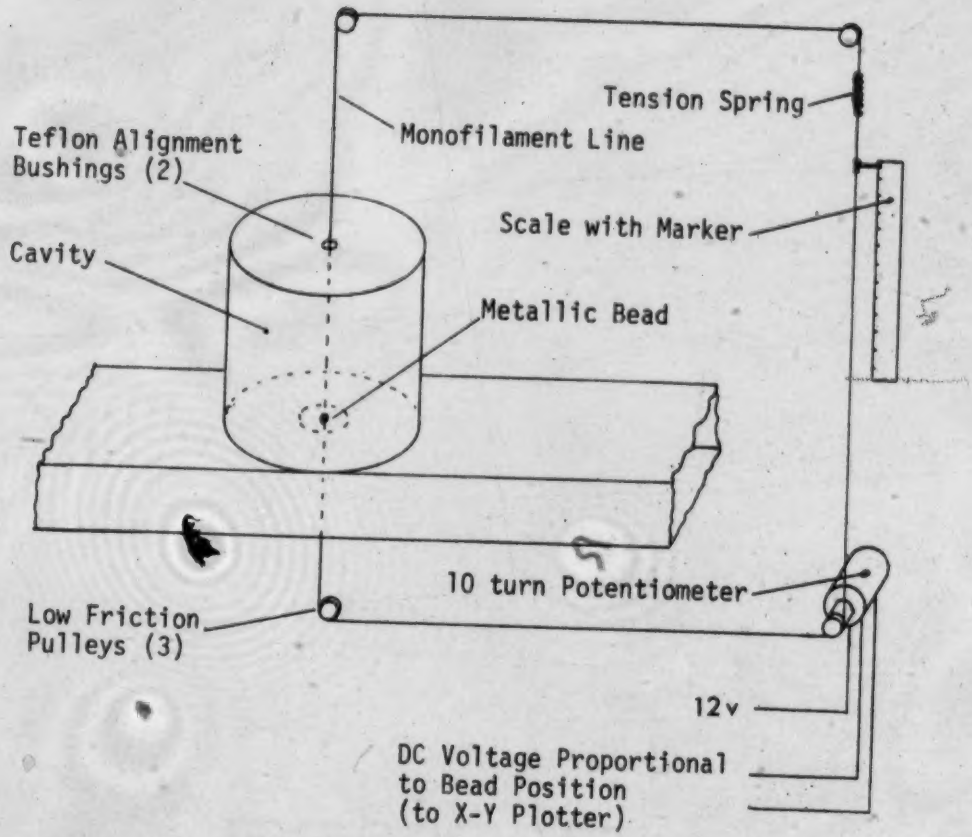

Figure 5.7 Physical Layout for Bead Perturbation Measurements

5.2.2.1 Effect of Bead Size on the Field Profile

The finite dimensions of the bead will introduce a certain error in the field profile since two assumptions necessary to equation 5.2.6 are not strictly valid. There does exist some H field, however slight, at the surface of the bead; and the E field may not be constant, especially at an iris or dielectric interface. A sufficiently small bead then is a compromise between the degree of error to be allowed and the minimum useful frequency perturbation. By recording field profiles for a number of different bead sizes and comparing, an optimum size can be chosen. The three beads used are specified in Table 5.1 and the profiles (normalized) for the two smaller are plotted in Figure 5.8 for the TM_{011} mode. The profile for the 4.45 mm bead is not shown since it was virtually identical to that of the medium size (3.15 mm) bead.

At first glance the deviation from the ideal profile (broken line) appears extensive, but in fact is consistent with the qualification, mentioned above, on the E field. What is significant is that the two bead profiles are nearly identical (assuming a smoothed curve through the plot for the small bead). The only obvious difference is at the top of the cavity (0 cm), where the smaller bead is completely out of the cavity resulting in only slight residual perturbation; whereas the 3.15 mm bead still has an appreciable effect since it tends to fill the small coupling iris.

Since the frequency perturbation of the large bead entailed

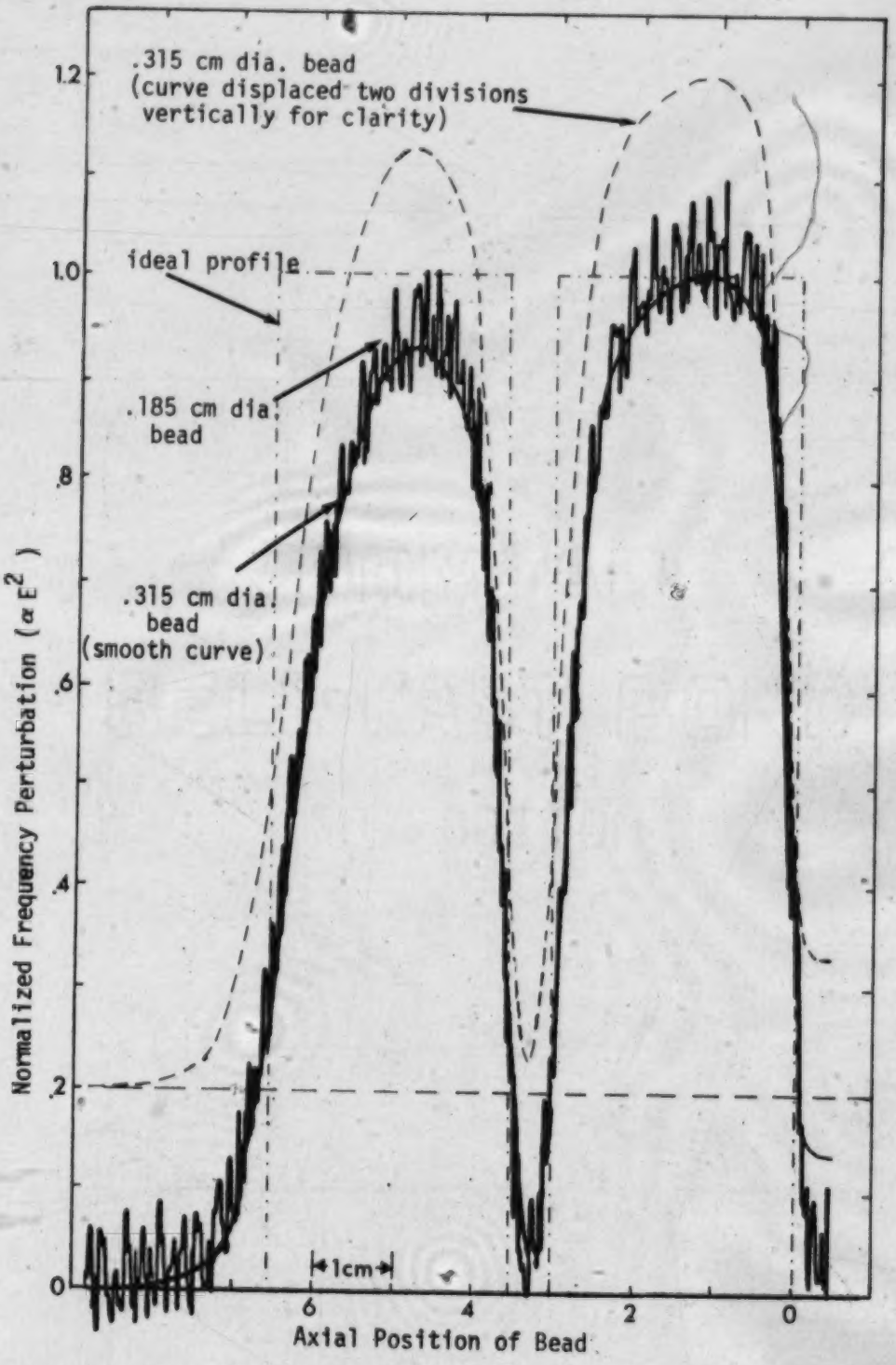

Figure 5.8 Effect of Bead Dimensions on Field Profile

frequency locking difficulty (see Figure 5.5)and that of the small bead (53 KHz) was close to the noise level of the system (about 5 KHz), the intermediate 3.15 mm diameter bead was chosen for most measurements.

5.2.2.2 Effect of the Waveguide-Cavity Coupling Iris

The calculations of section 4.1.4 specified a coupling iris diameter of 1.8 cm. This is relatively large compared to the cavity diameter and will affect the field distribution near the iris and is the main reason for the non ideal plot of Figure 5.8.

Using the TM_{010} mode, successive measurements were made as the iris diameter was increased by machining. The effect can be readily seen in Figure 5.9, especially in the region 1.5 to 5 cm from the top of the cavity. For the .92 cm iris the variation of E^2 over this distance is only .6%; whereas for the 1.8 cm iris it is 4.6%, corresponding to a difference of 2.3% in the E field.

Results were similar for the TM_{011} mode.

5.2.2.3 Effect of an Electron Beam Iris Through the Ceramic

To obtain a profile of the TM_{011} mode field it is necessary to provide a small hole through the ceramic disc on the axis of the cavity. This does not invalidate the results, since in a practical accelerator, there must be a similar iris sufficiently large as not to intercept the electron beam. Electron beams can be produced with diameters <1 mm, but due to defocussing effects along the axis, the iris should generally be an order of magnitude larger.

Measurements were made for different iris diameters as the discs were machined. With the smallest hole (.5 cm diameter) the fields near

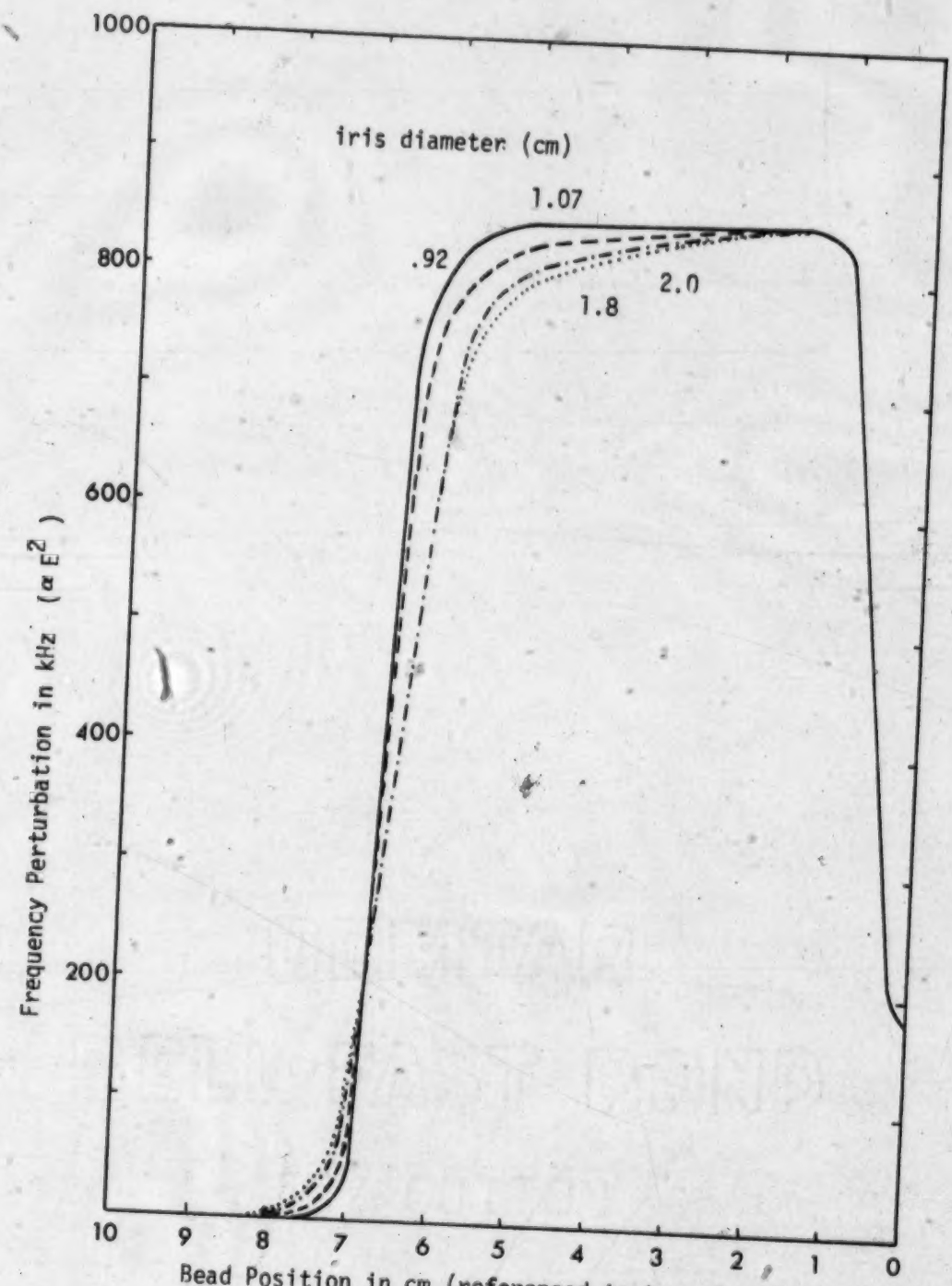

Figure 5.9 Effect of Coupling Iris on Field Profile

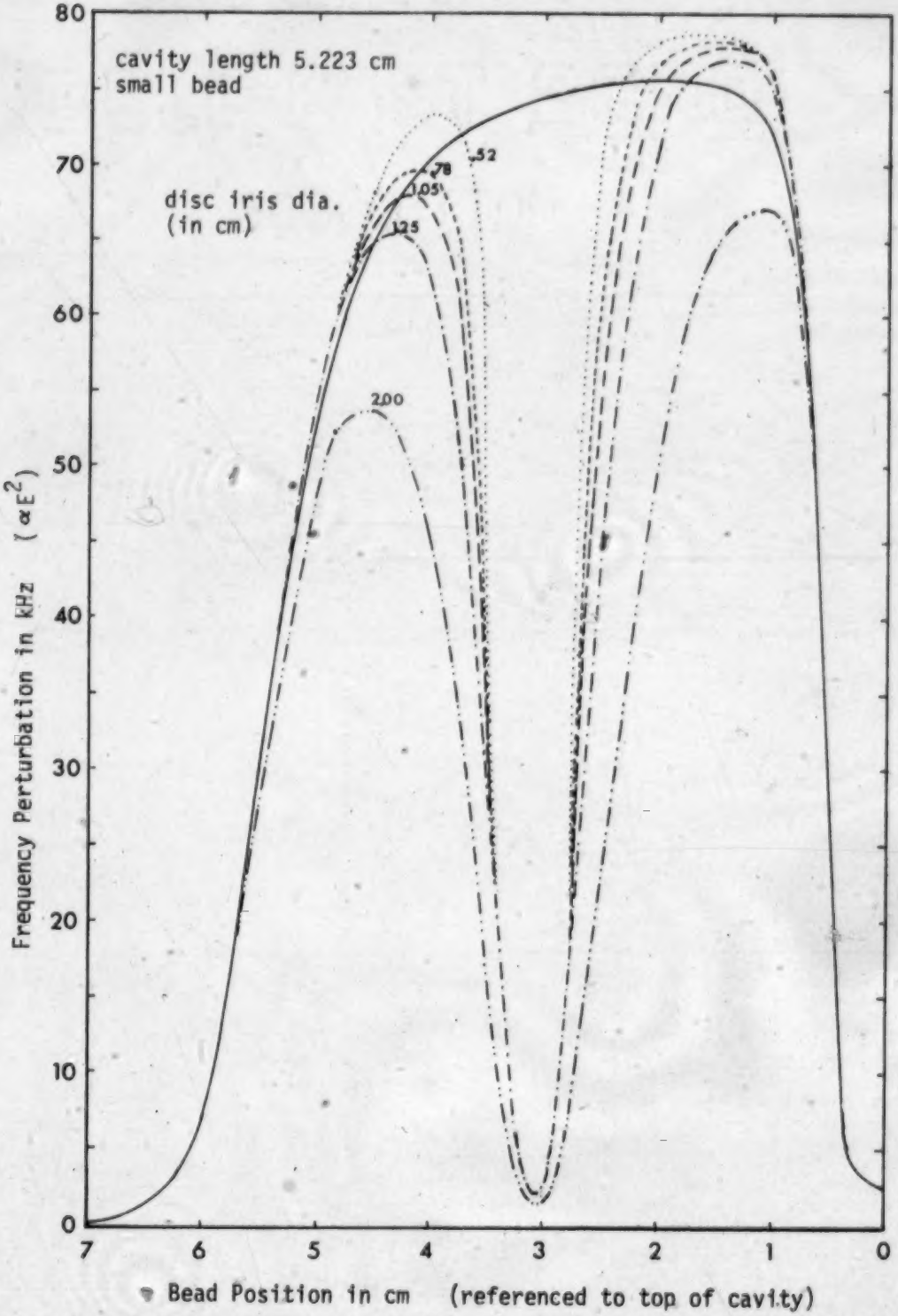

Figure 5.10 Effect of Disc Iris on the Field Profile

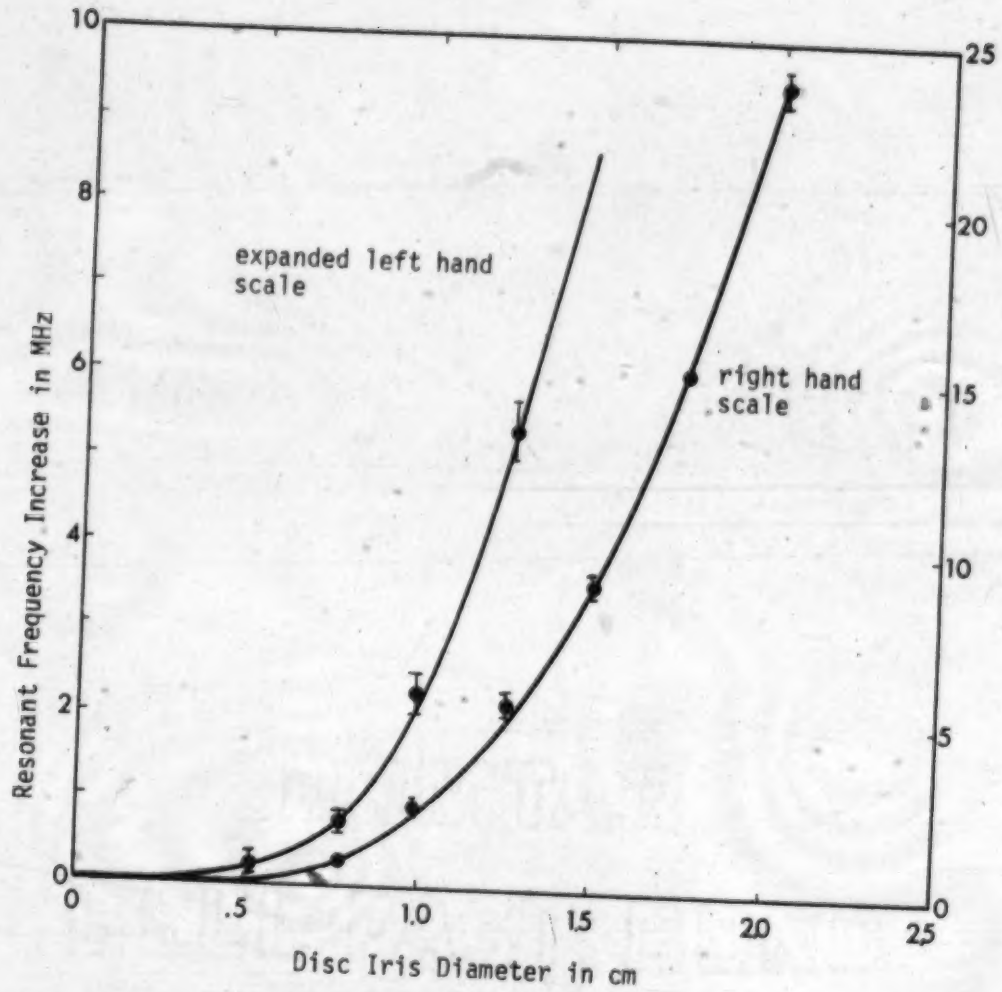

Figure 5.11 Effect of Disc Iris Diameter on Cavity Resonance (for same structure as Figure 5.10)

the ends of the cavity were similar to those in the TM_{010} mode except that the peak fields were 2% higher. In the disc iris there exists a fringing electric field that would not be present in a solid disc; hence, due to the finite size of the bead, there is no sudden step in the profile at the dielectric interface as would be deduced from equations 4.2(a) and 4.3(a). As the iris is increased the profile is degraded further from the ideal (Figure 5.10).

In this case the cavity was shorter (5.223 cm), a prototype for the structure to be described in Chapter 9. From this work it was determined to use the 1.25 cm diameter iris in the later structure; it was a compromise between adequate iris size and both sufficient field intensity and minimum frequency change (Figure 5.11). Reduction of the noise level to under 1 KHz in the frequency locking circuit enabled use of the small bead to minimize any dimensional effects.

5.2.3 Calculation of R_o/Q

Recalling the definitions of R_o and Q in equations 5.1 and 4.13, the ratio R_o/Q will be:

$$\frac{R_o}{Q} = \frac{(\int Ed1)^2}{2W} \times \frac{W}{\omega_o U} = \frac{(\int Ed1)^2}{2\omega_o U} \qquad 5.7$$

or in the TM_{010} case, E_z being constant,

$$\frac{R_o}{Q} = \frac{(EL)^2}{2\omega_o U} \qquad 5.8$$

Since $U = \frac{1}{2}\int \varepsilon E^2 dv = \frac{1}{2}\varepsilon\pi LR^2 J_1^2(k_c r) E^2$, substitution and evaluation gives:

$$\frac{R_o}{Q} = 185.07 \frac{L}{R} \Omega$$

for the TM_{010} mode.

R_o/Q can be determined experimentally from the bead frequency perturbations. Substituting equation 5.6 into 5.8:

$$\frac{R_o}{Q} = \frac{2L^2\Delta\omega}{k\omega_o^2 \varepsilon \delta\tau}$$

for any general bead shape of volume $\delta\tau$. In the specific case of a spherical conducting bead of radius a, the shape factor, k, is 3, and

$$\frac{R_o}{Q} = \frac{L^2\Delta\omega}{2\omega_o^2 \pi\varepsilon a^3}$$

In the perturbation experiments three beads were used. The relevant data is given in Table 5.1 for the TM_{010} mode.

5.2.4 R_o/Q Measurement-Micrometer Method

The values of R_o/Q in Table 5.1 may be in error due to the effect of the monofilament line and the uncertainty in the shape factor k. Ginzton [92] describes a more accurate method of determining R_o/Q using a micrometer to perturb one end of the cavity. The perturbing

Table 5.1 Bead Perturbation

bead	volume	Δf_{max}	R_o/Q
.445 cm dia sphere	46.1×10^{-3} cm^3	2310 KHz	315Ω
.315 cm dia sphere	16.4×10^{-3}	872 KHz	334Ω
.1875 cm dia cyl.	$.929 \times 10^{-3}$	50 KHz	339Ω
theoretical			303Ω

total cavity length L=6.576 cm

resonant frequency 2865 MHz

volume may be varied from a positive to a negative value, so that by plotting the resonant frequency versus the depth of penetration, one can determine the slope of the curve at zero penetration (Figure 5.12). Substitution into equation 5.11 yields R_o/Q.

The micrometer extension used had a diameter of .60 cm, the effective volume being $\pi r^2 \Delta h$, where Δh is the depth of penetration. Substituting

$$\frac{R_o}{Q} = \frac{2L^2}{\omega_o^2 k\varepsilon} \quad \frac{1}{\pi r^2} \quad \frac{\Delta\omega}{\Delta h} \qquad 5.12$$

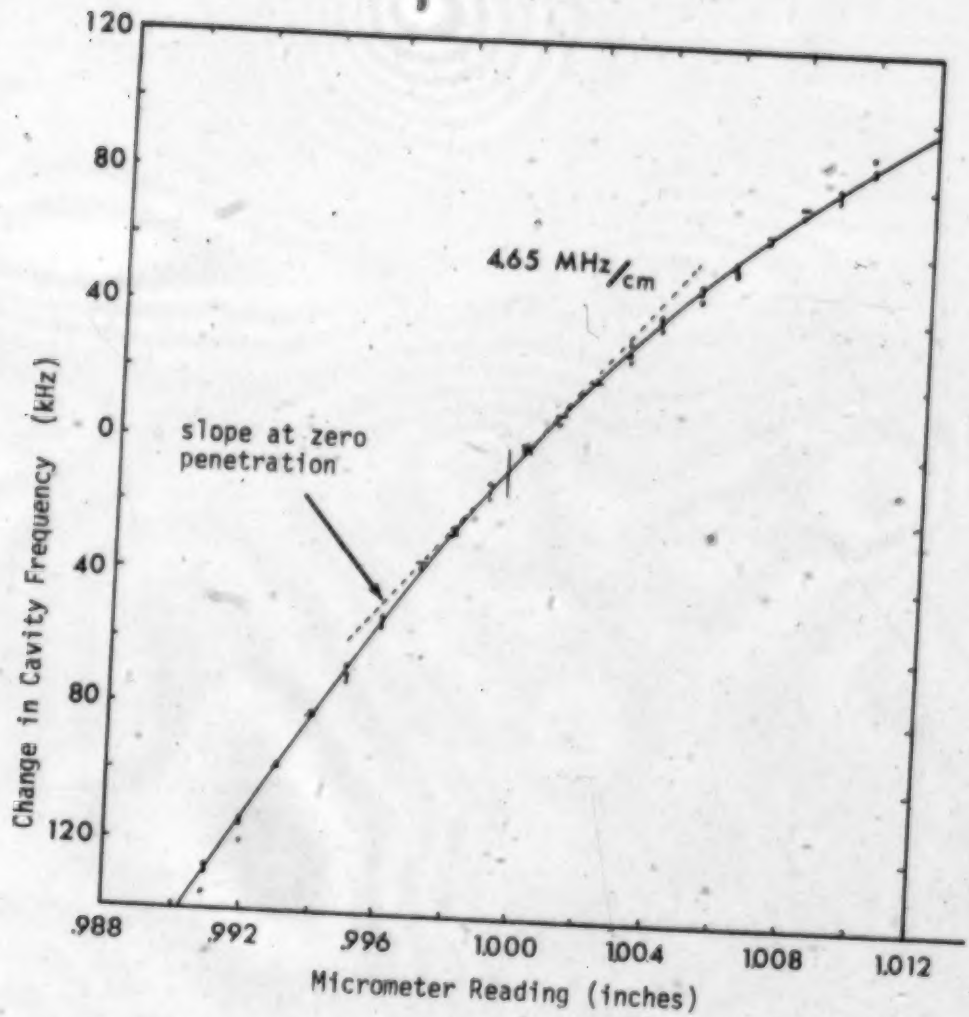

Figure 5.12 Perturbation Measurements Using Micrometer

and simplifying:

$$\frac{R_o}{Q} = 12.74 \times 10^{10} \left(\frac{L}{f_o} \right) \frac{\Delta f}{\Delta h} \Omega$$

$\frac{\Delta f}{\Delta h}$ is extracted from Figure 5.12 for the particular cavity of Table 5.1. The resulting $R_o/Q = 315\Omega$ compares well with the value obtained using the large bead. Evidently the field profile is sufficiently distorted by the coupling iris that the theoretical calculation is in error. The difference in the other two beads may be accounted for by inaccuracy in measuring their small dimensions and consequently in calculation of the volumes.

The R_o/Q obtained by the micrometer method is valid only near the end wall of the cavity but in conjunction with the field profile for the particular mode, the variation of R_o/Q at any point along the axis can be evaluated. The same procedure can be followed for the TM_{011} mode since the cavity dimensions are unchanged.

5.3 Determination of Peak Axial Field

5.3.1 Calculation of Q

The Q of a cavity is dependent on the material of the cavity, the dielectric in the cavity and the resonant frequency. Q can be calculated knowing the field inside the cavity on the basis of assumed values of $\tan\delta$ and ε by evaluating the stored energy and power dissipation in different parts of the cavity. Dividing the cavity into distinct regions and applying equation 4.2 and 4.3:

Energy storage U

$$\text{vacuum } U_{vac} = \frac{1}{2}\epsilon\int E^2 dv = \frac{1}{2}\mu\int H^2 dv$$

$$= 2\,\frac{\mu_o\omega^2(\epsilon_o E_o)^2}{2\,k_c^2}\int_o^p \cos^2\beta_o z\,dz\int_o^R J_1^2(k_c r)2\pi r\,dr$$

$$= \frac{\mu\pi\,\omega^2(\epsilon_o E_o)^2}{4\,\beta_o\,k_c^2} R^2 J_1^2(k_c R)(2p\beta_o + \sin^2 p\beta_o) \qquad 5.13$$

$$\text{dielectric } U_{diel} = \frac{\mu\pi\omega^2(\epsilon_r\epsilon_o E_2)^2}{4\,\beta_2 k_c^2} R^2 J_1^2(k_c R)(2\beta_2 q - \sin^2\beta_2 q) \qquad 5.14$$

Cavity Losses W

$$\text{end walls } W_{end} = \frac{2\pi\omega^2(\epsilon_o E_o)^2 R_s}{k_c^2}\,\frac{R^2}{2}\,J_1^2(k_c R) \qquad 5.15$$

$$\text{side walls } W_{side1} \text{ (region 1)} = 4\pi R R_s\,\frac{\omega^2}{k_c^2}(\epsilon_o E_o)^2 J_1^2(k_c R)\,\frac{(2\beta_o p+\sin 2\beta_o p)}{4\beta_o} \qquad 5.16$$

$$\text{(region 2) } W_{side2} = 4\pi R R_s\,\frac{\omega^2}{k_c^2}(\epsilon_r\epsilon_o E_2)^2 J_1^2(k_c R)\,\frac{(2\beta_2 q-\sin 2\beta_2 q)}{4\beta_2} \qquad 5.17$$

$$\text{in dielectric } W_{diel} = \omega\epsilon\tan\delta\, U_{diel}. \qquad 5.18$$

$$= \pi\sigma E_2^2\,\frac{R^2}{4}\,\frac{J_1^2(k_c R)}{\beta_2}\left(2\beta_2 q\left(1+\frac{\beta_2^2}{k_c^2}\right) + \sin 2\beta_2 q\left(\frac{\beta_2^2}{k_c^2} - 1\right)\right)$$

Note that the surface resistance for copper is given by

$$R_s = 2.61 \times 10^{-7}\, f^{1/2} = 1.40 \times 10^{-2}\,\Omega/\square \qquad 5.19$$

and that $\varepsilon_2 \dot{E}_2 = \frac{\cos\beta_o p}{\sin\beta_2 q} \cdot \varepsilon_o E_o$ (equation 4.4)

The Q for the TM_{010} mode cavity of section 4.1.3 could be calculated by substitution of p, q etc directly into equations 5.13 to 5.19. Using a tanδ of .00035, the resulting Q = 15649 is higher than the measured Q for this particular disc (13400-13760). The two uncertainties are tanδ and R_s.

Returning again to the TM_{010} mode, Ramo and Whinnery [93] give the standard formula:

$$Q = \frac{377 \times 2.405}{R_s \times 2 \times (1 + \frac{R}{L})} = \frac{377 \times 2.405}{1.592\ R_s} = \frac{284.76}{R_s} \qquad 5.20$$

and Q = 20340 for the theoretical R_s. Since the measured Q was 16700-17700 (typically 17200 or 84.6% of theoretical), the actual R_s was more than .014Ω/□ . Although increase of R_s can in part be attributed to contact resistance at the copper ring, because the TM_{011} mode uses the same components, a corrected R_s = .0176Ω/□ can be used for calculation of $Q_{TM_{011}}$.

$$\begin{array}{rl} U_{vac} & 376.42 \times 10^{18}\ E_o^2 \\ U_{diel} & 16.32 \times 10^{-18}\ E_o^2 \\ \hline U_{sum} & 392.74 \times 10^{18}\ E_o^2 \\ W_{end} & 96.61 \times 10^{-10}\ R_s\ E_o^2 \\ W_{side} & 155.69 \times 10^{-10}\ R_s\ E_o^2 \\ \hline W_{wall} & 252.30 \times 10^{-10}\ R_s E_o^2 \\ W_{diel} & 2.893 \times 10^{-7}\ \tan\delta\ E_o^2 \end{array} = 417.80 \times 10^{-12}\ E_o^2$$

Taking the best value of Q, 13760, for this disc the total losses should be $\frac{\omega U_{sum}}{Q} = 514.70 \times 10^{-12} E_o^2$ and the loss in the dielectric $96.90 \times 10^{-12} E_o^2$. The calculated tanδ is then .000335 and the disc accounts for 18.8% of the cavity losses. Each disc was evaluated in this manner, with the results summarized in Table 5.2. The scatter in tanδ can be attributed to the different lots in which the discs were received and the particularly high values of discs #3, 5 and 10 are due to defects in machining and impurities accidentally absorbed.

The presence of the thin alumina layer on the disc did not affect either the Q or resonant frequency. The titanium surface coating would, however contribute some additional loss to the cavity. Since the Ti thickness was much less than the skin depth, the field pattern can be considered to be unperturbed and the loss can be evaluated using the relation:

$$W_{Ti} = \frac{\sigma_{Ti}}{2} \int_0^R (E r_{z=p})^2 \, 2\pi \, r dr \qquad 5.21$$

where σ_{Ti} is the surface conductance (typically $\sigma_{Ti} = .1 m\mho/\square$)

Using equation 4.2(b)

$$W_{Ti} = \sigma_{Ti} \, \pi \, \frac{\beta_o^2}{k_c^2} \sin^2 \beta_o p \, \frac{R^2}{2} J_1^2(k_c R) \, E_o^2 \qquad 5.22$$

For both surfaces of disc #8, the loss would be $12.65 \times 10^{-12} E_o^2$ which must be added to the losses to evaluate Q. The effect of the coating is to reduce Q by 3% and increase the energy dissipation in the disc to 21.2%.

5.3.2 Measurement of Q

Q can be determined experimentally by a number of different methods; however the most direct is by recording the power transmitted through or reflected from a cavity while sweeping an oscillator through the resonance. Q may be defined in terms of the bandwidth, Δf, between two frequencies, $f_{\frac{1}{2}}$ and $f_{-\frac{1}{2}}$, at which the transmitted power is half that transmitted at resonance. From the plot of the incident power and the transmitted (or reflected) power versus frequency, Δf and the standing wave ratio can be obtained for calculation of Q_L and Q_o.

Since $P_t = P_i - P_r$, by maintaining constant incident power it is sufficient to measure either the transmitted or reflected power. In practice, this was accomplished using the circuit described in section 5.1.3 which normalized the reflected power to the incident power. Since the cavity was critically coupled ($\beta_c = 1$), Q could be obtained directly:

$$Q_o = 2Q_L = \frac{f_o}{f_{\frac{1}{2}} - f_{-\frac{1}{2}}}$$

Q's for the various discs are included in Table 5.2.

5.3.3 Calculation of the Axial Field

Knowing R_o/Q and Q, the shunt impedance R_o and the electric field as a function of peak power can be calculated. Equation 5. 1 may be rewritten:

$$R_o = \frac{(EL)^2}{2W} \quad \frac{(\int E\,dz)^2}{E^2L^2} \qquad 5.23$$

$\frac{(EL)^2}{2W}$ would be the shunt impedance measured with the micrometer: the second term would be derived from equation 4.2(a) or from the field profiles of section 5.2 normalized to the value at the position for which the first term is valid.

Initially assuming an ideal TM_{010} mode with constant E_z,

$$E_z = \frac{1}{L} (2R_o W)^{\frac{1}{2}}$$

$$= \frac{1}{L} \left(\frac{R_o}{Q}\right)^{\frac{1}{2}} (2Q)^{\frac{1}{2}} W^{\frac{1}{2}} \qquad 5.24$$

Referring to Table 5.2,

$$E_z = 339 (W)^{\frac{1}{2}} \text{ kV/cm (where W is in MW)}$$

$$R_o = 2.52 \text{ M}\Omega$$

In a real structure the coupling iris would tend to reduce both these values with increasing distance from the top end wall.

The TM_{011} mode considerations are more complex. First, the peak axial field at the disc surface is $E_o \cos\beta_o p$ (from equation 4.2(a)) or $.99E_o$. Secondly, assuming that the field falls away as the coupling iris is approached in the same manner as for the TM_{010} mode, the fields will be an additional .5% and 1% lower. The peak fields at the two disc surfaces will be $.985\ E_o max$ and $.98\ E_o max$ for the faces opposite the top of the cavity and coupling hole respectively.

Table 5.2 Summary of Low Power Tests

Disc #	Thickness 2q (cm)	Ring Size (cm)	Coating	R_o/Q (Ω)	Q_o	R_o (MΩ)	tanδ	Power Absorbed in Disc (%)	E_z Peak at 1MW (kV/cm)	Disc Batch #
TM_{010}	N/A	.575	N/A	315	16000	2.52			339	
0 (ref)	.50	.50	None	303	12300	1.86	.00035	19.2		1
00	.556	.570	None (unpolished)	331	12000	1.97	.00033	18.0	300	2
1	.5612	.570	$4\mu Al_2O_3$	312	12760	1.99	.00035	19.0	304	2
2	.559	.570	$1.2\mu Al_2O_3$	328	12900	2.12	.00032	17.7	308	2
3	.562	.570	None (unpolished)	331	10400	1.72	.00078	34.0	298	2
4	.530	.570	None (unpolished)	303	14640	2.22	.00024	14.6	321	3
5	.530	.570	$2\mu Al_2O_3$ + Ti	326	11960	1.95	.00048	24.1	292	3
6	.544	.775	$.8\mu Al_2O_3$+ Ti	344	14400	2.48	.00026	15.0	325	4
7	.541	.773	$.9\mu Al_2O_3$+ Ti	346	14350	2.48	.00026	15.3	324	4
8	.539	.778	$1.2\mu Al_2O_3$+ Ti	342	13760	2.35	.00034	18.8	315	4
9	.538	.775	$1.2\mu Al_2O_3$	343	14400	2.47	.00026	15.0	325	4
10	.545	.750	None (polished)	340	12960	2.20	.00044	23.4	305	4
11	.543	.770	None (polished)	327	14000	2.29	.00028	16.4	313	4

5.4 Cavity Thermal Characteristics

5.4.1 Introduction

The two quantities characterizing a resonant cavity, the resonant frequency, f_o, and the Q, which is related to the cavity losses, are in general temperature dependent. Bearing in mind the limited range that the magnetron can be tuned through, about 3 MHz for suitable output, and the temperatures calculated in section 4.2, there are obvious limitations on the frequency temperature coefficient that can be accepted. In addition, the perturbation measurements usually covered small variations of resonant frequency and the amount of error due to change in ambient temperature must be ascertained.

5.4.2 Frequency Dependence on Temperature

Although it was not considered in section 4.2, the copper portion of the cavity does absorb most of the power lost in the cavity and despite the high thermal conductivity of the cavity-mount system, does experience an increase of temperature. The frequency temperature coefficient is negative due to expansion. Introduction of titania into the cavity, with its large negative coefficient of ε_r (-9×10^{-4}/°C), compensates by adding a positive frequency temperature coefficient. Thus, with a cavity of suitable geometry, the two effects could be made to compensate over a range of temperatures (say 50°C). Calculation is complicated, however, by the non-uniform temperature distribution across the dielectric.

Consider the case of uniform copper-disc temperature; the temp-

erature coefficient can be calculated by differentiation of equation 4.8 with respect to the temperature dependent parameters, λ, λ_c, ε_r, p and q. Rewriting equation 4.6

$$\theta = \tan\beta_o p \tan\beta_2 q - (\varepsilon_r\beta_o)^{-1}\beta_2 \qquad 5.25$$

and taking partial derivatives:

$$\frac{\partial\theta}{\partial\lambda} = [\, p\sec^2\beta_o p \tan\beta_2 q + \beta_2\varepsilon_r^{-1}\beta_o^{-2} \,] \frac{\partial\beta_o}{\partial\lambda} +$$

$$[\, q\sec^2\beta_2 q \tan\beta_o p - (\varepsilon_r\beta_o)^{-1}] \frac{\partial\beta_2}{\partial\lambda}$$

$$= -\frac{(2\pi)^2}{\lambda^3} [\, \beta_o^{-1} p \sec^2\beta_o p \tan\beta_2 q + \beta_2\varepsilon_r^{-1}\beta_o^{-3} +$$

$$q\varepsilon_r\beta_2^{-1}\sec^2\beta_2 q \tan\beta_o p - (\beta_o\beta_2)^{-1}] \qquad 5.26$$

$$\left(\frac{\partial\theta}{\partial\lambda_c}\right)_{Cu} = [\, p\sec^2\beta_o p \tan\beta_2 q + \beta_2\varepsilon_r^{-1}\beta_o^{-2} \,] \frac{\partial\beta_o}{\partial\lambda_c}$$

$$= \frac{(2\pi)^2}{\lambda_c^3} [\, \beta_o^{-1} p\sec^2\beta_o p \tan\beta_2 q + \beta_2\varepsilon_r^{-1}\beta_o^{-3}] \qquad 5.27$$

$$\left(\frac{\partial\theta}{\partial\lambda_c}\right)_{TiO_2} = [\, q\sec^2\beta_2 q \tan\beta_o p - (\varepsilon_r\beta_o)^{-1}] \frac{\partial\beta_2}{\partial\lambda_c}$$

$$= \frac{(2\pi)^2}{\lambda_c^3} [\, \beta_2^{-1} q\sec^2\beta_2 q \tan\beta_o p - (\beta_o\varepsilon_r\beta_2)^{-1}] \qquad 5.28$$

$$\frac{\partial\theta}{\partial\varepsilon_r} = [\, q\tan\beta_o p\sec^2\beta_2 q - (\varepsilon_r\beta_o)^{-1}\,]\frac{\partial\beta_2}{\partial\varepsilon_r} + \beta_2\beta_o^{-1}\varepsilon_r^{-2} \qquad 5.29$$

$$\frac{\partial\theta}{\partial p} = \beta_o \tan\beta_2 q\sec^2\beta_o p \qquad 5.30$$

$$\frac{\partial\theta}{\partial q} = \beta_2 \tan\beta_o p\sec^2\beta_2 q \qquad 5.31$$

But

$$d\theta = \frac{\partial\theta}{\partial\lambda}d\lambda + \left(\frac{\partial\theta}{\partial\lambda_c}\right)_{Cu} d\lambda_{c_{Cu}} + \left(\frac{\partial\theta}{\partial\lambda_c}\right)_{TiO_2} d\lambda_{c_{TiO_2}} + \frac{\partial\theta}{\partial\varepsilon_r}d\varepsilon_r + \frac{\partial\theta}{\partial p}dp + \frac{\partial\theta}{\partial q}dq = 0 \qquad 5.32$$

therefore, rearranging

$$d\lambda = \frac{\left(\frac{\partial\theta}{\partial\lambda_c}\right)_{Cu} d\lambda_{c_{Cu}} + \left(\frac{\partial\theta}{\partial\lambda_c}\right)_{TiO_2} d\lambda_{c_{TiO_2}} + \frac{\partial\theta}{\partial\varepsilon_r}d\varepsilon_r + \frac{\partial\theta}{\partial p}dp + \frac{\partial\theta}{\partial q}dq}{-\left(\frac{\partial\theta}{\partial\lambda}\right)} \qquad 5.33$$

Since $f\lambda = c$, $df = -\frac{f}{\lambda}d\lambda$ and

$$\frac{df}{dT} = -\frac{f}{\lambda}\frac{d\lambda}{dT} \qquad 5.34$$

Considering the contribution of the copper expansion

$$\left(\frac{df}{dT}\right)_{Cu} = \frac{f}{\lambda}\frac{\left(\frac{\partial\theta}{\partial\lambda_c}\right)_{Cu}\frac{d\lambda_{c_{Cu}}}{dT}}{\frac{\partial\theta}{\partial\lambda}}$$

where $\frac{d\lambda_{c_{Cu}}}{dT} = \lambda_c \alpha_{Cu}$; therefore

$$\left(\frac{df}{dT}\right)_{Cu} = -\frac{f\lambda^2}{\lambda_c^2 D}\left(p\sec^2\beta_o p + \beta_o^{-1}\tan\beta_o p\right)\alpha_{Cu} \qquad 5.35$$

in which $D = p\sec^2\beta_o p + q + \beta_o^{-1}\tan\beta_o p(1 + \beta_o^2\beta_2^{-1}\varepsilon_r(q\beta_o\varepsilon_r\tan\beta_o p - 1))$

Similarly, the radial expansion of the ceramic gives:

$$\left(\frac{df}{dT}\right)_{TiO_2} = -\frac{f\lambda^2}{\lambda_c^2 D}\left(\varepsilon_r^{-1}q + \beta_o\beta_2^{-2}\tan\beta_o p(q\beta_o\varepsilon_r\tan\beta_o p - 1)\right)\alpha_{TiO_2} \qquad 5.36$$

and the corresponding contributions for change in ε_r, p and q are respectively:

$$\left(\frac{df}{dT}\right)_{\varepsilon_r} = -\frac{f}{2D}\left(q + \beta_o\beta_2^{-2}\tan\beta_o p\left(\varepsilon_r^2\beta_o q\tan\beta_o p - \varepsilon_r + \frac{\beta_2^2 2\lambda^2}{(2\pi)^2}\right)\right)\alpha_{\varepsilon_r} \qquad 5.37$$

$$\left(\frac{df}{dT}\right)_p = -\frac{f\lambda^2}{(2\pi)^2 D}\beta_o^2 p(\sec^2\beta_o p)\,\alpha_{Cu} \qquad 5.38$$

$$\left(\frac{df}{dT}\right)_q = -\frac{f\lambda^2}{(2\pi)^2 D}\left(\beta_2^2\varepsilon_r^{-1} + \beta_o^2\varepsilon_r\tan\beta_o p\right)q\,\alpha_{TiO_2} \qquad 5.39$$

Substituting the parameters for disc #8:

$p = .0312m$, $q = .002695m$, $f_o = 2870MHz$, $\beta_o = 4.393m^{-1}$, $\beta_2 = 582.8m^{-1}$ and knowing $\alpha_{Cu} = 16 \times 10^{-6}$, $\alpha_{TiO_2} = 8 \times 10^{-6}$ and $\alpha_{\varepsilon_r} = -9 \times 10^{-4}$ per °C:

$$\left(\frac{df}{dT}\right)_{Cu} = -43.8 \text{ KHz}$$

$$\left(\frac{df}{dT}\right)_{TiO_2} = -.01 \text{ KHz}$$

$$\left(\frac{df}{dT}\right)_{\varepsilon_r} = 57.4 \text{ KHz}$$

$$\left(\frac{df}{dT}\right)_{p} = -.12 \text{ KHz}$$

$$\left(\frac{df}{dT}\right)_{q} = -1.01 \text{ KHz}$$

giving a net frequency dependence of + 12.4 KHz/°C.

A thermostat controlled oven was used to measure the temperature dependence of the cavity. The temperature was increased by steps of 2 to 5°C, the cavity maintained at each level for about one hour until it stablized.

Figure 5.13 displays the results for the single celled cavity - the slope at 20°C being 17.5 kHz/°C. The difference between calculated and measured values is probably due to the former being the difference between two larger quantities, an error of 9% in α_{ε_r} resulting in a 40% error in $\frac{df}{dT}$.

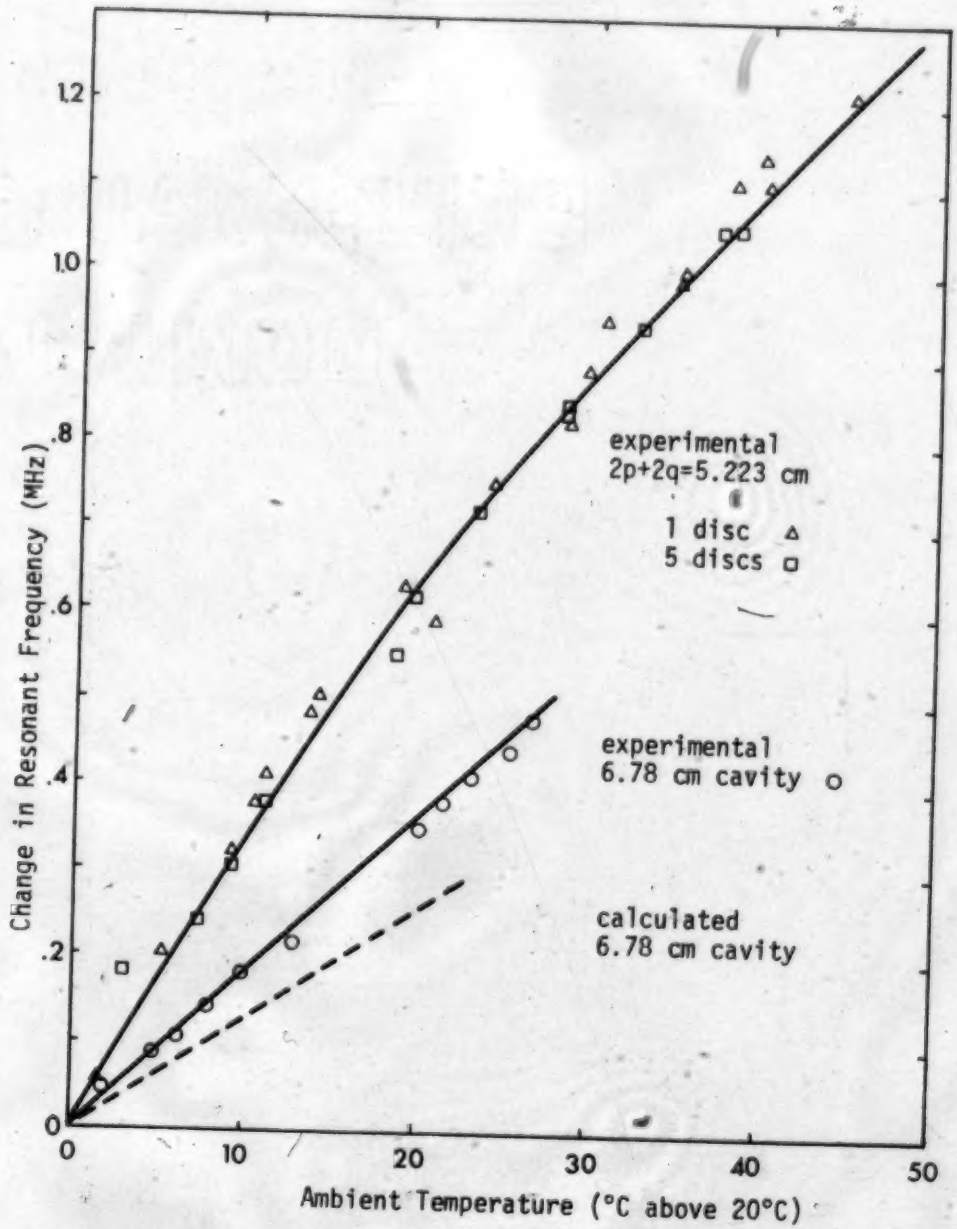

Figure 5.13 Cavity Temperature Dependence

In a second structure designed to operate in the confluent mode (L = 5.223 cm, 2q = .53 cm), the number of discs was varied from 1 to 5 by adding additional sections to the cavity. Again at 20°C, the slopes were constant at 32 kHz/°C, this time in good agreement with the calculated 32.78 kHz/°C. However, the discs had a 1.25 cm diameter central iris, indicating that the measured $\frac{df}{dT}$ is lower than would be expected for solid discs.

The transient response of the cavity to a 5°C step in temperature is shown in Figure 5.14. Allowance must be made for the oven settling time of 1-2 minutes, but the time constant of the cavity for increasing temperature is about 20 minutes. Evidently, the copper heated first and the high thermal resistivity of the titania delayed transport of the heat to the center of the disc. For decreasing temperatures the cavity settling time was considerably faster, about 2 minutes or less, but the oven utilized CO_2 cooling and the forced air flow would permit better convection heat transfer at the disc surface.

5.4.3 Dependence of Q on Temperature

Tan δ of the titania and the surface resistance, R_s, of copper both increase with temperature but at this frequency, for the restricted temperature range of 0-150°C, tan δ can be taken as constant. However, at 20°C the temperature coefficient of resistance for copper is .00393/°C. Since the Q of the cavity can be written as:

$$Q = \frac{\omega U}{W_{wall} + W_{diel}} \qquad 5.40$$

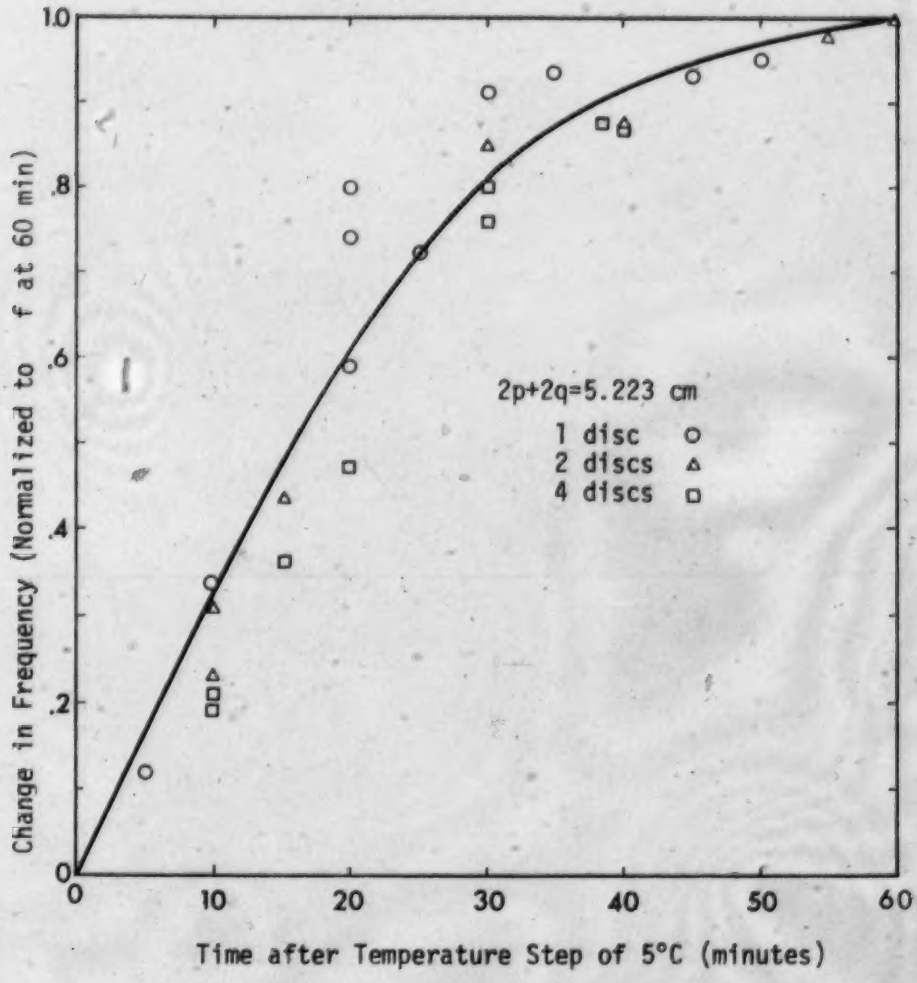

Figure 5.14 Thermal Time Constant of Cavity
(uniform heating in oven)

and

$$\frac{dQ}{dT} = - \frac{\omega U}{(W_{wall}+W_{diel})^2} \frac{dW_{wall}}{dT} \qquad 5.41$$

But since $W_{wall} \alpha R_s$: $\frac{1}{W_{wall}} \frac{dW_{wall}}{dT} = \frac{1}{R_s} \frac{dR_s}{dT}$,

thus

$$\frac{dQ}{dT} = - \frac{\omega U W_{wall}}{(W_{sum})^2} \frac{1}{R_s} \frac{dR_s}{dT} \qquad 5.42$$

Consequently, an increase of 10°C in temperature results in a 3.393% loss in cavity Q.

This is not a serious problem for a practical accelerator structure, since some form of coolant would be used to keep a constant cavity wall temperature. In the present set of tests at high power there will be some effect on Q and consequently R_o. The temperature (of either copper or titania) will no longer be proportional to average power input to the cavity but will have a dependence similar to that of Figure 5.15.

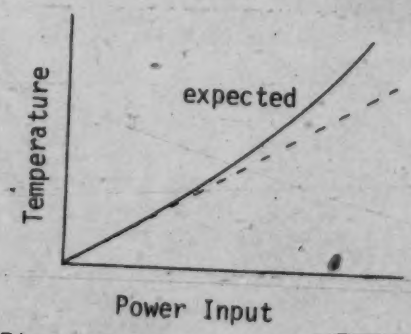

Figure 5.15

CHAPTER 6

EXPERIMENTAL SYSTEMS

6.1 Introduction

The microwave breakdown facility comprised a high power pulsed microwave source, the associated power monitoring circuits, a high field cavity within a vacuum chamber and the auxiliary instrumentation.

Initially these systems, like the sputtering system previously described, did not exist and the establishment of a laboratory was the first task. Because of the bulk of the system, especially of the modulator necessary to drive the microwave magnetron, and the safety precautions mandatory for high voltage - high radiation field apparatus, the systems were assembled in a single room designated for this particular application.

Figure 6.1 is a partial view of the laboratory. Most prominent is the vacuum envelope and cavity mount in the left foreground. Part of the turbomolecular pump can be seen below the envelope. Aluminum "I" beams are used to carry the high power waveguide components which are clamped into adjustable supports. The high aluminum enclosure at the end of the waveguide run houses the magnetron. In the center background is the modulator control console and to its right are the frequency counter, oscilloscope, the microwave power meters and the vacuum gauge control unit. Not shown is the 1/8" lead coated box cover which fitted over the vacuum envelope to reduce the radiation

Figure 6.1 View of High Power Facility

emitted from the cavity.

6.2 High Power Microwave Systems

6.2.1 The Pulse Modulator

The pulsed D.C. power for the magnetron was supplied by a line-type high power pulse modulator. Built under contract for the Defence Research Board by Marconi (Canada) in 1959-1960, (ECRDC Project T42), it was acquired by the Department of Electrical Engineering about 1965. Contained within five large modules (Figure 6.2) the modulator occupied 6.8 square meters of floor area. After extensive repairs and modification a satisfactory capability was available.

The modulator had the following published ratings [94]:

Maximum average power	20 KW (17 KW)
Maximum peak power	20 MW (14 MW)
Maximum pulse voltage	80 kV (72 kV)
Maximum pulse current	250 Amps
Pulse repetition frequency (modified to 20-600 pps)	50-500 pps
Output voltage DC supply	20 kV
Output current DC supply	1.5 Amps
Magnet supply	44 Amps at 60 volts
Filament supply	10 Amps at 100 volts
Pulse length (in steps)	.96 to 6.5 μsec

The maximum ratings were not reached in tests, however, the modulator was capable of delivering the values given in brackets. This was more than sufficient to drive the magnetron and it was not deemed feasible to exceed these ratings since the components were not readily replaceable. The theory of pulse modulator design and operation is beyond the scope of this work and is adequately covered in the Radiation Laboratory Series of reference books [95]. The block schematic in Figure 6.3 should suffice to illustrate how the pulse is generated.

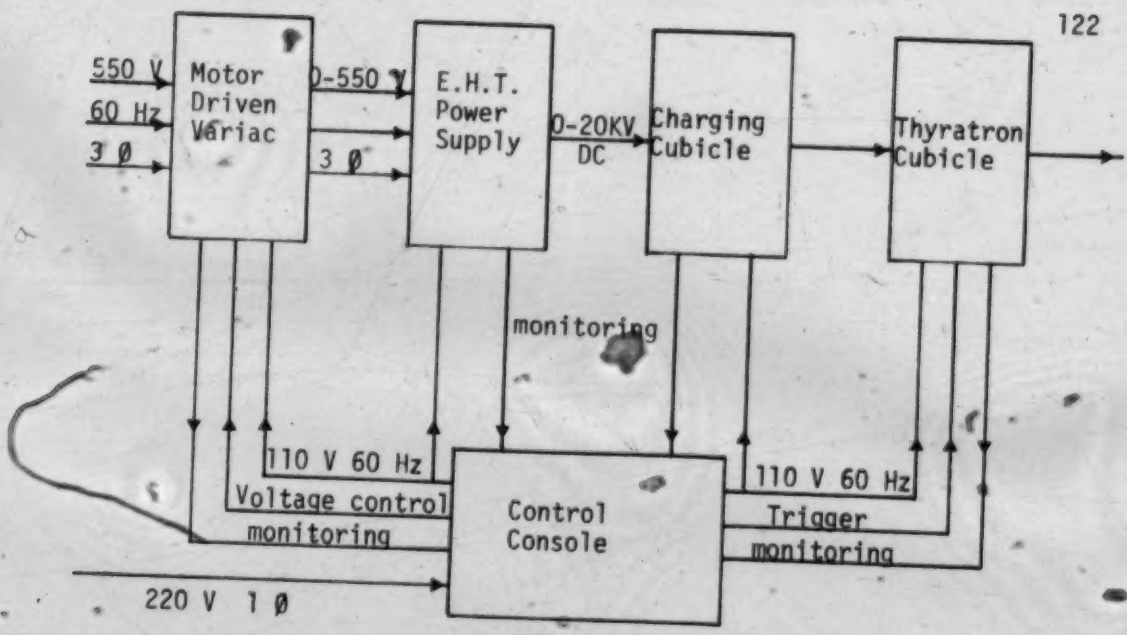

Figure 6.2 Block Diagram of Pulse Modulator

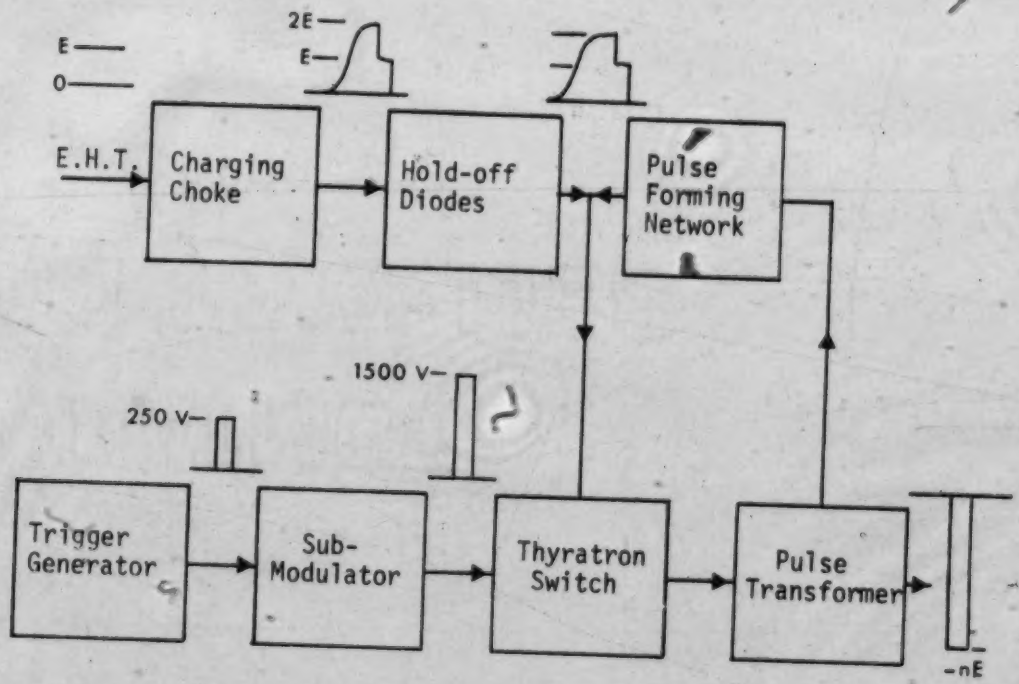

Figure 6.3 Block Schematic of Pulse Modulator

6.2.2 The Magnetron

The magnetron used was a Varian VC-701 having the following characteristics [96]:

Maximum peak power	2.5 MW
Maximum average power	3.5 kW
Pulse length	.5 to 5.5 μsec
Duty cycle (maximum)	.0015
Frequency	2870 MHz

(It is possible to exceed these ratings for short periods if the tube has been sufficiently aged)

The tube has been tested up to the following ratings:

Maximum peak power	1.6 MW (5.5 μsec pulse) 3.5 MW (3.12μsec pulse)
Maximum average power	2.2 kW

The operating regions are given in a chart from the manufacturer. The magnetron required a filament current of 14 amps at 12 volts and a magnetic field of 1500 G supplied by a 40 volt, 25 amp electromagnet. Cooling for the magnetron was provided by a recirculating water system with an air flow directed onto the output window. These supplies were built into the modulator. Spark gaps protected the magnetron and the operating personnel from overvoltages.

6.2.3 Waveguide Circuit for High Power

Figure 6.4 outlines the high power waveguide circuit. All waveguide was standard 3" x 1 1/2" S-band brass guide with choke-cover flange connections except for the vacuum section, which was manufactured out of OFHC copper. For high power transmission the waveguide was pressurized at 15-40 psig and a flow of air (1 cu ft/min - free volume) was maintained to cool the magnetron output window and other components

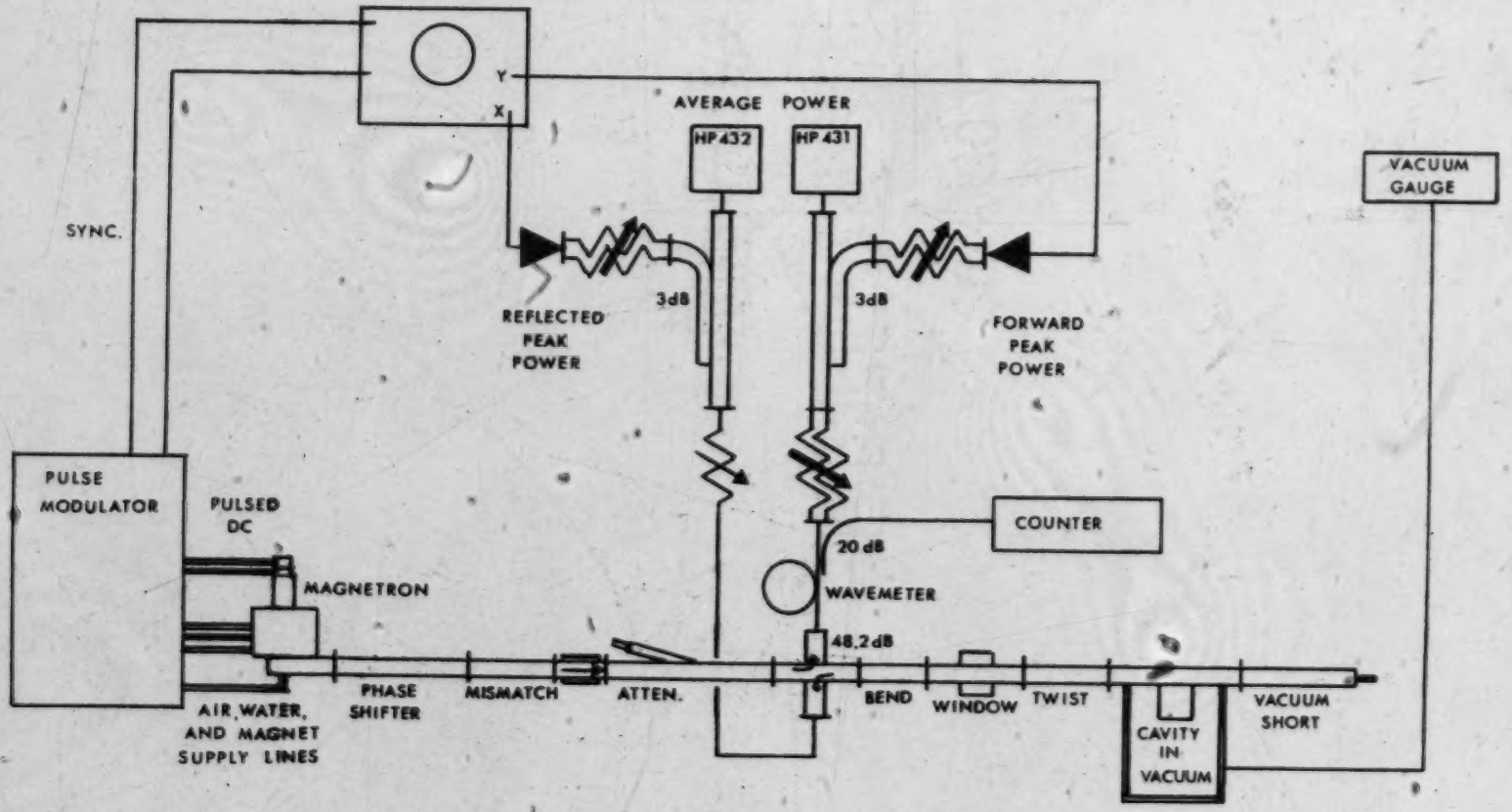

Figure 6.4 High Power System

within the guide.

A mismatch-phase shifter combination supplied with the magnetron allowed pulling of the frequency through a range of 10 MHz as indicated in Figure 6.5. The magnetron was separated from the rest of the guide by a Raytheon ISH-28 isolator having a minimum directivity of 17 dB.

The power attenuator probe consisted of two concentric glass tubes, the one end of the large tube being sealed so that cooling water flowing down the inner tube returned between the two. The probe was inserted into a section of waveguide at an angle of 17° to the axis to give up to 18.5 dB of attenuation. With a well matched load the attenuator was capable of handling 1 MW of peak power before breakdown, otherwise the limit was 700 kW when inserted. With the probe fully withdrawn the rating was essentially that of ordinary waveguide. The combination of the modulator and attenuator allowed a useful range of output power from .02 to 3.5 MW, corresponding to cavity field strengths of 40 to 600 kV/cm. The return loss was less than 15 dB.

The directional coupler was a standard Moreno type cross coupler with a coupling factor of 48.4 dB and a directivity better than 24 dB at 2870 GHz. These factors were dependent on the use of low reflection cable and attenuators in the secondary arms of the couple.

An alumina vacuum window obtained from the USNL separated the pressurized and evacuated sections of the waveguide. It operates in a TE circular mode and has matching irises on either side. No trouble has been encountered with this window.

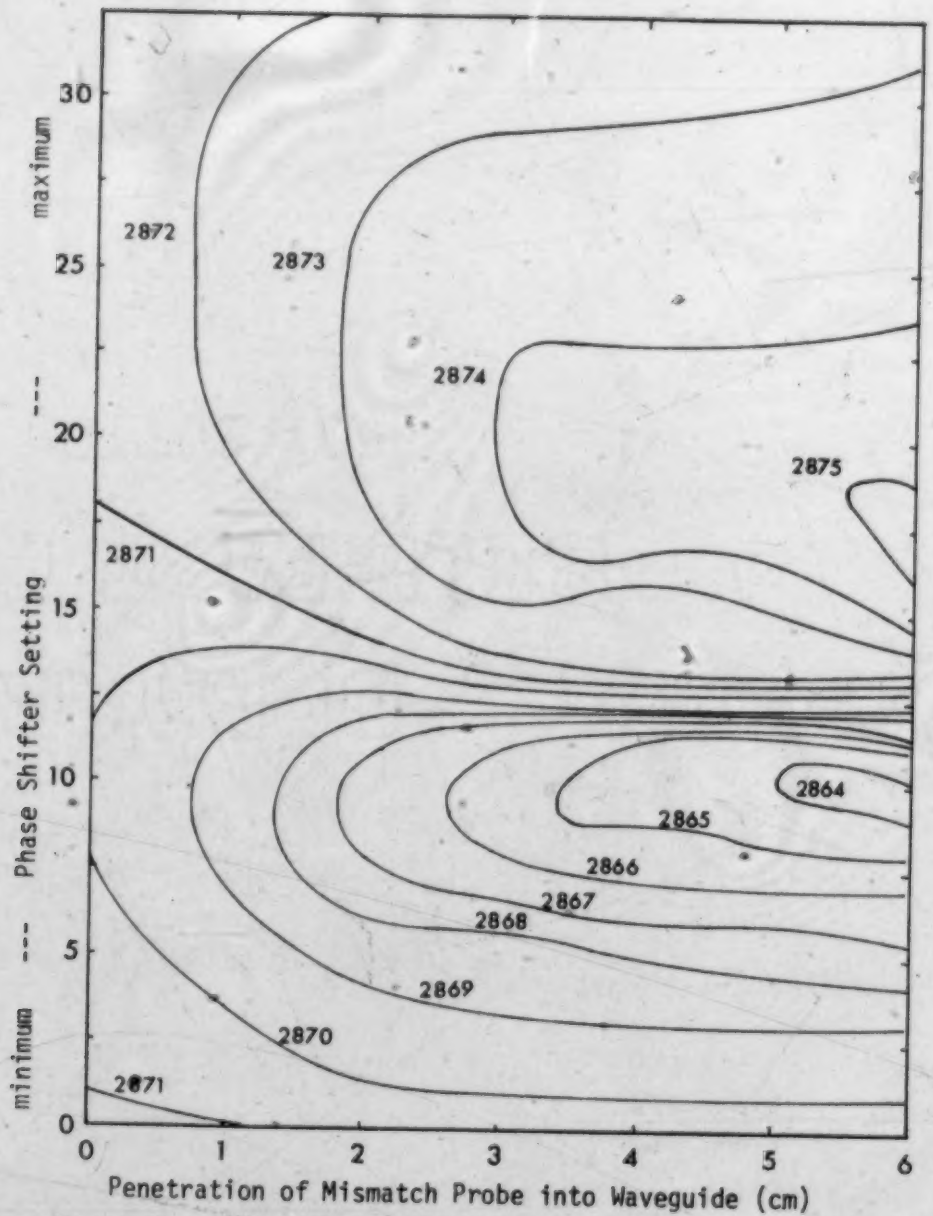

Figure 6.5 Frequency Pulling Characteristics of Magnetron (Frequency contours in MHz are functions of the phase shifter and mismatch settings)

Between the window and the cavity mount a twist section oriented the E plane horizontally. One flange also mounted a thermocouple vacuum gauge head.

The cavity mount was similar to that shown in Figure 4.4 except that it was vacuum sealed. The adjustable vacuum short compensated for any mismatch in the cavity coupling to enable maximum E field in the cavity.

The high power waveguide was supported on two 4" aluminum I beam sections as can be seen in Figure 6.1. One, holding the phase shifter, mismatch, isolator, attenuator and directional coupler, was fixed; whereas the other, at right angles to the first, and carrying the evacuated section of waveguide, was equipped with rollers to permit easy access to the cavity.

The components in the low power side of the Moreno cross coupler have already been described in section 5.1.

6.2.4 Calibration of the High Power System

Peak power is the fundamental quantity from which the electric field in the cavity is derived. Accurate calibration of the power monitoring instruments in the secondary arms of the directional coupler was therefore mandatory.

The power generated by the magnetron is best directly measured by calorimetric means. The vacuum section of the high power waveguide, (window, twist, cavity and short) was replaced by the waterload shown in Figure 6.6. The SWR of the load was better than 1.05 so that the total power can be assumed to be dissipated in the water flowing through

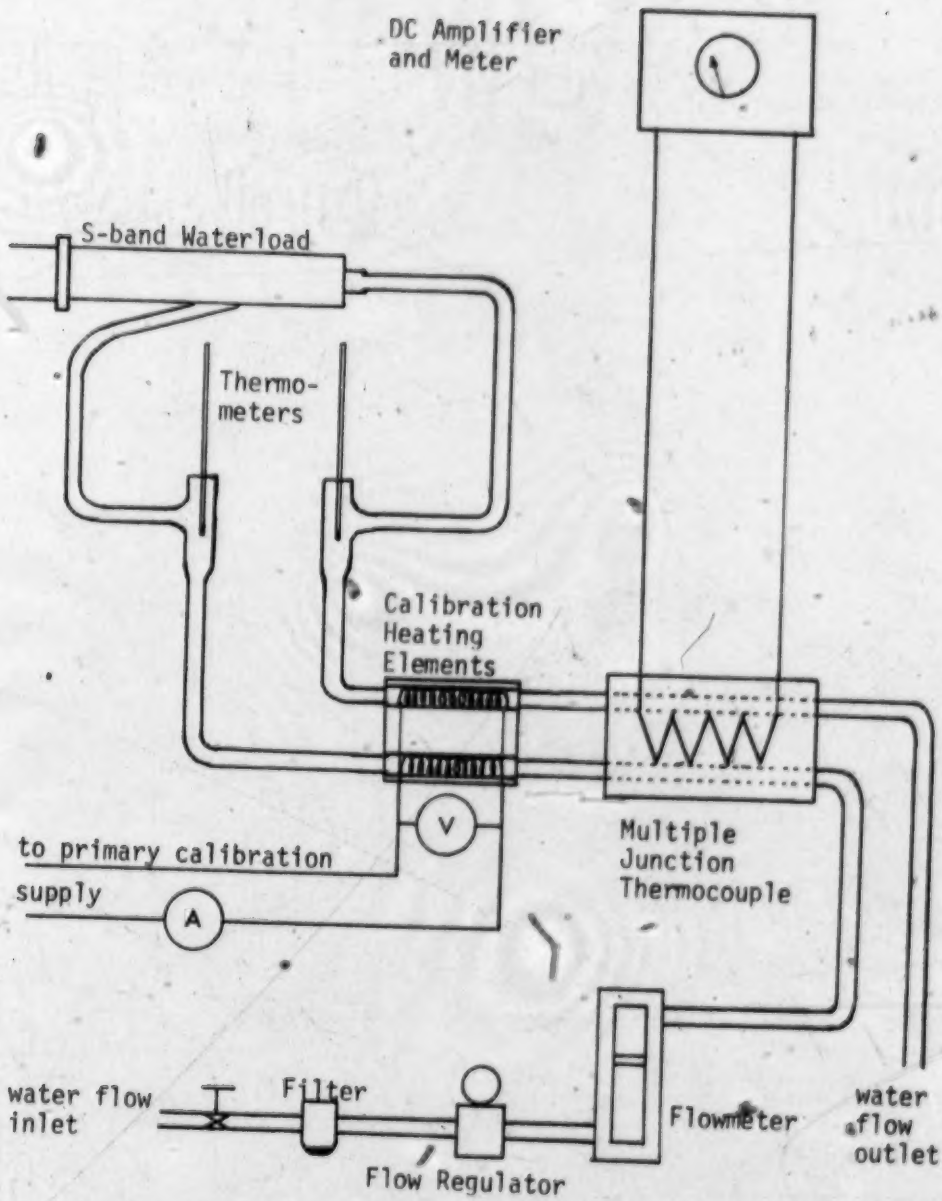

Figure 6.6 High Power Calibration Circuit

the load. The water flow was regulated and monitored by a flow meter; hence knowing the difference between the inlet and outlet temperatures, the power could be calculated by the formula:

$$P = \frac{\Delta T}{4.1816} \times \text{flow rate (gm/sec)} \qquad 6.1$$

The temperature differential was measured independently by a multiple junction thermocouple and dual thermometers located in the flow lines. Although equation 6.1 should give the absolute value, any uncertainty could be eliminated by substitution of the waterload by a resistance heating unit for which the input power could be accurately measured.

The attenuators in the secondary arms (see Figure 6.5) were set such that thermocouple power meters indicated a power level 60 or 70 dB below the actual in the main guide: thus 100 watts average would be read as .10 mWatt at 60 dB coupling.

An alternative method was to adjust the line attenuation in the secondary arm to 11.6 or 21.6 dB to add to the known 48.4 dB coupling of the directional coupler. While satisfactory for noncritical checks, this method could give an error of up to .5 dB due to the number of coaxial connections and was not used for accurate measurements.

Having calibrated the secondary arms with respect to the main guide at some average power, the crystal detectors could be calibrated to the power meters in order to determine the peak power.

The probable experimental errors are summarized in Appendix B, but certain instrumentation errors were eliminated at this stage. The

peak voltage detected by the crystals was typically .4 V. The ground loop voltages generated by the magnetron current pulse could superimpose an additional .1 V which, because of the nonlinear response of the crystal in this region, represented an error of 50% in power. It was necessary to lay additional heavy grounding cables from the oscilloscope to the main waveguide and to the modulator to eliminate this effect. This also eliminated a much smaller error registered on the power meters which theoretically should not have been affected. A secondary restriction was on the length of cable between the detector and oscilloscope to minimize distortion of the detected pulse envelope. These cables and the others used in the secondary arms had to be carefully selected to eliminate mismatches and attenuation which could introduce errors into the power readings.

6.3 Vacuum System

6.3.1 Description

To simulate the breakdown conditions in an electron beam structure the cavity must be evacuated to a pressure of at least 10^{-5} torr such that the mean free path of the gas molecules is greater than the characteristic dimensions of the cavity. To avoid oil contamination of the titania a turbo-molecular pump (Welch 3102) was used as the basis for the system. Figure 6.7 illustrates the actual arrangement of the envelope, gate valve, pump, gauges and the cavity mount.

The cavity mount was machined out of OFHC copper and soldered to a section of OFHC copper waveguide. The mount was attached to one end of the Tee envelope by bolts and sealed with a viton "O"-ring. The

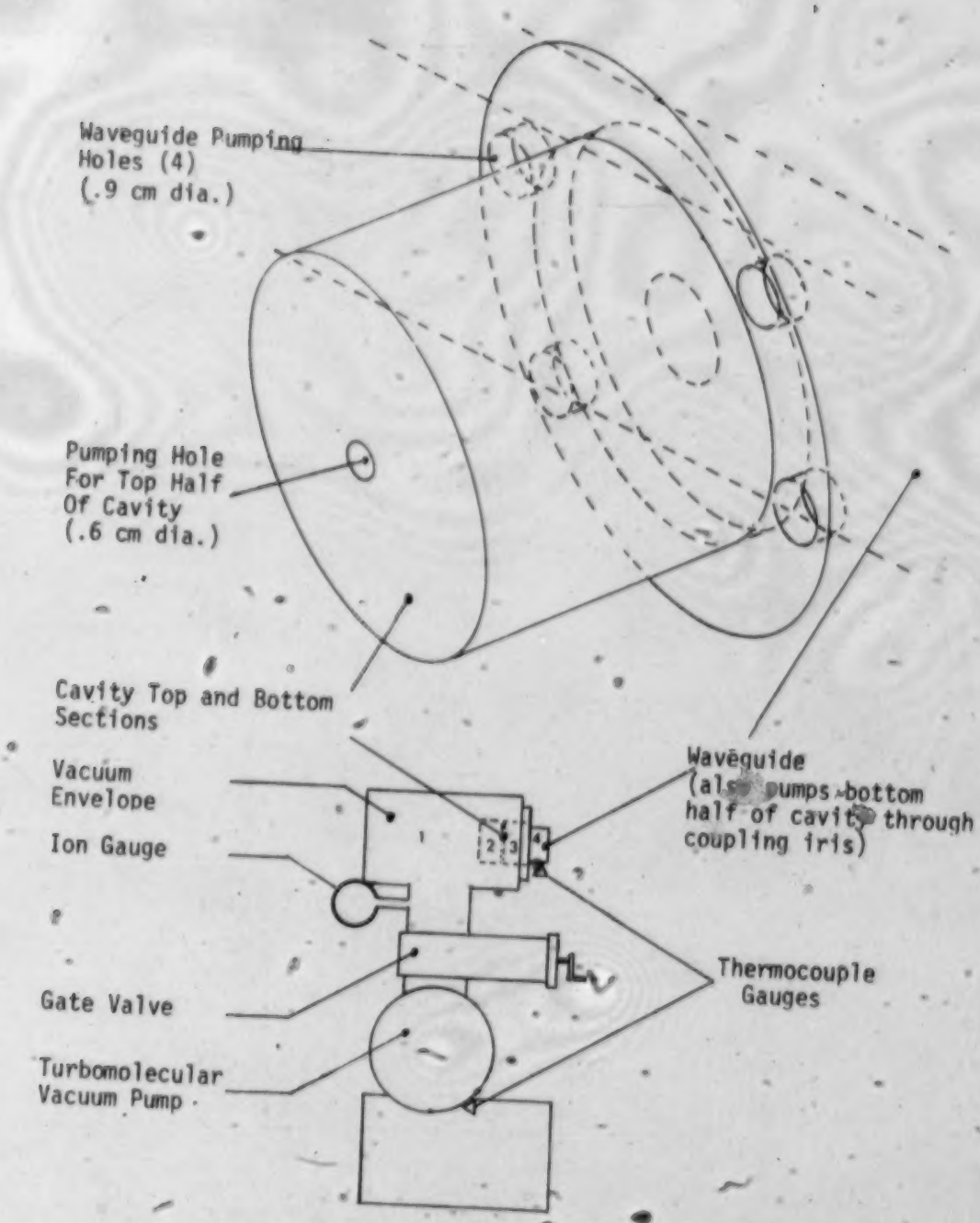

Figure 6.7 Vacuum System

sections of waveguide in the vacuum system were connected as usual since they were fitted with "O"-ring grooves to maintain air pressure in ordinary operation. The alumina microwave window sealed one end of the guide while an adjustable short with a vacuum sealed teflon sleeve terminated the other end. The waveguide and mount were supported on a separate section of aluminum I beam which could be rolled away from the vacuum chamber to facilitate access to the cavity.

At the other end of the "Tee" envelope was added an access port with RF feedthroughs and an observation window, all sealed by means of "O"-rings. The more permanent connections between the stainless steel components (Tee, gate valves, etc) used Varian Conflat flanges with copper gaskets. The vacuum envelope was constructed out of non-magnetic materials.

The gauge control unit (CHA IGC-12) was capable of reading pressures from atmosphere to 10^{-9} torr. Thermocouple gauges monitored the forepressure of the turbo-molecular pump and the waveguide pressure, while an ionization gauge measured the pressure inside the vacuum envelope.

6.3.2 Capabilities and Limitation of the Vacuum System

The volume evacuated can be separated into the four regions illustrated in Figure 6.7. In order to maintain a high Q in the cavity and restrict microwave radiation from the waveguide, the holes for pumping the cavity halves and waveguide had to be kept necessarily small. On the basis of assumed outgassing rates for copper and ceramic the hole sizes were specified as shown.

The low conductance of these pumping holes meant that the pressure in the cavity would be higher than the indicated envelope pressure. Tests were conducted by placing an ion gauge on one end of the cavity while pumping through the hole at the top of the cavity. The cavity pressure was never more than an order of magnitude higher than the pressure in the envelope despite the effective increase in the volume being pumped due to the gauge itself. Since the vacuum system could be pumped down to 4×10^{-8} torr with baking and the actual pressure attained before proceding with any tests was less than 3×10^{-7} torr, a sufficiently low pressure existed inside the cavity ($<10^{-5}$ torr). The time required to pump down to 3×10^{-7} torr was about 6 hours.

From experience with the turbo-molecular pump it was found that the vibration is excessive for delicate work such as with electron beams and requires at least a bellows between the pump and waveguide system. This however, did not prove serious in the breakdown experiments.

6.4 Other Instrumentation

6.4.1 Radiation Detectors

Film badges were introduced when the high power systems were ready. Badges were worn at all times by personnel in the test area, and two monitor badges were located in the region of the control console to indicate total dose over a 2 week period. For specific measurements additional film badges and Victoreen pocket dosimeters were distributed about the test area.

Radiation dose rates could be measured by an Ecko N596 ionization chamber type monitor capable of reading up to 300 mrad/hr and a Victoreen 440RF radiation detector with similar capabilities. Both were portable and shielded from microwave interference. Meters capable of higher scale readings were borrowed on occasion.

6.4.2 Temperature Measurements

For remote temperature monitoring a Higgins optical pyrometer with a 1° field of view and a useable temperature range from 70 to 300°C was used. It was calibrated using iron-constantan and copper-constantan thermocouples since it was necessary to compensate for differing emissivities of the various materials when observed through glass windows on the vacuum systems. To measure the temperature of the cavity under power, and in thermal tests, thermocouples were used; however, in some instances this was supplemented by observing colour change in Edmund Scientific liquid crystal sheets.

6.4.3 Photography

By placing a small viewing hole in the cavity mount, the surface of the disc could be observed during the high power tests. A small lens with a 2 cm focal length was positioned directly in front of the glass window so that it was possible to observe the surface of the disc up to a radius of 2 cm. A Graflex camera with Polaroid 3000 ASA film attachment or a 35 mm Miranda SLR 20 cm from the lens was then set for a time exposure of 2-5 min in the fully darkened laboratory. The 35 mm was prefered since it allowed colour slides by pushing Kodak High Speed Ektachrome Tungsten film to 600 ASA.

CHAPTER 7

EXPERIMENTS AT HIGH POWER

7.1 Experimental Procedure

7.1.1 Preliminary Considerations

Before high power was applied to any discs, experimental runs were conducted using either the waterload or the empty TM_{010} mode cavity. As the magnetron was new it required the essential aging or burn-in period at high power. Meanwhile, the high power systems were calibrated and modifications incorporated.

During this time, it was noted that the pulse waveform deteriorated at low magnetron power levels and that the magnetron, when feeding into a resonant load, was unstable near 2871 MHz. The adoption of the water attenuator enabled a single modulator setting to be used for cavity powers up to 700 kW or more. The modulator parameters, magnetron current and cathode voltage, could then be optimized for the best pulse shape from the magnetron operating nearer its designed region. The moding instability was in part eliminated by changing the number of wavelengths between the magnetron and the cavity, but henceforth cavities were designed to resonate at 2868 MHz. It should be noted at this point, that due to the true relative permittivity of air (experimentally determined: $\varepsilon_r = 1\text{-}5.92 \times 10^{-6}$), the resonant frequency in vacuum was about 800 kHz higher than in air; thus in fact cavities were tuned for 2867 MHz in air.

7.1.2 TM_{011} Mode Experiments

A total of eleven titania discs were systematically tested to destruction in the microwave cavity. The same basic procedure was repeated for each disc; however, as the system was improved in the course of the research, certain steps were modified or added.

After the final low power tests and any necessary coating, the disc was assembled into the cavity and fitted in the vacuum mount. The system was pumped to 10^{-7} torr, first by baking the vacuum envelope to 40°C and then by allowing the system to cool over 24 hours or more. At the end of this period the low power microwave circuit was attached to the vacuum window and final adjustments made on cavity coupling using the vacuum short. A last measurement was made of cavity Q before coupling the cavity to the high power waveguide.

The high power water attenuator was set for maximum attenuation of 18 dB and voltage was applied to the magnetron. At a peak power of 700 kW, the magnetron was allowed to stabilize before being tuned to the cavity resonance using the mismatch and phase shifter. Power to the cavity was increased by withdrawing the attenuator probe in steps of one or two dB. Each change of power level was separated by fifteen minutes or more to permit the cavity temperature and frequency to stabilize. During this period, the pulse shape was optimized and readings taken prior to increasing the power level again.

If there was a pressure pulse or cavity discharge, the high power was removed and the low power system reattached to ascertain any change in cavity Q. The cavity was then disassembled and the disc

inspected under a microscope for any surface irregularities. If no serious change was noticed, the cavity was reassembled and installed in the vacuum chamber following the same procedure as before, including repetition of the low power tests. High power was again applied and the attenuator gradually withdrawn. For powers greater than .7 MW the attenuator was set to its minimum and the modulator output voltage was increased. Unfortunately, this required more careful control of the pulse waveform and magnetron frequency, but as the magnetron approached its designed operating point it became better behaved.

After breakdown was achieved, low power measurements were repeated, the cavity disassembled and the disc microscopically analysed to determine the total damage.

To indicate the time scale involved, a typical disc required four test runs before failure, each run lasting for three to six hours and entailing approximately 12 changes in the power level. The time required to pump the cavity between runs would double the time.

The numbers allotted to the discs were for reference only and do not correspond to the sequence in which they were tested. The actual order was: 00, 3, 1, 2, 4, 10, 5, 9, 8, 11, 7, 6. (Disc #00, having been damaged during preparation, was expended in a trial run to establish operating procedure and results from this test are included only for completeness).

7.1.3 Experimental Quantities Monitored

The readings and observations made in the course of the test

runs may be summarized as follows:

1. Modulator
   (a) D.C. voltage
   (b) D.C. current
   (c) Magnet current
   (d) Pulse voltage
2. Microwave Power
   (a) Forward (incident) average power
   (b) Reflected average power
   (c) Forward peak power
   (d) Reflected peak power
   (e) Frequency (wavemeter and counter)
3. Envelope vacuum pressure
4. Radiation output of cavity (at about 1 m)
5. Cavity temperature (thermocouple)
6. Microwave probe resonance (to be described in Chapter 8)
7. Conditions inside the cavity visually observed and recorded by camera

The modulator readings were recorded at intervals as adjustments were made in pulse shape and modulator output power. The other parameters were recorded each time the power to the cavity was increased and in the event of transient phenomena such as a discharge or pressure fluctuation.

7.2 Experimental Measurements

7.2.1 Peak Power

Both the incident and reflected high power signals were continually monitored on a Tektronics 556 oscilloscope capable of displaying four

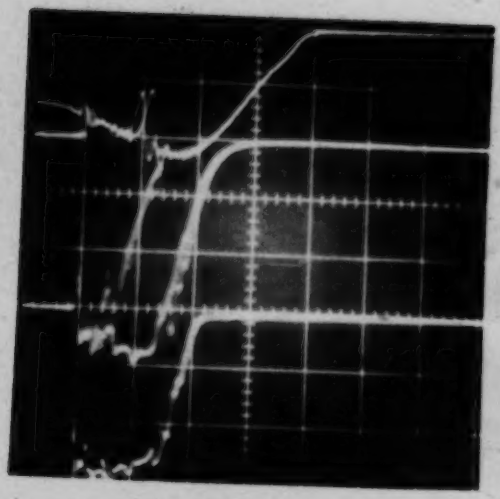

(a) Mismatch during Discharge (175 kW Peak Power)

(b) Prior to Breakdown (1.05 MW Peak Power)

(c) After Breakdown (1.2 MW Peak Power)

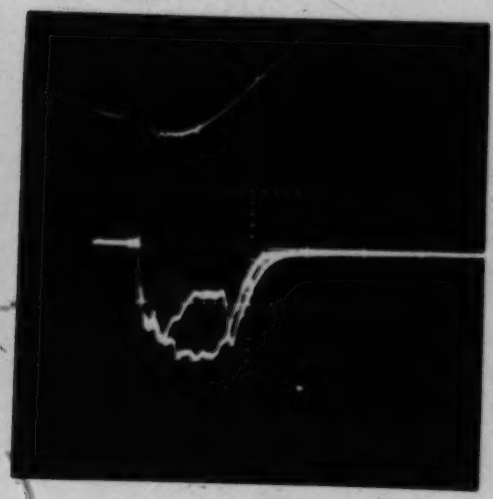

(d) After Breakdown (250 kW Peak Power)

Figure 7.1 Pulse Waveforms for Disc #8
The upper trace is of the microwave probe resonance: the two lower traces are the reflected and forward signals from the crystal detectors.

traces simultaneously. The sequence of waveforms in Figure 7.1 for tests with disc #8 are typical. Each frame includes three traces, but only the lower two pertain to this discussion: the upper waveform is of the microwave probe resonance which will be analysed separately in Chapter 8. The crystals having been calibrated with respect to the power meters and the calorimeter, both the cavity power dissipation and stored energy can be determined from the two pulses.

The power flowing into the cavity contributes to the build up of the stored energy in addition to the cavity losses. Since the unloaded Q is defined in terms of the stored energy and the cavity loss, the cavity energy is related to the input power by the differential equation

$$P = \frac{dU}{dt} + \omega_o \frac{U}{Q_o} \qquad 7.1$$

The stored energy of the cavity at some time, t, after the start of the pulse may be expressed as

$$U = \frac{4\ Q_L^2}{Q_{ext}}\ P_\infty\ (1 - e^{-t/\tau})^2 \qquad 7.2$$

where P_∞ is the steady state power level and τ is a time constant defined as $\frac{2Q_L}{\omega_o}$ [97]. The electric field is given by

$$E = E_\infty\ (1-e^{-t/\tau}) \qquad 7.3$$

as shown in Figure 7.2(a). In this case E_∞ would represent the field

evaluated by the equations of section 5.3.3, thus for pulses up to 3μsec in duration an additional correction term is necessary to determine the effective field for a high Q cavity energized by a pulsed input.

The power into the cavity also has an exponential dependence. From equation 7.1

$$P = P_{\infty} (1 - e^{-2t/\tau}) \qquad 7.4$$

This effect is seen in the reflected pulse of Figure 7.1(b). The non-linearity of the detector makes the apparent reflection 10%, but, in fact a power of 1 MW resulted in only .03 MW of reflected power.

The value of P_{∞} is derived from the incident pulse and may be defined in three ways. The equivalent peak power, calculated using the known average power, pulse repetition frequency and the pulse width (between half power points), would correspond to curve "a" in Figure 7.2(b). The smoothed peak value denoted by "b" would be a more realistic representation; however the actual pulse envelope "c" has a ripple some 5% higher than "b". In order to be consistent, the peak power was defined as the value of the smoothed pulse at the point of minimum reflected power. In this way any errors in the detected pulse because of mis-matches and reflections in the low power circuit and directional coupler were eliminated.

The input power is also affected by dynamic changes in cavity characteristics. Figure 7.1(a) indicates the increased reflection due to a momentary cavity discharge. In this case, there is a total mismatch;

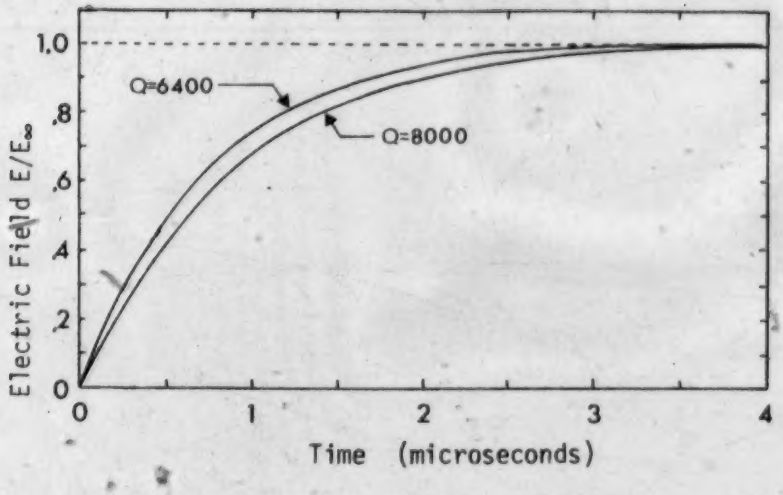

(a) Cavity Filling Time

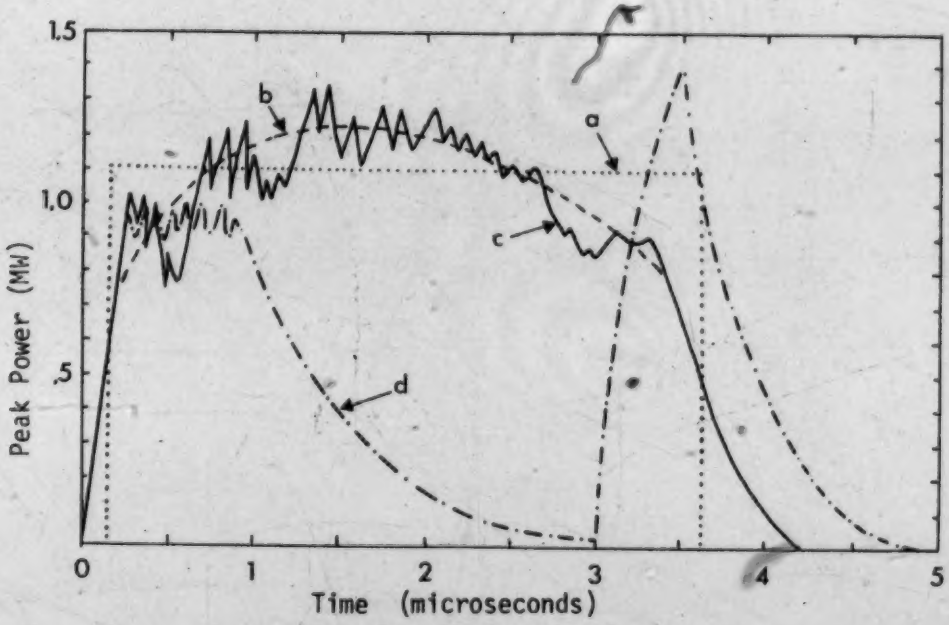

(b) Pulse Power Waveforms

Figure 7.2 Effect of Cavity Filling Time

that is, all incident power is reflected. The mismatch only occurs for a short time and if power is reduced it is possible to regain the matched condition. At breakdown however, the cavity loss increases and the cavity Q is reduced resulting in the partial reflection of Figure 7.1(c). The match is irreversibly altered and even at lower power (Figure 7.1(d)) there does exist a substantial reflection. The distinction between the two types of mismatch enables the point of breakdown to be determined accurately. The peak powers recorded for the respective discs are listed in section 7.5.

7.2.3 Pressure Fluctuations

A discharge in the cavity was registered by the ion gauge pressure. Although this could be caused by a real increase in the cavity pressure due to outgassing, most probably some of the ions generated in the discharge are actually collected by the gauge and give an incorrect reading.

There was a general increase in pressure as power was raised and the cavity became warmer. In each case the pressure was initially 3×10^{-7} torr or better. At the end of a run the pressure was as high as 10^{-6} torr and discharges increased this reading to 10^{-5} momentarily. After cooling the pressure returned to the 10^{-7} torr range.

7.2.3 Radiation Measurements

At peak powers less than 200 kW, no radiation was observed near the cavity. This may in part be attributed to the energy threshold of the meters used, about 10 keV. At higher powers the indicated dose rate

increased rapidly (dependence upon peak power was about P^5). When a cavity discharge occurred, the radiation increased by a factor of two or more; however, after breakdown no further radiation readings were recorded. This behaviour was no different to that observed with the empty cavity;hence high radiation does not necessarily indicate breakdown of the disc but only the presence of energetic electrons.

The dose rate at breakdown, as indicated by a meter 70 cm from the cavity mount was typically 50 to 100 mrad/hr. By introducing different thicknesses of lead sheet between the cavity and meter and noting the difference between readings, the probable peak X-ray energy (calculated using the known absorption coefficients of lead) was about 100 keV.

7.2.4. Thermal Measurements at High Power

Because of the high wall currents in the cavity a thermocouple element was resorted to instead of a more sensitive thermistor device. The voltage at a copper constantan junction securely attached to the cavity top was monitored on a milli-voltmeter. A liquid crystal sheet, applied to the outside surface of the cavity, verified that the temperature was uniform along the cavity to within two or three centigrade degrees.

In Figure 7.3 temperature is plotted versus the average power absorbed in the cavity along with two other parameters; the resonant frequencies of the TM_{011} and TE_{014} modes. The temperature coefficient for the TM_{011} mode is seen to be about 60 KHz/°C at low powers, three times that observed during low power tests (17.5 KHz/°C-section 5.4.2).

From this an estimation of the ceramic temperature can be made.

Recalling from section 5.4.2:

$$\left(\frac{df}{dT}\right)_{Cu} = -43.8 \text{ KHz/°C}$$

$$\left(\frac{df}{dT}\right)_{\varepsilon_r} = 57.4 \text{ KHz/°C}$$

Assuming a uniform ceramic temperature T_ε, the ratio of the ceramic temperature increase to that of the copper, $\frac{\Delta T_\varepsilon}{\Delta T_{Cu}}$ can be obtained by solving the equation:

$$\left(\frac{df}{dT}\right)_{\varepsilon_r} \frac{\Delta T_\varepsilon}{\Delta T_{Cu}} + \left(\frac{df}{dT}\right)_{Cu} = 60 \text{ KHz/°C}$$

$$\frac{\Delta T_\varepsilon}{\Delta T_{Cu}} = 1.8$$

Referring to the figure, at 40 watts (of which the disc absorbs 6 watts), the copper temperature is 9.5°C: the average disc temperature is 80% or 7.6° higher than that of the copper. This is consistent with equation 4.31 which gives a temperature differential of 7.5°. Of course in reality the disc temperature is not uniform but that given by Figure 4.6; hence the above results should not be weighted too heavily. The temperature at the center of the disc could be possibly twice as high.

Attempts to measure the titania surface temperature directly using an optical pyrometer were inconclusive. No temperatures were registered about 70°C, the lower useful limit of the instrument used.

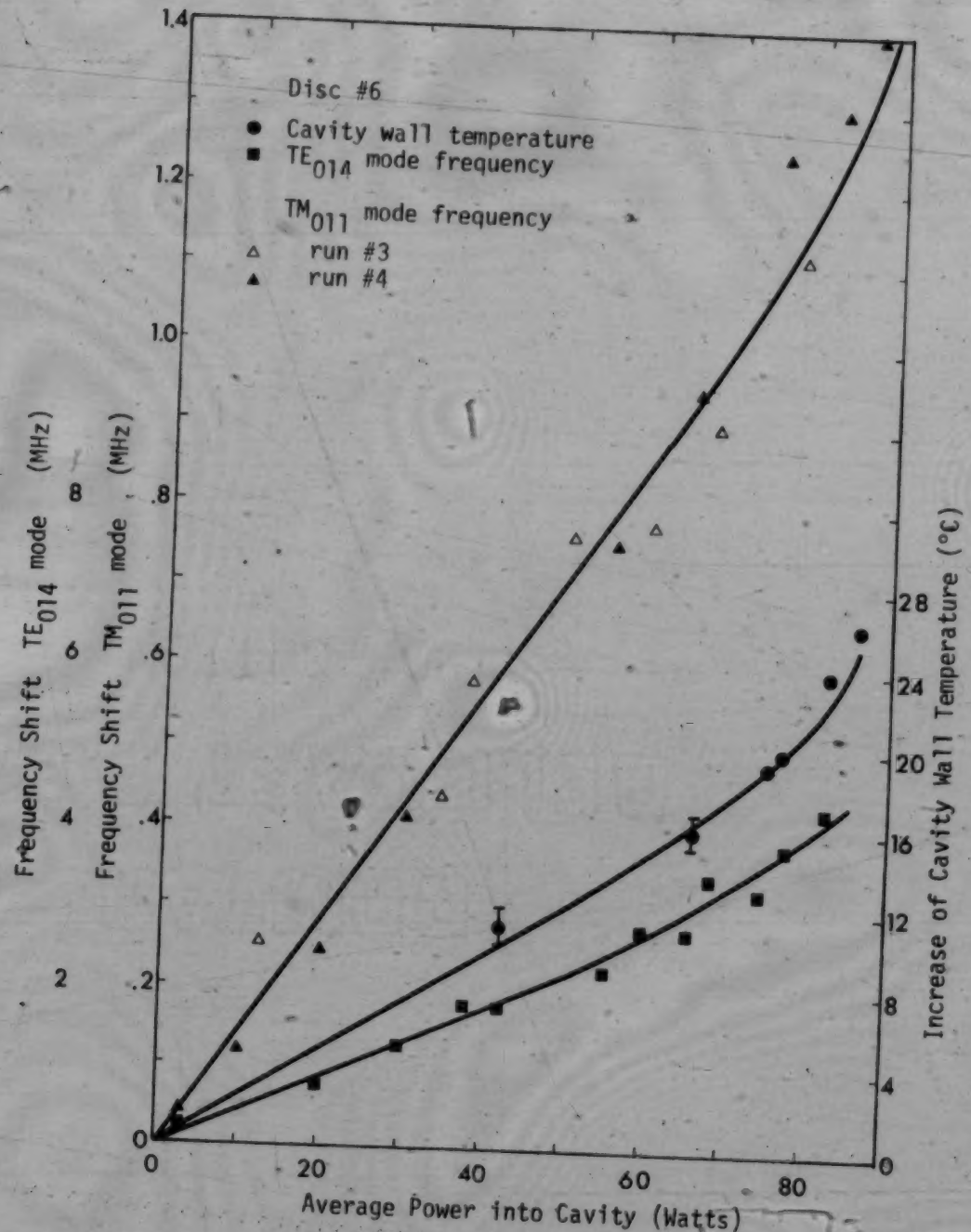

Figure 7.3 Variation of Cavity Parameters with Power

However, since discs after immediate removal from the cavity had surface temperatures over 50°C (measured using liquid crystal sheets) it was assumed that there was an error in calibrating the pyrometer.

As breakdown is approached in Figure 7.3, the slope of the temperature curve increases. This is to be expected as the cavity copper losses increase with temperature (see section 5.4.3).

7.3 Cavity Discharges

7.3.1 Introduction

The discharges observed within the cavity depended upon the presence of surface coatings and the power level and may conveniently be classified as low power, including conditioning and multipactor, and high power discharges, the division point being in the region of 400 kW.

7.3.2 Conditioning Discharges

In each test on a disc, during the first run, at powers in excess of 30 kW peak, discharges were observed which resulted in a mismatch in the main waveguide and a distinct blue glow in the cavity on each side of the disc. Since the discharges were intermittent and became less frequent in time and only increased if the power was increased, they were assumed to be conditioning type discharges due to outgassing of the cavity and ceramic. In each succeeding test run the conditioning time became shorter provided the system was not opened to air for more than a few minutes between runs. The random nature, making it difficult to specify a range over which conditioning occurred,

was compounded by the existence of a second low power discharge which was assumed to be due to multipactor.

7.3.3 Multipactor

In the tests with titanium coated discs, only the conditioning type discharge was present at low power; however, for the other discs, there existed a range of powers for which discharges occurred which did not diminish with time. Figure 7.4 shows the approximate fields required for this discharge which was probably of a multipactor nature. The response was identical to that of the conditioning discharge; high reflected signal and the characteristic blue glow; but was maintained for longer periods of time (typically the system was mismatched for 40% of the time).

For the alumina coated discs the discharge was more predictable, starting at 45 kW and lasting up to about 60 kW, the discharge being maintained even as the power was reduced to 30 kW. Only by increasing power to 45 kW could the discharge be initiated again once it had been extinguished. With uncoated discs the same effect was noticed at higher power but was not as consistent. The discharge was maintained over the narrow range 86 to 96 kW peak for disc #11. In this case the discharge was not constant but had a period which varied with power level as indicated in Table 7.1.

7.3.4 High Power Phenomena

Over 150 kW all three types of discs reacted similarly. Only occasional conditioning discharges occurred at rare intervals as power was increased to 500 kW, at which point a slight blue glow with a

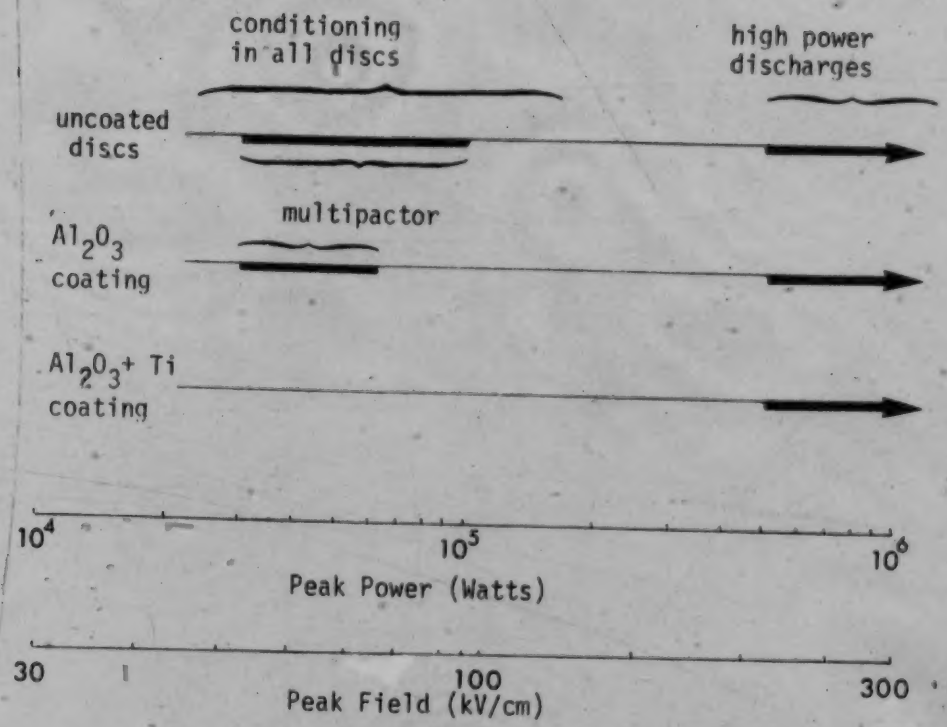

Figure 7.4 Discharge Regions

Table 7.1 Discharge Pulses

Power Level (kW peak)	<86	86	88	90	92	96	>96
Period Between Pulses (sec)	no pulses	2.5	2	2.5 to 3.5	3	4 to 8	no pulses

pulse duration .3 sec

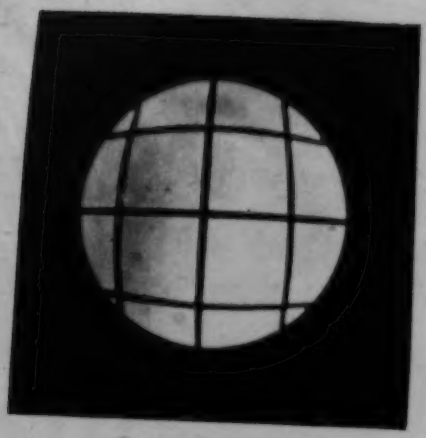

(a) 1 cm Calibration Grid

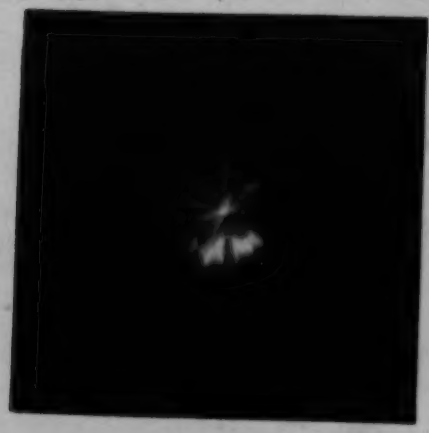

(b) 620 kW Peak Power

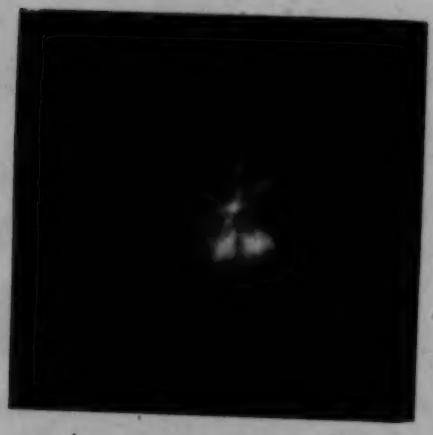

(c) 780 kW Peak Power

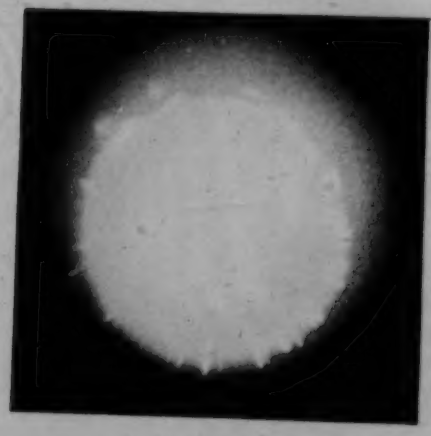

(d) 880 kW Peak Power

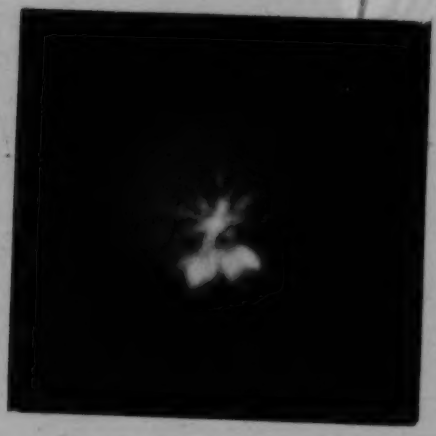

(e) 950 kW Peak Power

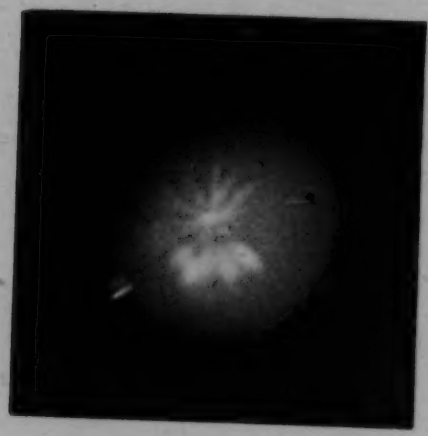

(f) 1.05 kW Peak Power

Figure 7.5 Luminescence on Ceramic Surface and Cavity Discharges Observed at High Power (Disc #11)

definite radial pattern could be distinguished at the center of the disc surface. By making a five minute exposure with a camera focussed onto the surface through the small observations window the intensity of the pattern could be recorded as power was increased. Figure 7.5(a) indicates the field of view over the disc surface, the grid spacing being 1 cm. The pattern became brighter with increasing power but disappeared momentarily if a discharge occurred.

At the same time that the glow was noticed, the first readings were made on the radiation meters. During a discharge the radiation level increased 2 to 5 times the normal.

Above 700 kW the discharges not only illuminated the cavity but extended to the glass window on the waveguide side opposite the coupling hole, as seen in Figure 7.5(d). Also observable in Figures 7.5(d) and (f) are minor needle shaped discharges apparently at the coupling iris. At these powers the glass windows on both ends of the vacuum system demonstrated a slight green fluorescence, due evidently to high energy electrons emitted from the cavity through the coupling and observation irises at the bottom and top of the cavity respectively.

These phenomena became more distinct as the ultimate field was approached, breakdown generally occurring after only a few of the high power discharges.

7.4 Microscopic Investigation of the Discs

A binocular microscope with an adapter for a 35 mm Miranda camera was used to scan the disc surfaces. Micrographs were taken of any

surface irregularities which were considered potential points for breakdown. These included uneven or chipped edges, defects in the surface coating and apparent impurities imbedded in the titania. Discs were surveyed before testing, between each test run and after breakdown.

After the first few test runs, but prior to breakdown, points of local reduction about 100μm in diameter were noticed around some of the impurity centers. Uncoated discs had one or two such points on each side; whereas in coated discs they only occurred where the alumina was thin or absent (due to accidental masking while being coated). The reduced areas did not subsequently enlarge at higher power and did not affect the low power characteristics of the disc.

In no case did the final point of damage coincide with any of the suspected regions micrographed. Usually failure was in the form of a crack extending inwards from the edge. Discs #2 and 4 had an obvious fracture over halfway across the disc. In the other discs (#6, 7, 8 and 11) they were less than a centimeter in length and in the case of disc #6 was first noticed under the microscope. When the copper ring was removed the last four dics showed type 5 damage, blackened points of reduction along the fracture, indicating edge discharge. A comparison was then made between all the copper coated discs and some aluminum coated discs also available. Although the copper film was not readily stripped off by the high radial fields, for the four discs in question, discharges occurred at pits within the film, causing edge breakdown and fracture. The films on the other discs were generally better, the aluminum films being the best when viewed under the microscope. The

difference was not attributed to the films but rather to the finish on the edge of the discs. The aluminum coated samples had been more carefully prepared prior to coating; however edge grinding of the larger discs had not been as successful and the copper film had not adhered uniformly. This would also account for the high film resistance referred to in section 3.4.

One disc, #10, had extensive treeing patterns on the perimeter. The larger, more intense patterns were over 1 cm long with the trunk reaching the edge. The other patterns, which had just started were centered about 3 mm from the edge and did not extend all the way to the edge. Most discs on removal from the cavity after breakdown had a region a few mm wide and 3 mm from the edge which was lighter colored than the rest of the surface. This returned to normal after a few hours but under the microscope there was evidence of particle bombardment at the same radius, especially on the alumina coated discs.

On the titanium coated discs, discharge tracks were observed in the film. Although the surface resistance was not appreciably changed, some of the titanium had been stripped off. If the discharges were allowed to proceed for a longer period, the loss of titanium could conceivably permit multipactor.

7.5 Quantitative Results

Table 7.2 summarizes the parameters of each disc at breakdown (or more precisely, immediately prior to breakdown). The type of damage incurred follows the classification of section 1.3.3 and the calculated

Table 7.2 Summary of High Power Breakdown Tests See also Table 5.2

Disc #	Pulse Length (μsec)	P.R.F. (Hz)	Duty Cycle x10^6	Average Power Forward (W)	Average Power Absorbed Cavity	Average Power Absorbed Disc	Peak Power (MW)	Peakfield (kV/cm) Axial	Peakfield (kV/cm) Radial	Type of Damage
TM_{010}	3.12	70	218	360			1.7	440		
^{0}(ref)	NOT USED									
00	3.12	100	312	350	170	~25	1.1	~300	~15	1,3,6
1	5.5	70	385	360	300	57	.70	250	12.8	1
2	5.5	70	385	420	295	52.2	.90	290	14.8	1,6
3	5.5	70	385	70	53	18.02	.165	104	5.3	
4	3.12	70	218	227	114	16.6	1.15	342	17.5	2,6
5	3.12	20	62.4	40	20	4.8	.75	252	12.9	6
6	3.12	100	312	172	86	12.9	.63	258	13.2	5,6
7	3.12	40	125	137	68.5	10.5	1.20	356	18.2	5,6
8	3.12	20	62.4	66	33	6.2	1.15	347	17.7	5,6
9	3.12	20	62.4	56	28	4.2	.95	316	16.2	2
10	3.12	20	62.4	65	32.5	7.5	1.15	325	16.6	3,4
11	3.12	20	62.4	53	31.5	5	1.05	320	16.4	5,6

peak fields are derived from the data from Table 5.2.

Despite the difference in surface coatings, the breakdown fields are strikingly similar for six discs (#4, 7-11), being in the range 316 to 356 kV/cm, well within the allowable error limits. The lower values for discs 1 and 2 may be attributed to the higher average power which they absorbed. Two other discs gave expectedly poor results. Disc #3 had been chipped in machining and attempts to repair the edge with a ceramic and epoxy filler resulted in outgassing and edge discharges. Disc #5 developed a slight crack while being fitted with the copper ring but still withstood 250 kV/cm. The failure of disc #6 was only explained after investigation under the microscope; the disc had not seated correctly in the copper ring and breakdown occurred at the slight gap between the disc edge and the copper. The disc #00 was the first tested and results were inconclusive since the actual point of breakdown was not observed. It is included because it also cracked in a manner similar to discs #2 and 4 at high average power.

The first observable correlation is between peak power (or field) and average power dissipated in the disc. At low average powers the discs can sustain .95 MW (corresponding to 310 kV/cm) but the peak permissible power must be derated at higher duty cycles as indicated in Figure 7.6. This supposes that preventable premature causes of breakdown such as occurred with disc #6 are avoided. At breakdown discs #1 and 2 fall into the region of possible failure in Figure 4.8.

The effect of the different coatings on the breakdown field is more difficult to assess. A first glance at Table 7.3 would tend to

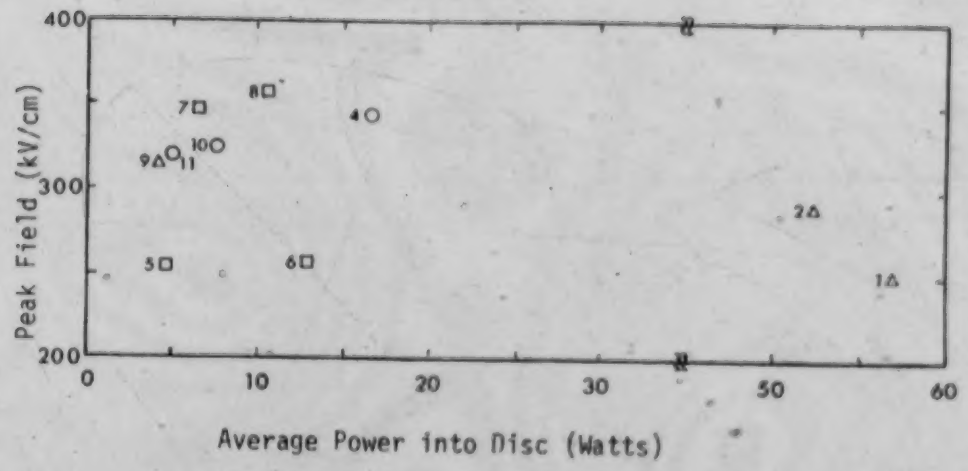

(a) Maximum Field

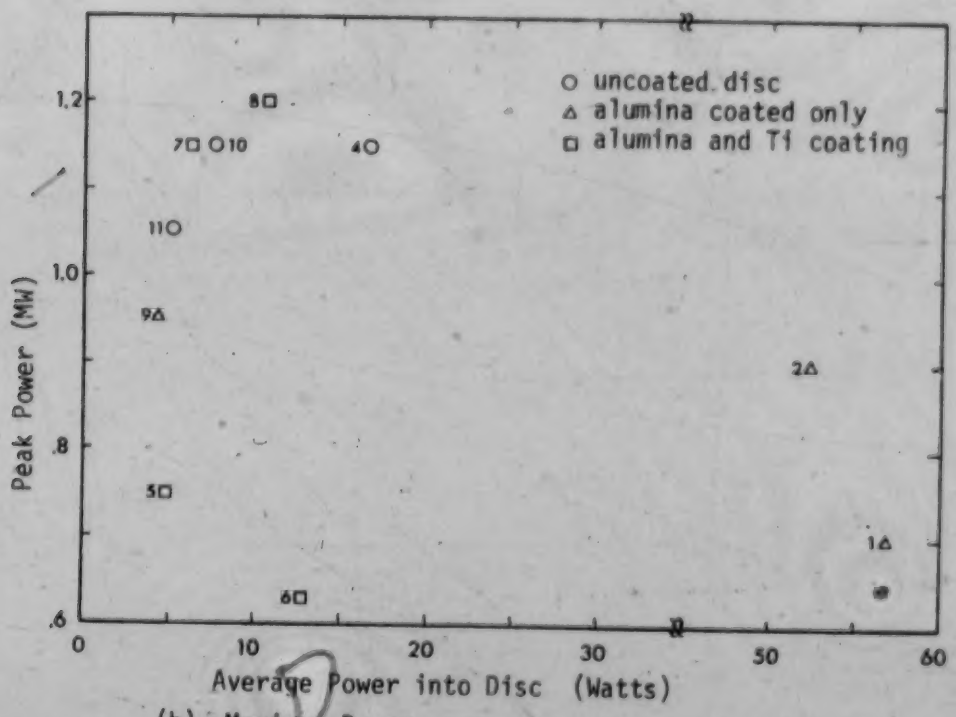

(b) Maximum Power

Figure 7.6 Summary of Breakdown Results for Titania Discs

Table 7.3 Comparison of Different Surfaces

Surface preparation	Discs Tested	Peak Power	Peak Axial Field
unpolished uncoated	#4	1.15 MW	342 kV/cm
polished uncoated	#10,11	1.10	328
polished coated Al_2O_3	#9	.95	316
	#1,2	.80	270
polished coated Al_2O_3 and Ti	#7,8	1.18	352
	#6#5	.69	255

suggest that the alumina coated discs (ones without a titanium coating) actually gave poorer results than the uncoated discs and that the use of both alumina and titanium results in only a marginal improvement. More relevant is the type of failure. Coated discs failed primarily due to thermal stresses induced either by high average power or from local heating at discharge points on the edge. Uncoated discs suffered from surface discharges alone or with additional stress failure. The sample of discs is too small to make any definite conclusions, but the surface coating does inhibit surface breakdown.

CHAPTER 8

DISCHARGE DIAGNOSTICS USING A MICROWAVE PROBE

8.1 Introduction

After experiments on the first few discs it became apparent that the data obtained prior to and during breakdown were limited to passive observation of power, radiation and pressure fluctuations or to insufficiently quantitative visual observations. Since the vacuum discharge may be described as a weak plasma, it was decided to use a microwave diagnostic technique such as proposed by Brown, Biondi and co-workers [98-100] for analysis of electron density in the afterglow of a pulsed discharge. A resonant cavity containing a plasma in general will exhibit increased loss and a perturbation of the resonant frequency. Knowing both the change in cavity Q and the frequency shift, the plasma conductivity and the electron density can be calculated. To measure the cavity response a low power microwave probe signal is coupled into one of the cavity modes independently of the breakdown field.

The method particularly recommends itself in this application since the same high power cavity may be retained with slight modifications for the probe circuit. The high power field pattern is therefore virtually undisturbed and since the influence of the probing field on electron motion is negligible compared to the high power field, the microwave probe may be considered contactless. Since it is independent of the pulsed field, cavity response can be measured continuously, and by sweeping through two or more higher order cavity modes information

can be gained on the spatial distribution of electron density.

8.2 Microwave Discharges in Vacuum

8.2.1 Electron Motion in the Cavity

The free electrons existing in the cavity even at low pressures due to ambient ionizing radiation and excitation possess relatively low thermal kinetic energy in the absence of any external force. This thermal motion may be neglected in comparison to the motion impressed upon the electrons by the applied cavity fields, and since the mean free path length in vacuum enables electron interaction to be disregarded, only a single particle need be considered. The electron motion is described by the Lorentz force equation:

$$\frac{d}{dt}(m_e\bar{v}) = e(\bar{E} + \bar{v} \times \bar{B}) \qquad 8.1(a)$$

which in cylindrical co-ordinates (r, ϕ and z) may be expressed as [102]

$$\ddot{r} - r\dot{\phi}^2 = \frac{e}{m_e}(E_r + \dot{r}\phi B_z - \dot{z}B_\phi) \qquad 8.1(b)$$

$$\frac{1}{r}\frac{d}{dt}(r^2\dot{\phi}) = \frac{e}{m_e}(E_\phi + \dot{z}B_r - \dot{r}B_z) \qquad 8.1(c)$$

$$\ddot{z} = \frac{e}{m_e}(E_z + \dot{r}B_\phi - r\dot{\phi}B_r) \qquad 8.1(d)$$

For the fields given in section 4.1, the respective components are:

$$\ddot{r} - r(\dot{\phi})^2 = \frac{eE}{m_e k_c} J_1(k_c r)\left[\beta_o \sin\beta_o z \cos(\omega t+\theta) + \frac{z\omega}{c^2}\cos\beta_o z \sin(\omega t+\theta)\right] \qquad 8.2(a)$$

$$\frac{1}{r}\frac{d}{dt}(r^2\dot{\phi}) = 0 \qquad 8.2(b)$$

$$\ddot{z} = \frac{eE}{m_e}\cos\beta_o z\left[J_o(k_c r)\cos(\omega t+\theta) - \frac{\dot{r}\omega}{c^2 k_c} J_1(k_c r)\sin(\omega t+\theta)\right] \qquad 8.2(c)$$

From equation 8.2(b), $r^2\dot{\phi}$ is a constant, but by kinetic theory $\overline{(r\dot{\phi})^2} = \frac{kT}{m_e}$ initially; hence, $\dot{\phi}=0$, and electron motion may be specified completely within the r-z plane. Recalling that $\beta_o z$ is a small quantity, the approximations $\sin\beta_o z = \beta_o z$ and $\cos\beta_o z = 1$ may be made, giving

$$\ddot{r} = \frac{eE}{mk_c} J_1(k_c r)\left[\beta_o{}^2 z\cos(\omega t+\theta) + \frac{\dot{z}\omega}{c^2}\sin(\omega t+\theta)\right] \qquad 8.3$$

$$\ddot{z} = \frac{eE}{m_e}\left[J_o(k_c r)\cos(\omega t+\theta) - \frac{\dot{r}\omega}{k_c c^2} J_1(k_c r)\sin(\omega t+\theta)\right] \qquad 8.4$$

The simplest case is that of an electron on the axis influenced only by the axial electric field. Taking the initial conditions $z=0$ and $\dot{z}=0$ at the time the field $E\cos(\omega t+\theta)$ is applied at $t=0$, successive integration of the last equation yields:

$$\dot{z} = \frac{eE}{m\omega}\left(\sin(\omega t+\theta) - \sin\theta\right) \qquad 8.5$$

$$z = \frac{eE}{m\omega^2}\left(\cos\theta - \omega t\sin\theta - \cos(\omega t+\theta)\right) \qquad 8.6$$

The corresponding electron kinetic energy (in eV) is

$$U = \tfrac{1}{2}\frac{e}{m_e}\frac{E^2}{\omega^2}\left(\sin(\omega t+\theta) - \sin\theta\right)^2 \qquad 8.7$$

An electron fully constrained by the field, as in the case where the field oscillations build up over several periods (the filling time for the high Q cavity is typical), will oscillate in simple harmonic motion about a fixed point on the axis, provided the excursion is not sufficient for it to reach any cavity surface. From equation 8.5, θ must be 0 and the electron energy $\frac{1}{2} \frac{e}{m_e} \frac{E^2}{\omega^2} \sin^2 \omega t$.

It should be noted however, that electrons are continually being 'created' by ionization and field emission from the cavity walls; consequently, there may exist electrons specified by $\theta \neq 0$, with a non-zero time averaged velocity, such that in a finite time they will drift toward the end of the cavity and be lost to the field. The maximum possible energy attainable by one of these electrons is for $\theta = \frac{\pi}{2}$ and is given by $2 \frac{e E^2}{m_e \omega^2}$.

Thus, the energy possessed by an electron is periodic in time, varying from a minimum of zero to a maximum between $\frac{1}{2} \frac{e E^2}{m_e \omega^2}$ to $2 \frac{e E^2}{m_e \omega^2}$, depending upon the phase relationship to the RF field.

Where fields are sufficient to develop relativisitic velocities, the electron motion is no longer simple harmonic and the following transformations are necessary:

$$v' = v \left(1 + \left(\frac{v}{c}\right)^2\right)^{\frac{1}{2}} \qquad 8.8$$

$$U' = m_e c^2 \left(1 + \left(\frac{v}{c}\right)^2\right)^{\frac{1}{2}} - 1 \qquad 8.9$$

The peak energies and maximum excursion of electrons for various

axial E fields are given below for the case $\theta = 0$, $r = 0$

Table 8.1 Cavity Electron Energies

Ez kV/cm	P_{max} MW	U_{max} keV	U'_{max} keV	z_{max} cm	z'_{max} cm
50	.0278	6.76	6.71	.541	.536
70	.0544	13.25	13.08	.757	.745
100	.111	27.05	26.37	1.082	1.047
200	.444	108.2	98.67	2.164	1.917
300	1.0	243.45	203.9	3.246	2.571

For the off-axis electron motion, equations 8.3 and 8.4 form a nonlinear set: a simple closed solution is consequently not realizable. Near the axis an approximate solution to equation 8.3 can be obtained by the substitution of equation 8.5. It indicates that on the axis an electron is in a metastable position: any perturbation off the axis results in a positive radial force. The net result of the outward motion is the eventual loss of the electron to the cavity cylindrical wall, even if collision with the end walls does not occur. The actual electron trajectories may be determined by programming an analog computer to satisfy equations 8.3 and 8.4 for various initial conditions in θ, r and z at t=0 (the initial velocity of a free or ionized electron is sufficiently small that it may be neglected). For this purpose a TR 48 computer incorporating a nonlinear function generator was utilized. In Figure 8.1 a number of the trajectories are plotted for electrons originating at different radii for various peak axial fields.

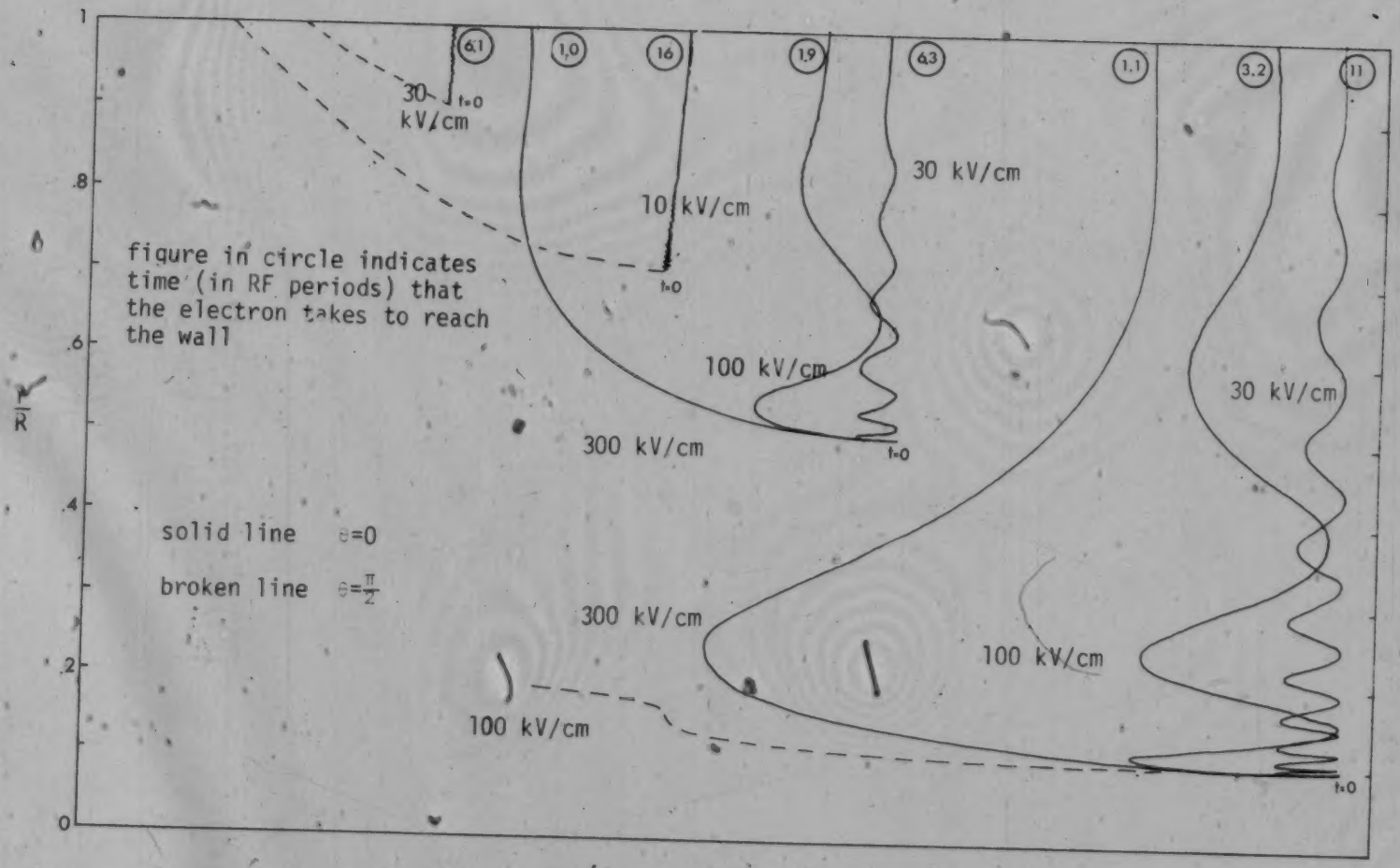

Figure 8.1 Electron Trajectories ($z_o = .75R_p$ in each case)

8.2.2 Ionization Efficiency of Energetic Electrons

The ionizing capability of a charged particle travelling through a gas is given in terms of ion pairs created per cm path length (usually called the first Townsend ionization coefficient α_i). The coefficient α_i is defined as $\frac{1}{n}\frac{dn}{dx}$ [101], where dn represents the increase in electron population as n electrons travel a distance dx. Expressed in terms of electron density, where n_o is the initial concentration, $n = n_o e^{\int \alpha_i dx}$. Electrons with kinetic energy less than the ionizing threshold of the gas molecules are incapable of exciting bound electrons sufficiently to produce ions. Peak ionization efficiency is observed for electrons with energies in the region of 100 eV and diminishes for higher energies due to the reduced interaction time as the particle velocity increases. Figure 8.2 indicates the ionization efficiency of electrons in air: the degree of ionization does depend upon the nature of the gas and is lower for inert gases but the peak remains within the range 50 to 150 eV so that the curve for air (primarily N_2 and O_2) can be taken as typical.

The energy gained by an electron in a high pressure gas is dependent upon the applied field and the mean free path between collisions. Avalanche ionization results when the average electron energy reaches the ionization threshold such that the rate of ionization exceeds the rate of electron loss by mechanisms such as recombination or diffusion to the walls. Since the loss of energy by electron collisions reduces the effective field there is little probability of high energy electrons existing.

The contrary situation exists in the evaculated cavity discussed in the preceding section where relativistic electrons were seen to be possible. Since ionization efficiency is greatest at low energies the ionization rate depends upon the time that the electron spends in the low energy region.

The rate of ionization (ion pairs per torr-RF cycle) is determined by integrating $\int \alpha_i dx = \int \alpha_i(\omega t)v(\omega t)d\omega t$. On the axis this may be readily calculated as having a maximum value of .47 at a peak field of 30 kV/cm, dropping to .25 for an axial field of 300 kV/cm. The case of $\theta = 0$ need only be considered since most other electrons are lost to the end walls in relatively few RF cycles.

Off the axis, calculation of the ionization rate is rendered difficult by the complex nature of the electron motion. For small r, the ionization rate is high for fields in excess of 30 kV/cm, but as radial velocity increases, the ionization capability of the electrons is diminished and the finite free lifetime of the electrons (about one RF period at 300 kV/cm) reduces the net ionizing effect of the off-axis electrons. The statistical nature of ionization phenomena further complicates the evaluation of ionization probability. It is therefore advisable to develop more simple criteria relevant to the particular problem.

8.2.3 Ionization Initiated Discharges

The differing forms of discharge noted in section 7.3, may be

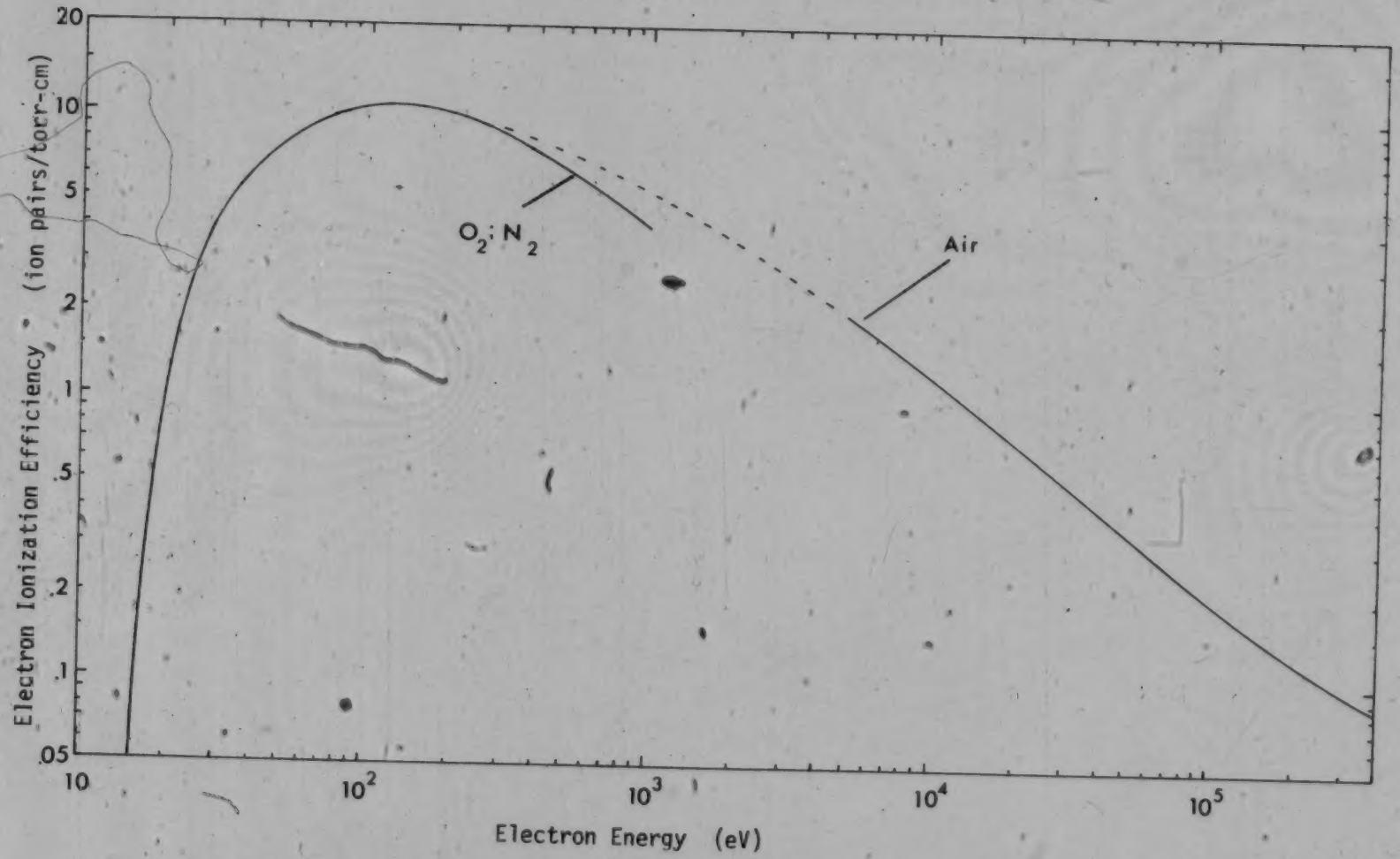

Figure 8.2 Ionization Efficiency of Electrons (Adapted from Lewin [103])

in part explained by referring to the foregoing section.

A clean vacuum surface is an impossibility since the surface is generally contaminated prior to being placed in the vacuum and even under ideal conditions gas molecules condensed from the vacuum form layers on the surface by the process of adsorption. If the surface is subsequently heated, the adsorbed gas is released and the vacuum degraded by what is termed outgassing. Molecules may also be extracted by high local electric fields or be knocked out by accelerated particles on impact with the surface. Electron density is dependent upon both the ionizing efficiency of free electrons and the gas pressure, thus, assuming the existence of the former, for a sufficiently high outgassing rate, an avalanche vacuum discharge will result.

For low fields, ionization probability is a maximum at the center of the cavity, diminishing toward the cylindrical wall. Conditioning discharges are then dependent upon the ceramic surface and the cavity end wall. If multipactor is possible, the electron density is increased significantly and interaction with outgassing molecules enables a more stable discharge, provided the electrons possess an adequate energy distribution.

At high power further complications may occur. The surface profile of the ground disc in Figure 2.1(a) readily indicates that depressions with dimensions of the order of tens of microns could be present on the unpolished circumference of the titania disc. If air, trapped within such a depression, were released due to expansion of the copper ring, there would be created at the edge a gas bubble expanding at a rate determined by the thermal velocity of the molecules (typically

$\dot{r} = 4 \times 10^4$ cm/sec). The necessary requirement for an avalanche discharge is that each electron ionized within the volume of the bubble must be capable of producing a minimum of one secondary electron. Using a characteristic dimension x, both for the interaction path of the ionizing electron and as the bubble radius (giving a volume $\sim x^3$), this requirement reduces in its simplest form to:

$$\alpha_i p x = \alpha_i \frac{P_o V_o}{x^3} \quad x > 1$$

Assuming a void volume $V_o = 10^{-7}$ cc with an initial pressure $P_o = 760$ torr, and taking maximum α_i, $x \sim .3$ mm. It is therefore evident that only electron motion near the copper wall adjacent to the ceramic need be considered.

Figures 8.3 and 8.4 show electron trajectories and the corresponding velocities of electrons originating in this region for peak axial fields of 300 and 100 kV/cm respectively. At 300 kV/cm, for $r_o > .995R$, the electrons do not posses sufficient average energy to maintain ionization; however $r_o = .99R$ is more than sufficient. At 100 kV/cm the corresponding radii are .98R and .97R. It may be noted that at 100 kV/cm the electron is generally moving towards a region of lower field, thus after a finite number of collisions, electrons will not possess sufficient energy to continue the ionization process. At the higher field strength, however, there exists a substantial possibility of electrons travelling into regions of higher field, yet the electron trajectories are compact, being .3 to 1mm in comparison to the 1 to 3mm lengths evident at 100 kV/cm. There then exists for each field strength, some

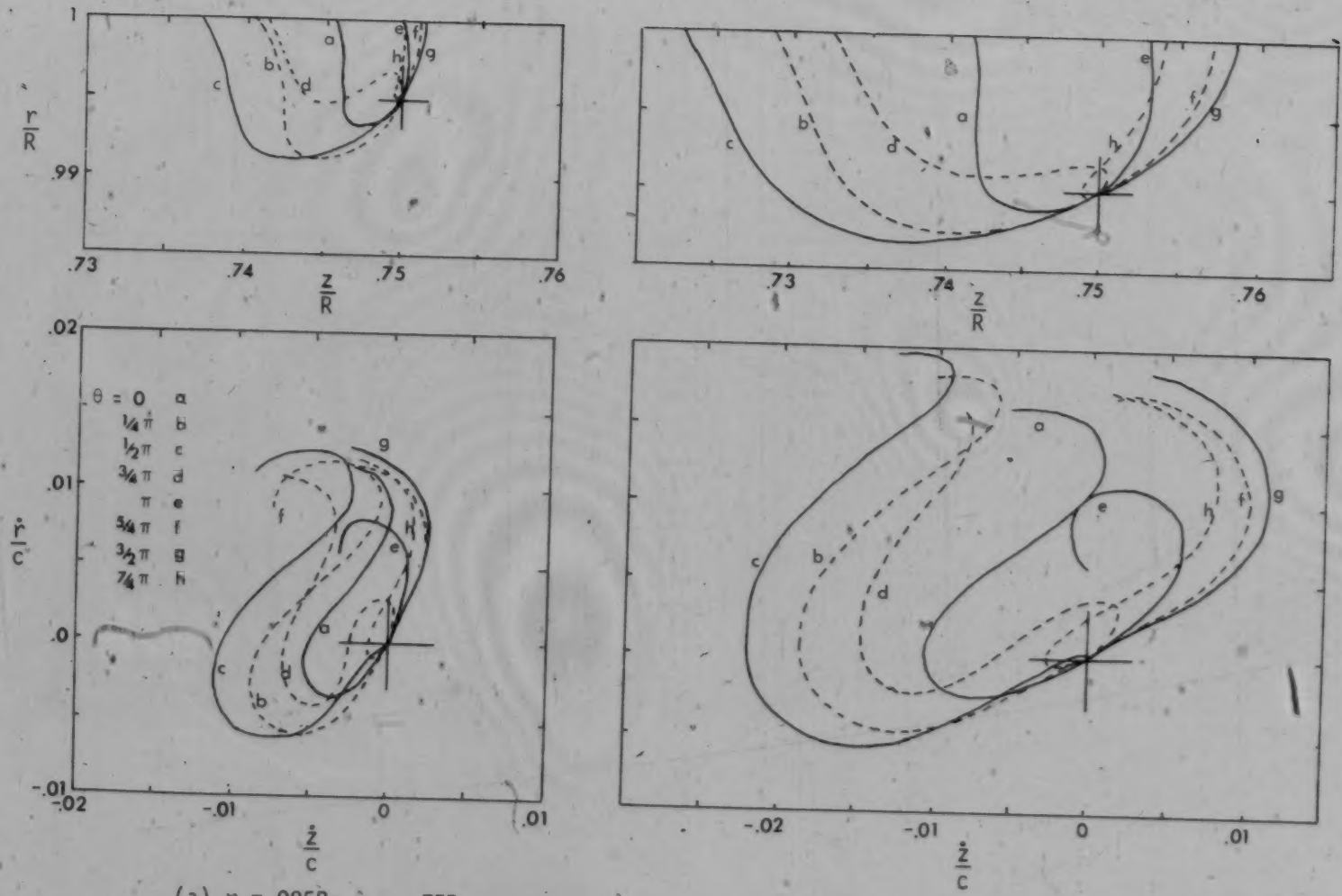

(a) $r_o = .995R$: $z_o = .75R$

(b) $r_o = .99R$: $z_o = .75R$

Figure 8.3 Electron Trajectories (top) and Velocities (bottom) at 300 kV/cm

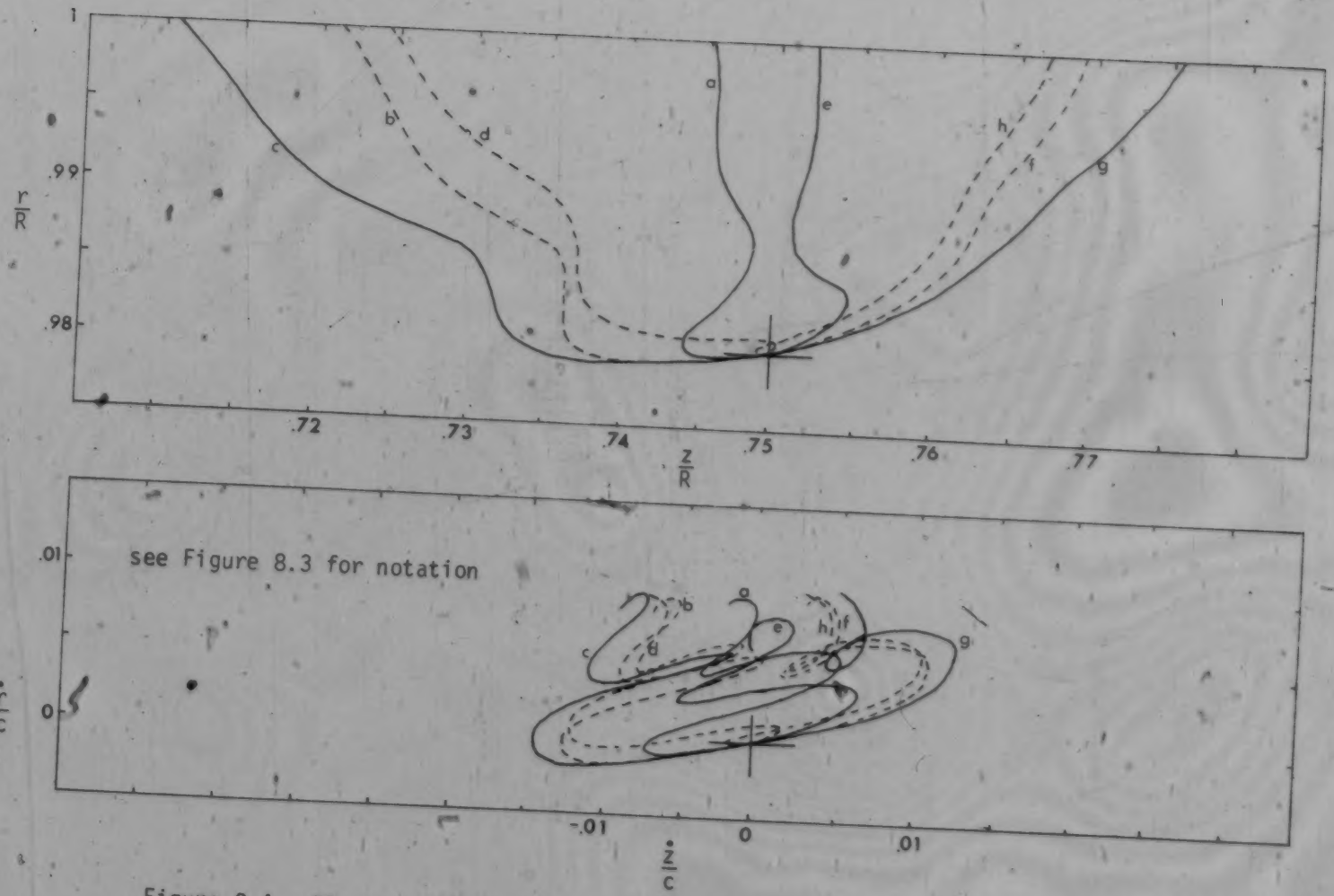

Figure 8.4 Electron Trajectories (top) and Velocities (bottom) at 100 kV/cm
(a) $r_o = .98R$: $z_o = .75R$

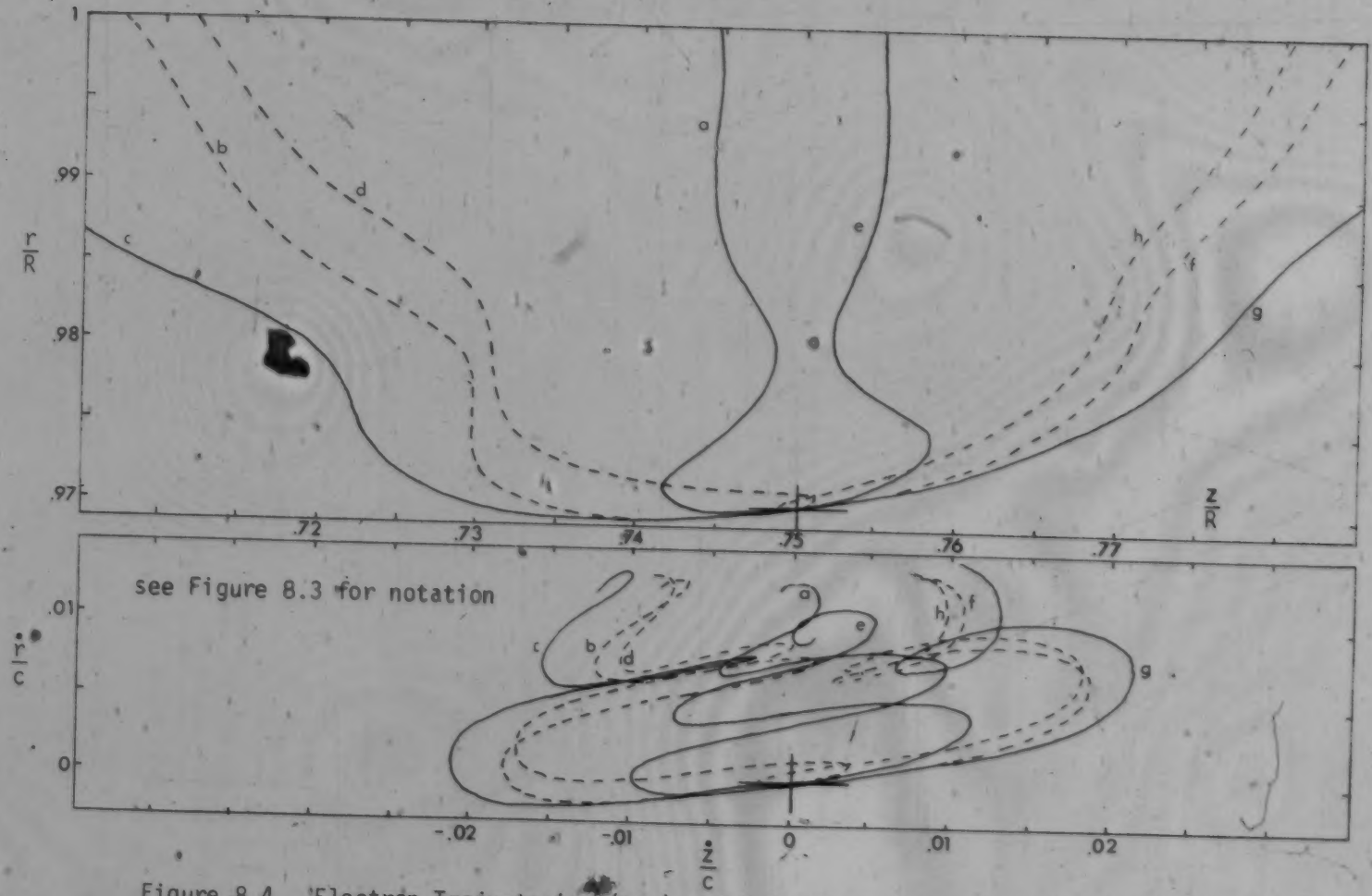

Figure 8.4 Electron Trajectories (top) and Velocities (bottom) at 100 kV/cm
(b) r_o = .97R: z_o = .75R

radius, r_{imax}, where the ionization probability is a maximum. For 300 kV/cm it is reasonable to take $r_{imax} \sim .99R$ and at 100 kV/cm $r_{imax} \sim .975R$. The condition necessary for avalanche is that r_{imax} coincides with an expanding gas bubble of sufficiently high pressure that $\int \alpha_i p dx > 1$. Assuming a free electron lifetime of one RF period, at the end of a single pulse (10^4 cycles) the final electron density would be of the order $n = n_o(\int \alpha_i p dx)^{10^4}$ A substantial number of electrons would be lost by diffusion, but for a sequence of gas bubbles at rapid intervals, avalanche breakdown becomes feasible.

Thus, the discharge is local and dissipates most of its energy over a limited area of the disc surface. Local reduction of the titania, followed by increased RF power dissipation ends eventually in breakdown. This is confirmed by the small treeing patterns observed about 2 mm from the edge of the uncoated discs. At lower powers the gas bubble may expand further before the corresponding r_{imax} is reached, thus not only is the effective internal pressure reduced, but the discharge energy is dissipated over a wider area.

The microwave probe was introduced in part to gather more information on the microwave discharges observed.

8.3 The Microwave Probe

8.3.1 Perturbation of EM Waves in a Plasma

Maxwell's equations for an EM wave are:

$$\nabla \times E = - \frac{dB}{dt} \qquad 8.10(a)$$

$$\nabla \times H = J + \frac{dD}{dt} \qquad 8.10(b)$$

$$\nabla \cdot D = \rho \qquad 8.10(c)$$

$$\nabla \cdot B = 0 \qquad 8.10(d)$$

Since $J = \sigma E$ and $D = \varepsilon E$, for a field $Ee^{j\omega t}$, equation 8.10(b) may be written:

$$\nabla \times H = (\sigma + j\omega\varepsilon) E \qquad 8.11$$

or by introducing the concept of a complex permittivity

$$\varepsilon_p = \varepsilon' - j\,\varepsilon'' = \varepsilon' - j\,\frac{\sigma}{\omega} \qquad 8.12$$

$$\nabla \times H = j\omega\,\varepsilon_p\, E \qquad 8.13$$

and the corresponding wave equation would be

$$\nabla^2 E = \mu\,\varepsilon' \left(1 - j\,\frac{\sigma}{\omega\varepsilon'}\right) \frac{d^2E}{dt^2} \qquad 8.14$$

For a low density plasma, where the electron density N_e is small compared to the gas density N_o, the equation of motion for an electron is

$$m\left(\frac{dv}{dt} + \nu_m v\right) = eE \qquad 8.15$$

where ν_m represents the collision frequency between electrons and molecules (electron-electron collisions are ignored by the definition of a low density plasma).

Assuming the electron follows the electric field, $\frac{dv}{dt} = j\omega v$ and equation 8.15 becomes:

$$v = \frac{eE}{m(\nu_m + j\omega)} \qquad 8.16$$

The convection current density is given by $J = N_e ev$ or

$$J = \frac{N_e\, e^2 E(\nu_m - j\omega)}{m\,(\nu_m^2 + \omega^2)} \qquad 8.17$$

and the plasma conductivity is:

$$\sigma = \frac{J}{E} = \frac{N_e\, e^2\, (\nu_m - j\omega)}{m\,(\nu_m^2 + \omega^2)} \qquad 8.18$$

In low vacuum where the collision frequency is high, the plasma conductivity has an appreciable real component; however, for the case in question, the pressure is 10^{-6} torr, collision effects can be ignored ($\nu_m << \omega$) and the conductivity taken as imaginary.

The effective permittivity of the plasma is then

$$\varepsilon_p = \varepsilon' - \frac{N_e\, e^2}{m\,\omega^2} \qquad 8.19$$

more usually written as

$$\varepsilon_p = \varepsilon' \left(1 - \frac{\omega_p^2}{\omega^2}\right) \qquad 8.20$$

where $\omega_p = \left(\frac{N_e e^2}{m_e \varepsilon'}\right)^{1/2}$ is defined as the plasma frequency.

Hence the presence of a low pressure, low density plasma reduces the permittivity and increases the phase velocity of an EM wave travelling through the plasma; or in the case of a resonant cavity would increase the resonant frequency.

The microwave probe method is typically used with low temperature plasmas where electrons are assumed to have low average kinetic energies. In applying the technique to high field vacuum discharge measurements, a number of points should be noted.

Electrons are influenced by two fields, the pulsed high power and the CW probing field. The latter can be considered to only slightly perturb the motion of electrons following the main field. Where relativistic energies exist, the effective mass of the electron must be substituted in the above equations, thus coupling the two fields. It is desirable that the two fields be in quadrature with each other and not be harmonically related in the frequency domain to minimize coupling effects. Fortunately in the present application the discharges are characterized by relatively low peak fields; therefore no relativistic correction need be applied.

8.3.2 Selection of Probing Modes

The cavity is capable of supporting numerous modes in the 2 to 10 GHz microwave band, but for practical reasons TE_{01n} modes were selected for this application. Not only are these fields in space quadrature with the TM_{011} high power mode, but coupling into the cavity can be achieved by means of a small slot machined into the end of the cavity. The narrow, radially oriented slot, being parallel to the surface current flow on the inside wall of the cavity did not distort the main field pattern.

On the basis of a .50 cm thick disc in the cavity of section 4.1.3, the calculated resonances were:

TE_{011}	1 GHz
TE_{012}	3.31 GHz
TE_{013}	6.01 GHz
TE_{014}	6.73 GHz
TE_{015}	6.97 GHz

These modes were excited through the slot by electric coupling of the TE_{01} mode propagating in a suitably oriented section of rectangular waveguide. J-band waveguide with a cut-off frequency of 4.3 GHz was chosen in order to attenuate any high power leakage from the cavity to the probe circuit. Attenuation of the 2.87 GHz signal would be given by [105]

$$\alpha\,(\text{dB}) = 8.86\,\frac{2\pi}{\lambda_c}\left(1 - \left(\frac{\lambda_c}{\lambda}\right)^2\right)^{1/2} \qquad 8.21$$

$$= 5.83\ \text{dB/cm}$$

The probe signal was to be about 100 mW, thus to reduce any 1 MW leakage to at least 1 mW, the section of waveguide would have to be 16 cm.

The waveguide excluded the use of both the TE_{011} and TE_{012} modes as they are below cut-off; whereas limitations on the power supplies available meant rejection of the TE_{016} and higher modes. Of the remaining three, the TE_{013} mode was too low to be useable so that measurements were restricted to the TE_{014} and TE_{015} modes. Field patterns were confirmed by perturbation using a thin dielectric rod fitted with a metallic bead.

8.3.3 Cavity Modifications for Probe

To install the J-band adapter for the probe signal, the cavity was modified by replacing the cavity top section by a cylindrical section with clamping grooves at both ends. A 6" length of J-band waveguide ($1\frac{1}{2}$" x $\frac{3}{4}$") was soldered to a grooved backing plate such that the axis of the guide was offset from the cavity axis by 1.925 cm in order to excite TE_{01n} modes. A .076 cm thick copper disc with a coupling slot .15 cm x 1.4 cm, again offset 1.925 cm, was placed between the backing plate and the cavity. By clamping the plate to the cavity in the normal manner, the disc became the end wall of the cavity.

A standard J-band flange at the other end of the waveguide mounted a coaxial-waveguide adapter and the waveguide itself was provided with vacuum pumping holes.

Figure 8.5 is an exploded view of the cavity with probe attachment. Also shown in the background is the unmodified cavity with micrometer attached for perturbation measurements. Figure 8.6 shows the modified cavity assembled in the cavity mount prior to being placed in the vacuum envelope.

There was no noticeable change in cavity Q or resonant frequency despite the increased complexity of the system.

8.3.4 The Microwave Probe Circuit

To obtain a sufficiently high signal level, a mechanically tuneable Varian VA244A reflex klystron with a 500 mW output was connected to a J-band waveguide run consisting of an isolator, wavemeter and directional couplers. The waveguide was coupled to the cavity adapter by coaxial cable and vacuum tight feedthroughs. Figure 8.7 outlines the probe circuit.

The TE mode resonances were displayed with the high power pulse waveforms on the 556 Tektronics oscilloscope. One timebase was used for the pulse signals: the horizontal sweep sawtooth of the second timebase was applied to the klystron reflector to sweep the klystron through the probe resonance. By delaying one timebase with respect to the other, the probe resonance could be placed at any time relationship with the high power pulse. The need for a high sweep speed (approximately

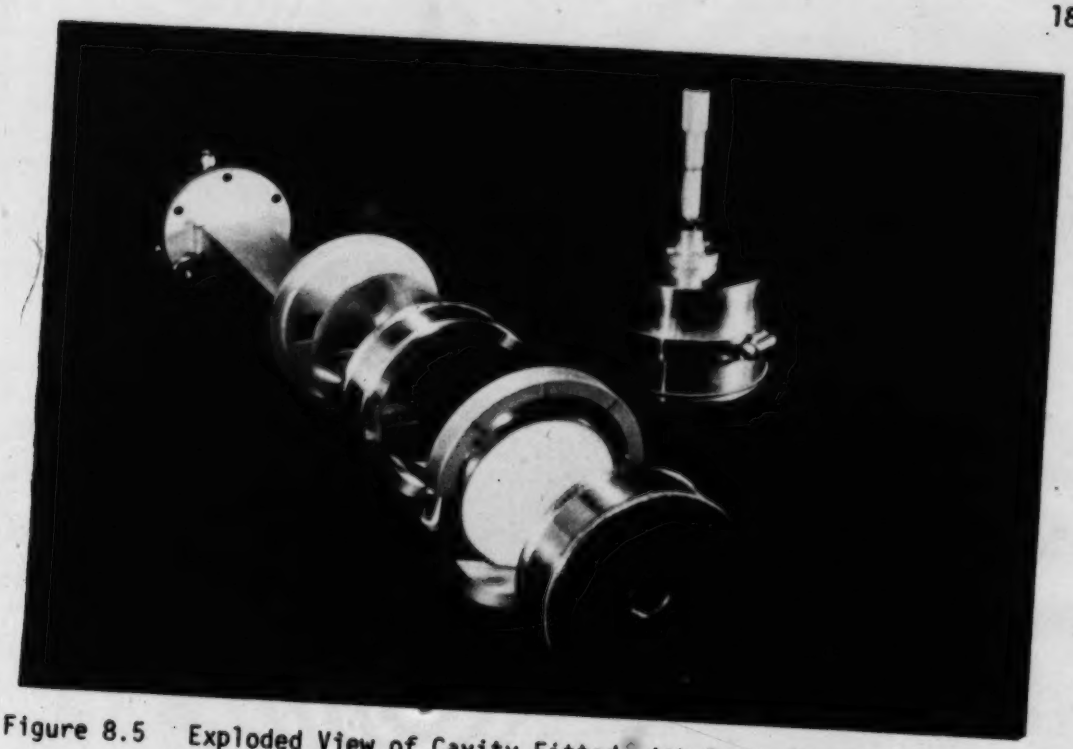

Figure 8.5 Exploded View of Cavity Fitted with Probe Adapter

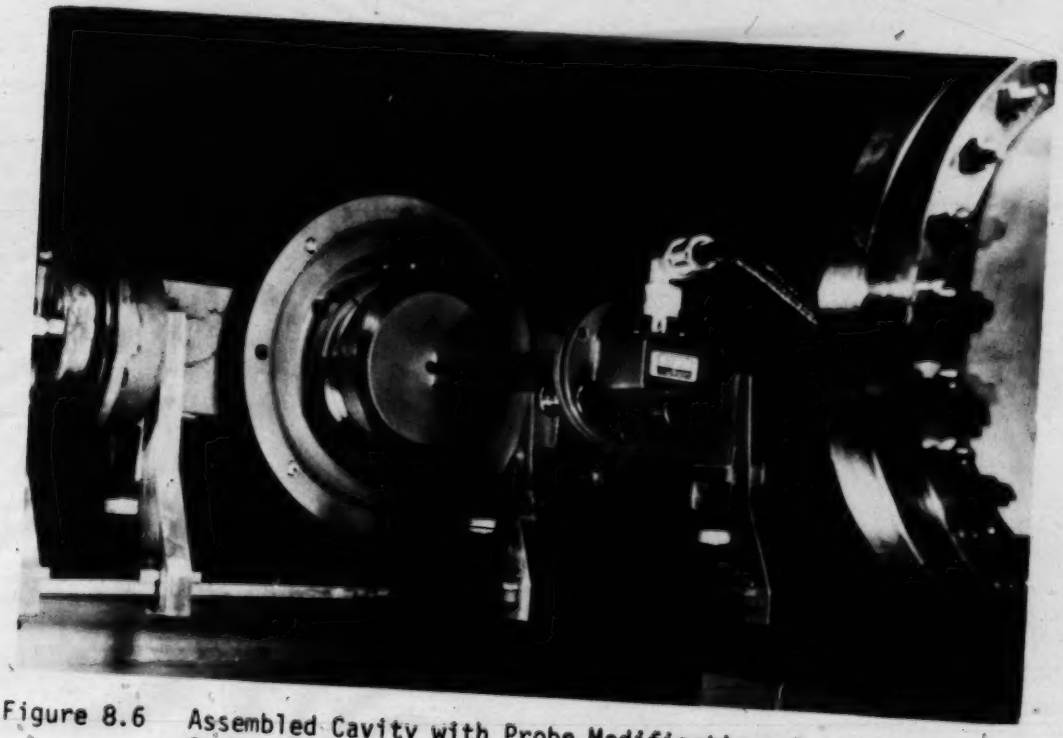

Figure 8.6 Assembled Cavity with Probe Modification, Installed in Cavity Mount Prior to Insertion into the Vacuum Envelope

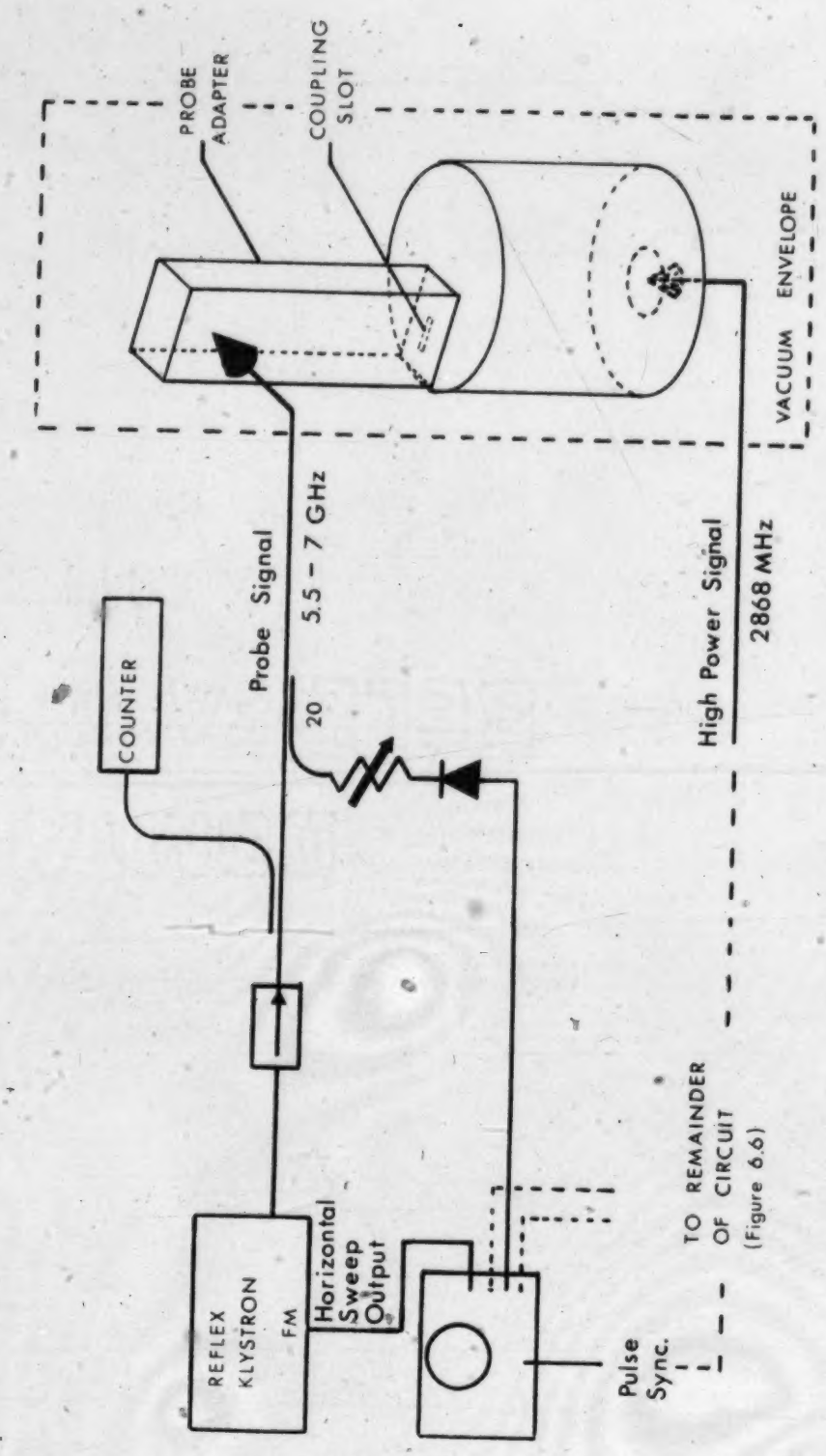

Figure 8.7 Microwave Probe Circuit

5 MHz/μsec) did result in a slightly degraded resonance due to response limitations of the klystron supply and the crystal detector.

The two modes could be obtained from the same klystron although this involved mechanical tuning. An attempt to display both modes by using two klystrons isolated with magic Tees was partially successful, but increased mismatch in the waveguide made observation of the crystal signals more difficult.

From Figure 7.1 it is seen that leakage of the high power was negligible compared to the probe signal.

8.4 Microwave Probe Measurements

The microwave probe was first used in a rudimentary form during the second run on disc #5. Improvements were made in the system and useful results were obtained with discs #9, 8, 11, 7 and 6.

In conjunction with the other breakdown parameters; power, pressure, and radiation output; the TE_{014} mode resonance was continually monitored except for occasional observations of the TE_{015} mode for comparison. The probe resonance is displayed as the top trace in each of the oscilloscope photographs in Figure 7.1. The first frame is a double exposure of unperturbed and mismatched signals: the displacement of the probe resonance can be readily observed. The degree of perturbation was measured using the oscilloscope sweep magnifier, the minimum shift resolution as determined by trace readability and jitter being equivalent to 100 kHz.

The results supported the observations of the previous chapter.

Three different types of perturbation, and hence discharge were noted. In each case conditioning occurred; for the interval of the discharge the probe resonance shifted about 600 kHz. Whereas conditioning discharges diminished in time for the Ti coated discs, those discs lacking the coating maintained the more stable multipactor type discharge over the limited power range referred to in section 7.3. The resonance shift was about the same, but lasted for sufficient time to evaluate the electron density through the period of the pulse. In Figure 8:8 the maximum perturbation and consequently electron density occurs at 3 μsec when the field is at its maximum and dies within 3 μsec after the pulse. Both modes gave similar results.

Over 100 kW occasional discharges were observed, the frequency perturbation varying between 500 and 1000 kHz.

At peak power levels over 700 kW, the probe reacted differently during the discharges. For the short interval that the discharge lasted, the probe resonance completely dissappeared. Tuning the klystron to frequencies up to 20 MHz higher did not aid in finding the displaced resonance. In one case where the discharge lasted sufficiently long, the resonance reappeared only when the delay between the input pulse and the probe sweep was 35 μsec. This would indicate that the duration of the discharge was 6 times that observed for low power discharges; however, this could not be confirmed since breakdown occurred in the other discs before measurements could be repeated.

The cavity was generally dismantled following the first high power discharge. Prior to the installation of the probe, visual observation was the best means of determining the existence of a cavity

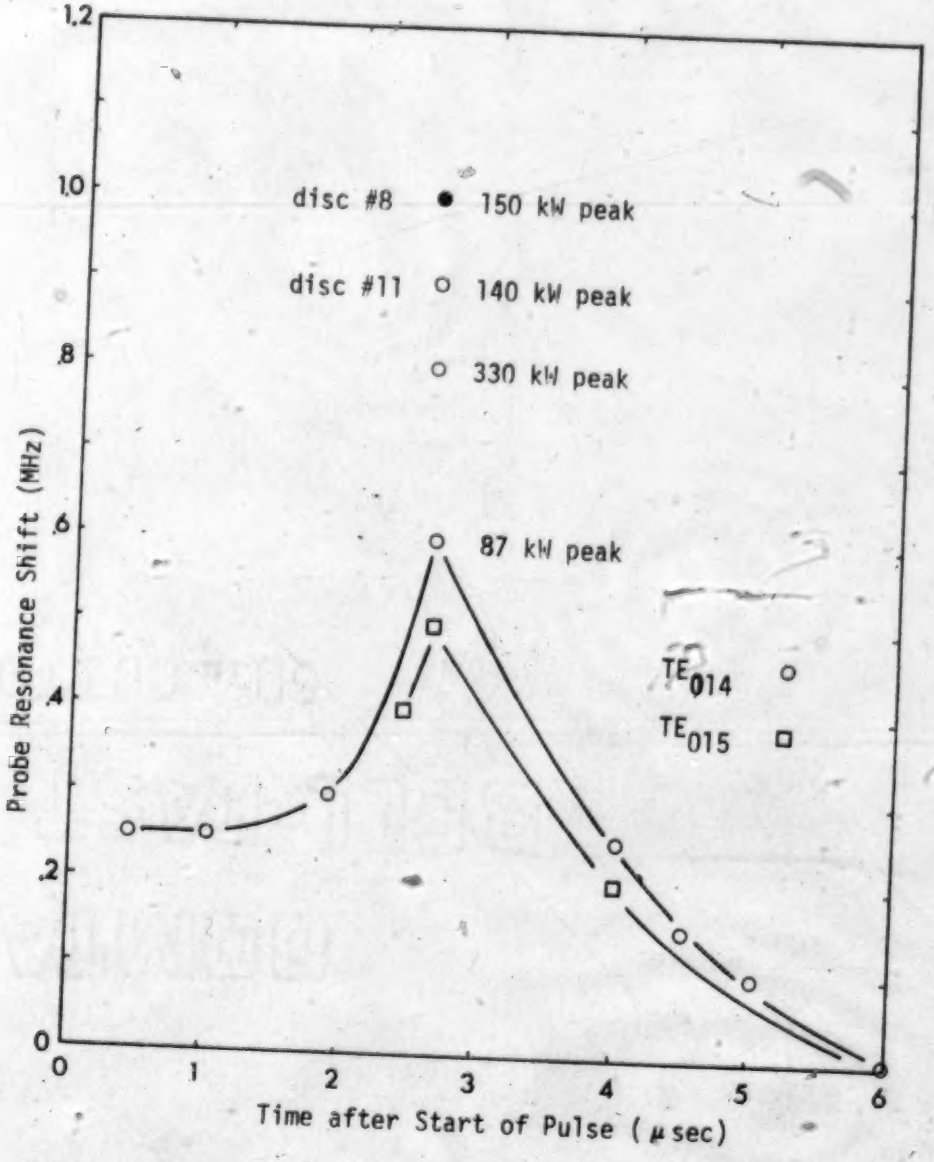

Figure 8.8 Perturbation of Microwave Probe at High Power

discharge, since a mismatch in the high power circuit could be due also to breakdown in the waveguide. By continually monitoring the probe response a cavity discharge could be readily noted.

8.5 Interpretation of the Probe Results

8.5.1 Frequency Dependence of TE_{01n} Modes

Equation 8.19 is valid for only small perturbations in ε, i.e., $\omega_p << \omega$. It may be rewritten as:

$$\varepsilon_p = \varepsilon + d\varepsilon \qquad 8.22$$

Therefore, $$\frac{d\varepsilon}{\varepsilon} = -\left(\frac{\omega_p}{\omega}\right)^2 = -\frac{N_e e^2}{m_e \varepsilon_o \omega^2} \qquad 8.23$$

This quantity and hence N_e can be related to the frequency perturbation in one of the TE modes.

For the TE modes the fields in the vacuum region are [106]

$$H_{zo} = B\, J_o(k_c r) \sin \beta_o z \qquad 8.24(a)$$

$$H_{ro} = -\frac{\beta_o}{k_c} B\, J_1(k_c r) \cos \beta_o z \qquad 8.24(b)$$

$$E_{\phi o} = -\frac{j\omega\mu}{k_c} B\, J_1(k_c r) \sin \beta_o z \qquad 8.24(c)$$

If n is odd the fields are symmetric about the plane $\eta = 0$, and the fields in dielectric are:

$$H_{z2} = B_2 J_1(k_c r) \cos\beta_2 n \qquad 8.25(a)$$

$$H_{r2} = -\frac{\beta_2}{k_c} B_2 J_1(k_c r) \sin\beta_2 n \qquad 8.25(b)$$

$$E_{\phi 2} = -\frac{j\omega\mu}{k_c} B_2 J_1(k_c r) \cos\beta_2 n \qquad 8.25(c)$$

and for n even (H_z and E_ϕ antisymmetric), the dielectric fields are:

$$H_{z2} = B_2 J_1(k_c r) \sin\beta_2 n \qquad 8.26(a)$$

$$H_{r2} = +\frac{\beta_2}{k_c} B_2 J_1(k_c r) \cos\beta_2 n \qquad 8.26(b)$$

$$E_{\phi 2} = -\frac{j\omega\mu}{k_c} B_2 J_1(k_c r) \sin\beta_2 n \qquad 8.26(c)$$

Following the same procedure as in section 4.1.2, and matching fields at the dielectric-vacuum interface, the conditional equations for matching are respectively:

$$\tan\beta_o p \ \tan\beta_2 q = \frac{\beta_o}{\beta_2} \quad \text{(for n odd)} \qquad 8.27$$

$$\tan\beta_o p \ \cot\beta_2 q = -\frac{\beta_o}{\beta_2} \quad \text{(for n even)} \qquad 8.28$$

Taking partial differentials (after the method of section 5.4) with respect to λ and ε, the frequency perturbation Δf and $d\varepsilon$ are related by:

$$\frac{d\varepsilon}{\varepsilon} = \frac{2\lambda_c^2}{\lambda^2}\left[1 + \frac{\varepsilon_r q\beta_o \sec^2\beta_2 q \tan\beta_o p + \beta_o^2 \varepsilon_r \beta_2^{-2}}{\beta_2 p \sec^2\beta_o p \tan\beta_2 q - 1}\right]\frac{df}{f} \qquad 8.29$$

$$\frac{d\varepsilon}{\varepsilon} = \frac{2\lambda_c^2}{\lambda^2}\left[1 + \frac{\varepsilon_r\beta_2 + \beta_o^2 q\sec^2\beta_2 q - \beta_o^2\varepsilon_r\beta_2^{-2}\tan\beta_2 q}{\beta_2 p\sec^2\beta_o p + \tan\beta_2 q}\right]\frac{df}{f} \qquad 8.30$$

For n odd and n even respectively. The corresponding relation for the TM_{011} mode is:

$$\frac{d\varepsilon}{\varepsilon} = \frac{2\lambda_c^2}{\lambda^2}\left[1 + \frac{\beta_o q\varepsilon_r[\beta_2^2\beta_o^{-2} + \tan\beta_o p] - \tan\beta_o p}{\beta_2^2\beta_o^{-2}[\beta_o p\sec^2\beta_o p + \tan\beta_o p]}\right]\frac{df}{f} \qquad 8.31$$

The above three equations have the form $\frac{d\varepsilon}{\varepsilon} = K\frac{df}{f}$ where K is a function of the mode and is calculated in Table 8.2 for two discs (#6 and #8).

8.5.2 Comparison of the TE_{014} and TE_{015} Modes

The quantity N_e in equation 8.23 is a space averaged density more correctly written as $\overline{N_e}$. The relationship between $\overline{N_e}$ and the true spatial distribution N_e being [100]

$$\overline{N_e} = \frac{\int N_e E^2\, dV}{\int E^2\, dV} \qquad 8.32$$

N_e is unknown, but one model might be that of an electron cloud of thickness d at the surface of the disc. This would be representative of the multipactor induced discharge at the ceramic surface. In its simplest form the distribution is

$$N_e = N_e(r) \quad p - z < d$$
$$0 \quad p - z > d \qquad 8.33$$

Table 8.2 Parameters for TM_{011}, TE_{013}, TE_{014} AND TE_{015} Modes

K is defined in $\frac{d\varepsilon}{\varepsilon} = K\frac{df}{f}$

Disc	Mode	f_o(GHz)	p(m)	ε(m)	$\beta_o(m^{-1})$	$\beta_2(m^{-1})$	K
#6	TM_{011}	2.868	.03115	.00272	4.39	582.8	2.01
#6	TE_{013}	5.61	.03115	.00272	68.6	1142	18.6
#6	TE_{014}	6.58	.03115	.00272	99.5	1341	4.45
#6	TE_{015}	6.75	.03115	.00272	104.3	1375.5	4.96
#8	TM_{011}	2.869	.0312	.002695	4.39	582.8	2.01
#8	TE_{013}	5.65	.0312	.002695	70.0	1150	19.9
#8	TE_{014}	6.58	.0312	.002695	99.5	1341	4.37
#8	TE_{015}	6.76	.0312	.002695	104.6	1378	5.24

$f_{c_{TM_{011}}}$ = 2.8616 GHz, $f_{c_{TE_{01n}}}$ = 4.558 GHz

The measured average density for the TE_{014} mode would be

$$\overline{N_e} = \frac{\int_{p-d}^{p}\int_{0}^{R} r N_e(r)\, J_1^2(k_c r)\, \sin^2\beta_{014} z\, 2\pi dz dr}{\int_{0}^{p}\int_{0}^{R} r J_1^2(k_c r)\, \sin^2\beta_{014} z\, 2\pi dz dr} \qquad 8.34$$

with a similar relationship for the TE_{015} mode. Taking the ratio $\overline{N_e}_{TE_{014}} \Big/ \overline{N_e}_{TE_{015}}$ and simplifying

$$\frac{\overline{N_e}_{TE_{014}}}{\overline{N_e}_{TE_{015}}} = \frac{\int_{p-d}^{p} \sin^2\beta_{014}\, z\, dz \int_{0}^{p} \sin^2\beta_{015}\, z\, dz}{\int_{p-d}^{p} \sin^2\beta_{015}\, z\, dz \int_{0}^{p} \sin^2\beta_{014}\, z\, dz} \qquad 8.35$$

Evaluating

$$\frac{\overline{N_e}_{TE_{014}}}{\overline{N_e}_{TE_{015}}} = \frac{[2\beta_{014}d + \sin 2\beta_{014}(p-d) - \sin 2\beta_{014}p][2\beta_{015}p - \sin^2\beta_{015}p]}{[2\beta_{015}d + \sin 2\beta_{015}(p-d) - \sin 2\beta_{015}p][2\beta_{014}p - \sin^2\beta_{014}p]} \qquad 8.36$$

Substituting values from Table 8.2, the variation of this ratio as d is increased to its maximum, p, is found to be that of Figure 8.9 .

Rewriting equation 8.23:

$$\overline{N_e} = \frac{\omega^2 m_e \varepsilon_o d\varepsilon}{e^2\, \varepsilon}$$

or, since $\frac{d\varepsilon}{\varepsilon} = K \frac{df}{f}$,

$$\overline{N_e} = \frac{\omega^2 m_e \varepsilon_o K df}{e^2\, f} = \frac{(2\pi)^2 \varepsilon_o m_e\, K f df}{e^2} \qquad 8.37$$

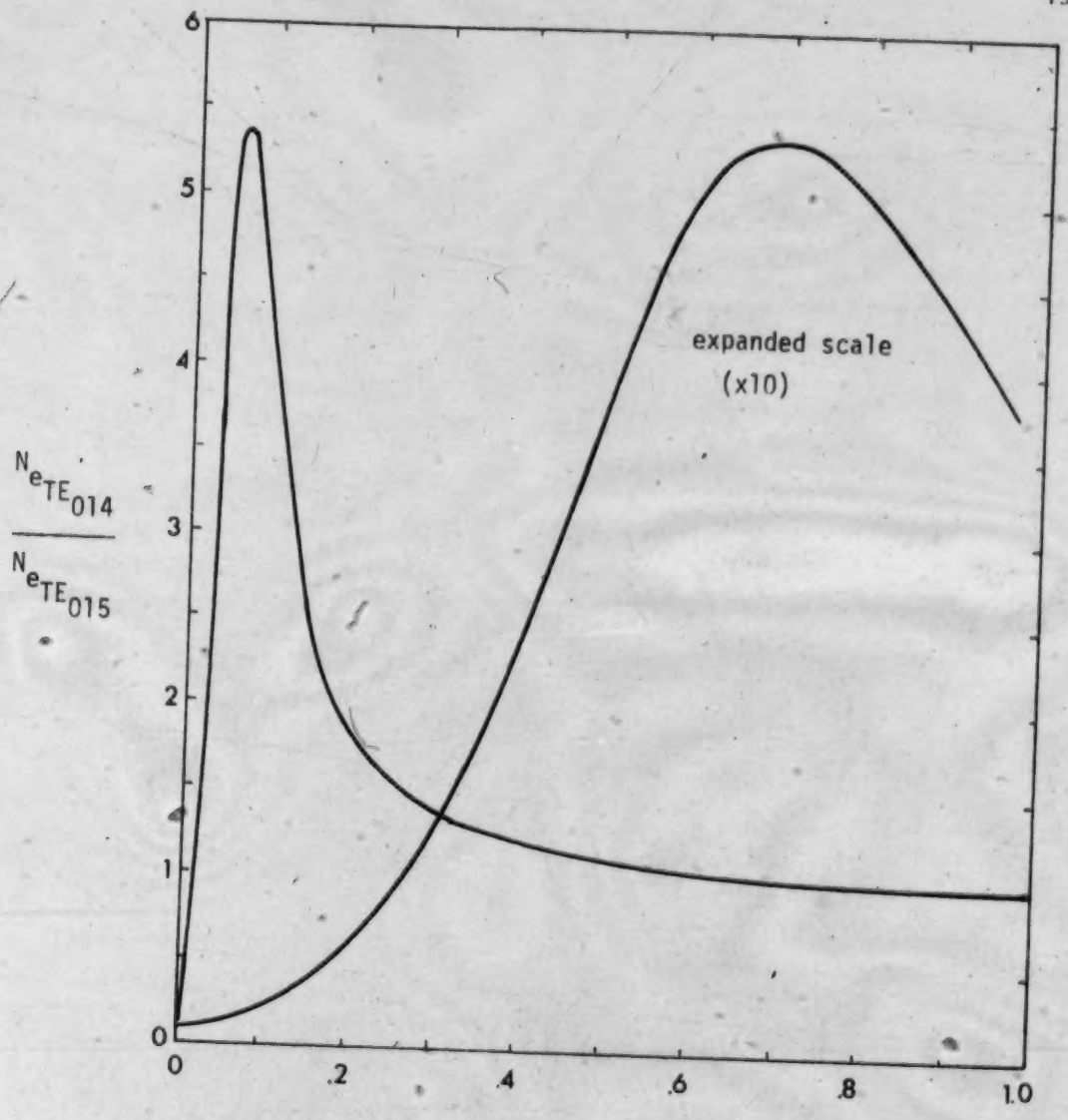

Figure 8.9 Comparison of TE_{014} and TE_{015} modes

Taking the ratio of the two modes and substituting the results from Figure 8.8:

$$\frac{\overline{N_e}_{TE_{014}}}{\overline{N_e}_{TE_{015}}} = \frac{(Kfdf)_{TE_{014}}}{(Kfdf)_{TE_{015}}} = .97 \pm .22 \qquad 8.38$$

Referring to Figure 8.9, equation 8.38 is satisfied for

$$.7 < d < .9 \text{ mm}$$

$$d > 1.25 \text{ cm}$$

From Table 8.1, the excursion of an electron is the order of 1 cm; hence, the latter case is physically more probable.

In the above analysis comparison has been made on the basis of one distribution model. By using a number of different modes and hypothesising several models the distribution of the discharge can be accurately estimated. The usefulness of the probe technique in discharge diagnostics is readily seen.

8.5.3 Comparison of TE_{014} and TM_{011} Modes

Extending the approach of the previous section, the model of the electron cloud must be amended to include radial dependence. It was seen in section 8.2 that the highest ionization probability is in the region of the circular wall (at moderate and high powers). Therefore, it

is feasible to propose a donut shaped cloud with the distribution -

$$\left.\begin{array}{ll} N_e = N_e & p - z > d;\ R-r > g \\ 0 & p - z < d;\ R-r < g \end{array}\right\} \qquad 8.39$$

where g is the radial thickness of the cloud measured from the copper wall.

For the TM_{011} mode equation 8.32 becomes

$$\overline{N_e} = \frac{\int N_e (E_z^2 + E_r^2)\, 2\pi r dr dz}{\int (E_z^2 + E_r^2)\, 2\pi r dr dz} \qquad 8.40$$

where E_r and E_z are defined in equation 4.1. The contribution of the radial term may conveniently be ignored by specifying a maximum limit upon r = .97 R. (See Section 8.2: the ionization probability rapidly approaches zero near the cavity wall at r=R.) At this radius, the ratio

$$\frac{E_r}{E_z} = \frac{\beta_o}{k_c} \frac{J_1(k_c r)}{J_o(k_c r)} \frac{\sin\beta_o z}{\cos\beta_o z}$$

has a maximum value at the ceramic surface of .141 and the error in the numerator of equation 8.40 would at most be 5%. (this error decreases with increasing g and d).

By thus simplifying equation 8.40, the numerator and denominator can be separated into integrals over r and z. Dividing into equation 8.34, we get the ratio $\overline{N_{e_{TE_{014}}}} \Big/ \overline{N_{e_{TM_{011}}}}$.

This may be written

$$\frac{\overline{N_{e_{TE_{014}}}}}{\overline{N_{e_{TM_{011}}}}} = \left[\frac{\overline{N_{e_{TE_{014}}}}}{\overline{N_{e_{TM_{011}}}}}\right]_r \left[\frac{\overline{N_{e_{TE_{014}}}}}{\overline{N_{e_{TM_{011}}}}}\right]_z \qquad 8.41$$

where

$$\left[\frac{\overline{N_{e_{TE_{014}}}}}{\overline{N_{e_{TM_{011}}}}}\right]_r = \frac{\int_{R-d}^{R} J_i^2(k_{c_{014}} r)r dr \int_0^R J_o^2(k_{c_{011}} r)r dr}{\int_0^R J_i^2(k_{c_{014}} r)r dr \int_{R-d}^{R} J_o^2(k_{c_{011}} r)r dr} \qquad 8.42$$

and

$$\left[\frac{\overline{N_{e_{TE_{014}}}}}{\overline{N_{e_{TM_{011}}}}}\right]_z = \frac{\int_{p-d}^{p} \sin^2\beta_{014}\, z\, dz \int_0^p \cos^2\beta_{011}\, z\, dz}{\int_0^p \sin^2\beta_{014}\, z\, dz \int_{p-d}^{p} \cos^2\beta_{011}\, z\, dz} \qquad 8.43$$

Evaluation of these two terms as $d \to p$ and $g \to R$, respectively, yields Figure 8.10.

Substituting equation 8.37 into equation 8.41 gives

$$\frac{\Delta f_{014}}{\Delta f_{011}} = \frac{(Kf)_{011}}{(Kf)_{014}} \left[\frac{N_{e_{TE_{014}}}}{N_{e_{TM_{011}}}}\right]_r \left[\frac{N_{e_{TE_{014}}}}{N_{e_{TM_{011}}}}\right]_z \qquad 8.44$$

Using this equation, Table 8.2, and Figure 8.10 the perturbation of one mode can be estimated if the other is known. Taking the case where the electron cloud entirely fills the cavity; i.e., $d = p$ and $r = R$, we get $\Delta f_{014} = .20\, \Delta f_{011}$. Thus, a perturbation of 600 kHz in

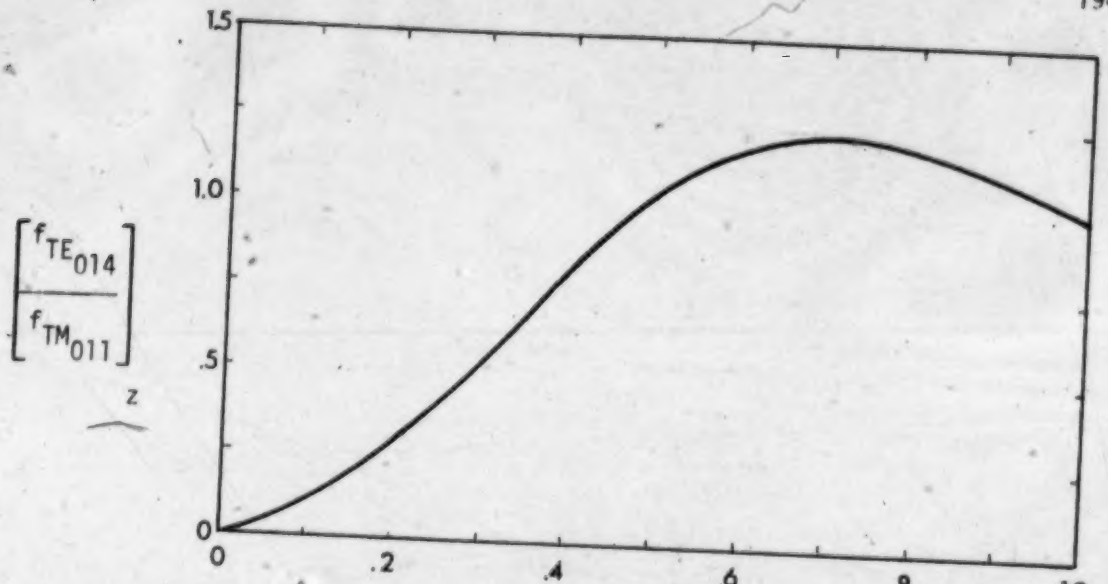

(a) Axial Dependence

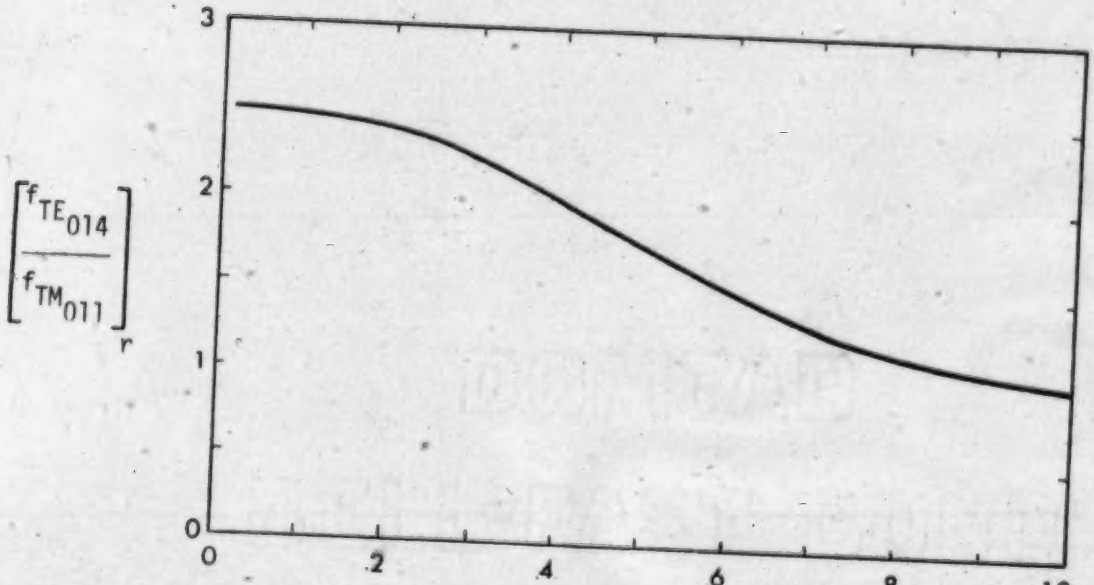

(b) Radial Dependence

Figure 8.10 Comparison of TE_{014} and TM_{011} modes

the TE_{014} mode would signify a perturbation of 3 MHz in the TM_{011} mode.

The power absorbed by a cavity perturbed Δf from its resonant frequency f_o is

$$P = \frac{P_o}{1 + \left(\frac{2\ \Delta f\ Q}{f_o}\right)^2} \qquad 8.45$$

where P_o is the absorption at the unperturbed resonance. The equivalent relation for the electric field is

$$E = \frac{E_o}{\left(1 + \left(\frac{2\ \Delta f\ Q}{f_o}\right)^2\right)^{1/2}} \qquad 8.46$$

Referring to Figure 8.8, the calculated 3 MHz shift occurred at a power of 87 kW peak (94 kV/cm). The effective perturbed field (taking $Q = 7000$) is 6.4 kV/cm. Most of the power is reflected, thus accounting for the high mismatch observed in the main guide during the discharges.

At 6.4 kV/cm the maximum electron energy is between 110 and 440 eV (equation 8.7), close to the minimum energy for unitary secondary electron emission for titania (Figure 2.2). Any further perturbation would result in too low an energy to support multipactor; hence, for the case of a resonant cavity, the perturbation is self limited accounting for the stability of the probing mode during multipactor discharge.

For discs coated with titanium to suppress multipactor the degree of perturbation is also determined by the electron energy; however, the criterion is the ionization efficiency. In conditioning, the absorbed

gas released by heating of the surface is ionized by energetic free electrons. The discharge will continue for the duration of the outgassing provided the field is sufficient to support ionization. Since ionization probability is highest for fields 10 to 30 kV/cm, the shift in resonant frequency is limited to that necessary to reduce the effective peak field to these levels.

8.5.4 Electron Density

In the foregoing, only a comparative analysis has been conducted. The actual electron density has not been calculated.

Taking equation 8.37 and substituting directly the constants for the TE_{014} mode, the averaged density for the recorded perturbation of 600 kHz is 2×10^8 electrons / cm^3. Densities up to 10^{11} cm^{-3} can be measured by this technique, so that this would be an accurate estimate for a multipactor plasma filling the entire volume.

Using this figure some insight can be gained about surface charging. Most of the electrons originate from the ceramic surface leaving a net positive charge. Since the distance from the cavity end wall to the disc was 3.12 cm, this translates as a surface charge density of 10^{-10} coul/cm^2. By Gauss's Law the surface charge gives rise to a field on each side of the interface:

$$E = \frac{\sigma}{\epsilon_0 + \epsilon_2}$$

which in vacuum is 11.8 V/cm. A field strength of this order will not directly affect breakdown; however, it may have other consequences. The

presence of a DC field will help to maintain multipactor even in low RF fields and also contribute to ionization near the disc surface.

Of course with titanium surface coatings the multipactor would be prevented. Even if the film were too thin to suppress electron emission, the surface conductivity would eliminate any subsequent surface charging.

Interpretation of the electron density during the high power discharge is impossible. Even if the perturbation could have been determined, the localized nature of the phenomenon would necessitate use of equation 8.32 to ascertain the true discharge electron density.

Two possible explanations are offered for the inability to measure the TE_{014} mode shift. If the perturbation were actually over 20 MHz the electron density would be excessively high. This also implies a perturbation of 40 MHz in the TM_{011} mode and a reduction of the effective field to 2.5 kV/cm, a value too low to support ionization. More likely is a second explanation: the perturbation was less than 20 MHz, but the electron density fluctuated as the released gas expanded into the cavity. The response of the probe circuit, primarily of the detector, which had a rise time of 100 nsec, was then inadequate to follow the rapidly moving resonance.

CHAPTER 9

EXPERIMENTS WITH MULTI-DISC CAVITY

9.1 Development of a Longer Structure

9.1.1 Introduction

The stated intention of the experiments with the single cell cavity was to simulate the conditions in an accelerating structure with minimum expenditure of discs. Although theoretically valid, in practice the limitations presented by the short cavity, namely, the effect of the coupling iris and the lack of a central hole through the discs, suggested that to make a more complete analysis, a number of experiments should be attempted utilizing a longer structure containing a suitable number of discs. In designing this structure it was intended to build a representative section of what could be a proper accelerator.

9.1.2 The Confluent Structure

One of the advantages of the dielectric structure over its metal counterpart is that it can be operated in the π mode, since confluence between adjacent pass bands is possible, allowing a real phase velocity and good separation between the π and adjacent modes. The confluent structure has been described by Walker and West [107] with emphasis on its advantages.

The basic requirement is that the characteristic wave impedances in the disc and vacuum be identical. These are

$$Z_2 = \left[\frac{\mu}{\epsilon_2} \left(\epsilon_r - \left(\frac{f_c}{f}\right)^2\right) \right]^{\frac{1}{2}} \qquad 9.1$$

$$Z_o = \left[\frac{\mu}{\epsilon_o} \left(1 - \left(\frac{f_c}{f}\right)^2\right) \right]^{\frac{1}{2}} \qquad 9.2$$

and equating gives the condition for confluence,

$$f = f_c \sqrt{\frac{1 + \epsilon_r}{\epsilon_r}} \qquad 9.3$$

Equation 9.3 provides the constraint on equation 4.6 mentioned in section 4.1.3 such that

$$\tan \beta_o p \tan \beta_o q = 1$$

and hence

$$\beta_o p + \beta_2 q = \frac{\pi}{2} \qquad 9.4$$

For a phase velocity = c in the structure the discs must be placed at intervals of $\frac{\lambda}{2}$, making

$$2p + 2q = \frac{\lambda}{2} \qquad 9.5$$

Solving these two equations,

$$p = \tfrac{1}{4} \left(\frac{\beta_2 \lambda - 2\pi}{\beta_2 - \beta_o} \right) \qquad 9.6$$

$$q = \tfrac{1}{4}\left(\frac{2\pi - \beta_o \lambda}{\beta_2 - \beta_o}\right) \qquad 9.7$$

Using titania, $\varepsilon_r = 95$ and a frequency of 2868 MHz the parameters of the structure would be

f_c = 2853 MHz (λ_c = .10453 m)
β_o = 6.14 m^{-1}
β_2 = 585.8 m^{-1}
R = 4.022 cm
2p = 4.736 cm
2q = .487 cm

9.1.3 Practical Considerations of the Confluent Structure

From Figure 5.11, the introduction of a 1.25 cm diameter iris through the disc increased the resonant frequency by 5½ MHz.

As the cavity length is increased to n sections, the perturbing effect of the coupling iris is reduced (see Figure 9.2) but to maintain near unity coupling with the main guide, the iris must be increased by a factor $n^{1/6}$ (from equation 4.12) and for shorter cavities this perturbation should be accounted for. For the case n=4, the measured perturbation was 3 MHz.

There is then a net increase of 8 to 9 MHz which must be compensated for by making the discs thicker. With 2q=.53 cm the 4 disc structure resonated at 2867 MHz in air.

9.2 Low Power Measurements

9.2.1 Introduction

Initial measurements were proceeded with as the discs were being machined and these results have already been incorporated into section 5.2. Once the structure was complete, more comprehensive measurements were conducted although the techniques were identical to those used for the single cell cavity.

9.2.2 Field Profile

Figure 9.1 is the field profile (E^2) of the 4 disc cavity. Similar patterns were made for cavities with from one to five discs and the maximum perturbation (indicating maximum field) in the inter-disc space is given in Table 9.1 for each case. Knowing the effective volume of the bead used (see section 5.2.4) the shunt impedance at any point on the axis may be determined from the profile. In the table the shunt impedance and field shown are for the maximum perturbation; values for other regions can be found by multiplying by the normalization factor in parentheses and its square root respectively.

9.2.3 Effect of Cavity Length on Parameters

As the volume of a cavity is increased the perturbing effect of the coupling iris is reduced. Figure 9.2 shows how, as the cavity is lengthened, the resonant frequency asymptotically approaches the frequency of the loosely coupled structure. There appears to be little difference whether the cavity has discs or is empty.

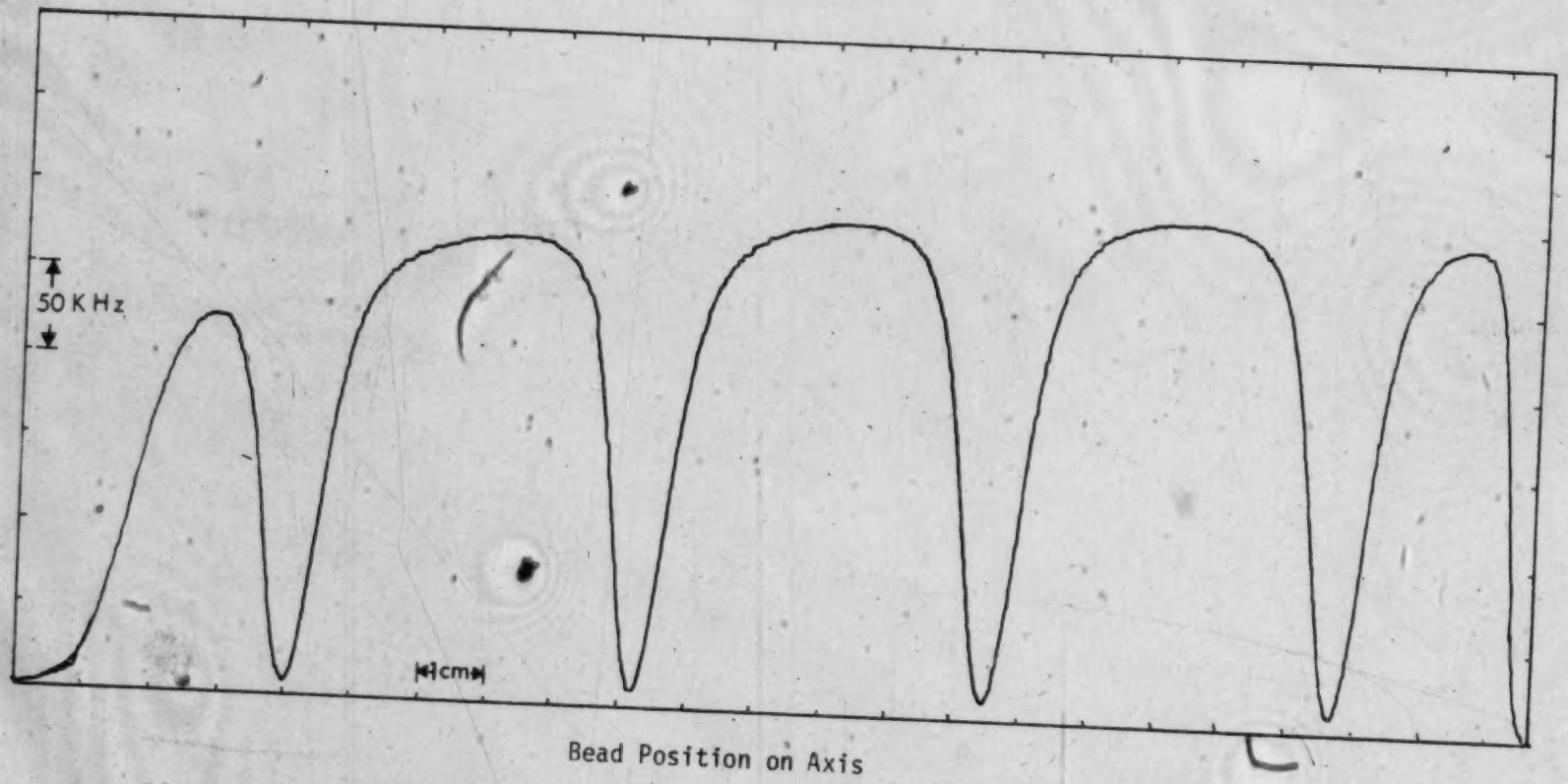

Figure 9.1 Field Profile in a Four Disc Structure
(Perturbation is proportional to E^2)

Table 9.1 Maximum Frequency Perturbation for Various Cavity Lengths (in KHz Using 3.14 mm Dia Bead)

n \ gap	0-1	1-2	2-3	3-4	4-5	5-6	Q_2	R_o/m MΩ/m	$E/W^{\frac{1}{2}}$ KV/cm (W in MW)
0	1010						8000	35.25	367.2
1	960 (.925)	1122 (1)					6750	33.05	355.7
2	460 (.887)	585 (1)	585 (1)				7000	35.73	261.5
3	292 (.850)	380 (.970)	404 (1)	400 (1)			7250	38.35	221.3
4	215 .833	275 (.942)	298 (.981)	310 (1)	300 (.984)		7600	41.0	202.6
5	172 .830	219 .936	230 .959	245 .790	250 (1)	240 (.980)	7750	42.26	179.9

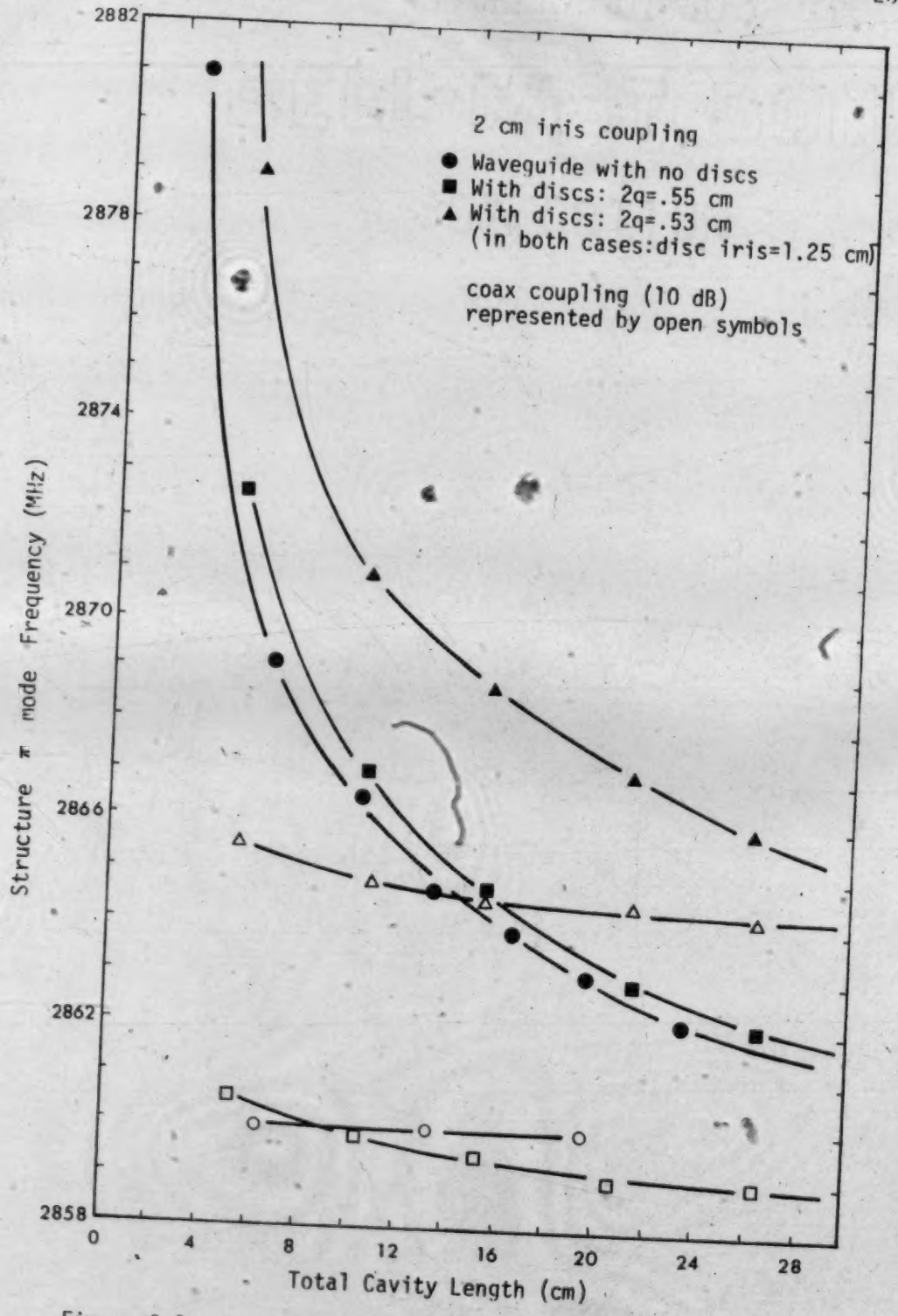

Figure 9.2 Resonant Frequency vs Cavity Length

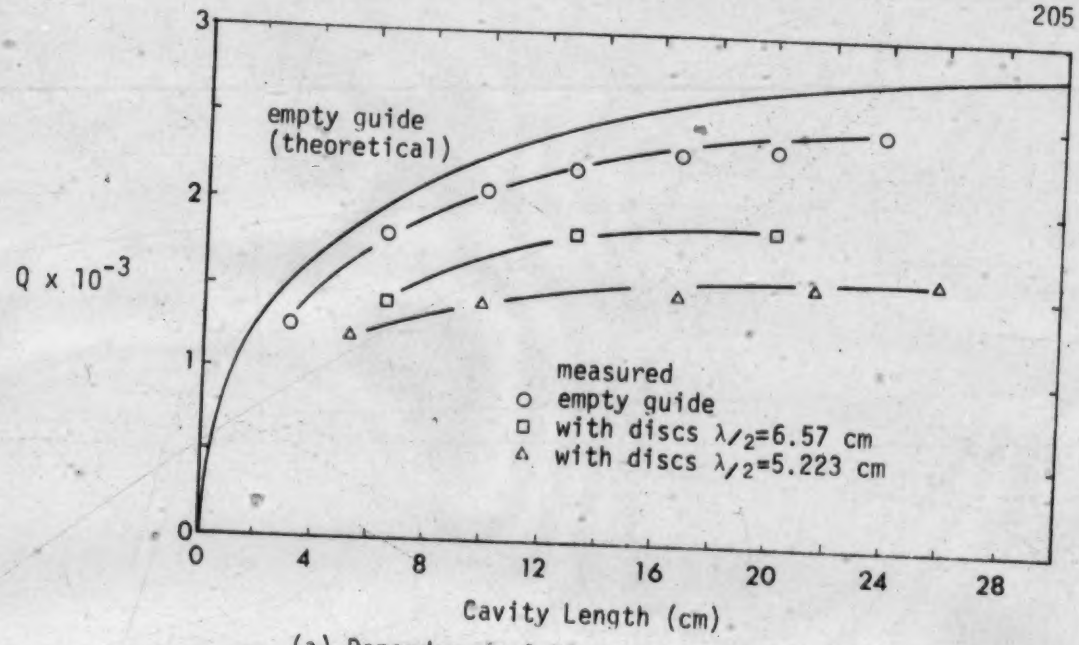

(a) Dependence of Q on Cavity Length

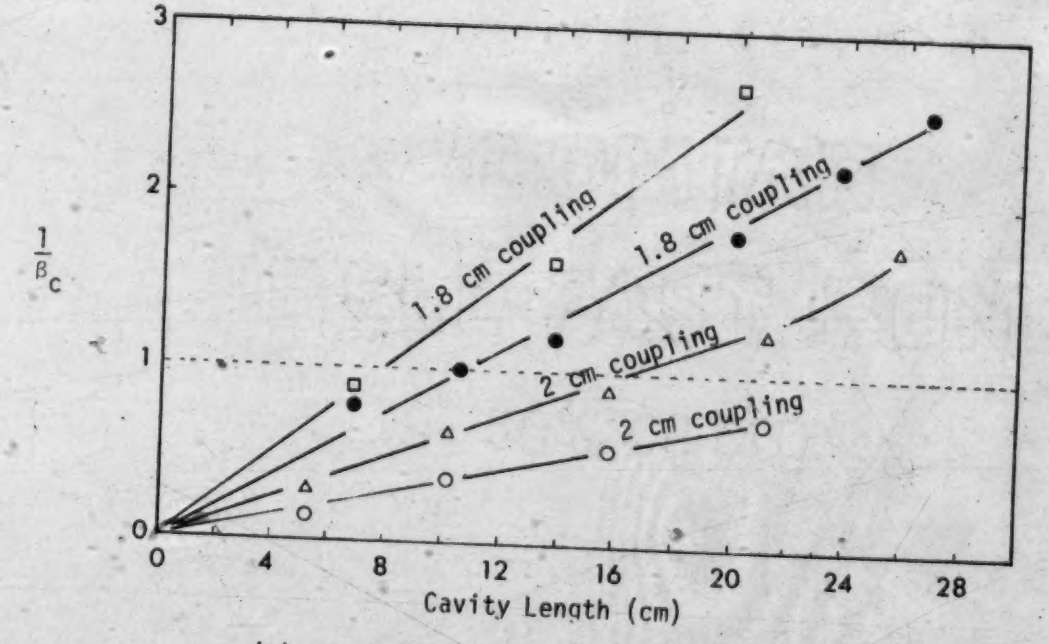

(b) Coupling Coefficient

Figure 9.3 Variation of Cavity Parameters with Cavity Length

The Q for the longer structure is higher than for the corresponding single celled cavity. The losses in the end walls need only be considered once; therefore, taking the notation of section 5.3, the Q may be taken as

$$Q = \frac{\omega U_{sum}}{W_{sum} - (1 - \frac{1}{n})W_{end}} \qquad 9.8$$

Using the values for disc #8, the Q of a three disc structure would be 1.37 times higher than that of the single disc cavity. The measured value was less (Figure 9.3(a)). The variation of Q for the TM_{010} mode was as expected; hence, the disagreement must be due to an error in assessing the loss in the disc. As the ceramic fills a larger proportion of the cavity volume, lengthening the cavity has less effect on Q.

A third parameter which is strongly dependent upon length is the coupling coefficient β_c. It can be seen in Figure 9.3(b) that the factor $\frac{1}{\beta_c}$ has a near linear dependence upon L. For a five disc structure (L =26.1 cm), the minimum iris diameter is 2.2 cm.

9.3 The Electron Gun and Detector Circuits

9.3.1 The Electron Gun

In order to further simulate accelerator conditions, provision was made for installation of an electron gun at one end of the cavity.

For simplicity, CRT electron guns were utilized. The gun, mounted on a plexiglas flange at one end of a glass cylinder, produced a controllable electron beam which was focussed through a 1 cm diameter hole in the aluminum flange at the other end and into the first cavity

section. Pumping of the gun envelope was through the same hole. While not ideal from a vacuum standpoint, such a simple arrangement enabled the mounting of the electron gun without extensive modification. The gun, electrically isolated from the cavity, was placed at -30 kV using a separate DC supply. The necessary anode bias voltages were obtained from resistor dividers and the filament was heated by a 30 kV isolation filament transformer. Coarse adjustment of the beam was mechanical by means of three adjusting bolts, and the CRT deflection plates were used for final alignment. Alignment and focussing was accomplished when the gun was energized, by using a 1 m length of plexiglas rod to rotate the respective potentiometers.

9.3.2 The Gun Trigger Circuit

To determine the effect of the electron beam on the structure operation, a triggering circuit was essential for a pulsed electron beam which could be adjusted in phase with respect to the high power pulse. Since the electron gun cathode and grid were at -30 kV some form of electro-optical coupling device was first considered to transmit the trigger signal to the grid, but because of component availability a microwave link was used. A pulse, extracted from the high power circuit, triggered a pulse generator with variable delay. The delayed pulse modulated a reflex klystron signal source to provide a low power microwave pulse at an antenna. A few cm away, the receiving antenna, at -30 kV, fed the pulse into a detector at the input of a pulse amplifier. The amplifier output was a positive going pulse which switched the CRT grid from -50 to 0 V for the duration of the trigger pulse. Power for

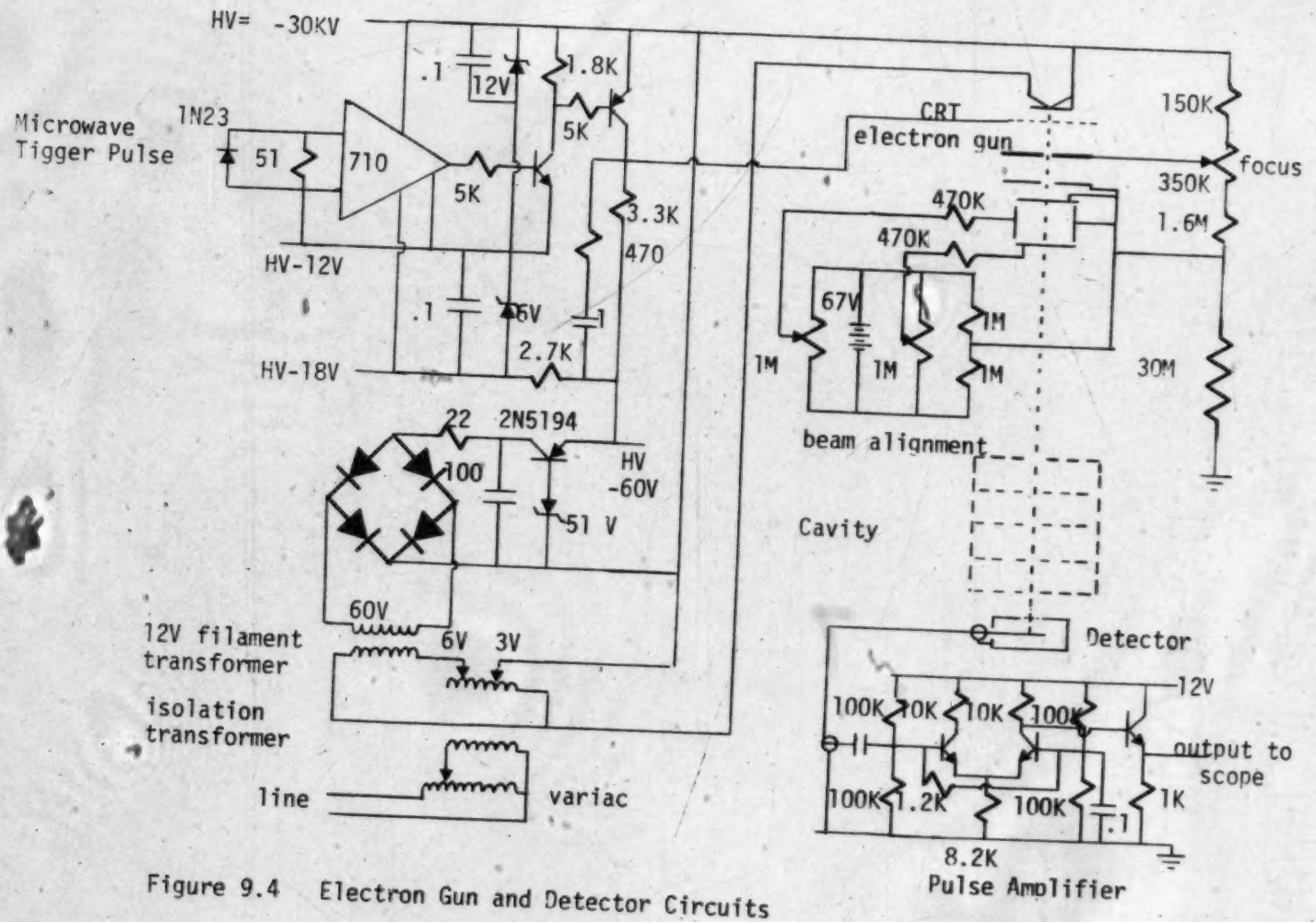

Figure 9.4 Electron Gun and Detector Circuits

the pulse amplifier circuit was derived from the secondary of the filament transformer. The circuit, shown in Figure 9.4, gave pulse lengths of 1 to 10 μsec with rise and fall times of .2 μsec.

The one difficulty inherent in this system was the possibility of leakage from the high power system triggering the circuit. In practice such a leakage occurred in the high power attenuator but simple shielding eliminated this once the source was discovered.

9.3.3 Electron Beam Detector

At the other end of the cavity section, a Faraday cage detector was placed to pick up the electron beam after transit of the cavity. The linear pulse amplifier of Figure 9.4 converted the current pulse to a voltage which could be monitored on an oscilloscope. Since no retarding field was provided, this detector also collected electrons created in the cavity by the microwave field in addition to the electrons in the beam. No provision was made for directly measuring electron energy since the structure was not a practical accelerator, and neither a buncher section nor a graded cavity section was used to preaccelerate the slow injected electrons (.33 c at 30 kV).

The electron beam current at the detector was 2 μamp with a diameter of about 2 mm as observed on a phosphor screen.

9.4 High Power Experiments

9.4.1 Introduction

It was intended to construct a six cavity structure for the experiments and for this purpose six discs were machined to the specifications of section 9.1.3. One of these cracked while being

polished and was discarded. The remaining discs were polished, coated and assembled into a truncated five disc cavity. The characteristics of these discs are given in Table 9.2.

One test was conducted with this structure. After the failure of one of the discs, this was replaced by disc #1 which had been reclaimed from the previous series of tests, and the experiment repeated.

In the third and last experiment, the cavity was shortened to four discs in order to incorporate the electron gun and detector assembly.

The procedure was similar to that followed with the single disc cavities except that no microwave probe was used.

9.4.2 Experimental Results

With the original structure breakdown occurred during the first high power run at 1.3 MW peak power. This corresponded to 205 kV/cm and was much lower than would be expected on the basis of the previous tests.

Failure had occurred in the disc nearest the coupling iris (#12). Investigation under the microscope revealed that this disc had not been properly seated in the copper ring and damage (type 3) was at the edge where a minute gap existed between the ceramic and the ring.

To preclude any multipactor effects due to the copper wall, at this time the interior walls of the cavity were sputtered with a film of titanium, thicker than that placed on the discs, but still much less than the skin depth for copper.

Table 9.2 Disc Characteristics

Disc #	Thickness 2q cm	Coating μm Al_2O_3	Q in TM_{011} mode	Tan δ x10^4	Disc Batch #
12	.530	.83 + Ti	13000	2.1	5
13	.530	.83 + Ti	12560	2.6	5
14	.530	.83 + Ti	13100	2.0	5
15	.530	.83 + Ti	13100	2.0	5
16	.530	.83 + Ti	12540	2.6	5
1	.5612	only Ti	12000	3.0	2
9	.538	1.2 + Ti	12500	2.7	4

Discs #1 and 9 were recovered from previous experiments but only #1 was used.

TM_{011} mode cavity length 5.223 cm

Disc #12 was replaced by disc #1, which was coated with titanium only, the alumina layer having been removed after the previous tests. Two more successful runs were carried out before failure at 1 MW peak power. The first disc, #1, had failed again in a similar manner (type 3) but incorrect seating could not be offered as an excuse. In this case, the absence of the alumina coating may be the explanation for earlier breakdown.

In both experiments the cavity was well behaved up to the point of breakdown. The normal conditioning discharges occurred at low powers but there was no evidence of multipactor. At high power the fluorescence on the glass windows and the distinctive blue glow on the disc surface were more intense than in the other experiments. The higher radiation readings would also suggest the presence of higher energy electrons in the cavity.

The titanium wall coating did not affect the characteristics of the cavity under high power.

9.4.3 Results Using 4 Disc Structure

Difficulties with RF leakage prevented the full use of the electron beam during the first two runs with the 4 disc cavity. These were solved and the beam was used until failure in the forth run at a peak power of 1.7 MW.

Both discs nearest the iris showed some damage on the surfaces facing each other. At a peak axial field of 264 kV/cm a discharge between these two discs resulted in treeing patterns on discs #13 and 14. Titanium was stripped off the cavity wall at two points adjacent

to disc #13. These regions were about 5 mm in diameter and coincided with the damage to this disc. There was evidence of surface discharge about the central iris of disc #14. Titanium had been stripped off the surface and the edge of the iris facing the electron gun had a thin black reduced region. The alumina layer was not damaged by this discharging. The other discs appeared to have had similar discharges on the surface but the titanium was generally intact and except for disc #13 were undamaged.

The discharges were possibly induced by the electron gun. At low power the cavity behaved the same way as in the previous two tests. However, when the electron beam was turned on, the cavity became mismatched to the line, in a similar manner to that encountered with the uncoated discs in the single disc cavity. The beam detector was saturated by free electrons generated within the cavity. By changing the phase of the beam pulse with respect to the power pulse the discharge could be easily controlled. At powers over 400 kW peak, the electron beam had no effect on cavity properties and only random discharges occurred. Prior to breakdown discharges in the cavity initiated discharges within the electron gun envelope. This was probably due to the relatively high pressure in the gun chamber because of the inadequate pumping hole and may have contributed to the failure of the discs.

9.4.4 Summary of Results

The conditions at breakdown for the three experiments are summarized in Table 9.3. The peak axial fields in the neighborhood of the discs are listed in Table 9.4.

Table 9.3 Summary of Breakdown Tests

Test	prf Hz	Average Power		Peak Power MW	Peak Field kV/cm
		Forward W	Into Cavity W		
5 discs #A	100	400	200	1.3	205
5 discs #B	100	380	210	1	180
4 discs #C	60	280	145	1.7	264

Pulse length 3.12 μsec

Table 9.4 Characteristics of Discs After Breakdown

Disc #	Test	Peak Field		Damage Observed
		Cavity kV/cm	At Disc kV/cm	
12	A	205	198	type 3
13	C	264	256	type 3
14	C	264	256	type 3
15	C	264	261	undamaged
16	C	264	264	undamaged
1	B	180	174	type 3

The copper edge coating did not fail in these tests; however, the breakdown fields were generally lower than those observed in the previous tests.

Although the alumina coated discs did stand a higher field than the single uncoated disc, the extent of the damage was about the same in each case. The alumina coating did not prevent treeing at the edge as it had done in the tests of Chapter 7; it should be noted however, that the film thickness of .83 μm was substantially less than that applied to the other discs. The surface protection did appear to be effective near the central iris of the discs where there was evidence of extensive surface discharging during experiments with the electron beam.

The response of the cavity to the electron beam supports the hypothesis of section 8.2.3 regarding ionization probability. The ultimate electron density is a function of the initial free electron density n_o and has an exponential dependence in $\int \alpha_i \, dz$. The electron beam results in a significantly higher n_o allowing discharging at low power when maximum ionization probability is near the axis. However, at high power the probability is considerably reduced on the axis, therefore, despite a high n_o the ultimate electron density is several orders of magnitude lower, insufficient to be recognized as a discharge.

CHAPTER 10

CONCLUDING REMARKS

A series of experiments have been described in which it was attempted to assess the feasibility of utilizing optical coatings to prevent discharge initiated breakdown at a ceramic-vacuum interface in a microwave cavity. The experimental equipment necessary for conducting the research has also been discussed in some detail.

Radio frequency reactive sputtering gave controllable uniform films having excellent adhesion to titania. The slight reduction of the titania evident in the early trials was corrected for by establishing a four stage procedure involving a preliminary 300 Å coating of alumina, subsequent heating of the disc to 825°C in atmosphere to reoxidize both the film and the substrate, further coating of alumina to the required thickness and finally heating of the disc a second time to ensure a fully oxidized alumina film.

Discs so treated evidenced greater probability of low power multipactor discharging than uncoated discs; therefore, Ti overcoating was resorted to in order to reduce secondary electron emission. A film thickness of about 30 Å, corresponding to a surface resistance of 7 kΩ/□ in atmosphere, was found to totally suppress multipactor without significantly contributing to cavity loss. Considerable care was essential in preparing thin Ti films since the metal is highly reactive with both oxygen and nitrogen. Consequently the coated ceramic

had to be at room temperature before exposure to atmosphere and was immediately placed in the vacuum test chamber to limit further oxidation.

Titania discs with the double coating were considerably better behaved in a microwave field than discs that were uncoated or had only the alumina layer. At low power levels, corresponding to peak axial fields less than 100 kV/cm, only occasional conditioning discharges were observed. In contrast multipactor type discharges were prevalent when discs lacking the titanium film were tested.

No disc failures were recorded in this low power region. As shown in section 8.2, a vacuum discharge, either due to multipactor or conditioning, involves an increase in the electron density. The electron cloud effectively changes the permittivity of the vacuum thus perturbing the cavity resonant frequency. The advantage of a resonant structure in such a case is quite obvious: any increase in the charged particle density is counteracted by a reduction in the effective field resulting in a controlled low energy discharge. At low power the discharge tends to fill the entire vacuum space, hence any energy transferred from the field to the electrons is expended over a wide area of the discharge chamber.

The use of the microwave probe technique proved to be very useful not only to determine discharge parameters such as electron density and electron energy but also to distinguish between the different types of discharge, especially those prevalent immediately prior to breakdown. By increasing the number of modes and hence parameters available the method would seem to be of considerable use in analyzing

vacuum discharges.

At higher power levels consideration must be given to thermal effects. In a practical high Q structure, filling time would dictate a pulse length over 3μsec and a reasonable pulse repetition frequency would be demanded; therefore the duty cycles used in the experiments may be considered representative. Power dissipation within the titania consequently becomes a decisive factor. As seen in section 5.4, the cavity resonant frequency is strongly dependent upon temperature, a fact which was readily verified during the experiments. This is overshadowed by the possibility of thermal breakdown at high average powers. Under normal conditions disc fracture could develop due to a 74°C temperature differential across the disc, but localized thermal stresses initiated by impurity defects or discharges will lower the breakdown threshold.

Seven of the eleven discs tested in the single cell cavity experienced some form of fracture. In two this was a result of normal thermal stresses: in the remaining five, the cracking was localized at the edge, evidently due to discharges between the ceramic and copper ring. The fact that two other discs withstood equivalent or higher fields indicated that the problem still lay with the edge coating. Although demonstrating good adhesion to the titania, and apparently uniform both electrically and visually, under microscopic investigation the copper coating was seen to have random holes up to a hundred microns in diameter. Since other discs with a better surface finish had more entire coatings, the source of the trouble was not the film or the coating method, but the ground surface on the circumference.

Having considered the implications of thermal breakdown some remarks can be made regarding discharge initiated breakdown. It was shown in section 8.2 that for the TM mode used, the ionization efficiency of free electrons is highest near the cavity axis for low peak fields and as power increases, the peak of ionization shifts towards the cylindrical wall until at the normally observed breakdown fields it is within a few mm of the wall. The increase of power also releases gas trapped in voids at ceramic and metal interfaces. The result is an intense discharge at the surface of the disc adjacent to the wall. Subsequent reduction of the titania at one point leads to increased loss, local heating and gradually more extensive reduction over a wider area.

The purpose of the surface coating, either glaze or aluminia, is to prevent the initial reduction of the surface. Hayes [108] states an improvement from 150 kV/cm up to 190 kV/cm by the use of the glaze: Free [109] allows that for titania in fields over 100 kV/cm there is no lasting solution unless the titania is glazed, in which case 300 kV/cm can be maintained. From the results obtained in the present work, considering those discs that may be fairly compared, it may be asserted that the alumina coating is as effective in preventing breakdown, allowing in one instance a field of 350 kV/cm. This statement must be qualified in light of comparative tests with uncoated discs and the tests involving the longer, more representative,structure. In the first case, uncoated discs were actually little inferior to the coated discs in ultimate breakdown strength; however, two of the three discs

demonstrated surface damage, whereas the coated discs failed only at the copper coating. In the second series of tests using up to five discs in a single structure, the coated and uncoated discs withstood 256 kV/cm and 174 kV/cm respectively, although the relatively thin alumina film did permit surface damage similar to that on the uncoated disc.

It might be noted that the latter set of tests was more representative of an actual accelerator structure and even then proved capable of withstanding fields over twice those common in operational metal loaded accelerators.

In view of the limited number of discs tested, the conclusions derived from these results must necessarily be guarded. It is seen that titania suitably prepared, when coated with at least one micron of alumina is capable of withstanding higher microwave fields than equivalent uncoated titania. The actual field strength will vary with the film thickness and the particular application but is in excess of 250 kV/cm. It should be noted that there appears to be no great advantage over the glaze at S-band frequencies considering the additional processing required including optical polishing and rather lengthy sputtering period: the advantages will accrue in higher frequency structures where disc dimensions are more diminutive.

REFERENCES

1. Shersby-Harvie, R.B.R., Mullett, L.B., Walkinshaw, W., Bell, J.S., Loach, B.G. "A Theoretical and Experimental Investigation of Anisotropic-Dielectric-Loaded Linear Electron Accelerators", Proc. IEE, 104B (1957) pp. 279-292.
2. Bartholemew, R.F., Frankl, D.R., "Electrical Properties of Some Ti Oxides", Phys. Rev., 187, #3, (1969), pp. 828-33.
3. Devries, R.C., Roy, R., "A Phase DIagram for the System Ti-TiO_2 Constructed from Data in the Literature", Am. Ceram. Soc. Bull. 33, #12, (1954), pp. 370-72.
4. Adler, D., "Insulating Metallic States in Transmission Metal Oxides", Solid State Phys., 21, (Academic Press 1968), pp. 1-113.
5. Frederikse,H.P.R., "Recent Studies on Rutile (TiO_2)", J.A.P., 32, #10, (1961), pp. 2211-15.
6. Hayes, R., "Phenomena Associated with Electrical Breakdown at Certain Dielectric Surfaces in Vacua", University of British Columbia, Department of Electrical Engineering, Report ML-4, (1961).
7. Englefield, C.G., Harwood, V.J., Toso, L.W., "High-Voltage Breakdown of TiO_2 in Vacuo", IEEE ED-14, #8, (1967), pp. 433-9.
8. Ryall, P.J.C., "An Optical Technique for Investigating Dielectric Breakdown", M.Sc. Thesis, University of Alberta (1970).

9. Stratton, R., "Theory of Dielectric Breakdown in Solids", Progress in Dielectrics, 3 (1961), pg. 231.

10. Whitehead, S., Dielectric Breakdown in Solids, Clarendon, Oxford, (1951).

11. Klein, N., "Electrical Breakdown in Solids", Advances in Elect. and Elect. Phys. 26 (1969), pg. 309.

12. O'Dwyer, J.J., Theory of Dielectric Breakdown in Solids, Clarendon, Oxford, (1964).

13. Grant, F.A., "Properties of Rutile (TiO_2)", Rev. Mod. Phys., 31, #3 (July 1959) pp. 646-74.

14. Von Hippel, A., "Electrical Breakdown of Solid Dielectrics", Trans. Faraday Soc., 42A, (1946) pp. 78-90.

15. Fröhlich, H., "Theory of Electrical Breakdown in Ionic Crystals", Proc. Roy. Soc., A160, (1937), pp. 230-41.

16. Seitz, F., "On the Theory of Electron Multiplication in Crystals", Phys. Rev., 76, (1949), pp. 1376-43.

17. Jasberg, J.H., Lebacqz, J.V., "High Power Microwave Windows", Proc. 5th Int. Conf. on Hyperfrequency Tubes Paris (Sept. 1964).

18. Neal, R.B. (Ed.), The Stanford 2-mile Accelerator, W.A. Benjamin Inc., N.Y. (1968), pp. 327-336.

19. Kreuchen, K.H., "Special Problems with Ceramics in High Power Valves", Special Ceramics 1962, Academic Press, (1963), pp. 387-398.

20. Livingston, M.S., Blewett, J.P., Particle Accelerators, McGraw Hill, J.Y. (1962), pg. 345.

21. Priest, D.H., Talcott, R.C., "On Heating of Tubes by Electron Bombardment", IEEE, ED8 (1961), pp. 243-51.

22. Vaughan, J.R., "Some High Power Window Failures", IEEE, ED 8, (1961), pp. 302-8.

23. Hawley, R., Zaky, A.A., "Conduction and Breakdown in High Vacuum", Progress in Dielectrics, 7, (1967), pp. 115-211.

24. Kilpatrick, W.D., "Criterion for Vacuum Sparking Designed to Include Both RF and D.C.", Rev. Sci. Inst. 28, #10, (1957), pp. 824-8.

25. Wakim, F.G., "Photoelectric Properties of Stoichiometric Flux-grown Rutile (TiO_2) Crystals", J.A.P. 44, #1, (Jan. 1973), pp. 496-7.

26. Walker, G.B., Hayes, R., "Vacuum Breakdown at a Glazed Ceramic Surface", Proc. IEE, VII, (1964), pp. 600-4.

27. Luthra, S.P., "Investigation into the Properties of Dielectrics for Microwave Tube Applications", University of British Columbia, Department of Electrical Engineering, Report ML-7, (1962).

28. Chute, F.S., "A Cylindrical Waveguide Resonator Investigation of Ceramic Breakdown at Microwave Frequencies." University of British Columbia, M.Sc. Thesis, 1963.

29. "Diffusion of O in Al_2O_3", Diffusion Data 2, #3, pg. 329.

30. Tigner, M., "Suppression of Multipactor in Evacuated Microwave Cavities", Rev. Sci. Inst., 38, (1967), pg. 444.

31. Talcott, R.C., "The Effects of Ti Films on Secondary Electron Phenomena in Resonant Cavities and at Dielectric Surfaces", IRE ED-9, (1962), pp. 405-10.

32. Dawson, D.H., "Secondary Electron Emission Yields of Some Ceramics", J.A.P. 37, (1966), pp. 3644-5.

33. Bruining, H., Secondary Electron Emission, Pergamon, N.Y., (1954).

34. Bronshtein, I.M., Fraiman, B.C., Vtorichnaya Elektronnaya Emissiya, Nauka, Moskva (1969).

35. Dekker, A.T., "Secondary Electron Emission", Solid State Phys., 6, (Academic Press 1958), pp. 251-311.

36. McKay, K.G., "Secondary Electron Emission", Adv. in Electronics, 1, (1948), pp. 66-130.

37. Hachenberg, O., Brauer, W., "Secondary Electron-Emission From Solids", Adv. in Electronics and Elect. Phys., 11, (1959), p. 413.

38. Seiler, H., "Einige aktuelle Probleme der Sekundarelectronen emission", Z. Angew. Phys., 22, #3 (1967), pp. 249-63.

39. Arifov, U.A., "Secondary Electron-Electron Emission", Interaction of Atomic Particles with a Solid Surface, Consultants Bureau Trans., (1969), pp. 265-87.

40. Bronshtein, I.M., Fraiman, B.C., op. cit [34] pg. 211.

41. Bronshtein, I.M., Fraiman, B.C., Inelastic Scattering of Electrons and Secondary Electron Emission from Certain Metals and Semiconductors", Sov. Phys. Sol. State., 3, #6, (Dec. 1961), pp. 1188-96.

42. Simon, R.L., Williams, B.F., "Secondary Electron Emission", IEEE, NS 15, #3 (1968), pp. 167-170.

43. Bronshtein, I.M., Dolinin, V.A., "Secondary Electron Emission of Solids at Large Angles of Incidence of Primary Beam", Sov. Phys. Sol. State, 9, #9, (1968), pp. 2133-40.

44. McQuillan, A.D., McQuillan, M.K., Titanium, Butterworths, London, (1956), pg. 247.

45. Larson, D.C., "Size Dependent Elect. Conduction in Thin Metal Films and Wires", Phys. Thin Films, 6, (1971), pp. 81-143.

46. Panchishin, R.S., Stasyuk, Z.V., Freik, D.M., "Investigation of Structure and Elect. Cond. of Mo and Ti Thin Films Deposited on NaCl Single Crystals", Sov. Phys. Sol. State. 10, (March 1969), pp. 2149-53.

47. Sondheimer, E.H., "Mean Free Path of Electrons in Metals", Adv. Phys. 1, (Jan 1952), pp. 1-42.

48. Gerstenberg, D., "Structure and Elect. Properties of Evaporated Ti Films", Ann. Phys., 11, #7/8 (1963), pp. 354-64.

49. Chander, R., Howard, J., "Electrical Properties of Thin Ti Films", Indian J.P. App. Phys., 5, #9, (1967), pp. 397-400.

50. Singh, B., Surplice, N.A., "Elect. Resistance and R-T Characteristics of Thin Ti Films", Thin Solid Films, 10, #2 (May 1972) pp. 243-53.

51. Navinchek, B., Carter, G., "Changes in Electrical Resistance of Thin Ti Films Bombarded by Low Energy Ions", Sov. Phys. Tek. Phys., 16, #12, pp. 2003-4.

52. Hass, G., "Preparation, Properties and Optical Applications of Thin Films of TiO_2", Vacuum, 2, (1952), pp. 331-45.

53. Laurenson, L., "Secondary Electron Emission of Evaporated Ti Films", Nature, 199, (20 July 1963), pg. 274.

54. Kaplan, A. Ye., "On the Reflectivity of Metallic Films at Microwave and Radio Frequencies", Rad. Eng. and Elect. Phys., 9, #10, pg. 1976.

55. Korolev, F.A., Gridnev, V.I., "Transmission of E.M. Waves Through Thin Silver Films", Rad. Eng. and Elect. Phys., 10, (Sept. 1965), pp. 1476-77.

56. Ramey, R.L., Lewis, T.S., "Properties of Thin Metal Films at Microwave Frequencies", J.A.P., 39, #3, (1968), pp. 1747-52.

57. Ramo, S., Whinnery, J.R., Van Duzer, T., Fields and Waves in Communication Electronics, J. Wiley and Sons, Inc., N.Y. (1965), pg. 252.

58. Grove, W.R., "On the Electro-Chemical Polarity of Gases", Phil. Trans. Roy. Soc., 142, (1852), pp. 87-101.

59. A Bibliography of Sputtering, R.D. Mathis Co., Long Beach, Calif.

60. Blevis, E.H., "Hot Cathode and RF Sputtering", R.D. Mathis Co., Long Beach, Calif. (1965), pg. 10.

61. Trillat, J.J., "Ionic Bombardment, A New Method for the Study of Surfaces", Ionic Bombardment: Theory and Applications, Gordon and Beach, Sci. Pub., N.Y. (1964) pg. 21.

62. Kaminsky, M., Atomic and Ionic Impact Phenomena on Metal Surfaces, Academic Press/Springer Verlag, (1965), pg. 170.

63. Maissel, L.I., "Deposition of Thin Films by Cathode Sputtering", Phys. Thin Films, 3, (Acad. Press 1966), pp. 103-6.

64. Maissel, L.I., op cit [63], pp. 100-102.

65. Holland, L., Vacuum Deposition of Thin Films, Chapman and Hall Ltd., London (1963), pg. 220.

66. Behrndt, K.H., "Film Thickness and Deposition Rate Monitoring Devices and Techniques for Producing Films of Uniform Thickness", Phys. Thin Films, 3, (1966), pp. 1-59.

67. Bennett, H.E., Bennett, J.M., "Precision Measurement in Thin Film Optics", Phys. Thin Films, 4, (1967), pp. 1-96.

68. King, D., Hoffman, G.R., "Observations on a Quartz Crystal Deposition Monitor", J. of Phys. E (Sci. Inst.), 4, (1971), pg. 993.

69. Holland, L., Priestland, C.R.D., "Influence of Sputtering and Transport Mechanisms on Target Etching and Thin Film Growth", Vacuum, 22, #4, (April 1972), 2 parts, pp. 133-149.

70. Priestland, C.R.D., Hersee, S.D., "Effects of Pressure on Deposition Rate in R.F. Sputtering Processes", Vacuum, 22, #3, (March 1972), pp. 103-106.

71. Banning, M., "Practical Methods of Making and Using Multilayer Filters", J. Opt. Soc. Amer., 37, (1947), pp. 792-97.

72. Granger, P., Priestland, C.R.D., "Design and Performance of an R.F. Sputtering Machine with Continuous Production Facility", Vacuum, 21, #6, (1971), pg. 304.

73. Carter, G., Colligon, J.S., Ion Bombardment of Solids, Heinemen, London, (1968), pp. 310-353.

74. Bennett, op. cit. [67].

75. Hayes, op. cit. [6], pg. 74.

76. Hayes, op. cit. [6], pg. 177.

77. Slater, J.C., Microwave Electronics, Dover, N.Y. (1969), pg. 152.

78. Carslaw, H.S., Jaeger, J.C., Conduction of Heat in Solids, Clarendon, Oxford, 2nd ed. (1959), pg. 191.

79. Timoshenko, S., Goodier, J.N., Theory of Elasticity, McGraw Hill, N.Y. 2nd ed. (1951), pp. 407-410.

80. Timoshenko, S., Strength of Materials (Pt. 2), Van Nostrand, N.Y. 3rd ed. (1956), pp. 205-212.

81. Benjaminson, A., "Phase Locking Microwave Oscillators to Improve Stability", Microwave Journal, 6, #1 (Jan 1961).

82. Zimmerer, R., "Transistor Phase Detector for Phase Locking of 30 GHz Klystron", Rev. Sci. Inst., 30, pg. 1052.

83. George, A.J., Teaney, D.T., "Transistorized Lock-in for Klystron AFC", Rev. Sci. Inst., 31, (1960), pg. 997.

84. Poynter, R.L., Steffenson, G.R., "A Tunable, High Stability Microwave Oscillator", Rev. Sci. Inst., 34, (1963), pp. 77-85.

85. Caplan, L.C., Stern, R., "An Inexpensive Lock-in Amplifier", Rev. Sci. Inst., 42, #5, (May 1971), pp. 689-95.

86. Harvey, A.F., Microwave Engineering, Academic Press, London, (1963), Chapter 19.

87. Handbook of Op. Amp. Applications, Burr Brown Res. Pub., (1963), pg. 66.

88. Data Specification Sheet - MFC6040, Motorola Semiconductor Products.

89. Handbook of Active R-C Networks, Burr Brown Res. Pub., (1966), pg. 91.

90. Data Specification Sheet - MC1494, (also Application Notes 489 and 490) Motorola Semiconductor Products.

91. Ginzton, E.L., Microwave Measurements, McGraw Hill, N.Y. (1952), pg. 438.

92. Ginzton, op. cit. [91] pg. 440.

93. Ramo, op. cit. [57], pg. 550.

94. Report on Pulse Generator ECRDC Project T42, Marconi (Canada).

95. Glasoe, G.N., Pulse Generators, Rad. Lab. Series, Vol. 5, MIT-McGraw Hill, N.Y. (1948).

96. Specification Sheet VC-701 Magnetron, Varian Associates.

97. Slater, op. cit. [77], pg. 101.

98. Huddlestone, R.H., Leonard, S.L., Plasma Diagnostic Techniques, Academic Press, N.Y. (1965), pg. 499.

99. Biondi, M.A., Brown, S.C., "Measurement of Ambipolar Diffusion in H_2 Using Microwaves", Phys. Rev., 75, #11 (1949), pg. 1700.

100. Heald, M.A., Watson, C.B., Plasma Diagnostics with Microwaves, J. Wiley and Sons, N.Y. (1965).

101. Nasser, E., Fundamentals of Gaseous Ionization and Plasma Electronics, Wiley-Inter Science, N.Y. (1971), pg. 547.

102. Green, H.S., Leipnik, R.B., Sources of Plasma Physics - I, Walters-Noordhoff Pub. Co., Neth., (1970), pg. 168.

103. Lewin, G., Vacuum Science and Technology, McGraw-Hill, N.Y. 1965, pg. 95.

104. Dougherty, C., Electrodynamics of Particles and Plasmas, Add. Wes., N.Y. (1969), pg. 140.

105. Ramo, op. cit. [57], pg. 443.

106. Luthra, op. cit. [27], pg. 23.

107. Walker, G.B., West, N.D., "Mode Separation at the π-mode in Dielectric Loaded Waveguide Cavity", Proc. IEE, 104C, (1957), pp. 381-7.

108. Hayes, op. cit. [6], pg. 218.

109. Free, J.M., "Use of Ceramic Materials in Particle Accelerators and Amplifiers Operating at Microwave Frequencies", Special Ceramics 1962, Academic Press (1963), pp. 411-426.

110. Specification Sheet for CT95 Ceramic, Schaefer Dielectrics, Cambridge, England.

111. Salmang,H., Ceramics: Physical and Chemical Fundamentals, Butterworths, London (1961), pg.345.

112. Buessen, W.R., Bush, E.A.,"Thermal Fracture of Ceramic Materials under Quasi-static Thermal Stresses (Ring Test)",J. Am. Ceram. Soc., 38,#1 (1955), pg.27.

113. Touloukian, Y.S.(Ed.), Thermo-Physical Properties of Materials, IFI, Plenum, N.Y. (1970), Vol.5 :Specific Heat, pg. 246.

114. op. cit. [113], Vol.2 :Thermal Conductivity, pg. 208.

115. op. cit. [113], Vol.8 :Thermal Radiative Properties, pg. 402.

APPENDIX A

PROPERTIES OF TITANIA

The relevant physical properties of titania are summarized in Table A.1. These values are strongly dependent upon conditions during manufacture and variables such as temperature at the time of testing. The values given by Schaefer [110] have been taken as relating to the actual ceramic used in the experiments; however they have been qualified in some instances by data from the literature and from measurements conducted in the course of the work.

Under test the ceramic was subjected to temperatures over a range from 20 to 200°C. Consequently the temperature dependence of individual properties must be taken into account. A particular case is thermal conductivity which may vary from sample to sample depending upon the method of manufacture and previous thermal treatment. The degree of uncertainty can be seen in Figure 4.9. Although DC resistance decreases with increasing temperature, the same is not necessarily true of $\tan\delta$ at microwave frequencies and it may be taken as constant within the stated temperature range.

The mechanical properties of titania, especially the failure stresses, can not be specified accurately; however from the range of observed values it is possible to assess a threshold under which there is little probability of fracture.

Table A.1 Physical Properties of Titania

Density	4.2 gm/cc	[110]
Melting Point	1830 - 1850 °C	[3]
Elasticity (Young's Modulus)	1.0×10^6 kg/cm^2	[110]
Rupture Strength	900-- 1500 kg/cm^2	[111]
Crushing Strength	3000 - 9000 kg/cm^2	[111]
Tensile Strength	300 - 800 kg/cm^2	[111]
Coefficient of Linear Expansion	8×10^{-6} /°C	[110]
	$6 - 8 \times 10^{-6}$ /°C	[112]
Heat Capacity	.17 - .19 cal/gm-°C	[113]
Thermal Conductivity	8×10^{-3} cal/cm-sec-°C	[110]
	(see Figure 4.9)	[114]
Dielectric Constant	95 ± 1	[110]
Thermal Coefficient	-9×10^{-4} /°C	[110]
	-8×10^{-4} /°C	[111]
Loss Tangent	<.001 (10^4 - 10^{10} Hz)	[110]
Resistivity	10^{13} - 10^{14} Ω cm	[111]
Dielectric Strength	160 kV/cm	[110]
	150 kV/cm (50 Hz)	[111]
Thermal Emissivity	.5	[115]

APPENDIX B

ERROR ANALYSIS

The numerical values derived from measurements are subject to experimental errors which may be evaluated by considering the individual instrument errors and the associated uncertainties in the calibration procedure. The sources of error and the estimated error limits are given below for the more important quantities.

Low Power Measurements

Frequency (1 ppm in 3 GHz for counter)	± 3 kHz
$\frac{R_0}{Q}$ frequency (Δf = 900 kHz)	± .3 %
X-Y recorder (±.2 % of full scale)	± .4 %
tracking error (Figure 5.5)	< ± 1 %
thermal drift (Figure 5.13)	< ± 2 %
total error in frequency	< ± 3.7 %
micrometer position	± 1 %
total error in $\frac{R_0}{Q}$	< ± 3.8 %
Q frequency (Δf = 400 kHz)	± .7 %
X-Y recorder	± .4 %
thermal drift	< ± 2 %
total error in frequency	< ± 3.1 %
divider linearity	± 2 %
X-Y recorder	± .4 %
total error in power ratio	± 2.4 %
total error in Q	< ± 4 %

High Power Measurements

Average Power Calibration

mass flow rate (flowmeter ±1 % of FS)	± 3.3 %
temperature (.05°C in 2°C)	± 1 %
calibration error	± 4.3 %

Average Power from Power Meter

initial calibration error	± 4.3 %
instrument error	± 1 %
attenuator resetability	± 2.2 %
error in average power	± 7.5 %

Peak Power

initial calibration error (from power meter specifications)	± 3.7 %
attenuator resetability	± 2.2 %
oscilloscope calibration error	± 2 %
oscilloscope reading error	± 2.5 %
error in peak power	± 10.4 %

Error in calculated peak field (from equation 5.24) $\frac{3.8 + 4 + 10.4}{2}$ $< \pm$ 9.1 %